POINT DEFECTS AND DEFECT-RELATED TRANSPORT OF MATTER IN TRANSITION METAL-CONTAINING ORTHOSILICATES

A Dissertation

Presented to the Faculty of the Graduate School

of Cornell University

in Partial Fulfillment of the Requirements for the Degree of

Doctor of Philosophy

by

Qi Tang

August 2012

© 2012 Qi Tang

All RIGHTS RESERVED

POINT DEFECTS AND DEFECT-RELATED TRANSPORT OF MATTER IN TRANSITION METAL-CONTAINING ORTHOSILICATES

Qi Tang, Ph.D.

Cornell University 2012

Point defects and defect-related transport properties of transition metal-containing orthosilicates with the olivine structure are interesting topics but are not yet well understood. At high temperatures, the transport properties of sufficiently pure olivines are governed by point defects. To improve the currently limited understanding of the defect structure and defect-related transport properties of olivine group compounds, the transport of matter in orthosilicates of the type Me_2SiO_4, with Me = Co and Mn, was experimentally investigated. The cation tracer diffusion of cobalt and manganese in cobalt and manganese orthosilicates, respectively, was studied as a function of crystal orientation, oxygen activity and temperature using high purity, synthetic cobalt and manganese orthosilicate single crystals grown by the floating zone method. Modeling of the observed oxygen activity dependancies of the cation tracer diffusion coefficients and of point defect concentrations was performed based on data obtained from this study in conjunction with other defect-related data reported in literature.

The oxygen activity dependence of the diffusion of cobalt in Co_2SiO_4 along the three principle orientations at 1300 °C at high oxygen activities is compatible with cobalt vacancies and holes as majority defects. At lower oxygen activities, the oxygen activity dependence of the cobalt tracer diffusion coefficients becomes smaller than at higher oxygen activities, which is most likely related to an increase in concentrations of cobalt interstitials. When using the space group Pbnm for assigning crystal orientations, the ratio found for the cobalt tracer diffusion coefficients at $a_{O_2} = 1$ is approximately $D^*_{Co[001]}:D^*_{Co[010]}:D^*_{Co[100]} = 30:3:1$.

The oxygen activity dependence of the diffusion of manganese in Mn_2SiO_4 along the three principle orientations at 1200 °C is, at high oxygen activities, compatible with manganese vacancies and holes as majority defects. The observed oxygen activity dependence of the diffusion of manganese in Mn_2SiO_4 also suggests that at high oxygen activities, high mobility minority defects, which are most likely associates formed between holes and manganese vacancies, also contribute very significantly to the manganese tracer diffusion. At lower oxygen activities, the observed weaker oxygen activity dependence of the Mn tracer diffusion coefficient compared to that at higher oxygen activities can be attributed to an increased concentration of manganese interstitials and their increased contribution to the transport of Mn in Mn_2SiO_4. A similar observation was found for the diffusion of Co in Co_2SiO_4 at lower oxygen activities. The ratio found for the manganese tracer diffusion coefficients at $\log a_{O_2} = -2.7$ is approximately $D^*_{Mn[001]}:D^*_{Mn[010]}:D^*_{Mn[100]} = 5.3:2.2:1$.

BIOGRAPHICAL SKETCH

Qi Tang was born on February 11, 1986 in Jiujiang, a city located at the southern shores of the Yangtze River in Jiangxi Province, China. She attended schools in her hometown through her high school. In Fall 2003, she began her undergraduate education at Harbin Institute of Technology in Harbin, a historical city in the northeast of China. Two years later, she studied at Hong Kong Polytechnic University for one semester as an exchange student. In 2007 she received a Bachelor of Engineering degree in Materials Science and Engineering with a concentration in ceramics. In Fall 2007 she came to the United States and joined the Ph. D. program to study ceramics with Professor Rüdiger Dieckmann in the Department of Materials Science and Engineering at Cornell University in Ithaca, New York.

TO MY PARENTS

ACKNOWLEDGMENTS

This work would not have been possible without the help of many people. In particular, I would like to express my deepest appreciation to my advisor, Professor Rüdiger Dieckmann, for his excellent guidance and tremendous support. His depth of knowledge, leadership, attention to details and hard work have always set an example to me as a researcher in science and engineering. His consistent encouragement has helped me through many frustrations throughout this research.

I would also like to express my appreciations to Professor Michael Thompson and Professor Michael Spencer for serving on my thesis committee and their valuable advice.

I extend my appreciations to the Dieckmann group members, my friends in Bard Hall for their friendship and assistance. Many thanks to facility managers at CCMR (Cornell Center for Materials Research) who taught me about many details related to materials characterization. I would like to particularly thank Dr. Maura Weathers, John Grazul, John Hunt and Paul Bishop for assistance related to a variety of topics. Special thanks to Dr. Michael Rutzke from the Department of Food Science, Cornell University, for allowing me to use facilities in his lab.

Finally I would like to thank my parents, my husband and my best friends for their love and support. They have taught me so many things in life and have always been there for me.

TABLE OF CONTENTS

LIST OF FIGURES x

LIST OF TABLES xx

1. INTRODUCTION 1

1.1. Introduction and Background 1

1.1.1. Classification of Silicates 1

1.1.2. Transition Metal-Containing Orthosilicates of Olivine Type 2

1.1.3. Structure of Olivines 3

1.2. Point Defects in Binary Non-Stoichiometric and Ternary Oxides 6

1.2.1. Classification of Defects in Crystalline Materials 6

1.2.2. Types of Point Defects in Ionic Compounds 7

1.2.3. Types of Disorder in Ionic Compounds 8

1.2.3.1. Thermal Disorder 9

1.2.3.2. Component Activity Dependent Disorder 10

1.2.4. Point Defect Thermodynamics 11

1.2.5. Point Defects in Binary Non-Stoichiometric Oxides 12

1.2.5.1. Oxygen Activity Dependence of Point Defect Concentrations 12

1.2.5.2. Influence of Impurities on Point Defect Concentrations 18

1.2.6. Point Defects in Ternary Non-Stoichiometric Oxides 21

1.3. Transport of Matter and Charge in Binary and Ternary Oxides . . . 25

1.3.1. Diffusion and Electrical Conduction 25

1.3.2. Transport of Matter and Charge in Binary Non-Stoichiometric Oxides 29

1.3.3. Transport of Matter and Charge in Ternary Non-Stoichiometric Oxides 32

1.4. Anisotropy in Transport Properties of Olivines 35
1.4.1. Representation of Diffusion Coefficients as Second Rank Tensors 35
1.4.2. Orientation Dependence of Transport Properties of Olivines 36
1.5. Single Crystal Growth of Olivines 38
1.5.1. Demand for Single Crystal Growth 38
1.5.2. Single Crystal Growth Techniques 39
1.6. Thesis Overview 47
References 49

2. FLOATING ZONE GROWTH AND CHARACTERIZATION OF COBALT ORTHOSILICATE, Co_2SiO_4 52
2.1. Abstract 52
2.2. Background 52
2.2.1. Previous Growth of Single Crystals of Co_2SiO_4 and Similar Orthosilicates 54
2.2.2. Thermodynamic Stability of Co_2SiO_4 58
2.3. Experimental 63
2.3.1. Powder Synthesis 63
2.3.2. Feed Rod Preparation 65
2.3.3. Seed Crystal Preparation 66
2.3.4. Crystal Growth 68
2.3.5. Characterization 69
2.4. Results and Discussion 74
2.5. Summary 83
References 85

3. ORIENTATION, OXYGEN ACTIVITY AND TEMPERATURE DEPENDENCIES OF THE DIFFUSION OF COBALT IN COBALT ORTHOSILICATE, Co_2SiO_4 90

3.1. Abstract 90
3.2. Introduction 91
3.3. Experimental 105
3.3.1. Crystal Growth 105
3.3.2. Cobalt Tracer Diffusion Experiments 106
3.4. Results 110
3.5. Discussion 115
3.5.1. Point Defect Chemistry 115
3.5.2. Comparison of Current Cobalt Tracer Diffusion Data with Earlier Diffusion Data 119
3.5.3. Orientation Dependence of Cobalt Tracer Diffusion 121
3.5.4. Temperature Dependence of the Cobalt Tracer Diffusion 125
3.5.5. Oxygen Activity Dependence of Cobalt Tracer Diffusion 127
3.6. Conclusions 134
References 136

4. FLOATING-ZONE GROWTH AND CHARACTERIZATION OF SINGLE CRYSTALS OF MANGANESE ORTHOSILICATE, Mn_2SiO_4 141
4.1. Abstract 141
4.2. Background 142
4.2.1. Previous Single Crystal Growth of Mn_2SiO_4 and Similar Orthosilicates 144
4.2.2. Thermodynamic Stability of Mn_2SiO_4 148
4.3. Experimental 155
4.3.1. Powder Synthesis 155

4.3.2. Feed Rod Preparation 159
4.3.3. Seed Crystal Preparation 160
4.3.4. Crystal Growth 167
4.3.5. Characterization 169
4.4. Results and Discussion 173
4.5. Summary 186
References 188

5. ORIENTATION, OXYGEN ACTIVITY AND TEMPERATURE DEPENDENCIES OF THE DIFFUSION OF MANGANESE IN MANGANESE ORTHOSILICATE, Mn_2SiO_4 192
5.1. Abstract 192
5.2. Background 193
5.3. Experimental 204
5.3.1. Single Crystal Growth 204
5.3.2. Manganese Tracer Diffusion Experiments 205
5.4. Results 208
5.5. Discussion 217
5.5.1. Point Defect Chemistry 217
5.5.2. Oxygen Activity Dependence of the Manganese Tracer Diffusion 221
5.5.3. Oxygen Activity Dependence of the Electrical Conduction in Mn_2SiO_4 231
5.5.4. Temperature Dependence of the Manganese Tracer Diffusion 232
5.5.5. Orientation Dependence of the Manganese Tracer Diffusion 236
5.6. Conclusions 238
References 239

6. SUMMARY AND CONCLUDING REMARKS 242

LIST OF FIGURES

Figure 1.1: Olivine crystal structure denoted by using the space group Pbnm. 4

Figure 1.2: Schematic plots of point defect concentrations in pure $Me_{1-\Delta}O$ as a function of oxygen activity for three cases: a) $K_F \ll K_e$, b) $K_F = K_e/4$ and c) $K_e \ll K_F$. 17

Figure 1.3: Kröger-Vink diagrams generated using the same equilibrium constants as those used for generating Figure 1.2b but with the presence of a) a small concentration of the alio-valent impurity M^+ ($[(M^{+}_{Me^{2+}})'] = K_e^{1/2}$), b) a large concentration of the alio-valent impurity M^+ ($[(M^{+}_{Me^{2+}})'] = 10 \cdot K_e^{1/2}$), c) a small concentration of the alio-valent impurity Mx^{3+} ($[(Mx^{3+}_{Me^{2+}})^{\bullet}] = K_e^{1/2}$), and d) a large concentration of the alio-valent impurity Mx^{3+} ($[(Mx^{3+}_{Me^{2+}})^{\bullet}] = 10 \cdot K_e^{1/2}$). M^+ and Mx^{3+} ions are assumed to be located on M-sites.. 20

Figure 1.4: Schematic plots illustrating the relationships between oxygen activity dependencies of a) concentrations of point defects, b) the deviation from stoichiometry Δ in $Me_{1-\Delta}O$, c) cation diffusion coefficients, and d) electrical conductivities in the model oxide $Me_{1-\Delta}O$ for the very special case when $K_F = K_e/4$. 31

Figure 1.5: Results from a systematic study of the point defect structure and of defect- related properties of $Fe_2SiO_{4+\delta}$ at 1130 °C performed by Tsai et al. [11]: a) Kröger-Vink diagram compatible with experimental results for the

variation of the oxygen content, the electrical conduction and the iron tracer diffusion in $Fe_2SiO_{4+\delta}$, b) relative mass changes observed in fayalite upon oxygen activity changes, c) orientation and oxygen activity dependencies of the iron tracer diffusivity in $Fe_2SiO_{4+\delta}$, and d) results of electrical conductivity measurements as a function of the oxygen activity and crystallographic orientation. 34

Figure 1.6: A schematic illustration of an assembly consisting of a feed rod, a molten zone and a seed crystal in a floating zone single crystal growth experiment and the vertical temperature distribution produced. 44

Figure 2.1: A diagram showing data related to the thermodynamic stability range of cobalt orthosilicate at high temperatures at 1 atm total pressure. Information about the data used to derive this diagram is provided in Section 2.2.2. 59

Figure 2.2: Photographs showing single crystals of Co_2SiO_4 grown along the three principle orientations: a) [100], b) [010] and c) [001]. 74

Figure 2.3: Laue back reflection patterns for single crystals of Co_2SiO_4 grown along different principle orientations: the top row shows experimentally obtained patterns and the bottom row simulated patterns. B stands for the number 11. 75

Figure 2.4: Photographs and schematic drawings of cross sections of single crystals of Co_2SiO_4 grown along different principle directions: left [100], middle [010], and right [001]. 76

Figure 2.5: Photograph of the surface of a Co_2SiO_4 disc prepared by cutting perpendicular to the growth direction [010] after etching by using an aqueous solution of HCl. The photograph was obtained by using an optical microscope. 78

Figure 2.6: TEM picture of a part of a single crystal of Co_2SiO_4 with a few precipitates most likely consisting of SiO_2. 81

Figure 3.1: An oxygen activity vs. temperature diagram showing data related to the thermodynamic stability range of cobalt orthosilicate, Co_2SiO_4, at high temperatures at 1 atm total pressure. Information about the data used to derive this diagram can be found in Ref. [10]. 95

Figure 3.2: Data available from the literature [7,8] for the deviation from stoichiometry, δ, in $Co_2SiO_{4+\delta}$ at $a_{SiO_2} = 1$. The slopes of the lines shown are compatible with $\delta \propto a_{O_2}^{1/6}$, suggesting that vacancies on cobalt sites and holes are the majority defects at the conditions considered in this figure. 97

Figure 3.3: Data available from the literature [9,11] for the electrical conductivity of Co_2SiO_4. The line summarizing the data from Ref. [11] corresponds to $\sigma \propto a_{O_2}^{1/7.7}$. 99

Figure 3.4: Temperature dependence of diffusion coefficients for Co, Si and O diffusing in Co_2SiO_4 in air at atmospheric pressure available from the literature. The values for D^*_{Co} are from Ref. [17] and for D^*_{Si} from Ref. [12]. One value for D^*_O at 1320 °C is from Ref. [12] and the second one for 1220 °C was found cited in Ref. [17]. 101

Figure 3.5: Normalized residual radioactivity profile, A(x,t)/A(x=0,t) vs. x. A(x,t) is the residual radioactivity measured when material of the thickness x has been removed from the sample and A(x=0,t) is the residual radioactivity before any material removal. t is diffusion-annealing time. The data shown are for a tracer diffusion experiment performed at 1300 °C at log $a_{O_2} = -1.69$ with a diffusion-annealing time $t \approx 687{,}500$ s. 109

Figure 3.6: Plot of the inverse function of the error function of the argument [1−A(x,t)/A(x=0,t)] vs. x for the same experiment as that considered in Figure 3.5. This type of plot was generated for all performed tracer diffusion experiments when determining values for cobalt tracer diffusion coefficients by fitting Equation (3.3) to the experimental data. 110

Figure 3.7: Tracer diffusion coefficients measured for the diffusion of cobalt in Co_2SiO_4 at 1300 °C and $a_{SiO_2} = 1$ along the principle orientations [100], [010] and [001] as a function of the oxygen activity. One data point from the literature [17] for the diffusion of Co in polycrystalline Co_2SiO_4 is also shown for comparison. The lines shown are guides to the eye only. 112

Figure 3.8: Temperature dependencies of cobalt tracer diffusion coefficients measured for Co_2SiO_4 at $a_{SiO_2} = 1$ between 1200 and 1300 °C along the principle orientations [100], [010] and [001] in pure oxygen at 1 atm total pressure. Two data points from the literature [17], extrapolated to $a_{O_2} = 1$, for the diffusion of Co in polycrystalline Co_2SiO_4 are also shown for comparison. The lines shown were generated by fitting Equation (3.13) to the experimental data shown in the plot. 120

Figure 3.9: A partially estimated, somewhat speculative Kröger-Vink diagram for $Co_2SiO_{4+\delta}$ at 1300 °C and $a_{SiO_2} = 1$ which is compatible with all currently available information on oxygen activity dependencies of the deviation from stoichiometry, δ, the cobalt tracer diffusion and the electrical conductivity. 131

Figure 3.10: Comparison of oxygen activity dependencies obtained, departing from Figure 3.9, a) for the tracer diffusion coefficient of Co, D^*_{Co}, and b) for the electrical conductivity, σ, for Co_2SiO_4 at 1300 °C. To obtain values for D^*_{Co}, it was assumed that the diffusion via interstitials is 0.37 times as fast as that via vacancies. For the electrical conductivity three cases were considered; it was assumed that the mobility of electrons, m_e, is 0.5, 1 and 2 times, respectively, that of holes, m_h. 135

Figure 4.1: A diagram showing data related to the thermodynamic stability range of manganese orthosilicate at high temperatures close to the melting temperature of Mn_2SiO_4 at 1 atm total pressure. Information about the data used to derive this diagram can be foundin Ref. [4]. The abbreviations used in this figure and their meanings are T = tephroite (Mn_2SiO_4), L = liquid silicate, HT = hausmannite (α-Mn_3O_4), HS = cubic Mn_3O_4 (β-Mn_3O_4), R = rhodonite ($MnSiO_3$), B = braunite (nominally Mn_7SiO_{12}), M = Mn and MO = MnO. 149

Figure 4.2: Phase diagram for the system Mn_3O_4-SiO_2 at $\log_{10} a_{O_2} = -2.5$ and 1 atm total pressure after Muan [19]. In addition to the abbreviations used in Figure 4.1, S is used as an abbreviation for tridymite (SiO_2). The dashed lines in the figure refer to the possibility that metastable phases could be formed upon cooling due to decomposition of Mn_2SiO_4 and $MnSiO_3$. 151

Figure 4.3: Oxygen activity vs. temperature diagram for Mn_2SiO_4 grown from the melt surrounded by a CO/CO_2 gas atmosphere containing 20 vol% CO. Lines representing data for the local oxygen activity in a grown single crystal versus temperature for limiting cases possible for compositional changes in Mn_2SiO_4 during cooling are shown in comparison with lines referring to different phase equilibria. The limiting cases considered with regard to compositional changes in Mn_2SiO_4 are i) that no compositional changes occur after solidification and ii) that compositional changes occur in such a way that the non-stoichiometric compound $Mn_2SiO_{4+\delta}$ has at every

location at a given temperature the value of δ corresponding to that of $Mn_2SiO_{4+\delta}$ being in equilibrium with a CO/CO_2 mixture containing 20 vol% CO. The diagram suggests that in the case of no or limited local compositional changes in a grown Mn_2SiO_4 crystal during cooling some decomposition may occur. 154

Figure 4.4: Schematic drawing of a newly designed and built passive afterheater to solve cracking problems which occurred during the growth of manganese orthosilicate single crystals. 165

Figure 4.5: Photographs showing single crystals of Mn_2SiO_4 grown along the [100] orientation: a) image of a crack-free crystal grown using the passive afterheater described in Figure 4.4, and, for comparison, b) a photograph of a severely cracked single crystal of Mn_2SiO_4 grown without using an afterheater. 166

Figure 4.6: Absorption coefficients, α, for the transition metal-containing orthosilicates Co_2SiO_4, Fe_2SiO_4 and Mn_2SiO_4 as a function of the wavelength in comparison with a spectrum typical for the type of tungsten halogen lamp used in this study for heating during crystal growth. The data for Co_2SiO_4 are from Ref. [24] and those for Fe_2SiO_4 from Ref. [25]. The data for α for Mn_2SiO_4 have been derived from transmittance data reported in Ref. [6]. single crystal of Mn_2SiO_4 grown without using an afterheater. 174

Figure 4.7: Laue back reflection patterns for single crystals of Mn_2SiO_4 grown along different principle orientations. The top row shows experimentally obtained patterns and the bottom row simulated ones. 176

Figure 4.8: XRD spectrum of a powder obtained by crushing and grinding a grown Mn_2SiO_4 single crystal and mixing this powder with silicon powder to provide a standard for lattice parameter determination. This spectrum suggests also that there was no significant decomposition of Mn_2SiO_4 into braunite, nominally Mn_7SiO_{12}, upon cooling. The only phase identified was that of Mn_2SiO_4. The symbol ☆ denotes peaks related to the Si standard. The symbols × and + both refer to peaks related to Mn_2SiO_4 and indicate which peaks were used in the cell refinement for determining lattice parameters (×) and which ones not (+) 177

Figure 4.9: Back-scattered electron image of a part of a single crystal of Mn_2SiO_4 which shows a precipitate of $MnSiO_3$ that further decomposed upon cooling, most likely into Mn_2SiO_4 and silica (SiO_2). 178

Figure 4.10 Image of the surface of a disk of Mn_2SiO_4 prepared by cutting perpendicular to the growth direction [100] after polishing and etching by using an aqueous solution of HCl. The image was obtained by using an optical microscope. 183

Figure 5.1: Data available from the literature [7,8] for the oxygen activity dependence of the electrical conductivity of Mn_2SiO_4 in equilibrium with $MnSiO_3$ at about 1200 ℃. 200

Figure. 5.2: Data available from the literature [3] for the deviation from stoichiometry, δ, in $Mn_2SiO_{4+\delta}$ at $a_{MnSiO_3} = 1$ at 1200 ℃. The line summarizing the data from Ref. [3] corresponds to $\delta \propto a_{O_2}^{1/6}$. 202

Figure 5.3: Example for experimental data: a) Normalized residual radioactivity profile, A(x,t)/A(x=0,t) vs. x. A(x,t) is the residual radioactivity measured after material of the thickness x has been removed from a sample and A(x=0,t) is the residual radioactivity before any material removal. t is diffusion-annealing time. The data shown are for a tracer diffusion experiment performed at 1200 ℃ at $\log a_{O_2} = -6.68$ with a diffusion-annealing time t ≈ 340,000 s. Data available from the literature [3] for the deviation from stoichiometry, δ, in $Mn_2SiO_{4+\delta}$ at $a_{MnSiO_3} = 1$ at 1200 ℃. The line summarizing the data from Ref. [3] corresponds to $\delta \propto a_{O_2}^{1/6}$. 209

Figure 5.4: Tracer diffusion coefficients measured for the diffusion of manganese in Mn_2SiO_4 at 1200 ℃ and $a_{MnSiO_3} = 1$ along the principle orientations [100], [010] and [001] as a function of the oxygen activity. One data point from the literature [12] for the diffusion of Mn in a single crystal of Mn_2SiO_4 along the [001] orientation is also shown for comparison. The lines shown in the figure were obtained based on the defect modeling described in Section 4.1. The value of −3.7 used for $\log_{10} a_{O_2}$ for the data point

reported by Morioka [12] is only an estimate by the authors of this article based on the statement in Ref. [12] that the diffusion occurred in a nitrogen atmosphere. 215

Figure 5.5: Temperature dependencies of manganese tracer diffusion coefficients measured for Mn_2SiO_4 at $a_{MnSiO_3} = 1$: a) for the diffusion of Mn-54 along the principle orientations, [100], [010] and [001], at $\log_{10} a_{O_2} \approx -2.7$ at 1 atm total pressure between 1150 and 1250 ℃, and b) for the diffusion of Mn-54 along the [001] orientation at $\log_{10} a_{O_2} \approx -9.8$ at 1 atm total pressure between 1150 and 1300 ℃ . The lines shown were generated by fitting Equation (5.13) to the experimental data shown in the plot. 216

Figure. 5.6: An estimated Kröger-Vink diagram for $Mn_2SiO_{4+\delta}$ at 1200 ℃ and $a_{MnSiO_3} = 1$ which is compatible with all currently available, reliable information on oxygen activity dependencies of the deviation from stoichiometry, δ, the cation tracer diffusion and the electrical conductivity. 225

Figure. 5.7: Comparison of oxygen activity dependencies obtained, departing from Figure 5.6, a) for the tracer diffusion coefficient of Mn-54 diffusing along the direction [001], D^*_{Mn}, b) for the electrical conductivity, σ, for the directions [100] and [010] (the data points shown are from Ref. [7]), and c) for the deviation from stoichiometry, δ, for $Mn_2SiO_{4+\delta}$ in equilibrium with $MnSiO_3$ at 1200 ℃. 229

LIST OF TABLES

Table 1.1: Relation between lattice parameters when switching between using the space groups Pnma and Pbnm. 5

Table 2.1: Lattice parameters of Co_2SiO_4 (space group: Pbnm) reported in the literature in comparison with values obtained in this study. 55

Table 2.2: Impurities considered and concentrations determined for them by using the ICP-AES technique in grown single crystals of cobalt silicate, Co_2SiO_4. Here, ppm refers to the number of moles of an element analyzed for per mole of Co_2SiO_4. 81

Table 3.1: Cation tracer diffusion coefficients, D^*_{Co}, experimentally determined in this study for Co_2SiO_4 at a_{SiO_2} = 1 and different oxygen activities. D° = 1 cm^2/s. The errors reported in this table are from least squares fits of Equation (3.3) to normalized residual radioactivity profiles. The overall errors are estimated to be of the order of 5 %, as discussed in Section 3.4 113

Table 3.2: Data for selected olivine structure oxides: lattice parameters [1,27], ionic radii of divalent metal ions in six-fold coordination [28], diffusion coefficient sequences, and ratios characterizing the anisotropy of tracer diffusion coefficients. # The diffusion coefficient sequence refers for $(Fe_xMg_{1-x})_2SiO_4$ to interdiffusion coefficients for about 8 mol% Fe_2SiO_4; the given ratio is a mean value for T = 1000 - 1150 °C. * T = 1300 °C, ** T = 1130 °C, ***

T = 1200 ℃, **** T = 1100 ℃. ¶ Mg_2SiO_4 containing varying levels of impurities. The letters a, b and c refer to diffusion along the principle directions [100], [010] and [001], respectively. 124

Table 3.3: Data derived from fitting Equation (3.13) to the cobalt tracer diffusion data for $a_{O_2} = 1$ shown in Figure 3.8. The data for single crystals with different orientation are from this work and those for polycrystalline samples from Ref. [17], extrapolated to $a_{O_2} = 1$. 124

Table 4.1: Lattice parameters of Mn_2SiO_4 reported in the literature in comparison with values obtained in this study. Space group used: Pbnm. The standard deviations are given in parentheses in units of the last digit of the cited value. 183

Table 4.2: Impurities considered and concentrations determined for them by using the ICP-AES technique for analyzing reaction products at different stages of the sol-gel synthesis and of a grown single crystals of manganese silicate, Mn_2SiO_4. Here, ppm refers to the number of moles of an element analyzed for per mole of Mn_2SiO_4 185

Table 5.1: Manganese tracer diffusion coefficients, D^*_{Mn}, experimentally determined in this study at $a_{MnSiO_3} = 1$ and different oxygen activities. D° = 1 cm^2/s. The errors reported in this table are from least squares fits of Equation (5.3) to normalized residual radioactivity profiles. The overall errors are estimated to be of the order of 5 %, as discussed in Section 5.4. 211

Table 5.2: Values obtained for pre-exponential factors, D°_{Mn}, and for activation enthalpies, ΔH, by fitting Equation (5.13) to manganese tracer diffusion data for $\log_{10} a_{O_2} = -2.7$ and diffusion along the three principle orientations [100], [010] and [001], see Figure 5.5a, and data for $\log_{10} a_{O_2} = -9.8$ for diffusion along the [001] orientation, see Figure 5.5b. One data point available from Ref. [12], denoted by the symbol * in this table, is also listed. ** The value of −3.7 for $\log_{10} a_{O_2}$ is only an estimate which is based on the statement in Ref. [12] that the diffusion occurred in a nitrogen atmosphere and on an estimate by the authors of this article. 234

CHAPTER 1

INTRODUCTION

1.1. Introduction and Background

1.1.1. Classification of Silicates

A silicate is a compound containing silicon bearing anions. Silicate minerals are the most abundant and important class of rock-forming minerals, constituting about 90 percent of the Earth's crust and mantle [1]. The majority of silicate compounds are oxides. In oxygen-containing silicates, silicon is tetrahedrally coordinated by four oxygen atoms or, in some rare cases, octahedrally coordinated by six oxygen atoms. Silicate compounds containing SiO_4^{4-} tetrahedra can be classified by how those tetrahedra are linked and they are introduced in the following in the order of increasing complexity.

Nesosilicates, orthosilicates, or island silicates contain isolated SiO_4^{4-} tetrahedra connected only with other cations. Overall they have the silicon-to-oxygen atomic ratio of 1:4. Examples of compounds in this group include olivines, e.g., $(Mg,Fe)_2SiO_4$, garnets, e.g., $Fe_3Al_2(SiO_4)_3$ and zircons, e.g., $ZrSiO_4$.

Sorosilicates or disilicates contain isolated $Si_2O_7^{6-}$ groups of two tetrahedra sharing one common oxygen. Cyclosilicates or ring silicates consist of SiO_4^{4-} tetrahedra sharing two oxygen ions, linked together to form rings. The silicon-to-oxygen atomic ratio in this type of silicate is 1:3. Inosilicates or chain silicates are

formed by interlocking chains of silicate tetrahedra. The silicon-to-oxygen atomic ratio is 1:3 for single chain and 4:11 for double chain silicates. Phyllosilicates or sheet silicates consist of parallel sheets of silicate tetrahedra with a silicon-to-oxygen atomic ratio of 2:5. Tectosilicates or framework silicates form when all SiO_4^{4-} tetrahedra are linked by corners as a three-dimensional framework, e.g., Quartz, SiO_2 [1].

1.1.2. Transition Metal-Containing Orthosilicates of Olivine Type

Olivines, which are orthosilicates with an orthorhombic crystal structure, are one of the most important silicate phases because they represent the major components of the Earth's upper mantle. Natural olivines are magnesium-iron silicates, with an approximate composition of $Fa_{10}Fo_{90}$ (Fa: fayalite, mineral name for Fe_2SiO_4 and Fo: forsterite, mineral name for Mg_2SiO_4). Minority cations commonly contained in naturally occurring olivines are Ca, Mn, Ni and Co, substituting for Mg and Fe [2]. In transition metal-containing olivines, due to the presence of transition metal cations, which are subject to valence state changes, oxygen can be added to or removed from transition metal-containing olivines, leading to a variation in the oxygen content and a variation of the concentrations of point defects in such olivines. Variations in the oxygen content in transition metal-containing olivines can be described by introducing a deviation from stoichiometry, represented by the symbol δ, into the general chemical formula of olivine-type compounds, $Me_2SiO_{4+\delta}$, with Me representing one or more types of metal cations.

The point defect structure and defect-related properties of olivine group compounds have been the subject of many previous investigations, especially conducted by Earth scientists, on naturally occurring or synthetic olivines containing Fe and Mg. Systematic studies on the point defect structure and defect-related physical properties in non-stoichiometric, ternary and transition metal-containing orthosilicates, including deviation from stoichiometry, tracer diffusion and electrical conduction, can improve the understanding of the crystal chemistry of orthosilicates in general and provide fundamental insights into transport processes occurring in the Earth's upper mantle. For the current study, the olivine group compounds cobalt orthosilicate and manganese orthosilicate were selected as model compounds to better understand the defect structure and defect-related transport properties in non-stoichiometric transition metal-containing orthosilicates with the olivine structure.

1.1.3. Structure of Olivines

As stated before, olivines are orthosilicates with an orthorhombic crystal structure. The crystal structure, as shown in Figure 1.1, is composed of isolated SiO_4^{4-} tetrahedra linked by Me cations in an octahedral coordination. The olivine structure can be alternatively considered as an almost hexagonally densely packed array of oxygen ions, in which the Me cations are located on octahedral interstices of the oxygen sublattice, while the Si cations are located on tetrahedral interstices. Each oxygen is bonded to one silicon and three octahedrally coordinated Me cations. Olivine group compounds have a relatively dense packing

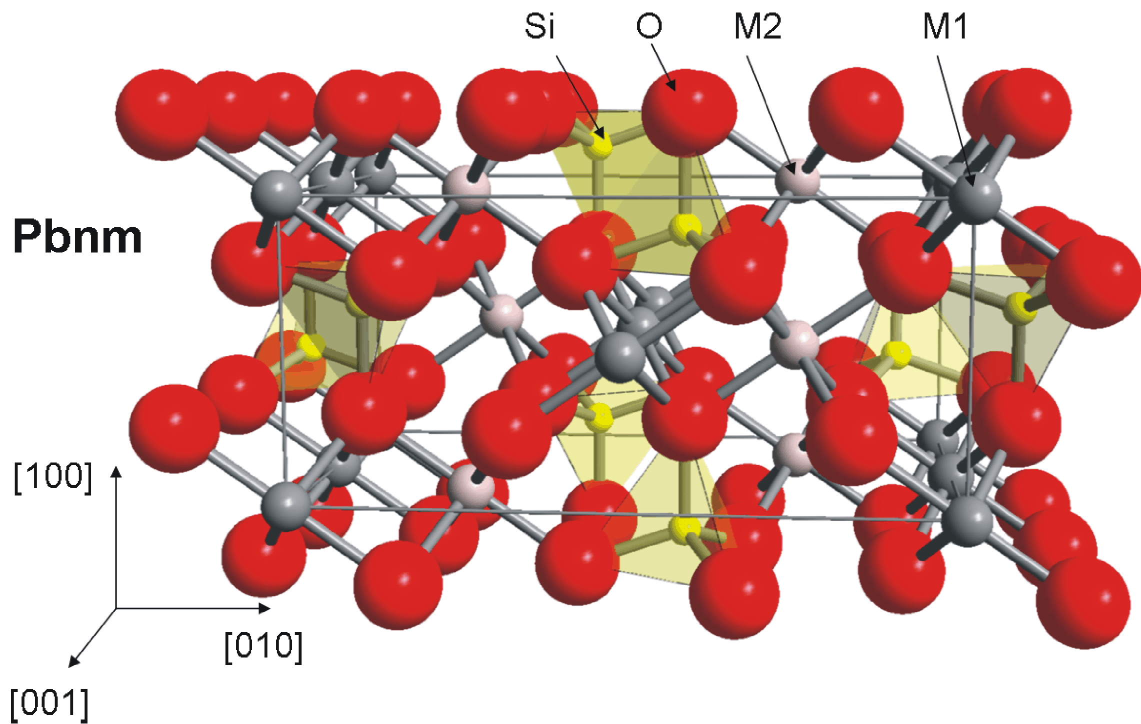

Figure 1.1: Olivine crystal structure denoted by using the space group Pbnm.

(3.2 - 4.4 g/cm^3) [2] of four units of Me_2SiO_4 per unit cell, the lattice parameters of which are roughly 5 × 10 × 6 Å [2]. The crystal symmetry is denoted by using the space group Pbnm.

The standard denotation for the space group of olivines is Pnma while the denotation used for the crystal symmetry of olivines throughout this dissertation is the space group Pbnm which is most commonly used for olivines [3]. If α, β, and γ represent values for the lattice parameters for the orientations [100], [010] and [001] of olivines described by using the space group Pnma, as shown in Table 1.1,

switching from the space group Pnma to Pbnm yields a = γ, b = α and c = β for values of the lattice parameters for the orientations [100], [010] and [001] of olivines denoted by the space group Pbnm.

Table 1.1: Relation between lattice parameters when switching between using the space groups Pnma and Pbnm.

lattice parameters when using the space group Pnma	lattice parameters when using the space group Pbnm
a = α for [100]	a = γ for [100]
b = β for [010]	b = α for [010]
c = γ for [001]	c = β for [001]

There are two non-equivalent octahedral sites for the Me cations with distinct symmetries, M1 and M2. M1 sites are located at the centers of the symmetries and M2 sites are present on the mirror planes perpendicular to the [001] orientation. One special feature of the structure is that all M1 sites are lined up in the [001] direction. One consequence of the non-cubic structure is anisotropy, causing an orientation dependence of transport properties such as the tracer diffusion of ions and of the electrical conduction, which will be discussed later in more detail.

At sufficiently high pressures and temperatures, olivine compounds may be transformed to their polymorphs that have a spinel structure, with a cubic symmetry corresponding to the space group Fd3m [2]. In the spinel structure, the oxygen ions are present in the form of a face-centered cubic closed package. A

spinel unit cell contains eight formula units and is composed of 32 oxygen ions, 32 octahedral interstices and 64 tetrahedral interstices. One half of the octahedral interstices are occupied by Me cations and one eighth of the tetrahedral interstices are occupied by Si cations. Both olivine and spinel forms of orthosilicates have Si cations in a tetrahedral coordination and Me cations in an octahedral coordination. The major difference between those two polymorphs is the type of edge sharing between cation polyhedra. Whereas each SiO_4^{4-} tetrahedron in olivines shares three edges with MO_6 octahedra, SiO_4^{4-} tetrahedra in the spinel share no edges. Furthermore, in olivines M1 octahedra share six of their twelve edges with other polyhedra whereas M2 octahedra share only three edges. All the octahedra in the spinel share six of its edges with other octahedra [2]. The important structure difference between olivine and spinel is the key for the higher pressure stability of the silicate spinels compared with their polymorphs with olivine structure.

1.2. Point Defects in Non-Stoichiometric Binary and Ternary Oxides

1.2.1. Classification of Defects in Crystalline Materials

An ideal crystal structure without any imperfections does not exist in reality. Crystals in reality always deviate from ideal ones. Deviations from the ideal crystal structures are called the defects of the crystal lattice [4]. Based on Gibbs energy considerations, zero-dimensional defects, i.e., point defects, usually exist in a state of thermodynamic equilibrium, especially at high temperatures. One-, two- and three- dimensional defects, such as dislocations, grain boundaries and voids, which are usually introduced during preparation and handling of crystalline

samples, are non-equilibrium defects [5]. The concentrations of non-equilibrium defects are not determined by thermodynamic equilibria. One- and higher-dimensional defects can be very stable, especially at lower temperatures, but it is impossible to create them thermally in an ideal crystal only by slowly raising its temperature [5]. Annealing at high temperature can decrease the concentrations of those defects but can never completely remove them because the driving forces for their removal are relatively small and the rate of their removal is usually low [6]. Hence in real materials there are always one- or higher-dimensional non-equilibrium defects present in addition to equilibrium point defects.

If the concentrations of one- and higher-dimensional non-equilibrium defects are small compared to point defect concentrations, at sufficiently high temperature and established thermodynamic equilibrium, the influence of one- and higher-dimensional defects on certain transport properties in ionic compounds can be ignored. In this case, point defects are the most important defect species and determine the defect structure, which in turn controls the transport properties of materials [6].

1.2.2. Types of Point Defects in Ionic Compounds

In ionic crystals, possible point defect types include a) vacancies, e.g., missing ions, on regularly occupied cationic and anion lattice sites, b) cations and anions on interstitial sites which are usually empty, and c) electronic point defects, e.g., electrons, e', and holes, $h^{\bullet}$, for charge compensation. If the impurity concentrations in ionic compounds are sufficiently small, then the defect structure

of the crystal is dominated by the point defects listed under a) to c); otherwise impurities as point defects need also to be taken into account which may significantly influence the concentrations of all other point defects. The majority of the point defects in ionic compounds listed under a) to c) are charged species and hence there are Coulomb interactions between them, which lead at high defect concentrations to reduced values of activity coefficients of point defects and in addition possibly to the formation of associates between oppositely charged point defects or even larger aggregated defects, called clusters. Only in the case of very dilute solutions of point defects in ionic solids point defects can be considered as being present in an ideal solutions [7].

The ionic Kröger-Vink notation [8] is used throughout this dissertation to denote point defects as structural elements, expressed as $(S_p)^c$. S is the species considered, e.g., an ion, a vacancy, etc.. P is the site denoted by its regular occupancy, e.g., an ion being regularly located at this site. C is the charge of the species S relative to that of the regular occupant of the crystallographic site considered. The following symbols are used to denote the relative charge: $'$ = negative, $^{\bullet}$ = positive and $^{\times}$ = neutral.

1.2.3. Types of Disorder in Ionic Compounds

When determining the types of disorder, i.e., the presence of different types of majority defects, in ionic crystals, it needs to be taken into account that there is a coupling between the concentrations of all charged defects due to the charge balance requirement, i.e., the electroneutrality condition. Only combinations of

oppositely charged point defects can be considered as being the majority defects due to this electroneutrality requirement unless a majority defect is electrically neutral and a single type of point defect is present as the majority defect [7].

Different types of disorder can exist in ionic compounds, which are characterized by the types of the majority defects present. Generally they can be sorted by two different categories, i) different types of thermal disorders and ii) component activity dependent disorders, the latter being often predominant in non-stoichiometric compounds.

1.2.3.1. Thermal Disorder

In the case of a predominant thermal disorder, no material exchange with the environment occurs when point defects are formed. Three basic types of thermal disorder exist, including two types of thermal ionic disorder, Schottky type and Frenkel-type, and one type of thermal electronic disorder. The characteristic of the Schottky disorder is that the majority defects are cation and anion vacancies. An example of a prevailing Schottky disorder is found for sodium chloride, NaCl, where the majority defects are negatively charged cation vacancies, $(V_{Na^+})'$, and positively charged anion vacancies, $(V_{Cl^-})^{\bullet}$. The hallmark of a Frenkel disorder is that the majority defects are ions on interstitial sites and vacancies on the sublattice where the ions being present on interstial sites are usually located. The formation of cation vacancies $(V_{Ag^+})'$ and that of cation interstials $(Ag_I^+)^{\bullet}$ as the majority defects in silver bromide, AgBr, is an example of a Frenkel disorder

related to the cation sublattice. The thermal electronic disorder is characterized by electronic defects, i.e., electrons, e', and holes, $h^{\bullet}$, are the majority defects.

1.2.3.2. Component Activity Dependent Disorder

For non-stoichiometric ionic compounds containing transition metals, there are exchanges of material with the environment during defect formation, e.g., in the case of transition metal-containing oxides, the addition or removal of oxygen when there is an oxygen activity change at given values of temperature and total pressure. Examples of non-stoichiometric oxides are simple binary oxides, $Fe_{1-\Delta}O$ (Δ ~ 0.1), $Co_{1-\Delta}O$ (Δ ~ 0.01), $Ni_{1-\Delta}O$ (Δ ~ 0.001) [7] and more complex transition metal-containing ternary oxides, such as Fe_2SiO_4, Co_2SiO_4 and Mn_2SiO_4. In non-stoichiometric oxides, in most cases a component activity dependent disorder predominates. For a non-stoichiometric binary model oxide $Me_{1-\Delta}O$ with a component activity-dependent disorder, for example, assuming that cation vacancies, $(V_{Me^{2+}})''$, and holes, $h^{\bullet}$, are the majority defects, the following component activity dependent defect formation reaction can be formulated

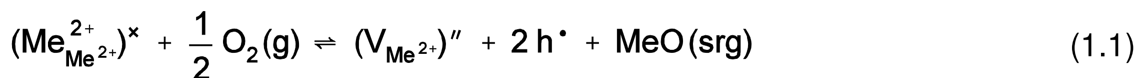

$$(Me^{2+}_{Me^{2+}})^{\times} + \frac{1}{2} O_2(g) \rightleftharpoons (V_{Me^{2+}})'' + 2\,h^{\bullet} + MeO(srg) \qquad (1.1)$$

The abbreviation srg stands for sites of repeatable growth. If the point defects, which are formed by a defect formation reaction such as described in Equation (1.1), are the majority defects in the ionic compound considered, the disorder is component activity-dependent.

1.2.4. Point Defect Thermodynamics

The predominant disorder type and the concentration of point defects in ionic compounds can be determined by indirect defect-related property measurements of the deviation from stoichiometry, diffusion of ions and electrical conduction as a function of thermodynamic variables. The approach used in this study as well as in many other studies is to investigate experimentally the dependence of defect-related properties on thermodynamics variables, such as oxygen activity and temperature, in non-stoichiometric oxides at thermodynamic equilibrium. By making use of the relationships between defect-related properties and concentrations of point defects, information related to the point defect structure of the crystals considered at thermodynamic equilibrium can be obtained. This requires the use of thermodynamic concepts and the derivation of the relationships between point defect concentrations and defect-related properties.

The main assumption usually made when considering the point defect thermodynamics of ionic compounds with a small deviation from stoichiometry, where the concentrations of point defects are considered to be small, is that the point defects can be treated as structural elements that are dissolved ideally in the solvent crystal [4]. By formulating appropriate defect formation reactions and equilibrium constants for these reactions, followed by applying the electroneutrality condition, expressions for point defect concentrations as a function of chosen independent thermodynamic variables, e.g., component activities, can be

obtained. The concepts of point defect thermodynamics can be used to derive the dependence of the defect concentrations on component activities.

In ionic crystals with n components, e.g., n = 2 and 3, respectively, for binary and ternary oxides, according to the Gibbs phase rule, at constant temperature and total pressure, the concentrations of the point defects present in thermodynamic equilibrium are fixed by $n-1$ thermodynamic variables in addition to temperature and total pressure. In the case of non-stoichiometric binary oxides, at given values of total pressure and temperature, only one additional thermodynamic variable needs to be fixed. The variable that can be controlled most conveniently is the oxygen activity ($a_{O_2} = P_{O_2}/P^{\circ}_{O_2}$ with $P^{\circ}_{O_2} = 1$ atm; P_{O_2} = oxygen partial pressure in atm). For non-stoichiometric ternary oxides, in addition to temperature, total pressure and oxygen activity, another thermodynamic variable needs to be fixed to unequivocally determine the defect concentration. Possible choices for the additional thermodynamic variable to be fixed will be discussed later.

1.2.5. Point Defects in Binary Non-Stoichiometric Oxides

1.2.5.1. Oxygen Activity Dependence of Point Defect Concentrations

As discussed above, in non-stoichiometric oxides, e.g., $Me_{1-\Delta}O$, usually a component activity dependent disorder predominates. For the purpose of demonstrating the derivation of component activity dependencies of point defect concentrations in non-stoichiometric compounds, one can consider the oxygen

activity dependence of point defect concentrations in a non-stoichiometric pure binary compound $Me_{1-\Delta}O$ with cation vacancies, $(V_{Me^{2+}})''$, and holes, $h^{\bullet}$, as the majority defects. The word "pure" indicates that the concentrations of impurities are assumed to be significantly smaller than all other point defects concentrations so that the influence of impurities can be ignored. The component activity dependent defect formation reaction was described before in Equation (1.1). The equilibrium constant, K_a, for this defect formation reaction can be formulated assuming that an ideal solution of defects exists. The result is Equation (1.2).

$$K_a = \frac{[(V_{Me^{2+}})''] \cdot [h^{\bullet}]^2 \cdot a_{MeO(srg)}}{[(Me^{2+}_{Me^{2+}})^{x}] \cdot a_{O_2}^{1/2}} = \frac{[(V_{Me^{2+}})''] \cdot [h^{\bullet}]^2}{a_{O_2}^{1/2}} \tag{1.2}$$

In Equation (1.2) the terms [I] denotes the concentrations of the species I per lattice molecule of $Me_{1-\Delta}O$. The latter equality in Equation (1.2) is obtained because the thermodynamic activity of MeO, a_{MeO}, is practically equal to 1 and that $[(Me^{2+}_{Me^{2+}})] \approx 1$.

The concentrations of holes and cation vacancies are coupled to each other by the electroneutrality condition

$$2\,[(V_{Me^{2+}})''] = [h^{\bullet}] \tag{1.3}$$

Inserting the electroneutrality condition into Equation (1.2) leads to

$$K_a = \frac{4\,[(V_{Me^{2+}})'']^3}{a_{O_2}^{1/2}} \tag{1.4}$$

The final result for the oxygen activity dependence of the concentrations of the considered point defects is

$$[h^\bullet] = 2\,[(V_{Me^{2+}})''] \propto a_{O_2}^{1/6} \tag{1.5}$$

In the above derivation, only cation vacancies and holes are considered as the majority defects. However the disorder type may vary as a function of the thermodynamic variables, e.g., the oxygen activity. There might be a transition from one disorder type to another. In that case, a more general procedure for obtaining component activity dependencies of defect concentrations is required, which will be discussed below.

The non-stoichiometric pure binary compound $Me_{1-\Delta}O$ is continued to be considered as a model compound. For the sake of simplicity, it is assumed that there is no disorder involving oxygen ions.

The first step of the thermodynamic treatment of point defects again involves formulating a point defect formation reaction related to an exchange of material between the ionic compound and the environment as considered in Equation (1.1). The equilibrium constant, K_a, for this defect formation reaction was given by Equation (1.2) and remains unchanged.

In addition to the component activity dependent defect formation reaction, the recombination reaction between holes and electrons

$$0 \rightleftarrows e' + h^\bullet \tag{1.6}$$

as well as the point defect formation reaction for the Frenkel disorder on the cationic sublattice,

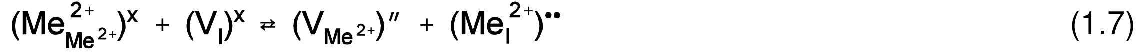

$$(Me^{2+}_{Me^{2+}})^{x} + (V_I)^{x} \rightleftarrows (V_{Me^{2+}})'' + (Me_I^{2+})^{\bullet\bullet} \tag{1.7}$$

should be considered.

The equilibrium constant for the thermal electronic disorder reaction described in Equation (1.6), K_e, is

$$K_e = [e'] \cdot [h^{\bullet}] \tag{1.8}$$

and that for the Frenkel disorder reaction denoted in Equation (1.7), K_F, is

$$K_F = [(V_{Me^{2+}})''] \cdot [(Me_I^{2+})^{\bullet\bullet}] \tag{1.9}$$

The electroneutrality condition is given by Equation (1.10).

$$2\,[(V^{2+}_{Me})''] + [e'] = 2\,[(Me_I^{2+})^{\bullet\bullet}] + [h^{\bullet}] \tag{1.10}$$

The equation system considered above can be used for given values of the equilibrium constants K_a, K_e and K_F to calculate the concentrations of all point defects denoted in Equation (1.10) as a function of oxygen activity at constant temperature and total pressure.

Results obtained for defect concentrations as a function of oxygen activity for three cases for pure $Me_{1-\Delta}O$ are schematically plotted in Figures 1.2 a) $K_F \ll K_e$,

b) $K_F = K_e/4$ and c) $K_e \ll K_F$. Diagrams shown in Figure 1.2 are called Kröger-Vink or Brouwer diagrams.

Figure 1.2a shows a case where $K_F \ll K_e$. As it can be seen in Figure 1.2, at high oxygen activities, cation vacancies and holes are the majority defects, at intermediate oxygen activities, thermal electronic disorder dominates and at low oxygen activities cation interstitials and electrons are the majority defects.

Figure 1.2b is a Kröger-Vink diagram generated for a very special case, where $K_F = K_e/4$. This very special case can, if at all, occur only at one temperature at constant total pressure. As it is shown in Figure 1.2b, at high oxygen activities, cation vacancies and holes are the majority defects, while at low oxygen activities, cation interstitials and electrons become the majority defects. For this very special case,

$$[h^{\bullet}] = 2\,[(V_{Me^{2+}})] \propto a_{O_2}^{1/6} \tag{1.11}$$

and

$$[e'] = 2\,[(Me_I^{2+}] \propto a_{O_2}^{-1/6} \tag{1.12}$$

This very special case will be considered further in detail in later sections on the influence of impurities on point defect equilibria and the relationship between the point defect structure and defect-related properties.

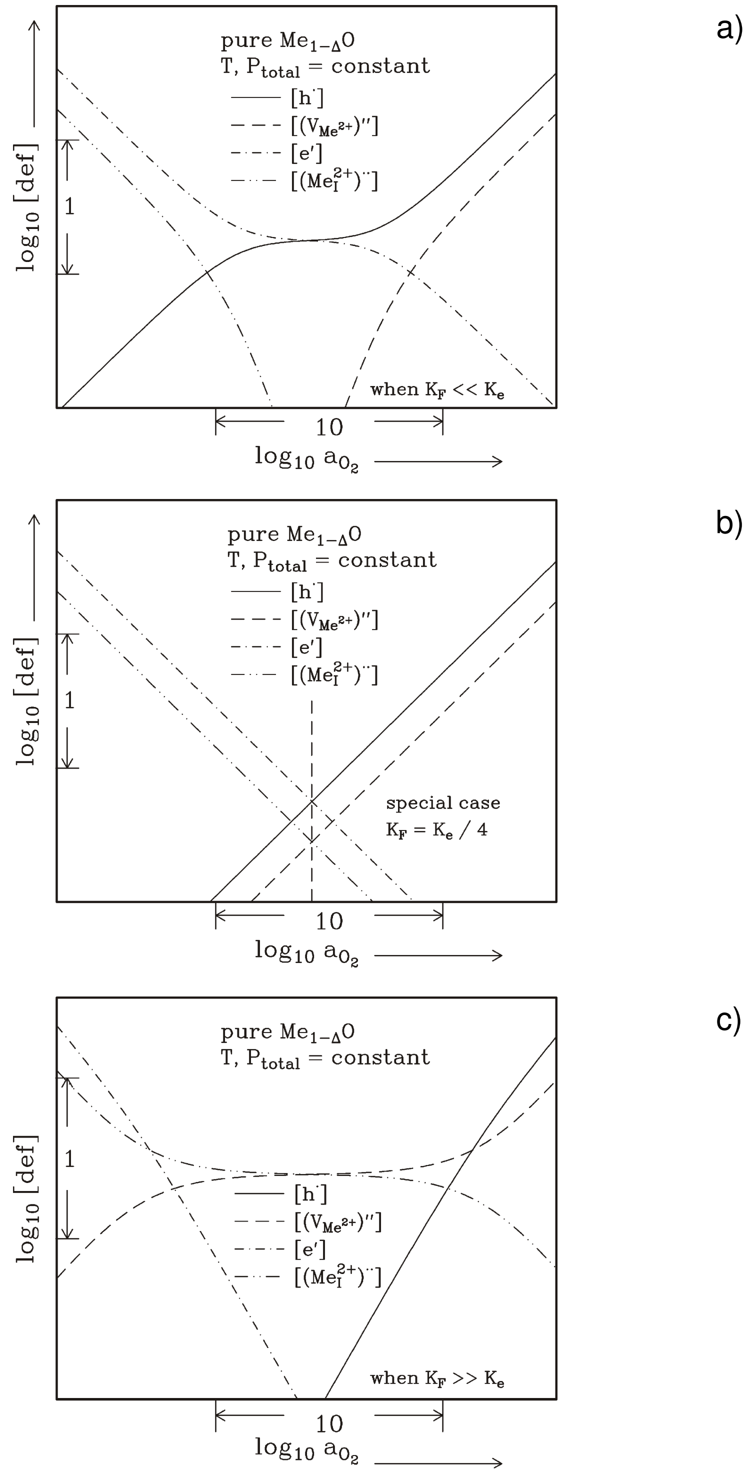

Figure 1.2: Schematic plots of point defect concentrations in pure $Me_{1-\Delta}O$ as a function of oxygen activity for three cases: a) $K_F \ll K_e$, b) $K_F = K_e/4$ and c) $K_e \ll K_F$.

Figure 1.2c shows a case where $K_e \ll K_F$. At high oxygen activities, cation vacancies and holes are the majority defects. At intermediate oxygen activities thermal ionic disorder dominates and at low oxygen activities, cation interstitials and electrons become the majority defects.

The deviation from stoichiometry, denoted as Δ in the formula $Me_{1-\Delta}O$, is the difference between the concentrations of cation vacancies and those of cations on interstitial sites. Δ also equals to one half of the difference between the concentrations of holes and electrons.

$$\Delta = [(V_{Me^{2+}})''] - [(Me_I^{2+})^{\bullet\bullet}] = \frac{[h^\bullet] - [e']}{2} \tag{1.13}$$

The oxygen activity dependency of Δ can be derived from the oxygen activity dependence of the concentrations of cation vacancies and cation interstials. For the very special case at the temperature where $K_F = K_e/4$, one finds

$$\Delta = m \cdot a_{O_2}^{1/6} - n \cdot a_{O_2}^{-1/6} \tag{1.14}$$

where m and n are constants.

1.2.5.2. Influence of Impurities on Point Defect Concentrations

In the above calculations, it was assumed that the ionic compounds considered were sufficiently pure and the influence of impurities on point defect equilibria was ignored. In real materials, impurities are always present. Impurities may cause changes in point defect populations via the electroneutrality condition. Assuming that ions of the type M^+ and Mx^{3+} are present as impurities (assumed to be present

on Me^{2+} sites), the electraneutrality condition changes to

$$2\,[(V_{Me^{2+}})''] + [e'] + [(M^{+}_{Me^{2+}})'] = 2\,[(Me_I^{2+})^{\bullet\bullet}] + [h^{\bullet}] + [(Mx^{3+}_{Me^{2+}})^{\bullet}] \qquad (1.15)$$

Figure 1.3 shows Kröger-Vink diagrams generated by using the same equilibrium constants K_a, K_e and K_F used for generating the Kröger-Vink diagram shown in Figure 1.2b but with the presence of a) a small concentration of the alio-valent impurity M^+ ($[(M^{+}_{Me^{2+}})'] = K_e^{1/2}$), b) a large concentration of the alio-valent impurity M^+ ($[(M^{+}_{Me^{2+}})'] = 10 \cdot K_e^{1/2}$), c) a small concentration of the alio-valent impurity Mx^{3+} ($[(Mx^{3+}_{Me^{2+}})^{\bullet}] = K_e^{1/2}$), and d) a large concentration of the alio-valent impurity Mx^{3+} ($[(Mx^{3+}_{Me^{2+}})^{\bullet}] = 10 \cdot K_e^{1/2}$). For the calculations it was assumed that M^+ and Mx^{3+} ions are accommodated on M-sites.

Figure 1.3 shows that the presence of alio-valent impurities can significantly influence the point defect concentrations. Since the presence of impurities changes point defect concentrations and hence influences defect-related properties, in order to improve the fundamental understanding of intrinsic defects and defect-related properties in oxides, pure samples with low impurity concentrations that have negligible effect on point defect concentrations are needed. If this is not possible, at minimum one requires samples with well-defined, small impurity concentrations.

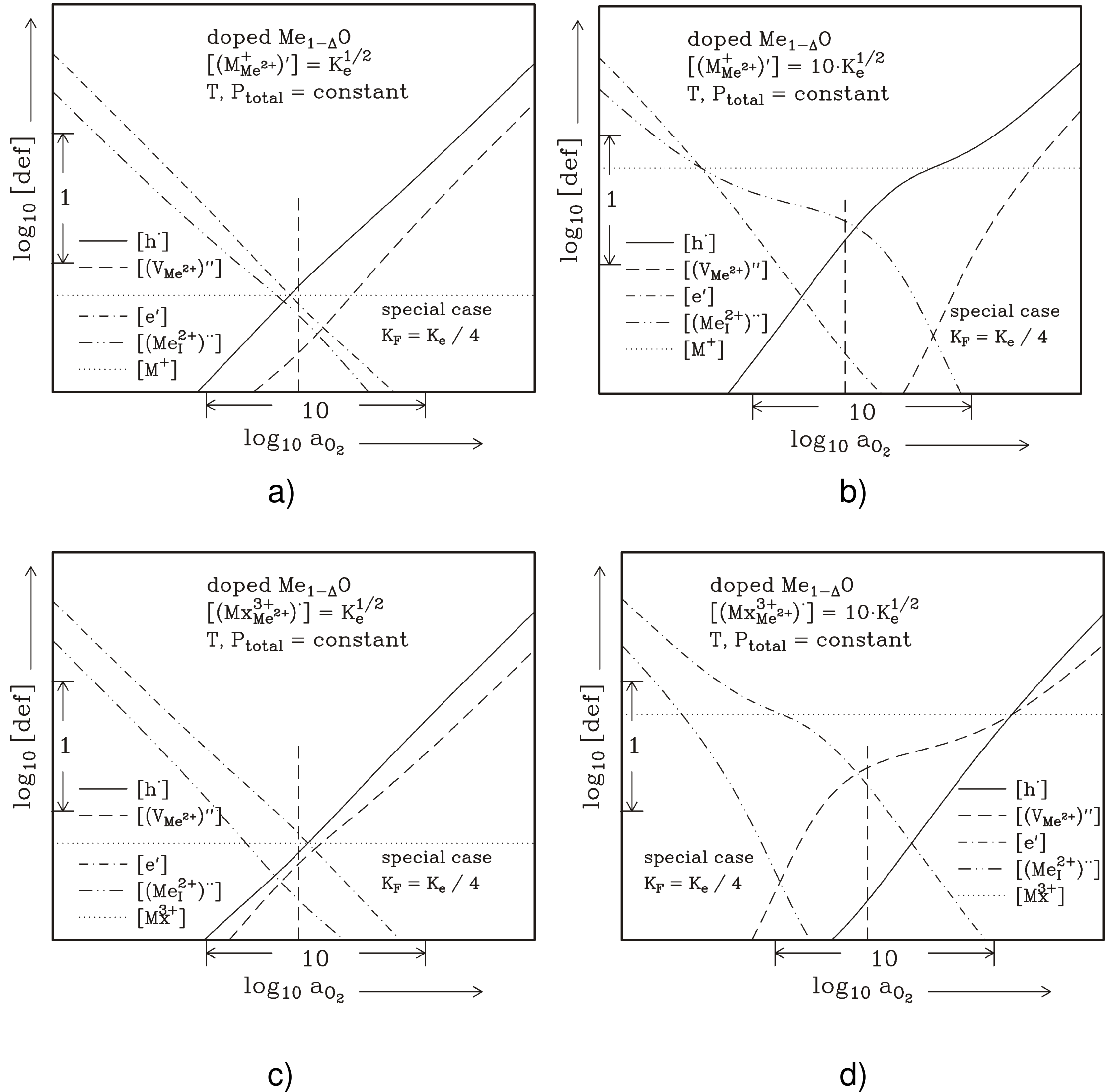

Figure 1.3: Kröger-Vink diagrams generated using the same equilibrium constants as those used for generating Figure 1.2b but with the presence of a) a small concentration of the alio-valent impurity M^+ ($[(M^+_{Me^{2+}})'] = K_e^{1/2}$), b) a large concentration of the alio-valent impurity M^+ ($[(M^+_{Me^{2+}})'] = 10 \cdot K_e^{1/2}$), c) a small concentration of the alio-valent impurity Mx^{3+} ($[(Mx^{3+}_{Me^{2+}})^{\bullet}] = K_e^{1/2}$), and d) a large concentration of the alio-valent impurity Mx^{3+} ($[(Mx^{3+}_{Me^{2+}})^{\bullet}] = 10 \cdot K_e^{1/2}$). M^+ and Mx^{3+} ions are assumed to be located on M-sites.

1.2.6. Point Defects in Ternary Non-Stoichiometric Oxides

The discussion in the previous section of point defects in non-stoichiometric ionic compounds was for a simple binary oxide of the type $Me_{1-\Delta}O$, but in principle it applies also to more complex ternary non-stoichiometric oxides, e.g., to compounds of interest for this study of the type $Me_2SiO_{4+\delta}$, as well. Since $Me_2SiO_{4+\delta}$, if Me denotes only one type of element, is a ternary compound, at fixed total pressure and temperature, in addition to the oxygen activity, one additional thermodynamic variable needs to be fixed to unequivocally define the thermodynamic state of the crystal. Possible choices are fixing the Me to Si ratio, the activity of a Me-rich secondary phase or the activity of a Si-rich secondary phase. The first possibility is ruled out due to the incapability of a sufficiently precise control of the Me to Si ratio. The second possibility is also ruled out because of potential changes of the type of the Me-rich secondary phase possibly being present in equilibrium with $Me_2SiO_{4+\delta}$, e.g., Me, MeO, Me_3O_4, etc., when there are changes in oxygen activity. Therefore the additional thermodynamic variable chosen to be fixed in this study in addition to the oxygen activity, is the activity of a Si-rich secondary phase, either SiO_2 or a compound of the type $MeSiO_3$, depending on the specific orthosilicate considered.

The most widely studied transition metal-containing orthosilicate, $Fe_2SiO_{4+\delta}$, is selected as an example for discussing the point defect structure of non-stoichiometric ternary orthosilicates. If the influence of impurities can be ignored, at high temperatures, possible point defects in $Fe_2SiO_{4+\delta}$ are vacancies on Fe-, Si-

and O- sites, Fe, Si and O ions on interstitial sites, Fe cations on Si sites and Si cations on Fe sites and electrons and holes for charge compensation. The exchange of sites between cations and anions is assumed to be negligible due to strong repulsive Coulomb interactions.

In the following point defect chemistry discussion, oxygen vacancies and oxygen interstials are not considered for several reasons. Oxygen interstials are ignored based on size and space arguments since it is energetically very expensive to accommodate large oxygen ions on interstitial sites. Oxygen vacancies are ignored due to the strong bonding between Si and O atoms which is about 3 times stronger than the “weaker” metal cation-oxygen bonds [2]. Based on the above arguments, the oxygen anion sublattice is considered as being undisturbed.

For point defects involving Si ions or sites, Si being present on interstitial positions has been discussed by Andersson et al. [9]. It was pointed out by Anderson et al. that Si is the slowest diffusing species among Me, Si and O in olivines. Since mobilities of species located on interstial sites are usually large, this indicates that the concentration of Si interstials must be very low. From an electrostatic energy point of view it is also unlikely that a large number of vacancies will form on Si sites. Low concentrations of silicon vacancies and interstials could very well be the result of the strong covalent bonding between Si and O. As pointed out by Tsai et al. [11], it is likely that some of the Fe cations initially present on M sites change their coordination and move to Si Sites, leaving

behind vacant M sites, when the oxygen activity in Fe_2SiO_4 with a constant Fe to Si-ratio is increased. The cations available to do this in fayalite are Fe^{2+} and Fe^{3+} ions. Based on electrostatic and cation size considerations, Fe^{3+} ions are more favorable for being accommodated on Si sites.

When analyzing defect-related properties of olivine, one needs in principle to take into account the presence of two different types of M sites, M1 and M2. Distinguishing between M1 and M2 sites complicates the defect chemistry very significantly and can not be properly done when studying point defects by experimentally determining the dependence of the diffusion of transition metal cations on thermodynamic variables in orthosilicates as done in this work. As a result, in the following discussion, no distinction is being made between M1 and M2 sites.

Based on the preceding considerations, for studies on point defects which govern the variation of oxygen content, the cation tracer diffusion and the electrical conduction in olivines, the point defects which need to be considered are vacancies on Fe sites, $(V_{Fe^{2+}})''$, Fe^{3+} ions on Si sites, $(Fe^{3+}_{Si^{4+}})'$, Si^{4+} on Fe^{2+} sites, $(Si^{4+}_{Fe^{2+}})^{\bullet\bullet}$, Fe^{2+} ions on interstitial sites, $(Fe^{2+}_{I})^{\bullet\bullet}$, electrons, e', and holes, $h^{\bullet}$. Si^{4+} on Fe^{2+} sites, $(Si^{4+}_{Fe^{2+}})^{\bullet\bullet}$, are most likely just present as minority defects due to electrostatic considerations.

The variation of the oxygen content in synthetic fayalite was investigated thermogravimetrically at 1130 °C as a function of oxygen activity by Nakamura and Schmalzried [10] and later by Tsai et al. [11]. It was found that the deviation from

stoichiometry, δ, has a positive dependence on the oxygen activity with no inflection point observed in the oxygen activity ranges investigated. This suggests that cation vacancies, $(V_{Fe^{2+}})''$, are the majority defects in the oxygen activity ranges investigated and that Fe^{2+} ions on interstitial sites, $(Fe_I^{2+})^{\bullet\bullet}$, need only to be considered as minority defects. As pointed out in Ref. [11], the thermogravimetric measurements by Nakamura and Schmalzried [10] were performed with olivine samples held in a Pt-30%Rh container. It is known that the interaction between Pt (or Pt-based alloys) and transition metal oxides may lead to a very large mass change in thermogravimetric measurements, especially at low oxygen activities. The use of a Pt-30%Rh container must have caused errors in the thermogravimetry measurements performed by Nakamura and Schmalzried [10]. The results of measurements of the deviation from stoichiometry in $Fe_2SiO_{4+\delta}$ by Nakamura and Schmalzried [10] and by Tsai et al. [11] are shown later in Figure 1.5b for comparison in Section 1.3.3. in conjunction with results of other point defect-related property measurements performed by Tsai et al. [11]. It was reported by Tsai et al. [11] that the observed oxygen activity dependence of the deviation from stoichiometry, δ, in $Fe_2SiO_{4+\delta}$ is compatible with cation vacancies, $(V_{Fe^{2+}})''$, holes, $h^{\bullet}$ and Fe^{3+} ions on Si sites, $(Fe_{Si^{4+}}^{3+})'$, as majority defects.

The preceding discussion of majority point defects in fayalite was based on the variation in the oxygen content (related to point defect concentrations) in $Fe_2SiO_{4+\delta}$. However, it is impossible to come to an unequivocal conclusion with regard to the point defect structure just based on the results of oxygen content variation measurements alone. To unequivocally develop an appropriate defect

model for transition metal-containing orthosilicates, it is necessary to perform careful measurements of other different point defect-related properties, such as most transport properties, including cation tracer diffusion (related to defects via which the considered tracer is transported) and electrical conduction (related to defects via which electrical charges are transported), preferably on very pure single crystals to avoid possible influences from grain boundaries and dislocations. In the following section, defect-related transport properties of matter and charge in ionic compounds and their relationships to point defect concentrations are discussed. After that further conclusions on the point defect structure in $Fe_2SiO_{4+\delta}$ can be made based on experimental findings for transport properties of $Fe_2SiO_{4+\delta}$.

1.3. Transport of Matter and Charge in Binary and Ternary Oxides

1.3.1. Diffusion and Electrical Conduction

Diffusional transport processes in ionic compounds in the absence of potential gradients are described by diffusion coefficients which are defined by mean square displacement, denoted by $\overline{R}_n^2$, of the considered moving species. Diffusion coefficients can be expressed in terms of the square of an elementary jump length, a_i, jump frequency $\Gamma_{i,eff}$, and a geometrical factor g_i.

$$D_i = \lim_{t \to \infty} \frac{\overline{R}_n^2}{6 \cdot t} = g_i \cdot a_i^2 \cdot \Gamma_{i,eff} \quad (1.16)$$

In general, the effective jump frequency is related to the elementary jump

frequency Γ_i, an availability factor β_i, and a correlation factor f_i:

$$\Gamma_{i,eff} = \Gamma_i \cdot \beta_i \cdot f_i \tag{1.17}$$

The elementary jump frequency Γ_i is related to completely random motion in the case that all neighboring potential jump sites are available for a subsequent jump. The availability factor β_i gives the fraction of the potential jump positions that are available for a subsequent jump to proceed. Lastly, the correlation factor f_i denotes the fraction of proceeded jumps, which is effective for transport in the sense of the mean square displacement.

For the diffusion of ions and of point defects that are involved in the diffusion of these ions, the effective jump frequencies are different, while the geometric factor and the jump length are the same. The self-diffusion coefficients of ions and of point defects involved in the motion of these ions are related by

$$D_{ion} = \sum D_{def} \cdot x_{def} \tag{1.18}$$

where x_{def} is a ratio of concentrations of point defects and ions transported via point defects. The diffusion coefficient D_{def} is described in Equation (1.19),

$$D_{def} = g_{def} \cdot a_{def}^2 \cdot \Gamma_{def} \tag{1.19}$$

The tracer diffusion coefficient and the self-diffusion coefficient of the diffusing

ions are related by a correlation factor f^{*}_{Ion} which takes into the fraction of jumps ineffective for transport due to the distinction between normal and tracer ions.

$$D^{*}_{ion} = f^{*}_{ion} \cdot D_{ion} \tag{1.20}$$

When considering the temperature dependence of the diffusion coefficients of an ion as described in Equations (1.18) and (1.19), f_{ion}, g_{def} and a_{def} are practically independent of temperature while x_{def} and the elementary jump frequency Γ_{def} are temperature dependent. The temperature dependence of the diffusion coefficient of an ion is given by

$$D_{ion} = D_0 \cdot \exp\left(-\frac{\Delta H^{\circ}_f + \Delta H_m}{RT}\right) \tag{1.21}$$

where

$$D_0 = g_i \cdot a_i^2 \cdot v_i \cdot \exp\left(\frac{\Delta S^{\circ}_f + \Delta S_m}{R}\right) \tag{1.22}$$

In Equations (1.21) and (1.22) ΔS^{o}_{f} and ΔH^{o}_{f} are the changes in entropy and enthalpy related to the formation of defects, respectively, v_i is the elementary vibration frequency of the diffusing atom/ion i, and ΔS_m and ΔH_m are the changes in entropy and enthalpy related to the motion of an atom/ion from one position to another, respectively.

For the transport of charge in binary and ternary oxides, the field-induced drift of a single ionic species is often described by partial ionic conductivity, σ_i.

$$\sigma_i = c_i \cdot u_i \cdot z_i \cdot F \tag{1.23}$$

where c_i is the concentration of species i, u_i is the mobility of the species i, z_i is the charge number of the species i and F is the Faraday constant.

The overall electrical conductivity σ in an ionic compound is the sum of partial ionic and electronic conductivities,

$$\sigma = \sum \sigma_i = \sum \sigma_{ion} + \sigma_{e'} + \sigma_{h^\bullet} \tag{1.24}$$

Transference numbers, $t_{el} = \sigma_{el}/\sigma$ and $t_{ion} = \sigma_{ion}/\sigma$, describe the fractions at which the different types of charge carriers contribute to charge transport. In insulators there is a tight bonding of electrons to atoms, which very often leads to an electrical current at high temperatures due to mostly the motion of ions and not of electrons or holes. However, in transition metal-containing oxides this is usually not the case and electrical charge is usually transported by means of electrons and holes, leading to, $t_{el} \approx 1$ and $t_{ion} \approx 0$. Consequently the electrical conductivity in transition metal-containing oxides can be written as

$$\sigma = \sigma_{e'} + \sigma_{h^\bullet} \tag{1.25}$$

If it is assumed that the mobility of electrons and holes in transition metal-containing oxides are independent of the oxygen activity, the oxygen activity

dependence of the electrical conductivity is determined by the oxygen activities dependencies of the concentrations of electrons and holes.

1.3.2. Transport of Matter and Charge in Binary Non-Stoichiometric Oxides

For discussing transport of matter and charge, the model oxide $Me_{1-\Delta}O$ considered earlier for the special case $K_F = K_e/4$ is used again as an example. The Kröger-Vink diagram of $Me_{1-\Delta}O$ for this special case was shown earlier in Figure 1.2b. The same figure is shown again in Figure 1.4a in comparison with three other figures illustrating defect-related properties. As stated before, in this special case, at high oxygen activities cation vacancies and holes are the majority defects and at low oxygen activities cation interstials and electrons are the majority defects. Based on the relationship between point defect concentrations and defect-related properties, the oxygen activity dependencies of defect-related properties, including cation tracer diffusivity, electrical conductivity and deviation from stoichiometry can be obtained.

The deviation from stoichiometry, Δ, in $Me_{1-\Delta}O$, is equal to the difference between the concentrations of cation vacancies and interstials, see Equation (1.13). The oxygen activity dependence of Δ in $Me_{1-\Delta}O$, is shown in Figure 1.4b.

If the mobilities of the ionic point defects are independent of their concentrations, for a binary non-stoichiometric compound $Me_{1-\Delta}O$ for $K_F = K_e/4$ the following oxygen activity dependence of the cation self-diffusion coefficient results:

$$D_{Me} = D_V \cdot a_{O_2}^{1/6} + D_I \cdot a_{O_2}^{-1/6} \tag{1.26}$$

Figure 1.4c shows a schematic plot of the oxygen activity dependence of the self-diffusion coefficient assuming that D_V is smaller than D_I. The diffusion coefficient usually measured for the diffusion of ions in solids is the tracer diffusion coefficient, D^*_{Ion}, instead of the self-diffusion coefficient, D_{ion}.

Assuming that the ionic conduction is negligibly small, the expression describing the oxygen activity dependence of the electrical conductivity, σ, is:

$$\sigma = \sigma_{el} = \sigma^{\circ}_{h^{\bullet}} \cdot a_{O_2}^{1/6} + \sigma^{\circ}_{e'} \cdot a_{O_2}^{-1/6} \tag{1.27}$$

For a case where the mobility of electrons is larger than that of holes, the dependence of the logarithm of electrical conductivity, σ, on the logarithm of oxygen activity is illustrated in Figure 1.4d.

The Kröger-Vink diagram for the compound $Me_{1-\Delta}O$ shown in Figure 1.4a is compatible with the oxygen activity dependence of the defect-related properties shown in Figure 1.4b to 1.4d.

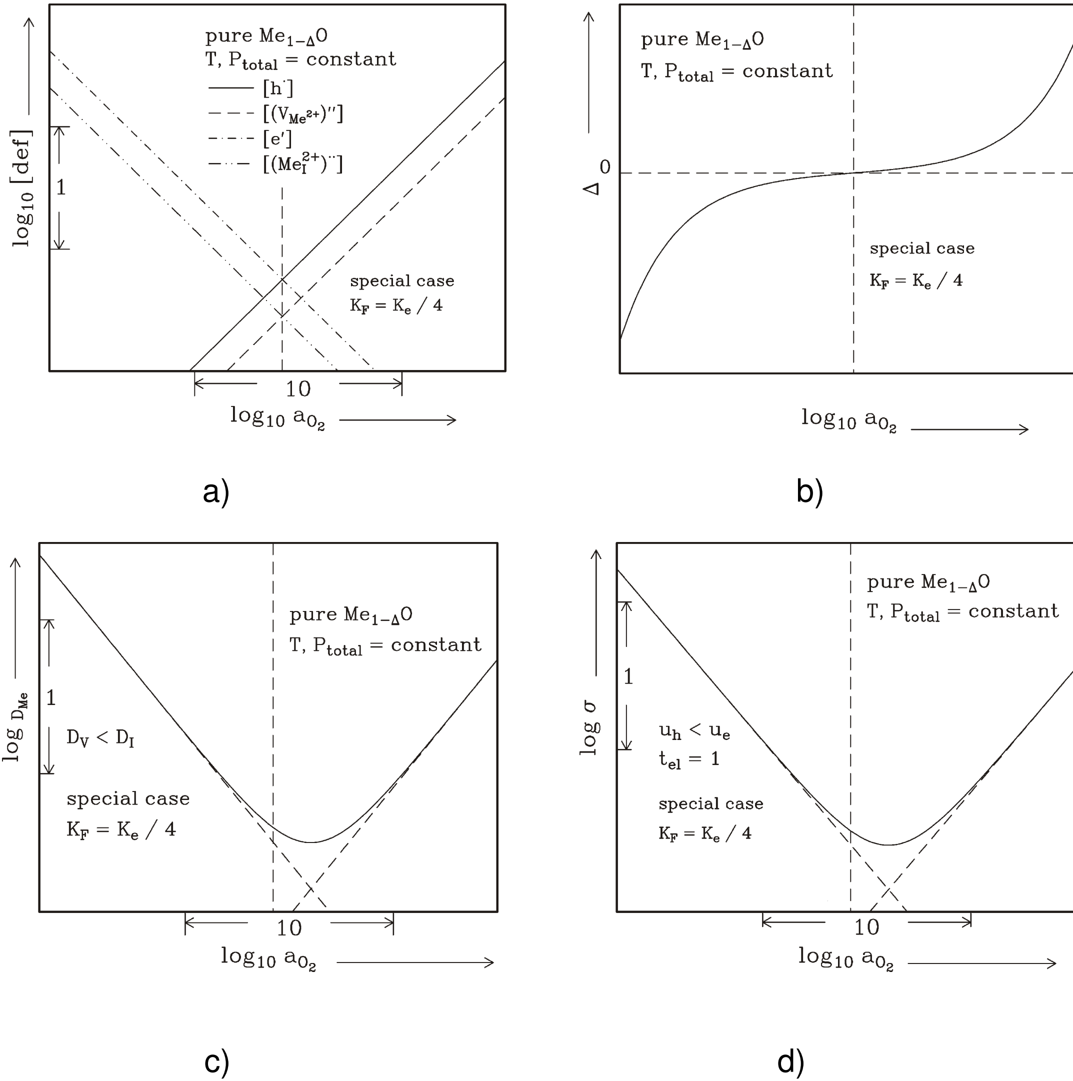

Figure 1.4: Schematic plots illustrating the relationships between oxygen activity dependencies of a) concentrations of point defects, b) the deviation from stoichiometry Δ in $Me_{1-\Delta}O$, c) cation diffusion coefficients, and d) electrical conductivities in the model oxide $Me_{1-\Delta}O$ for the very special case when $K_F = K_e/4$.

1.3.3. Transport of Matter and Charge in Ternary Non-Stoichiometric Oxides

The preceding discussion of point defect-related properties of a binary non-stoichiometric oxide in principle also applies to ternary non-stoichiometric compounds. This section continues the previous discussion of the point defect structure of $Fe_2SiO_{4+\delta}$. This oxide is used as a model compound for discussing the results of investigations related to the point defect structure of non-cubic ternary non-stoichiometric oxides with the olivine structure by studying component activity dependencies of transport properties.

A systematic study of the defect structure of iron-containing olivines was performed by Tsai et al. [11]. Results for the variation of the oxygen content of synthetic $Fe_2SiO_{4+\delta}$ single crystals by Tsai et al. [11] were discussed in the previous section. Figure 1.5b shows the results related to the oxygen activity dependence of the variation in the oxygen content at 1130 °C in $Fe_2SiO_{4+\delta}$ by Tsai et al. [11]. The results are compatible with cation vacancies, $(V_{Fe^{2+}})''$, holes, $h^{\bullet}$, and Fe^{3+} ions on Si sites, $(Fe^{3+}_{Si^{4+}})'$, as the majority defects. Furthermore, Tsai et al. studied the tracer diffusion of iron in synthetic fayalite single crystals, $Fe_2SiO_{4+\delta}$, at the same temperature as a function of orientation and oxygen activity. Figure 1.5c shows results of their iron tracer diffusion measurements in fayalite. The observed oxygen activity dependencies of the iron tracer diffusion suggest that iron ions move via different cation vacancies, most likely isolated cation vacancies, $(V_{Fe^{2+}})''$, and possibly neutral associates $\{2(Fe^{3+}_{Me^{2+}})^{\bullet}\cdot((V_{Me^{2+}})''\}^{\times}$, which could be present as minority defects with high mobility [11]. Results of electrical conductivity

measurements using fayalite single crystals as samples are shown in Figure 1.5d as a function of crystal orientation and oxygen activity at 1130 °C. The observed oxygen activity dependencies of the electrical conductivity is compatible with $(V_{Fe^{2+}})''$, $(Fe^{3+}_{Fe^{2+}})^{\bullet}$ and $(Fe^{3+}_{Si^{4+}})'$ as the majority defects at high oxygen activity and with $h^{\bullet}$ and e' as the majority defects at low oxygen activities. A Kröger-Vink diagram, which is compatible with the oxygen activity dependencies of the deviation from stoichiometry, the iron tracer diffusivity and the electrical conductivity, see Figures 1.5b, c and d, respectively, was generated by Tsai et al. [11] and is shown in Figure 1.5a.

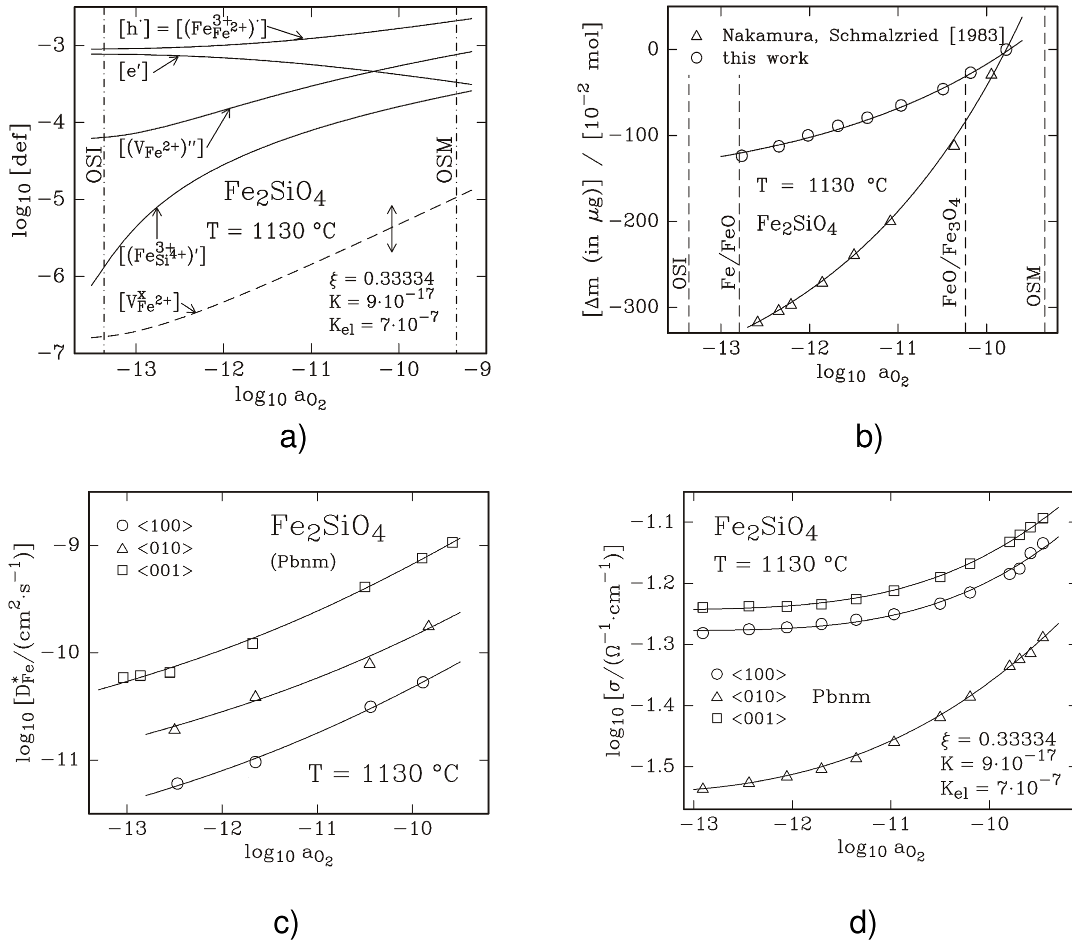

Figure 1.5: Results from a systematic study of the point defect structure and of defect- related properties of $Fe_2SiO_{4+\delta}$ at 1130 °C performed by Tsai et al. [11]: a) Kröger-Vink diagram compatible with experimental results for the variation of the oxygen content, the electrical conduction and the iron tracer diffusion in $Fe_2SiO_{4+\delta}$, b) relative mass changes observed in fayalite upon oxygen activity changes, c) orientation and oxygen activity dependencies of the iron tracer diffusivity in $Fe_2SiO_{4+\delta}$, and d) results of electrical conductivity measurements as a function of the oxygen activity and crystallographic orientation.

1.4. Anisotropy in Transport Properties of Orthosilicates with Olivine Structure

1.4.1. Representation of Diffusion Coefficients as Second Rank Tensors

As it can be seen in Figure 1.5c and 1.5d, the iron tracer diffusion and electrical conductivity in fayalite depend on the crystal orientation. That is due to the non-cubic nature of the olivine structure. Therefore it is at this point appropriate to address the second rank tensor representation of the diffusion coefficient and of the electrical conductivity in oxides with non-cubic crystal structure including olivines.

The driving force in a diffusion process can be a chemical potential gradient, and the response is a flux. A diffusion coefficient is a physical property that relates these two quantities. Since the flux and the chemical potential gradient are both vectors, the diffusion coefficient is a second rank tensor, except in the case of a cubic structure; in that case, the diffusion coefficient is a scalar due to the high symmetry in the cubic structure [12]. The diffusivity tensor is symmetric, thus, in general, it has 6 independent components. Like all symmetrical tensors, it can always be diagonalized by transformation into a set of principle axes so that

$$D = \begin{bmatrix} D_{11} & 0 & 0 \\ 0 & D_{22} & 0 \\ 0 & 0 & D_{33} \end{bmatrix} \qquad (1.28)$$

From Equation (1.28) it can ben seen that there are only three parameters D_{11}, D_{22} and D_{33}, in the second rank tensor representation of a diffusion coefficient D. The information for the other three parameters is contained in the orientations of the principle coordinate axes. D_{11}, D_{22} and D_{33} are called the principal diffusion coefficients [12].

In particular, a crystal that has an orthorhombic symmetry, such as compounds of the olivine group have, must have the principle axes of the diffusion coefficient parallel with the crystal axes; thus only three parameters, D_{11}, D_{22} and D_{33}, are required to specify its diffusivity as discussed above. In that case, three measurements of diffusion coefficients along the three crystallographic orientations [100], [010] and [001] are needed to specify D_{ij} [12]. The same is also true for the electrical conductivity as a second rank tensor. Only three measurements of the electrical conductivities along the three crystallographic orientations are needed to specify σ_{ij}.

1.4.2. Orientation Dependence of Transport Properties of Olivines

Orientation dependencies of transport properties of olivines are not yet well understood. Results from studies of orientation dependencies of transport properties of olivines vary with the type of transport phenomenon being investigated. With regard to the cation tracer diffusion in Me_2SiO_4, there exist experimental studies of the orientation dependence of the tracer diffusion of Mg in Mg_2SiO_4 [13] and of the tracer diffusion of Fe in Fe_2SiO_4 [11]. Besides, there exist investigations on the interdiffusion of Fe and Mg in $(Fe_xMg_{1-X})_2SiO_4$ solid

solutions with varying Fe content [14]. There also exist studies on the kinetics of the point defect relaxation in Fe_2SiO_4 after sudden oxygen activity changes [15]. The results of all studies denoted above are related to the diffusion of cations and/or point defects in Me_2SiO_4 and show that the diffusion of cations along the [001] orientation occurs fastest. For fayalite, the results for the iron tracer diffusion [11] and for the point defect relaxation [15] show that $D_{Fe[001]} > D_{Fe[010]} > D_{Fe[100]}$. However for forsterite, the diffusion of Mg [13] and interdiffusion results [14] indicate that $D_{[001]} > D_{[100]} > D_{[010]}$.

For the orientation dependence of the electrical conductivity in Me_2SiO_4, there exist studies on synthetic Mg_2SiO_4 and other olivines [16], and on Fe_2SiO_4 [11]. While the sequence $\sigma_{[001]} > \sigma_{[100]} > \sigma_{[010]}$ is the same for all results obtained from electrical conductivity measurements, the ratios of the conductivities along the different principle orientations are different. The orientation dependence of the electrical conductivity in Mn_2SiO_4 has also been studied [17] along two of the principle orientations [100] and [010]. The results [17] show that in manganese silicate $\sigma_{[100]} > \sigma_{[010]}$.

The mechanisms of the cation diffusion and of the electrical conduction in orthosilicates are far from being well understood. Buening and Busek [14] proposed that the fastest diffusion in the [001] orientation is due to the fact that the M1 sites are lined up in that direction. It has also been proposed that based on calculations that the zig-zag jumps between M1 and M2 sites are the most suitable explanation for the fastest diffusion along the [001] direction. However it was

argued by Miyamoto and Takeda [18] that, based on energy minimization calculations, only M1 sites are involved in the diffusion along the [001] orientation.

In addition, at present it is unknown to what extent the orientation dependence of transport properties of different transition metal-containing orthosilicates, e.g., the ratios of cation tracer diffusion coefficients and of electrical conductivities for different orientations, is related to the crystal structure and to which extent to the type of the Me ions.

A thorough understanding of the details behind the observed orientation dependencies in the cation diffusion and the electrical conduction in orthosilicates is still far from being complete. Further investigations of the crystal orientation dependence of the cation tracer diffusion in conjunction with results for the electrical conductivity are needed to obtain more insight into that fundamental question.

1.5. Single Crystal Growth of Olivines

1.5.1. Demand for Single Crystal Growth

Sizeable and high-quality orthosilicate single crystals are essential for studying the anisotropy of transport properties of orthosilicates. Natural crystals or synthetic polycrystalline samples have been used in many previous studies. However, many problems exist. Natural olivine samples contain different kinds of imperfections such as cracks, inclusions and dislocations. Polycrystalline samples have many grain boundaries which introduce complexity into the study of bulk diffusion. All

non-equilibrium defects hinder the measurement of the bulk transport properties. In addition, the presence of a variety of alio-valent impurities changes the point defect population in olivines and hence changes all defect-related transport properties of such materials. The results obtained by using naturally occurring samples or synthetic samples with uncontrolled impurity concentrations are to a large extent influenced or even completely controlled by the presence of impurities. This suggests that any fundamental investigations related to the point defect structure of olivines require the use of very pure samples with thermodynamically controlled point defect concentrations and known sufficiently small impurity concentrations. In this study a control of the thermodynamic state is achieved by adding a small excess of SiO_2 into the samples used and by fixing the oxygen activity at given values of temperature and total pressure. In addition, the study of the anisotropy of transport properties of olivines requires the use of single crystals of sufficient sizes. In order to fulfil the needs denoted above, a suitable single crystal growth technique needs to be chosen for preparing sizeable and high-quality orthosilicate single crystals with sufficiently low impurity concentrations.

1.5.2. Single Crystal Growth Techniques

Single crystals may be produced by the transport of crystal constituents in the solid, liquid or vapor phase. On that basis, crystal growth may be classified into three categories: a) solid growth, i.e., solid-to-solid phase transformation, b) liquid

growth, i.e., liquid-to-solid phase transformation, and c) vapor growth, i.e., vapor-to-solid phase transformation.

Solid-to-solid crystal growth methods involve the transformation of fine-grained polycrystals into a single crystal by grain boundaries being swept through and being pushed out of the crystal. Solid-state diffusion processes, even at high temperatures, have relatively low rates. As a result, solid-to-solid state crystal growth is commonly not used to grow any large single crystals. In vapor growth, the formation of a crystal is achieved by a phase transition from the gas phase to a solid phase. Examples of vapor growth techniques include physical vapor deposition (PVD) and chemical vapor deposition (CVD). Physical vapor deposition involves the evaporation or sputtering of the target materials into the gas phase, the transport of that material in the gas phase though a concentration or temperature gradient, and then the condensation of material from the gas phase onto a growing surface [19]. Chemical vapor deposition processes are characterized by the formation of the vapor phase via a chemical reaction involving one or more reagent gases containing the constituents of the material to be deposited [19]. Vapor growth techniques are often used to grow single crystal thin films, platelike crystals or whiskers, rather than large single crystals. Last but not least is liquid growth, which is more often used for growing larger sized single crystals compared to such obtained by solid growth and/or vapor growth. Liquid growth can be further divided into two sub-categories by whether the liquid involved is composed only of the same component as the crystallized solid (melt

growth) or contains components in addition to those present what is in the solid phase (solution growth).

Melt growth techniques are most widely used for the growth of large single crystals. The driving force of melt growth is a temperature gradient. Many different types of melt growth techniques have been developed, such as the Verneuil, the Bridgman, the Czochralski and the floating-zone techniques.

The Verneuil process, also known as flame fusion process, was the first industrial crystal growth technique developed. It is primarily used to grow oxides such as ruby and sapphire. During the Verneuil growth, fine powders of target substance are fed though an oxygen-hydrogen flame, become melted droplets and fall onto the top surface of a crystal holder. The droplets form a sinter cone on the holder while there is always a molten cap on the sinter cone. When more molten droplets fall onto the molten cap, a single crystal starts to form. The crystal holder is slowly moved downward allowing further growth of the single crystal by solidification of the molten droplets on the first single crystal grown. The Verneuil method has the advantage of being crucibleless and allowing growth of high melting temperature large single crystals. A disadvantage of the technique is that the growing crystal is exposed to a very steep temperature gradient which often leads to cracking of grown crystals. The principles of the Verneuil method have been applied to many melt growth techniques developed later on. The Verneuil process is regarded as the foundation of melt growth techniques.

In the Bridgman technique, a vertical cylindrical crucible with a conical bottom is used to melt materials to be grown. To initiate the crystal growth, the container filled with the melt is moved gradually from the hot zone of a furnace to the cold zone. Due to the thermal gradient, the melt starts to crystallize at the point bottom of the crucible. The growth of the crystal usually continues from the first formed nucleus. Advantages of the Bridgman technique include that it is a relatively simple technique and allows for control of vapor pressure, shape and size of crystals. Disadvantages of the Bridgman technique include possible mismatch of thermal expansion of crucible and crystal, crystal perfection degradation from the seed, no visibility during crystal growth and not being suitable for growth of materials with high melting point.

The Czochralski technique is a very widely used method for crystal growth because it can produce large and high quality single crystals in a relatively short time. In the growth using the Czochralski method, a suitable "non-reaction" container is used to melt the target material by induction or resistance heating. The atmosphere during the crystal growth can be controlled by pumping gases through the growth apparatus. After the melt has formed, a seed crystal is lowered to reach the melt. Since the temperature of the seed is lower than that of the melt, the melt which is in contact with the seed will crystallize on the bottom tip of the seed. Then the seed is pulled upwards while being rotated to allow further single crystal growth. Advantages of the Czochralski method include that it allows growth of large oriented single crystals and convenient control of the atmosphere. Disadvantages of the Czochralski method include that it is not suitable for growth

of high vapor pressure materials and possible contamination of the melt by crucible material.

Another important melt growth technique is the floating zone method. Figure 1.6 shows a schematic plot of a floating zone system and the temperature variation in the area of crystal growth.

As it can be seen in the figure, at the top there is a feed rod which is made of a polycrystalline sintered rod. At the center there is a molten zone. The lower part is a seed crystal. During the crystal growth, the feed and seed rods are counter-rotated to achieve more uniform heating and mixing within the melt. The formation of the molten zone in the center is achieved by establishing a vertical temperature gradient as illustrated in Figure 1.6. Crystal growth proceeds by moving the assembly consisting of a feed-rod, molten zone and a seed crystal downwards as the melt starts to crystallize on the seed at the seed/melt interface. The heating source used for growing orthosilicates is usually infrared radiation and sometimes a laser. The most obvious advantage of the floating zone method is that no crucible is needed. Other advantages of the floating zone method include control of crystal shape, surface tension, vapor pressure and atmosphere during crystal growth. In addition, it allows the growth of both congruently and incongruently melting materials. Disadvantages of the floating zone method include not being suitable for growth of materials with high vapor pressure, low surface tension, of high viscosity and materials which undergo a phase transformation during cooling.

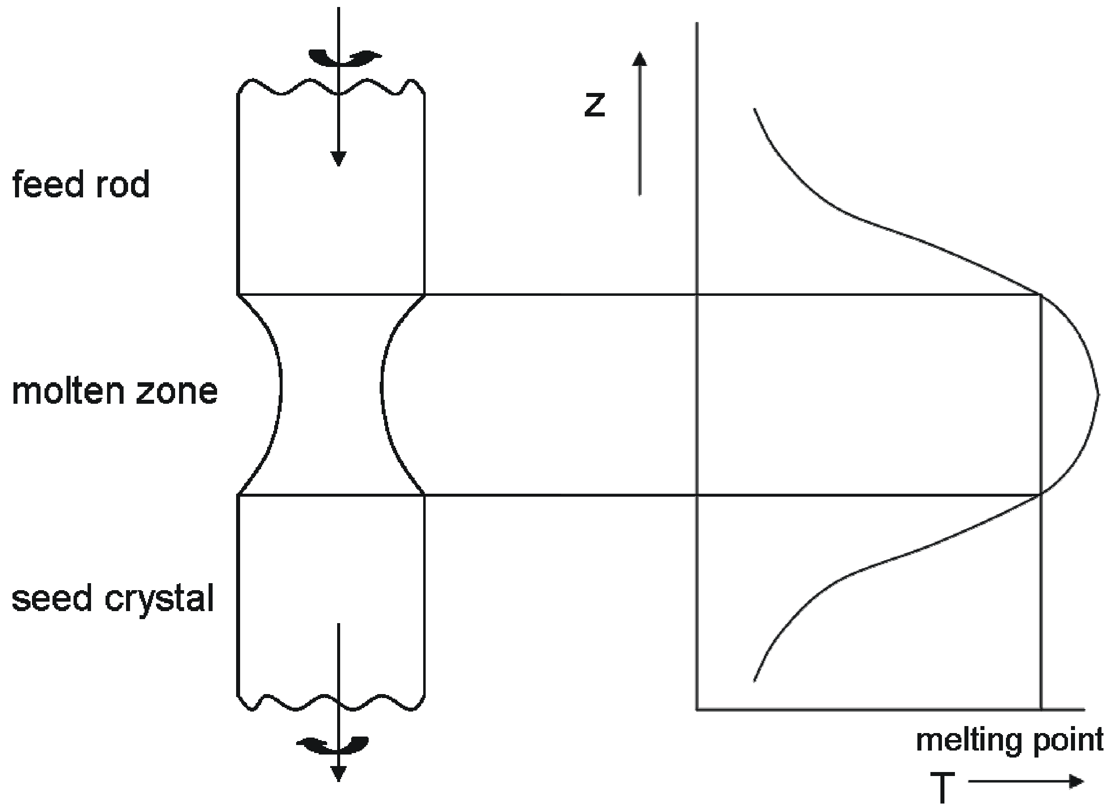

Figure 1.6: A schematic illustration of an assembly consisting of a feed rod, a molten zone and a seed crystal in a floating zone single crystal growth experiment and the vertical temperature distribution produced.

The Bridgman, Czochralski and floating zone methods are useful for the growth of silicate compounds. They have been employed in the past to grow single crystals of Fe_2SiO_4, Co_2SiO_4 and Mn_2SiO_4. A comprehensive summary of employing melt growth techniques for growing transition metal-containing orthosilicates was published by Takei [20].

Besides of melt growth methods, solution growth techniques, such as the flux method, are also important because many minerals have only been successfully grown by that method at present [20]. The flux method is a crystal growth technique where the components of the target substance are dissolved in a solvent, i.e., in a flux. The effect of adding a flux to the material of interest is that the melting point is decreased. A saturated solution is prepared by maintaining the constituents of the desired crystal and the flux at a temperature slightly above the saturation temperature long enough to form a complete solution. Then the crucible containing the flux and the constituents of the crystal is slowly cooled, which leads to the precipitation of the desired crystals. Nucleation occurs in the cooler part of the crucible. An appropriate flux used needs to readily dissolve the desired sample components to have a low vapor pressure and needs to be able to be separated from the target material upon cooling. Typical choices of flux used are Ga, In, Pb, low melting halides and oxides. For the purpose of silicate crystal growth, the MoO_3-Li_2O system is known to be an excellent flux due to the fact that SiO_2 dissolves in this type of flux very well [20]. In high-temperature flux growths, the flux is normally maintained at atmospheric pressure. Hydrothermal growth, as one type of flux growth technique, makes use of high-pressure high-temperature aqueous solutions (sometimes non-aqueous solutions) in order to dissolve the target substances that are insoluble at atmospheric pressure. Advantages of the flux method include that it allows to grow both congruently and incongruently melting materials and that the grown crystals display natural facets which are suitable for optical experiments. Disadvantages of the method include that flux

growth usually produces relatively small crystals, that traces of the flux remain in the grown crystals and that some contamination of a growing crystal by impurities present in the flux.

After reviewing methods potentially of interest for the growth of transition metal-containing orthosilicates, it was essential to select the most suitable crystal growth technique for this study. As stated before, the grown orthosilicate single crystals were intended to be used for studying the orientation dependence of defect-related transport properties of olivines. At high temperatures the transport properties of olivines are governed by point defects in olivines, which can be influenced by the presence of alio-valent impurities in the samples used. Therefore any possible contamination of single crystals during the crystal growth needed to be avoided. In addition, sizeable crystals were needed in order to perform measurements of transport properties. Based on these requirements, the floating zone method, which requires no use of a crucible and is capable of producing sizable silicate single crystals, was decided to be the most suitable technique for this study. In addition, examinations of the physical properties, e.g., melting behavior, absorption of heat radiation, of cobalt orthosilicate and manganese silicate, lead to the conclusion that these oxides could be grown by the floating zone method. More details on the single crystal growth of orthosilicates of interest are reported in Chapters 2 and 4 of this dissertation.

1.6. Thesis overview

Single crystal growth of cobalt orthosilicate and manganese orthosilicate was performed by using the floating zone method. Both a ceramic and a sol-gel synthesis route were used to prepare polycrystalline feed rods used for the floating zone single crystal growth. The grown single crystals were used to measure cation tracer diffusion coefficients as a function of crystal orientation, oxygen activity and temperature. The transport of matter, i.e., tracer diffusion of transition metal cations, in orthosilicates of the type Me_2SiO_4 with Me = Co or Mn was experimentally studied to improve the current understanding of the defect and defect-related properties of transition metal-containing orthosilicates. Modeling of observed oxygen activity dependencies of transport properties and of point defect concentrations were performed based on experimental results obtained from this study and data available in the literature.

In this dissertation, there are five chapters in addition to this introduction. Chapter 2 focuses on the synthesis of cobalt silicate powder via both a ceramic and a sol-gel route, the preparation of polycrystalline feed rods and the floating zone single crystal growth of cobalt orthosilicate. Chapter 3 describes the orientation, oxygen activity and temperature dependencies of the cobalt tracer diffusion and modeling of point defects in cobalt orthosilicate. Chapter 4 deals with the synthesis of manganese orthosilicate powder, the preparation of polycrystalline feed rods and the floating zone single crystal growth of Mn_2SiO_4 using a similar approach as it was described in Chapter 2 for the preparation of cobalt

orthosilicate samples. Chapter 5 focuses on manganese tracer diffusion measurements in manganese silicate as a function of orientation, oxygen activity and temperature and on the modeling of point defects in manganese silicate. Chapter 6 contains a summary and concluding remarks.

REFERENCES

[1] W.A. Deer, R.A. Howieand and J. Zussman, “An Introduction to the Rock-forming Minerals,” 2nd Ed., Longman Scientific & Technical, Harlow, Essex, UK, [1992].

[2] G.E. Brown, Jr., “Olivines and Silicate Spinels,” in 'Reviews in Mineralogy, Vol. 5: Orthosilicates, 2nd. Ed.,' P.H. Ribbe, Ed., Mineralogical Society of America, Washington, D.C., U.S.A., [1982] 275-381.

[3] “International Tables for X-ray Crystallography,” Vol. 1: “Symmetry Groups,” N.F.M. Henry and K. Lonsdale, Eds., The Kynoch Press, Birmingham, U.K., [1965] Table 6.2.1, p. 548.

[4] H. Schmalzried, “Point Defects in Ternary Ionic Crystals.” Prog. Solid State Ch., **2** [1965] 265-301.

[5] R. Dieckmann, “Point Defects and Transport Properties of Binary and Ternary Oxides,” Solid State Ionics, **12** (1) [1984] 1-22.

[6] R. Dieckmann, “Point Defects and Transport in Non-stoichiometric Oxides: Solved and Unsolved Problems,” J. Phys. Chem. Solids, **59** (4) [1998] 507-525.

[7] R. Dieckmann, MSE 6040, “Kinetics of Reactions in Condensed Matter,” Lecture Notes, Cornell University.

[8] F.A. Kröger and H.J. Vink, "Relations Between the Concentrations of Imperfections in Crystalline Solids," in: F. Seitz and D. Turnbull, Eds., Solid State Physics - Advances in Research and Applications, Vol. 3, Academic Press, New York, U.S.A. [1956] 307-435.

[9] K. Andersson, G. Borchardt, O. Müller and G. Róg, "A Point-Defect Approach to the Silicon Sublattice in Orthosilicates at High Temperatures", in: 'Nonstoichiometric Compounds,' C.R.A. Catlow and W.C. Mackridt, Eds., Advances in Ceramics, **23** [1987] 399-407.

[10] A. Nakamura and H. Schmalzried, "On the Nonstoichiometry and Point Defects of Olivines," Phys. Chem. Minerals, **10** (1) [1983] 27-37.

[11] T.-L. Tsai, K.-D. Becker and R. Dieckmann, "Point Defects and Orientation-dependent Transport of Matter and Charge in Iron-containing Olivines," Solid State Ionics, **194** (1) [2011] 17-32.

[12] J.F. Nye, "Physical Properties of Crystals: Their Representation by Tensors and Matrices," Oxford University Press, Oxford, U.K. [1957].

[13] S. Chakraborty, J.R. Farver, R. A. Yund and D.C. Rubie, "Mg Tracer Diffusion in Synthetic Forsterite and San Carlos Olivine as a Function of P, T and f_{O_2}," Phys. Chem. Miner., **21** (29) [1994] 489-500.

[14] D.K. Buening and P.R. Buseck, "Fe-Mg Lattice Diffusion in Olivine," J. Geophys. Res., **78** (29) [1973] 6852-6862.

[15] K. Ullrich and K.D. Becker, “Kinetics and Diffusion of Defects in Fayalite,” Solid State Ionics, **141-142** (1) [2001] 307-312.

[16] R.N. Schock, A.G. Duba and T.J. Shankland, “Electrical Conduction in Olivine,” J. Geophys. Res., **94** (B5) [1989] 5829-5839.307-312.

[17] Q. Bai, Z.C. Wang and D.L. Kohlstedt, “Manganese Olivine I: Electrical Conductivity,” Phys. Chem. Miner., **22** (8) [1995] 489-503.

[18] M. Miyamoto and H. Takeda, “Atomic Diffusion Coefficients Calculated for Transition Metals in Olivine,” Nature, **303** (16) [1983] 602-603.

[19] H.J. Scheel and P. Capper, “Crystal Growth Technology, from Fundamentals and Simulation to Large-scale Production,” Wiley-VCH, Weinheim, Germany [2008] 54-56.

[20] H. Takei, S. Hosoya and M. Ozima, “Synthesis of Large Single Crystals of Silicates and Titanates,” in 'Materials Science of the Earth’s,' I. Sunagawa, Ed., Terra Scientific Publishing Company, Tokyo, Japan, [1984] 107-130.

CHAPTER 2

FLOATING-ZONE GROWTH AND CHARACTERIZATION OF SINGLE CRYSTALS OF COBALT ORTHOSILICATE, Co_2SiO_4 *

2.1. Abstract

Good quality single crystals of high purity cobalt silicate, Co_2SiO_4, were successfully grown by the floating-zone method in air at atmospheric pressure along the three principle orientations. The grown crystals were 30 to 60 mm in length and 6 to 10 mm in diameter. Well developed facets were found on all crystals grown. Impurity levels and the degree of a desired excess of silicon in grown crystals were determined by using the ICP-AES technique. In addition, the presence of a small amount of inclusions in the matrix of grown crystals due to a small excess of silica was confirmed by TEM. Dislocation densities were determined upon etching; the observed densities were on the order of 10^5 to 10^6 cm^{-2}.

2.2. Background

Cobalt orthosilicate, Co_2SiO_4, is a member of the olivine mineral family. Olivines are major components of the Earth's upper mantle and are therefore of geological and geophysical importance. Many geophysical and geochemical processes active in the upper mantle depend on the type and concentrations of

---

* Reprinted with permission from Qi Tang and Rüdiger Dieckmann, J. Cryst. Growth., **317** (1) [2011] 119–127. Copyright © 2011, Elsevier.

point defects in olivines at high temperatures. At present, the basic knowledge of the point defect structure and of defect-related properties of olivines is still relatively limited. Many previous studies of defect-related properties of olivines have been performed using natural mineral samples. The chemical nature and the concentrations of impurities present in such samples can vary very significantly with the origin of the samples. As a consequence, results obtained from experimental studies of defect-related properties using natural mineral samples may vary very significantly. Another complication is that some defect-related properties of olivines are orientation-dependent due to the orthorhombic crystal structure of olivines.

All this suggests that any meaningful fundamental studies of defect-related properties require at least the use of very pure samples. If any properties of interest are orientation-dependent one needs to use sufficiently pure single crystals grown along specific orientations. Suitable samples fulfilling the needs outlined above cannot be found in nature as minerals. Consequently, to possibly reach a detailed understanding of point defects and point defect-related, orientation-dependent properties of olivines, it is necessary to have high quality olivine single crystals available. Such crystals must be of high purity, well characterized and, in addition, also thermodynamically well defined. The latter can in principle be achieved by very precisely controlling the cobalt-to-silicon ratio or by forcing precipitates of a secondary phase to be present, in the case of Co_2SiO_4, of silica or of cobalt metal or oxide. Usually the precision of composition control,

which can be achieved experimentally, is not sufficient to produce single-phase material with a precisely known cobalt-to-silicon ratio.

2.2.1. Previous Growth of Single Crystals of Co_2SiO_4 and Similar Orthosilicates

Several different techniques have been used in the past to grow cobalt orthosilicate single crystals, including chemical transport reactions, the use of fluxes, the Bridgman technique and the floating-zone method.

In chemical vapor transport reactions involving fluorides as the transported species Schmid [1] observed the formation of small single crystals of Co_2SiO_4. The reactions were performed using a platinum crucible containing CoO inside of a tube of silica. Small crystals of Co_2SiO_4 were observed near the top of the Pt crucible, but not on the walls of the silica tube. This suggests that the transported species leading to the formation of Co_2SiO_4 were very likely oxygen and fluorides of Co and Si. The obtained crystals were only up to about 1 mm in size. Further details on the obtained crystals were not communicated.

Naka et al. [2] studied the growth of Co_2SiO_4 single crystals by the Bridgman technique in air at atmospheric pressure. Differential thermal analysis (DTA) was utilized to observe the melting and crystallization behavior of Co_2SiO_4. Platinum crucibles of four different shapes were tested for growing crystals. The best results were obtained when growing at rates between 0.5 and 1.8 mm/h and using a crucible in the last 13 mm near the bottom necked to 3-4 mm and terminated in a 60° cone. The temperature at which solidification occurred was reported to be

around 1410 ℃, which is according to Naka et al. [2] 10 ℃ below the melting temperature of Co_2SiO_4 in air. Single crystals of cobalt olivine were grown only a few times. The direction of growth was typically along the [001] orientation. This orientation denotation refers to the space group Pbnm, which is used throughout this article. Optical microscopy was employed to observe polished and subsequently etched surfaces of grown crystals. Etch pits were visible after exposing polished surfaced to 6N HCl for 1.7 hours at 26 ℃. Lattice parameters were determined by X-ray powder diffraction (XRD); the data obtained by Naka at al. [2] are listed in Table 2.1.

Table 2.1: Lattice parameters of Co_2SiO_4 (space group: Pbnm) reported in the literature in comparison with values obtained in this study.

a (Å)	b (Å)	c (Å)	Year	Reference
4.779	10.340	5.996	1963	[25]
4.778	10.301	6.005	1963	[26]
4.781(3)	10.289(7)	5.993(3)	1965	[27]
4.7823	10.310	6.0074	1966	[28] (ASTM)
4.787	10.275	6.010	1968	[2]
4.7823(3)	10.3044(8)	6.0036(4)	1968	[29]
4.782	10.302	6.003	1974	[30]
4.7837	10.3168	6.0095	1981	[5]
4.7797(8)	10.2976(6)	5.9986(3)	1983	[31]
4.7816(1)	10.3005(1)	6.0028(1)	2008	[32]
4.784(4)	10.284(5)	6.008(6)	present study	

Wanklyn [3] grew small single crystals of Co_2SiO_4 from a flux of PbO-SiO_2 with an excess of SiO_2. Platinum crucibles of 0.5 mm wall thickness and with closely fitting lids were used during growth. After growth, the flux was hot drained and the crystals were cleaned in a “warm 1:10 HNO_3 solution”; further details were not reported. Different kinds of fluxes were used in attempts to grow single crystals of Co_2SiO_4 and several other orthosilicates. The sizes of the Co_2SiO_4 crystals grown were up to 6 × 5 × 2 mm when using a PbO-SiO_2 flux. Large crystals of Co_2SiO_4 with sizes up to 10 × 5 × 5 mm were obtained when using a PbO-PbF_2-SiO_2 flux. When a PbF_2-SiO_2 flux with a small amount of MoO_3 was used, well-formed prisms of Co_2SiO_4 with sizes up to 10 × 3 × 1 mm were formed. The use of other fluxes led only to very small crystals of Co_2SiO_4. Results from any other characterization efforts were not reported.

Hosoya and Takei [4] were the first authors to synthesize sizable single crystals of Co_2SiO_4 by using the floating-zone method. In their one page publication these authors reported that the growth rate was 1.5 - 5 mm/h and that the crystals grown were 5 to 10 mm in diameter and 20 to 70 mm in length. The growth axes were [100] and [010] (specific space group information was not provided, most likely the space group Pbnm was used). X-ray powder diffraction was employed to identify the phase being present. The grown crystals were inspected by optical microscopy; details of any observations made were not reported. A picture in Ref. [4] showing the cross-section of a crystal grown along the orientation [010] reveals that the cross-section had an oval shape.

When aiming for the growth of oxide spinels containing Co and Mn, Strobel and Le Page [5] observed in addition to the formation of oxide spinel also the growth of single crystals of Pt and of Co_2SiO_4, the latter up to 2 mm in length. The authors attributed the growth of the two latter types of crystals to side reactions. During the chemical vapor transport crystal growth experiments, a mixture of Co_3O_4 and Mn_3O_4 was heated in a platinum capsule and transported through the gas phase by using $TeCl_4$ as the transporting agent. The chemical vapor transport was carried out with a Pt capsule containing Co_3O_4 and Mn_3O_4 being located in an evacuated silica tube using a two-zone furnace. To produce a temperature gradient, the temperature in the growth zone was decreased from 1200 to 980 K at a rate of 2 K/h. Thereafter growth was allowed to take place for 7 to 10 days. Microscopic observation of the silica tube ends showed that some larger crystals of Co_2SiO_4 were present on the silica tube wall. It was suggested that the formation of cobalt silicate did occur by a reaction between gaseous cobalt chloride species and solid silica from the tube walls. X-ray diffraction (XRD) was used to confirm the presence of Co_2SiO_4 and to determine its lattice parameters; for the values obtained see Table 2.1.

Other transition metal-containing orthosilicates have been grown by several authors. Fe_2SiO_4 single crystals have been grown hydrothermally by Hirano et al. [6]. The Czochralski method was used to grow Fe_2SiO_4 single crystals by Finch et al. [7]. A floating zone method was used to grow Fe_2SiO_4 single crystals by Takei [8] and later by Tsai et al. [9]. Mn_2SiO_4 single crystals have been grown by using a Czochralski method by Takei [10] and by Finch et al. [11]. Single

crystals of Ni_2SiO_4, which is an incongruently melting compound, were grown by Ozima [12] using a MoO_3-Li_2O flux.

After reviewing all methods employed before to grow Co_2SiO_4 single crystals and other transition metal-containing orthosilicates, the floating zone technique was chosen by authors of this paper to grow single crystal of Co_2SiO_4 for defect-related studies. As discussed before, any meaningful fundamental studies of defect-related properties require the use of very pure samples. Unlike other crystal growth methods discussed, the floating zone method involves no crucible which excludes contamination by crucible material during growth.

2.2.2. Thermodynamic Stability of Co_2SiO_4

Knowing the thermodynamic stability range of Co_2SiO_4 is very important for the growth of single crystals of Co_2SiO_4 and also for experimental studies involving this material, e.g., for studies of point defects and of the orientation dependence of transport of matter and charge at high temperatures. After not being able to find a suitable summary on the phase stability range of cobalt silicate in the literature, individual thermodynamic data from the literature were reviewed to produce such a summary. As a result of this data collection the diagram shown in Figure 2.1 was obtained. Since the thermodynamic stability of Co_2SiO_4 varies at a constant total pressure as a function of temperature, oxygen activity and the cobalt-to-silicon ratio, one needs in principle a three-dimensional plot to fully describe the phase stability limits. The stability range of Co_2SiO_4 corresponds to a three-dimensional object in the temperature / oxygen activity / cobalt-to-silicon ratio space and is

limited by curved surfaces in this space. The two-dimensional plot shown in Figure 2.1 represents a projection of phase stability data for a total pressure of one atm, corresponding to lines on the curved surfaces denoted above, onto the temperature vs. oxygen activity plane in a three-dimensional plot with the cobalt-to-silicon ratio as a third axis.

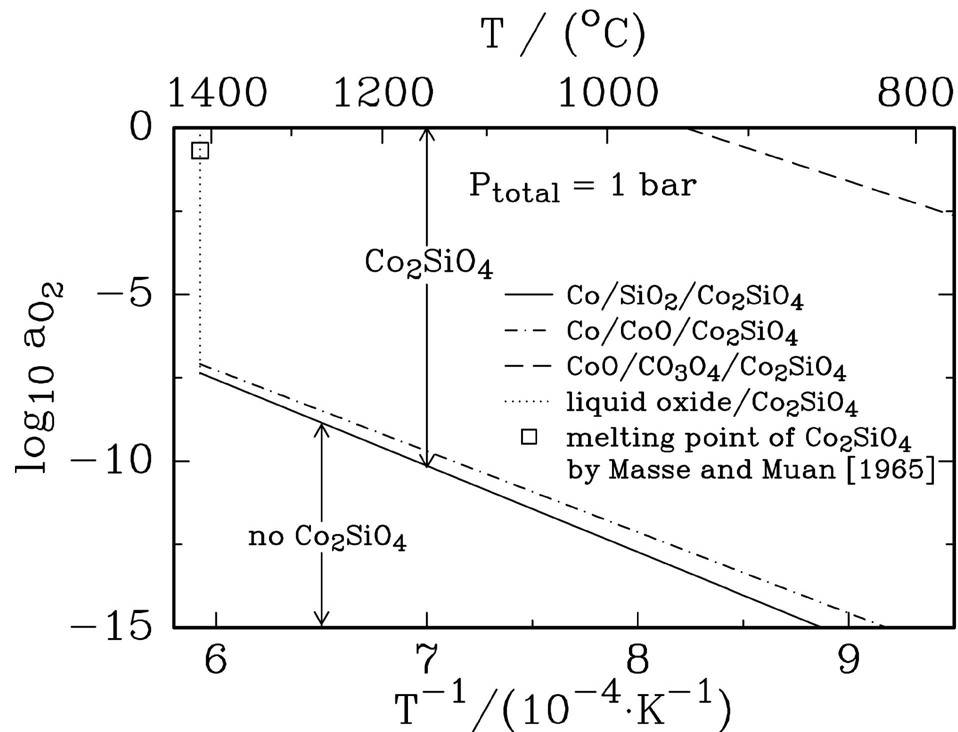

Figure 2.1: A diagram showing data related to the thermodynamic stability range of cobalt orthosilicate at high temperatures at 1 atm total pressure. Information about the data used to derive this diagram is provided in Section 2.2.2.

The line in Figure 2.1 corresponding to the equilibrium between Co, Co_2SiO_4 and SiO_2 was generated by using Equation (2.1) which is based on data published

by Lebedev and Levitskii in 1962 [13], Róg et al. in 1974 [14] and O'Neill in 1987 [15].

$$\log_{10} a_{O_2}(Co/Co_2SiO_4/SiO_2) = 7.99 - \frac{25900}{T} \quad (2.1)$$

Lebedev and Levitskii [13] determined the composition of CO/CO_2 gas mixtures in equilibrium with Co, Co_2SiO_4 and SiO_2 at temperatures between 810 and 1150 °C and calculated oxygen activities from the experimentally determined CO/CO_2-ratios by making use of thermodynamic data from the literature for the equilibrium between CO, CO_2 and O_2. Róg et al. [14] measured electrochemically oxygen activities for the equilibrium denoted above for temperatures between 1000 and 1400 °C by using CaO-doped zirconia as electrolyte and oxygen at 0.2 atm for establishing a reference activity of oxygen. O'Neill [15] also performed electrochemical measurements by using CaO-stabilized zirconia as electrolyte at temperatures between 687 and 1124 °C. This author used the equilibria between Ni/NiO and Fe/"FeO" for establishing reference oxygen activities.

The line in Figure 2.1 corresponding to the equilibrium between Co, CoO and Co_2SiO_4 was derived by using Equation (2.2) which was obtained by using data published by Róg et al. in 1974 [14], Enoki et al. in 1977 [16]. and O'Neill in 1987 [15].

$$\log_{10} a_{O_2}(Co/CoO/Co_2SiO_4) = 7.31 - \frac{24300}{T} \quad (2.2)$$

All the authors denoted above performed electrochemical measurements of oxygen activities for the Co/CoO equilibrium by using CaO-doped zirconia as

electrolyte; Co_2SiO_4 was not present. It is reasonable to assume that the co-existence of Co_2SiO_4 with the phases Co and CoO has practically no influence on the oxygen activities related on the equilibrium between Co and CoO. The experiments by Róg et al. covered the temperature range between 800 and 1400 ℃, those by Enoki et al. the range between about 700 and 1110 ℃ and those by O'Neill temperatures between 527 and 1124 ℃. The reference oxygen activities used by Róg et al. and by O'Neill were the same as denoted above; Enoki et al. used air at atmospheric pressure for this purpose.

Data for the equilibrium between CoO, Co_3O_4 and Co_2SiO_4 were taken from studies by Bugden and Pratt [17] and Enoki et al. [16]. Both studies used electrochemical measurements to determine oxygen activities for the equilibrium between CoO and Co_3O_4. Reference oxygen activities were defined in both studies by the Ni/NiO equilibrium and in the study by Budgen and Pratt also by the Cu/Cu_2O equilibrium. The study by Bugden and Pratt covered the temperature range between about 530 and 930 ℃ and that by Enoki et al. temperatures between about 580 and 790 ℃. By using the results from the studies just described, the authors of this article have derived Equation (2.3) for drawing the line for the $CoO/Co_3O_4/Co_2SiO_4$ equilibrium shown in Figure 2.1.

$$\log_{10} a_{O_2}(CoO/Co_3O_4/Co_2SiO_4) = 17.0 - \frac{20700}{T} \tag{2.3}$$

It was assumed that the oxygen activities for the coexistence of CoO and Co_3O_4 are practically not altered if Co_2SiO_4 is present as a third phase.

Experimental data for the melting temperature of cobalt orthosilicate as a function of the oxygen activity and/or the Co/Si-ratio at a total pressure of 1 atm are could not be found at all. The only data that could be found were for the melting temperature of Co_2SiO_4 in air at atmospheric pressure. The most recent experimentally determined data point is that obtained by Masse and Muan in 1965 [18] when these authors compiled a phase diagram for the system CoO-SiO_2 in air at atmospheric pressure; they reported a value of 1415 ± 5 ℃. These authors also reported that the temperatures for the eutectic points for Co_2SiO_4 and SiO_2 in equilibrium with melt, 1381 ℃, and for Co_2SiO_4 and CoO in equilibrium with melt, 1407 ℃, were practically unchanged within the limit of error (± 5 ℃) when atmospheres consisting of pure oxygen or of 84 vol% CO_2 and 16 vol% H_2 at a total pressure of 1 atm were used. Earlier experimental data for the melting temperature of Co_2SiO_4 in air at atmospheric pressure were published by Asanti and Kohlmeyer in 1951 [19] and by Biltz and Lemke in1932 [20]. While the first group of authors reported a value 1420 ℃, the latter authors communicated a value of 1345 ℃. The reason for the large discrepancy between the Blitz and Lemke result and the other ones denoted above is unknown. In more recent phase diagram calculations values between 1410 and 1417 ℃ were adopted. Zabdyr et al. [21] published in 2003 results of a modeling of the phase equilibria in the CoO-SiO_2 system performed using the CALPHAD approach; these authors adopted 1417 ℃ as the melting temperature of Co_2SiO_4 in air at atmospheric pressure. In 2007 Jung et al. [22] adopted a value of 1410 ℃ for the melting temperature of Co_2SiO_4 at 1 atm total pressure at a variety of oxygen activities

ranging between that of air at 1 atm total pressure and that corresponding to the equilibrium between metallic cobalt, cobalt silicate and melt.

Based on the discussed findings for the melting temperature of Co_2SiO_4 it was assumed for the single crystal work performed in this study that in the range of oxygen activity of interest for the growth of single crystals of Co_2SiO_4 the melting point of cobalt orthosilicate exhibits no significant change with the oxygen activity, corresponding to a vertical line in Figure 2.1.

The compiled data shown in Figure 2.1 and listed above were used to select proper parameters (temperature and oxygen activities) for calcination, sintering and single crystal growth.

2.3. Experimental

The experimental work performed in this study includes the preparation of powders of Co_2SiO_4 via two different synthesis routes, making relatively dense, polycrystalline rods of this material, the generation of small single crystals of Co_2SiO_4 with different orientations for being used as seed crystals for growing larger single crystals, the growth of such larger crystals, and finally some characterization of the single crystals grown.

2.3.1. Powder Synthesis

Two synthesis routes, a ceramic and a sol-gel route, were used to produce fine-grained powders of Co_2SiO_4. Initially, a ceramic route was employed because this is a relatively simple approach for the synthesis of ceramic materials. In this

synthesis route, the two starting materials, Co_3O_4 (Noah, 99.5 %) and SiO_2 (Strem, 98 %), were combined in a 2:3 molar ratio, mixed by ball milling using Teflon® balls in polyethylene bottles for 24 hours and then calcined in air at atmospheric pressure and at a temperature of 1050 °C for 2 days. In order to avoid an explosion-like transition from Co_3O_4 to CoO, the heating rate of the furnace used for calcining was kept at about 30 °C/h in the temperature range between 850 and 950 °C. After calcination manual grinding utilizing a porcelain mortar and a pestle was used to decrease the grain size of the resulting powder. The type of atmosphere and the temperature used for calcination were selected based on existing knowledge on the thermodynamic stability range of Co_2SiO_4, see Figure 2.1. In the calcined powder, by using X-ray powder diffraction, three phases, Co_2SiO_4, CoO and SiO_2, were found. The intensities of peaks related to the different phases observed suggested that most of the powder consisted of Co_2SiO_4.

A sol-gel route was used to synthesize Co_2SiO_4 powders of high purity and with an intended silica excess of about 0.5 mol%. A major advantage of using a sol-gel route for powder synthesis is that this type of synthesis allows to achieve homogeneity almost down to the atomic level. In this synthesis route, cobalt metal (Strem, 99.9+ %) was dissolved in nitric acid (Sigma-Aldrich, 99.999 %) in a glass flask. The cobalt metal was submerged in de-ionized water, heated and slowly exposed to increasing levels of HNO_3. An amount of tetraethyl orthosilicate (Sigma-Aldrich, 99.999 %) appropriate for the formation of Co_2SiO_4 with an excess of 0.5 mol% SiO_2 was added to the cobalt nitride solution together with a suitable

amount of ethanol (Sigma-Aldrich, 99.5+ %). Ethanol was added to prevent a too rapid gelation. The solution was stirred and heated at 40 °C for about 12 hours to perform a slow hydrolysis leading to gelation. Ammonium hydroxide solution (Sigma-Aldrich, 99.99 %) was added to the solution to adjust the pH-value to 7-8. Before drying, the gels were frozen by using liquid nitrogen to prevent severe foaming at the beginning of the freeze drying process. A freeze drier (Labconco Freeze-zone 7750020) was used to remove the solvents, including ethanol and water containing ammonium hydroxide, under vacuum until very fine-grained powders were obtained. These powders were then heated to 500 °C and held at this temperature for 10 hours in air at atmospheric pressure to decompose organic and nitrate residues. X-ray powder diffraction was unable to detect any crystalline phases in all sol-gel route derived powders.

2.3.2. Feed Rod Preparation

Fine-grained powders obtained by the synthesis routes described above were used to prepare feed rods for seed production and subsequent growth of single crystals of Co_2SiO_4. Powders were filled into latex tubes (North America Latex; tube dimensions: length = 12 cm, diameter = 12 mm, wall thickness 0.1 mm). After a latex tube was filled with a suitable amount of powder, it was sealed by a metallic clamp at the open end. Each tube filled with powder was isostatically pressed for about 20 minutes at a pressure of approximately 1.5×10^8 Pa using glycerine as fluid medium present in the surrounding of the powder-filled latex tube. The resulting cylindrical green bodies were sintered at 1300 °C in a muffle furnace in air at atmospheric pressure for 3 days for rods made from powder prepared by the

ceramic route and for 1 day for powder produced via the sol-gel route. The resulting sintered rods were usually 6 to 7 mm in diameter and between about 40 and 70 mm in length. The densities of the sintered rods varied between 80 and 90 % of the theoretical density of Co_2SiO_4. In these rods Co_2SiO_4 was the only crystalline phase that could be identified by XRD powder diffraction within the resolution limit of this method which is about 1 to 2 %.

2.3.3. Seed Crystal Preparation

The growth apparatus used for Co_2SiO_4 seed crystal generation and subsequent single crystal growth by the floating zone method was a NEC model SC-N35HS/50XS single ellipsoid image furnace. The heat radiation of a halogen lamp (3.5 kW) located at one of the two focal points of an ellipsoid is focused at the second focal point and used for heating and subsequent melting. Two holders allow both feed and seed rods to be moved vertically into the second focal point region, where the melting occurs, and to be rotated during crystal growth. The first Co_2SiO_4 single crystal seeds were obtained by using polycrystalline sintered rods prepared from powders produced by the ceramic route as feed and seed rods. The growth was performed in air at atmospheric pressure. During the single crystal growth, the ends of the two sintered rods were moved into the hot zone, melted, and then joined to form a floating melt zone. The two melt-connected rods were lowered slowly at rates smaller than 4 mm/h. Both feed and seed rods were counter-rotated at rates around 10 rpm. The rate for lowering the bottom rod was initially larger then that for lowering the top rod so that the diameter of the floating

zone was reduced to about 2 to 3 mm. In this process, the number of grains being present in the newly grown rod was reduced towards the solid/melt interface. Thereafter, by decreasing the rate for lowering the bottom rod and/or increasing the rate for lowering the top rod, the size of the crystals being present in the lower rod next to the melt was increased. In order to end a growth experiment, the vertical movements of the feed and seed rod were stopped and the temperature was slowly reduced. Due to further solidification in combination with the surface tension of the melt, the length and the cross-sectional area of the melt both decreased until the melt separated into two droplets, one at the bottom of the feed rod and one at the top of the bottom rod, which finally both solidified. The entire procedure described above was repeated several times by using the top of the bottom rod obtained as described before as starting rod at the bottom for another zone melting procedure for further reducing the number of remaining grains and for increasing their size until only one grain was left. The Laue back reflection technique was used to confirm that this was the case. Many individual float zone melting experiments over a period of several weeks were performed until a first crack-free cobalt silicate single crystal seed was obtained. After the first seed had been generated, it was oriented by using the Laue back reflection technique to the [001] orientation and sectioned by using a wire saw along the [001] orientation for seeds for subsequent single crystal growth. Several single crystals were grown along the [001] orientation by using these [001] seed crystals and feed rods produced from powders obtained by using the ceramic route described in Section 2.3.1. The typical diameter of these single crystals was 6 to 10 mm. The

length varied between about 30 and 50 mm. In order to obtain seeds for the [010] orientation, one of the single crystals grown along the [001] orientation was cut perpendicular to the [001] orientation into slices with a thickness of about 3 mm. These slices were then oriented perpendicular to the [001] orientation by using the Laue back reflection technique to identify the [010] orientation and then sectioned along the [010] orientation for needle-like seeds with this orientation. Seed crystals for single crystal growth along the [100] orientation were produced using the same approach.

2.3.4. Crystal Growth

After a sufficient supply of Co_2SiO_4 seed crystals oriented along the three principle orientations had been obtained, these seeds were used to grow single crystals of Co_2SiO_4 with larger sizes. Polycrystalline rods prepared by using powders of Co_2SiO_4 obtained by the sol-gel synthesis route were employed as feed rods. Most of the parameters used in the bulk single crystal growth were the same as those used during seed single crystal growth, including the type of lamp employed, rotation speeds for the feed rod and the seed crystal and the power used to operate the halogen lamp. In order to successfully grow Co_2SiO_4 single crystals, it was critical to carefully center both the feed rod and the seed crystal relative to the shafts used to rotate them within the image furnace during crystal growth, especially when having a needle-like crystal as the seed. To prepare for single crystal growth, the bottom end of the feed rod and the top surface of the seed crystal were moved close to the focal point where the hot zone later appeared upon heating before increasing the power used for operating the lamp.

This was done in order to avoid large temperature gradients possibly being caused by fast vertical movements for joining the two rod ends to form a floating zone. After generating a float zone upon heating and starting single crystal growth, the rate of lowering the seed rod was between 1 and 2 mm/h. The rate of lowering the feed rod was selected in such a way that the diameter of the solidifying crystal remained approximately constant. Single crystals along the three principle were successfully grown. Most of them were 6 to 8 mm in diameter and 3 to 5 cm in length.

2.3.5. Characterization

The Laue back reflection technique was used to orient all single crystals grown and also to determine the orientations of well developed facets found for the crystals grown. Laue back reflection patterns were obtained using a real-time back reflection Laue camera system (model MWL 110, Multiwire Laboratories, Ltd., Ithaca, NY, U.S.A.). By making use of software (NorthStar, Version 5.10) provided with the instrument, these patterns were used to identify orientations of single crystals.

In order to determine values for the density of dislocations, discs of cobalt silicate single crystals grown along the three principle orientations were carefully polished and subsequently etched at room temperature with aqueous solutions of HCl. For surfaces perpendicular to the orientations [100] and [010] a solution containing about 21 wt% ($\approx$ 12 mol%) HCl was used; for surfaces perpendicular to the [001] orientation a solution containing 7 wt% (= 3.6 mol%) HCl was applied.

For the [100] orientation the etching time was 18 hours while it was 8 minutes for the [010] orientation and 10 hours for the [001] orientation. Optical microscopy was used to analyze etched surfaces with regard to the presence of etch pits developed at dislocations intersecting with the polished surfaces. Photographs were taken and evaluated fo determining the number of dislocations per unit area.

The lattice parameters of a grown crystal were determined by using X-ray powder diffraction. The instrument employed was a theta-theta X-ray diffractometer (Scintag, model PAD-X) and the software used (Jade, Version 7) was from Materials Data, Inc., (MDI). To produce a powdered sample for X-ray analysis, a piece of a grown Co_2SiO_4 single crystal was crushed and finely ground. Then fine-grained silicon powder was added and carefully mixed with the Co_2SiO_4 powder. The silicon was added for using it as an internal standard during scanning. Spectra resulting from several such scans were then calibrated relative to the silicon standard peak at 28.4422° and analyzed by using the software denoted above. This software allows to perform a least squares fit of diffraction intensities related to the orthorhombic crystal structure of Co_2SiO_4 to an experimentally obtained diffractogram. Lattice parameter values for Co_2SiO_4 were obtained as the result of the such a fit. Several scans were performed to determine suitable instrument settings and scan times. The final scan covered the range between 20° and 55° and was performed at a rate of 0.04° per minute.

Grown cobalt silicate single crystals, expected to be of high purity, were characterized by using the inductively coupled plasma atomic emission

spectroscopy (ICP-AES) technique to determine the cobalt-to-silicon ratio and the concentrations of a variety of impurities. After some initial difficulties to be discussed below, a step-by-step ICP analysis was performed to determine the impurity levels being present and also the cobalt-to-silicon ratio after each step involved in producing cobalt orthosilicate single crystals, beginning with the sol-gel synthesis. The samples analyzed were cobalt metal dissolved in aqueous HNO_3 (Sample #1), the solution just considered with added TEOS and ethanol (Sample # 2), a sintered polycrystalline rod of Co_2SiO_4 (Sample # 3) and a grown single crystal (Sample # 4).

In initial attempts of ICP analyses, an appreciable amount of a mixture of HCl and HF was used to fully dissolve slices of grown crystals at 50 °C over a period of about 3 days. Teflon beakers were used to contain the solution during the dissolution. After a cobalt silicate single crystal had been fully dissolved, the solution was diluted to a certain level so that a reliable ICP analysis became feasible. Though the cobalt-to-silicon ratio in the starting materials of sol-gel synthesis route was 2:1.005, a much larger silicon excess was found by ICP analyses. For some time it was believed that this large excess was due to losses of CoO during the different high temperature treatment steps involved in the sample preparation and in crystal growth as a result of the significant vapor pressure of CoO at high temperatures. Later, after very carefully examining all procedures involved in the ICP-AES analyses, it was realized that a nebulizer made of glass and being used in the ICP analyzer was the reason for misleading results of the ICP analyses. Since there was a residue of HF in the solutions

prepared for ICP analyses, partially dissolving the glass nebulizer by remaining HF had introduced extra silicon into solutions being analyzed. This was confirmed by analyzing a diluted solution of HF in water for silicon. The analysis performed suggested that a significant amount of silicon was present although the analyzed aqueous solution of HF was free of silicon. After identifying this problem, a different procedure was employed to prepare sample solutions for ICP analyses. A concentrated aqueous solution of HCl was used to dissolve slices of grown crystals at 50 °C in a Teflon beaker. Only a few droplets of HF were added to the solutions for several times during the dissolution process until a grown crystal was fully dissolved after about two weeks. The resulting solutions were then used for ICP-AES analyses. The instrument used for this purpose was an ICP-AES system Model ICAP 61E (Thermo Electron, Waltham, MA).

Transmission electron microscopy was employed to confirm the presence of some silica precipitates in the matrix of cobalt silicate single crystals grown from starting materials intentionally containing a small excess of silica. To prepare a sample for cross-sectional view of TEM imaging, a piece of a grown crystal was polished by diamond lapping on a polishing machine (Allied High Tech Products, Inc., MultiPrep™ System). The thickness of the sample was further decreased by using a focused ion beam (FEI Company, Strata 400). Two different transmission electron microscopes were tried to be used, a Tecnai T12 instrument (FEI Company) and a Tecnai F20 microscope (FEI Company). The Tecnai T12 is a 120 kV field emission transmission electron microscope. The Tecnai F20 is a

200 kV field emission transmission electron microscope with monochromator, 1 Å in TEM and 1.4 Å in STEM.

Finally, using the radioactive isotope Co-60, the diffusion of cobalt ions in Co_2SiO_4 was investigated by performing cobalt tracer diffusion measurements. Initial measurements were performed at 1300 °C in the oxygen activity range between $\log_{10} a_{O_2} = -3.7$ and 0 by using single crystals of Co_2SiO_4 grown along the three principle orientations. Here, $a_{O_2} = P_{O_2}/P°$ is the oxygen activity, P_{O_2} is the oxygen partial pressure and $P°$ is a standard pressure of 1 atm. Oxygen activities were established by mixing oxygen or air with nitrogen in proper ratios and pumping gas mixtures through the annealing furnace at a rate of about 20 liter/h. Details about the diffusion experiments will be reported elsewhere [24].

2.4. Results and Discussion

High quality single crystals of cobalt orthosilicate were successfully grown along the three major orientations [100], [010] and [001] (Pbnm) by the floating-zone method. Figure 2.2 shows photographs of single crystals of Co_2SiO_4 grown along the different principle orientations, [100], [010] and [001]. As it can be seen in Figure 2.2, the crystals grown were black in color and had shiny, smooth surfaces. The grown crystals were 6 to 10 mm in diameter and 30 - 60 mm in length. As stated before, the Laue back reflection technique was used to orient

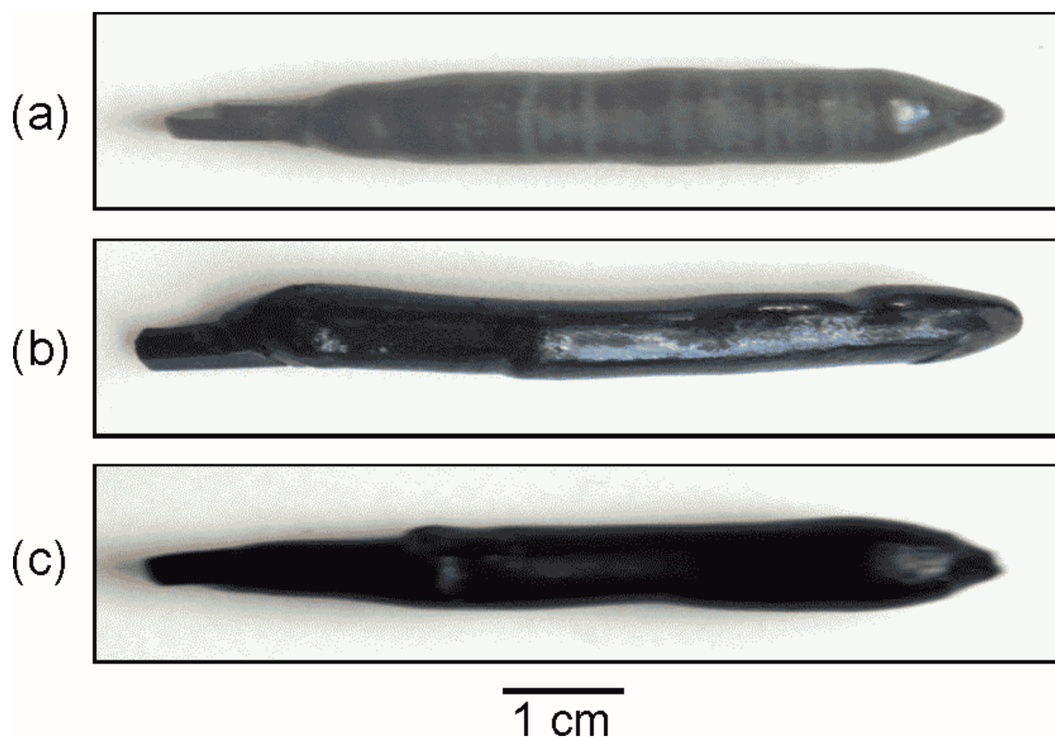

Figure 2.2: Photographs showing single crystals of Co_2SiO_4 grown along the three principle orientations: a) [100], b) [010] and c) [001].

these single crystals. Figure 2.3 shows experimental Laue diffraction patterns obtained for single crystals of Co_2SiO_4 grown along different principle orientations in comparison with simulated patterns for the three orientations of interest. As one can see from the figure, the experimental and simulated pattern agree very well with each other, confirming that single crystals of Co_2SiO_4 were successfully grown for the orientations denoted above.

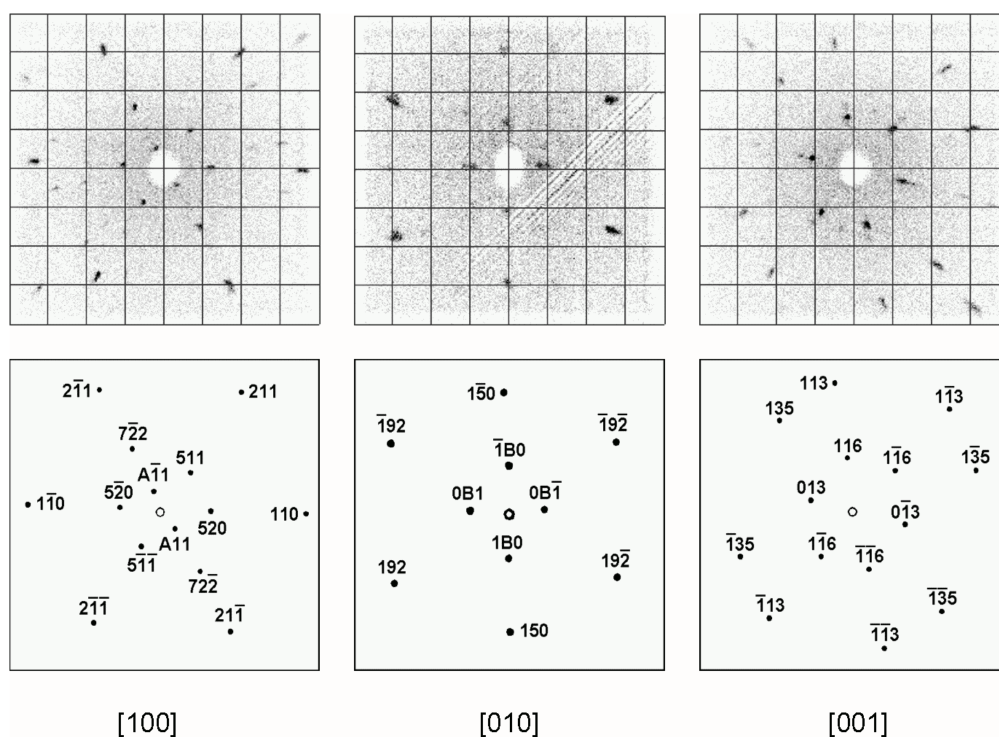

Figure 2.3: Laue back reflection patterns for single crystals of Co_2SiO_4 grown along different principle orientations: the top row shows experimentally obtained patterns and the bottom row simulated patterns. B stands for the number 11.

Well developed facets were found on crystals of cobalt silicates grown along the three principle orientations. Figure 2. 4 shows the cross sections of such cobalt silicate crystals. For comparison, schematic drawings of the cross sections of these crystals are also shown. For crystals grown along the [100] direction, the cross sections have an almost round shape. One pair of small facets along the (010) plane was usually found. For crystals grown along the [010] and [001] directions, the cross sections had oval shapes. Two symmetrical facets, in Figure 2.4 designated as a and b, were observed; these facets were off the (100)

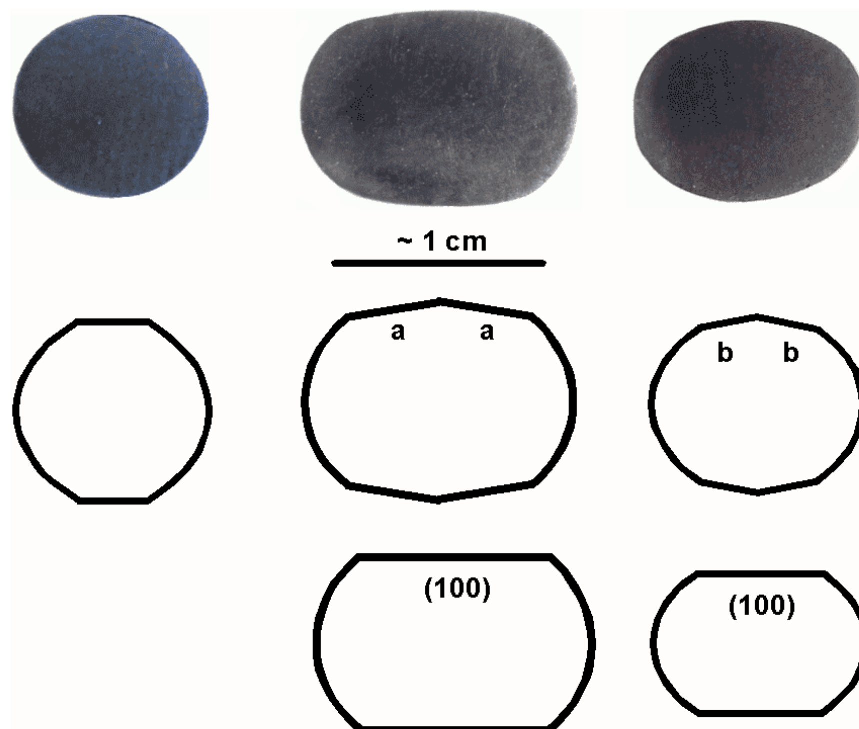

Figure 2.4: Photographs and schematic drawings of cross sections of single crystals of Co_2SiO_4 grown along different principle directions: left [100], middle [010], and right [001].

planes by a few degrees. Similar observations for the shapes of cross sections and the presence of facets have been reported earlier by Tsai et al. [86] for single crystals of iron silicate, Fe_2SiO_4, grown along the orientations [100], [010] and [001].

The lattice parameters of a grown crystal were determined by X-ray powder diffraction as described in Section 2.5. The values found were a = 4.784(4) Å, b = 10.284(5) Å and c = 6.008(6) Å. The standard deviations in parentheses refer to the digit shown before the bracket. A comparison with lattice parameter values reported in the literature [2,5,25,26,27,28,29,30,31,32] is provided in Table 2.1. The data obtained in this study agree reasonably well with all the data listed in this table, including those reported on the ASTM index card #15-0865 [28]. Some of the discrepancies between the different data sets may be related to residual stresses in the different sample materials investigated while others may be due to differences regarding to calibrations.

Etching discs prepared by cutting perpendicular to the growth direction from single crystals grown along the [100] and [010] orientations with an aqueous solution containing about 21 wt% HCl was successful in producing at room temperature etch pits useful for determining dislocation density values. For crystals grown along the [001] orientation etching with a solution containing about 7 wt% HCl was successful. Prior to etching, the single crystal discs were first polished with silicon carbide papers with grain sizes down to 6 µm and then fine-polished with a polishing paste containing alumina particles with a grain size of 0.05 µm.

After practically scratch-free surfaces were obtained, the polished discs were immersed in the etching solution at room temperature. The etching time was 18 hours for a disc cut perpendicular to the [100] orientation, 8 minutes for two discs cut perpendicular to the [010] orientation and 10 hours for one disc cut perpendicular to the [001] orientation. A picture obtained for one of the samples cut perpendicular to the [010] orientation by using an optical microscope and depicting the etch pits produced after etching at the conditions described above

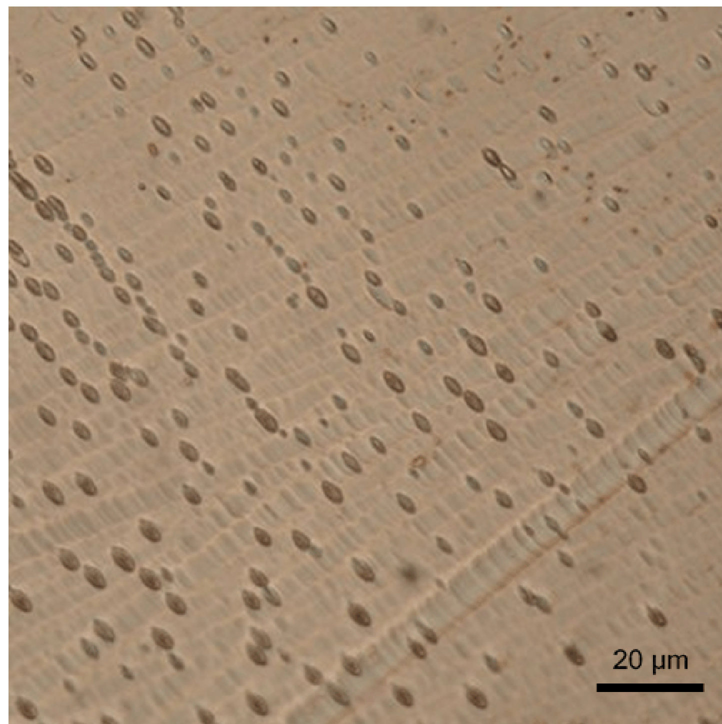

Figure 2.5: Photograph of the surface of a Co_2SiO_4 disc prepared by cutting perpendicular to the growth direction [010] after etching by using an aqueous solution of HCl. The photograph was obtained by using an optical microscope.

is shown in Figure 2.5. The dislocation densities for all discs investigated were found to be on the order of 10^5 to 10^6 per cm^2.

Samples of materials obtained at different stages of the cobalt silicate preparation, see above, were analyzed for the levels of impurities being present. Table 2.2 contains a complete list of the impurities analyzed for. Some of these impurities were selected for the analysis because they are alio-valent species and, if present in larger concentrations, could therefore significantly change defect-related properties. Some other impurities were considered because they also could have contaminated the samples during calcination, sintering and crystal growth based on sample handling and the types of materials present near samples during the high temperature treatments denoted before. Sodium and aluminum were the only two impurities found in these analyses as being present in significant concentrations. The sodium concentration was found to be in the range between 80 and 120 ppm (here ppm refers to the number of moles of Na per mole of Co_2SiO_4) and that for aluminum was found to be in the range between 60 and 80 ppm. Though the detected concentrations of both of these impurities were not as low as desired, the potential effects the impurities of Na and Al can have on the point defect population of cobalt orthosilicate are only relatively small. Since the charge states of these two impurities are +1 and +3, respectively, leading to excess charges of −1 and + 1 for Na and Al, respectively, both assumed to be present on cobalt sites, these opposite relative charge states let the two impurities cancel out each other to some extent with regard to their influence on point defect equilibria in Co_2SiO_4.

Table 2.2: Impurities considered and concentrations determined for them by using the ICP-AES technique in grown single crystals of cobalt silicate, Co_2SiO_4. Here, ppm refers to the number of moles of an element analyzed for per mole of Co_2SiO_4.

elements	concentrations (ppm)
Na	80 - 120
Al	60 - 80
Zn	< 6
Ca	< 4
Cr	< 2
Mn	< 2
As, B, Ba, Cd, Cu, Fe, K, Mg, Mo, Ni, P, Pb, S, Se, Sr, Ti, V, Y	not detected

For determining cobalt-to-silicon ratios by ICP analyses, Samples # 2, # 3 and # 4 were used. In the sol-gel synthesis, the Co/Si ratio for the starting materials was 2:1.005. The Co/Si ratio determined for Sample # 2 (for a description see above) was 2:1.007. The Co/Si ratio determined for a sintered cobalt silicate rod, Sample # 3, was 2:1.012 and that found for a grown single crystal, Sample # 4, was 2:1.015. These results suggest that the losses of CoO during high temperature sample preparation steps are only relatively small and also that the goal of having a small excess of silica present has been reached. It is expected that the achieved excess of silica is sufficient to maintain a thermodynamic activity of SiO_2 of one in experimental investigations of point defects and defect-related

propertied of Co_2SiO_4 without having any significant influence on the properties to be studied such as electrical conductivities and cobalt tracer diffusivities.

Transmission electron microscopy was used to check for the presence of secondary phases, such as silica. It was very difficult to obtain clear TEM pictures of cobalt silicate. The first problem occurred was that no stable images could be obtained when using the T12 microscope. This was due to the fact that cobalt is magnetic so that the sample interacted with the electromagnetic field of the beam. In order to solve this problem, samples with smaller sizes were prepared for imaging and ion milling was used to decrease the thickness of the samples. For

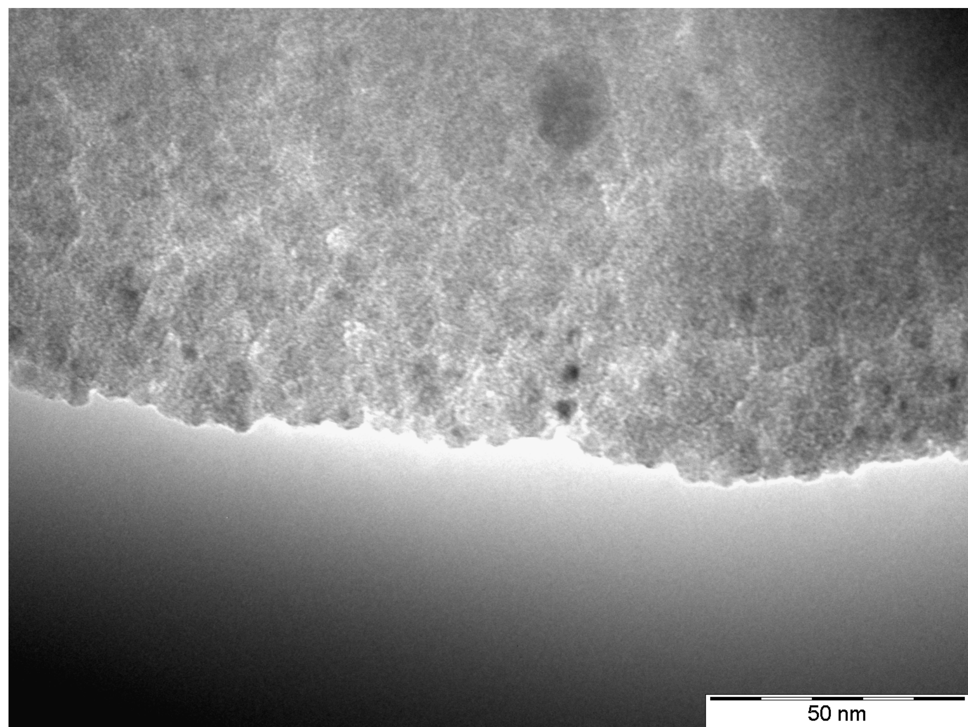

Figure 2.6: TEM picture of a part of a single crystal of Co_2SiO_4 with a few precipitates most likely consisting of SiO_2.

obtaining useful images, it was decided to switch to the F20 microscope which has an electron beam with a higher energy than the T12 microscope. Another problem was that only about 1 % of the volume of a grown crystal was expected to consist of silica precipitates. Due to this small amount of silica, it took a significant amount of time to find such precipitates under the microscope. Some TEM images of a few tiny precipitates were obtained after extensively searching when using the microscope. A third problem was that it was not possible to use either X-ray diffraction or electron energy loss spectroscopy (EELS) to unequivocally confirm that the finally observed precipitates were silica. No significant increases in silicon- or silica-related peak heights were observed in either EELS spectra or X-ray diffractograms due to the fact that the sizes of the beams were not small enough to just accumulate signal originating from precipitates. Since the samples were prepared beginning with a small excess of silica and some cobaltous oxide is lost during high temperature treatments, taking also into account phase stability information for the system Co-Si-O, it was concluded that the few observed precipitates are most likely silica and cannot be attributed to any cobalt-containing oxide. A TEM image showing a few such precipitates (see the dark spots) in the matrix of a single crystal is shown in Figure 2.6. The location where the image was taken was about 2 mm away from the crystal surface. According to a TEM expert at Cornell University the texture visible in the image is most likely related to a trenching effect resulting from ion-milling for a long time and is not related to any polycrystallinity [23].

Preliminary results of cobalt tracer diffusion experiments have been obtained for the orientations [001], [010] and [100] of cobalt orthosilicate at 1300 °C in the oxygen activity range between $\log_{10} a_{O_2} = -3.7$ and 0. These results indicate that the cobalt diffusion occurs fastest in the [001] direction and slowest in the [100] direction. The diffusion in the c-direction is about 35 times faster than that in the a-direction and the diffusion in the b-direction is by a factor of about 3 faster than that in the a-direction. The rate of the diffusion increases with increasing oxygen activity approximately proportional to $a_{O_2}^{1/6}$. The observed oxygen activity dependence is compatible with a diffusion of cobalt ions via cobalt vacancies. Details of the performed tracer diffusion measurements, their results and the interpretation of these results will be published elsewhere [24].

2.5. Summary

High quality single crystals of Co_2SiO_4 were successfully grown along the three principle orientations [100], [010] and [001] by using the floating zone method in air at atmospheric pressure. The grown crystals were 30 to 60 mm in length and 6 to 10 mm in diameter. Well developed facets were observed for all crystals grown. The cobalt-to-silicon ratio was determined to be about 2:1.015. As expected for such a silica excess and intended for experimental studies of defect-related properties, a few precipitates assumed to be silica were observed by TEM in a grown crystal. Two types of impurities, Na and Al, were identified to be present in significant concentrations in grown crystals by the ICP-AES technique; the concentrations of both of these impurities were at a level of about 100 ppm.

Dislocation densities were found to be on the order of 10^5 to 10^6 cm^{-2}. Using single crystals grown in this study, some cation tracer diffusion experiments were conducted at 1300 °C in the oxygen activity range between $\log_{10} a_{O_2} = -3.7$ and 0. The measured cobalt tracer diffusion coefficients, D^*_{Co}, show the trend $D^*_{Co[001]} > D^*_{Co[010]} > D^*_{Co[100]}$.

REFERENCES

[1] H. Schmid, "Synthesis of Cobalt (II) Orthosilicate by Transport of SiO_2 via SiF_4 and Reaction of CoF_2 (Solid) with SiO_2 (Solid)" (in German), Z. Anorg. Allg. Chem., **327** (1-2) [1964] 110-112.

[2] S. Naka, H. Furuhashi and T. Noda, "Crystal Growth of Cobalt Olivine (Co_2SiO_4)," J. Ceram. Soc. Jpn., **76** (6) [1968] 179-183.

[3] B.M. Wanklyn, "Growth of Silicate and Germanate Crystals from PbO-SiO_2 (GeO_2) Fluxes," J. Cryst. Growth, **37** (1) [1977] 51-56.

[4] S. Hosoya and H. Takei, "Growth of Co_2SiO_4 by the Floating-Zone Method," J. Japan. Assoc. Cryst. Growth, **5** (3) [1978] 101.

[5] P. Strobel and Y. Le Page, "Side-Reactions in Chemical Vapor Transport: Growth of Pt and Co_2SiO_4 Crystals," Mat. Res. Bull., **16** (2) [1981] 223-228.

[6] S. Hirano, Y. Iwai, S. Somiya and S. Saito, "Hydrothermal Growth of Fayalite Crystals," in 'High-Pressure Science and Technology, Vol. I: Physical Properties and Material Synthesis,' K.D. Timmerhaus and M.S. Barber, Eds., Plenum, New York, NY, [1979] 970-976. (Proceedings 6th AIRAPT Conference, 1977, University of Colorado)

[7] C.B. Finch, G.W. Clark and O.C. Kopp, "Czochralski Growth of Single-Crystal Fayalite under Controlled Oxygen Fugacity Conditions," Am. Miner., **65** (3-4) [1980] 381-389.

[8] H. Takei, “Growth of Fayalite (Fe_2SiO_4) Single Crystal by the Floating-Zone Method,” J. Cryst. Growth, **43** (4) [1977] 463-468.

[9] T.L. Tsai, S.A. Markgraf and R. Dieckmann, “Floating-Zone Growth and Characterization of Fe_2SiO_4 Single Crystals,” J. Cryst. Growth, **169** (4) [1996] 759-763.

[10] H. Takei, “Czochralski Growth of Mn_2SiO_4 (Tephroite) Single Crystal and Its Properties,” J. Cryst. Growth, **34** (1) [1976] 125-131.

[11] C.B. Finch, G.W. Clark and O.C. Kopp, “Growth of Single-Crystal Mn_2SiO_4 (Tephroite) by Czochralski and Edge-Defined Film-FED (EFG) Techniques,” J. Cryst. Growth, **29** (3) [1974] 269-272.

[12] M. Ozima, “Growth of Nickel Olivine Single Crystals by the Flux Method,” J. Cryst. Growth, **33** (1) [1976] 193-195.

[13] B.G. Lebedev, V.A. Levitskii and V.A. Burtsev, "Equilibrium in the Reduction of Cobalt Orthosilicate by Carbon Monoxide,” Russ. J. Phys. Chem., **36** (4) [1962] 460-462.

[14] G. Róg, B. Langanke, G. Borchardt and H. Schmalzried, "Determination of the Standard Gibbs Free Energies of Formation of the Silicates of Cobalt, Magnesium, and Strontium by EMF Measurements", J. Chem. Thermodyn., **6** (12) [1974] 1113-1119.

[15] H.S.C. O'Neill, "Free Energies of Formation of NiO, CoO, Ni_2SiO_4 and Co_2SiO_4," Am. Miner., **72** (3-4) [1987] 280-291.

[16] K. Enoki, S. Hagiwara, H. Kaneko and Y. Saito, "Studies on the Oxidation of Cobalt Using a Solid-State Galvanic Cell," Nippon Kinzoku Gakkhaishi, **41** (5) [1977] 505-510.

[17] W.G. Bugden, J.N. Pratt "Solid Electrolyte Galvanic Cell Studies: Free Energies of Formation of CoO and Co_3O_4," Trans. Inst. Min. Metall., Sect. C, **79** (Sept.) [1970] C221-C225.

[18] D.P. Masse and A. Muan, "Phase Relations in the System CoO-SiO_2," Trans. AIME, **233** (7) [1965] 1448-1449.

[19] P. Asanti and E.J. Kohlmeyer, "On the Thermal Properties of Compounds of Cobalt with Oxygen and Sulfur" (in German), Z. Anorg. Allg. Chem., **265** (1-3) [1951] 90-98.

[20] W. Biltz and A. Lemke, "Molecular and Atomic Volumes. XXXVIII. Volumes of some Silicates" (in German), Z. Anorg. Allg. Chem., **203** (1) [1932] 330-344.

[21] L.A. Zabdyr, G. Garzel and O.B. Fabrichnaya, "Phase Equilibria in the CoO-SiO_2 System," Calphad, **27** (2) [2003] 127-132.

[22] I.-H. Jung, S.A. Decterov and A.D. Pelton, "Thermodynamic Modeling of the $CoO-SiO_2$ and $CoO-FeO-Fe_2O_3-SiO_2$ Systems," Int. J. Mater. Res., **98** (9) [2007] 816-825.

[23] J.L. Grazul, personal communication.

[24] Q. Tang and R. Dieckmann, "Orientation and Oxygen Activity Dependence of the Diffusion of Cobalt in Cobalt Orthosilicate," Solid State Ionics, **212** [2012] 66-76.

[25] A.E. Ringwood, "Olivine-Spinel Transformation in Cobalt Orthosilicate," Nature, **198** (4875) [1963] 79-80.

[26] C.W.F.T. Pistorius, "Some Phase Relations in the Systems $CoO-SiO_2-H_2O$, $NiO-SiO_2-H_2O$ and $ZnO-SiO_2-H_2O$ to High Pressures and Temperatures," Neues Jahrb. Mineral., Monatsh., (2/3) [1963] 30-57.

[27] S.-I. Akimoto, T. Katsura, Y. Syono, H. Fujisawa and E. Komada, "Polymorphic Transition of Pyroxenes $FeSiO_3$ and $CoSiO_3$ at High Pressures and Temperatures," J. Geophys. Res., **70** (20) [1965] 5269-5278.

[28] H.E. Swanson, M.C. Morris and E.H. Evans, "Standard X-ray Diffraction Powder Patterns, Section 4 - Data for 103 Substances," NBS Monograph, **25** (4) [1966] 1-83. (Data used on ASTM index card #15-0865 for Co_2SiO_4, see pp. 11-12).

[29] Y. Matsui and Y. Syono, "Unit Cell Dimensions of Some Synthetic Olivine Group Solid Solutions," Geochem. J., **2** (1) [1968] 51-59.

[30] N. Morimoto, M. Tokonami, M. Watanabe and K. Koto, "Crystal Structures of Three Polymorphs of Co_2SiO_4," Am. Mineral., **59** (5-6) [1974] 475-485.

[31] O. Tamada, K. Fujino and S. Sasaki, "Structures and Electron Distributions of α-Co_2SiO_4 and α-Ni_2SiO_4 (Olivine Structure)," Acta Crystallogr., Sect. B: Struct. Sci., **B39** (6) [1983] 692-697.

[32] A. Sazonov, M. Meven, V. Hutanu, V. Kaiser, G. Heger, D. Trots and M. Merz, "Structural Behaviour of Synthetic Co_2SiO_4 at Low Temperatures," Acta Crystallogr., Sect. B: Struct. Sci., **B64** (6) [2008] 661-668.

CHAPTER 3

ORIENTATION, OXYGEN ACTIVITY AND TEMPERATURE DEPENDENCIES OF THE DIFFUSION OF COBALT IN COBALT ORTHOSILICATE, Co_2SiO_4 [*]

3.1. Abstract

To contribute to a better understanding of point defects and defect-related transport properties in cobalt orthosilicate, Co_2SiO_4, the orientation-dependent diffusion of cobalt in high purity, synthetic single crystals of Co_2SiO_4 being in thermodynamic equilibrium with silica was experimentally studied as a function of crystallographic orientation, oxygen activity and temperature. The oxygen activity dependence of the diffusion of cobalt in Co_2SiO_4 along the three principle orientations at 1300 °C is at high oxygen activities compatible with cobalt vacancies and holes as majority defects. At lower oxygen activities the oxygen activity dependence of the cobalt tracer diffusion coefficients becomes smaller than at high oxygen activities. This is most likely related to an increase of the concentrations of cobalt interstitials at lower oxygen activities and at such oxygen activities also to an increased influence of the impurity ions being present in the samples used. The latter is due to smaller overall point defect concentrations at lower oxygen activities compared to those found at higher oxygen activities. The temperature dependence of the cobalt tracer diffusion along the orientations

---

[*] Reprinted with permission from Q. Tang and R. Dieckmann, Solid State Ionics, **212** [2012] 66-76. Copyright © 2012, Elsevier.

denoted above was investigated in the range between 1200 and 1300 °C at a_{O_2} = 1 ($a_{O_2} = P_{O_2}/P^{\circ}_{O_2}$ and $P^{\circ}_{O_2}$ = 1 atm). The results obtained suggest that the anisotropy of the diffusion of Co in Co_2SiO_4 does not very significantly vary with the temperature. When using the space group Pbnm when assigning crystal orientations the ratio found for the cobalt tracer diffusion coefficients at a_{O_2} = 1 is approximately $D^*_{Co[001]}:D^*_{Co[010]}:D^*_{Co[100]}$ = 30:3:1.

3.2. Introduction

Cobalt orthosilicate, Co_2SiO_4, has an orthorhombic, olivine-type crystal structure as it is usually found for naturally occurring olivine minerals of the type $(Fe,Mg)_2SiO_4$ [1]. The symmetry of the olivine structure can be described by using the space groups Pnma or Pbnm [2]. While the first type of space group is the standard, the second type is most commonly used for olivines. All orientations denoted in this article refer to the latter space group. As discussed in Ref. [1], the olivine crystal structure is based on a distorted hexagonal closed packing of oxygen ions, in which Me cations are located on octahedral interstices of the oxygen sublattice, while Si cations are located on the tetrahedral interstices of this sublattice. There are two types of octahedral M sites, M1 and M2. The M1 sites are located at centers of symmetry and the M2 sites are present on mirror planes. M1-related octahedra are smaller and slightly more distorted than M2-related octahedra. Normally only one-half of the octahedral sites are occupied by Me and one eighth of the tetrahedral sites are occupied by Si ions. Olivines can also be considered as consisting of isolated SiO_4^{4-} tetrahedra linked by metal cations in octahedral coordination. As a consequence of the non-cubic structure of olivines

many point defect-related properties of phases crystallizing in this structure, e.g., the electrical conductivity and the diffusivities of ions, are anisotropic.

From a geoscientific point of view, olivine minerals, which are solid solutions containing primarily forsterite (Mg_2SiO_4), fayalite (Fe_2SiO_4) and some tephroite (Mn_2SiO_4), are very important because they are the major mineral components of the Earth's upper mantle [1]. Transport of matter and charge in the mantle are important factors in creep and zoning and depend on the type and mobility of point defects present in olivines and are usually significantly influenced or almost completely controlled by the impurities present in olivine minerals. However, if at sufficiently high temperatures and in the absence of larger impurity concentrations the influence of non-equilibrium defects such as dislocations and grain boundaries on certain properties of oxides crystallizing with the olivine structure is only small, mass and charge transport in such oxides is mainly controlled by point defects. Systematic investigations of the point defect structure and of defect-related transport properties of olivine-structure oxides at high temperature can contribute to a better understanding of the behavior of such oxides. Studies of these subjects for transition metal-containing compounds of the type Me_2SiO_4 as model compounds can contribute to reach a better fundamental understanding of transport of matter and charge in olivine-structure materials. This study focuses on Co_2SiO_4. At present, the knowledge of non-stoichiometry, cation diffusion and electrical conduction in Co_2SiO_4 is only relatively limited.

Many previous studies of transport properties of olivines have been conducted using natural mineral samples, see, for example, Refs. [3,4,5]. Problems related to using such samples are significant variations of chemical compositions and impurity concentrations. As a consequence, results of measurements performed using natural mineral samples may significantly vary, depending on the specific samples investigated, and are difficult to be compared with each other and conclusions with regard to fundamental defect-related properties are often only possible to a very limited extent or not at all.

To avoid such problems, for any fundamental research on defects and defect-related transport properties it is more appropriate to use very pure samples in which the defect concentrations are thermodynamically controlled in an unequivocal way. To have thermodynamically well defined samples of Co_2SiO_4, the cobalt-to-silicon ratio needs to be fixed, or alternatively, a small amount of inclusions of a secondary phase (SiO_2, cobalt metal or oxide) must be present. As discussed in Ref. [6], it is practically impossible to achieve a sufficiently precise control of the transition metal-to-silicon ratio in a transition metal-containing orthosilicate like Co_2SiO_4 due to an insufficient precision of composition control during synthesis, including crystal growth. Therefore, in this study (and also in some previous studies [7,8,9]) an excess of SiO_2 being present within Co_2SiO_4 samples was used to fix the thermodynamic activity of silica. Any studies of the orientation dependence of transport properties require in addition to the thermodynamic control of sample compositions the use of sufficiently pure single

crystals with different specific orientations. Since such crystals are not readily available, they need to be grown departing from very pure starting materials.

To achieve a detailed understanding of point defects and point defect-related, orientation-dependent transport properties of Co_2SiO_4, well characterized and thermodynamically well defined single crystals of high quality and high purity are needed. Single crystals fulfilling the requirements denoted above were successfully grown in air at atmospheric pressure along the three principle orientations by using the floating-zone method [10]. The grown crystals were 30 - 60 mm in length and 6 - 10 mm in diameter. Impurity levels and the degree of a desired excess of silicon were determined by using the ICP-AES technique. For more details see Ref. [10].

Before discussing previous work on point defects and the transport properties of cobalt orthosilicate, it is appropriate to review the conditions at which Co_2SiO_4 is thermodynamically stable in the temperature range of interest in this study. After not being able to find a suitable summary on the stability range of cobalt silicate, thermodynamic data from the literature were reviewed to produce such a summary. Details about this effort and the results obtained can be found in Ref. [10]. Figure 3.1, which shows a projection of thermodynamic stability data onto the oxygen activity-temperature plane, provides information on the stability range of cobalt silicate for a total pressure of 1 atm at high temperatures. This figure has been generated by making use of data discussed in Ref. [10].

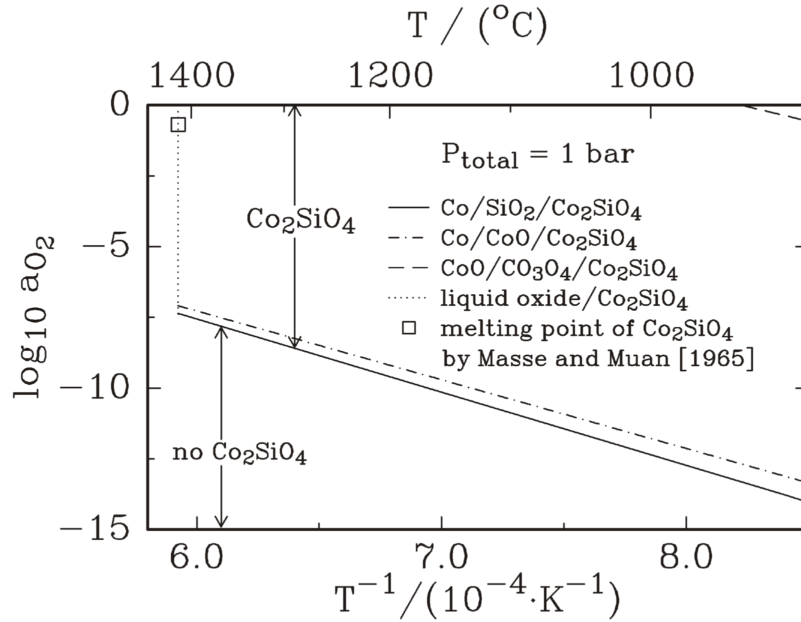

Figure 3.1: An oxygen activity vs. temperature diagram showing data related to the thermodynamic stability range of cobalt orthosilicate, Co_2SiO_4, at high temperatures at 1 atm total pressure. Information about the data used to derive this diagram can be found in Ref. [10].

Due to the capability of cobalt ions to change their valence state with the oxygen activity from +2 to +3, cobalt silicate is a non-stoichiometric material. When the oxygen activity is changed, oxygen is added or removed from the sample. Variations in the oxygen content of cobalt orthosilicate can be described by introducing a deviation from stoichiometry, δ, into the formula $Co_2SiO_{4+\delta}$. This representation is not intended to and does not reflect the distribution of ions between different crystallographic positions and it also ignores any changes in the Co/Si-molar ratio due to dissolving or exsolving traces of SiO_2 in cobalt orthosilicate.

Only a very few results of systematic investigations on the point defect structure of cobalt orthosilicate have been reported in the literature. Greskovich and Schmalzried [7] determined concentrations of point defects and their relation to the non-stoichiometry of $Co_2SiO_{4+\delta}$ based on the results of tensi-volumetric measurements between oxygen partial pressures of $2 \cdot 10^{-1}$ and $1 \cdot 10^{-4}$ atm at 1145 °C. A traditional ceramic synthesis route was used for sample preparation. To fix the thermodynamic activity of silica at unity an excess of 2 mol% SiO_2 was present in the Co_2SiO_4 samples investigated. For the tensi-volumetric measurements performed, an apparatus consisting of two identical fused silica tubes, a system of valves, a vacuum pump and a micro-membrane being capable to measure very small pressure differences was used. One of the silica tubes contained the sample while the second one was empty. After pre-annealing the investigated sample for a sufficient time at given values of oxygen activity and temperature and performing an oxygen pressure jump, the two tubes were separated by one of the valves of the system. The change in the oxygen pressure in the sample environment causes a re-equilibration of the non-stoichiometric oxide by absorbing or releasing oxygen. This leads to a very small change in the pressure in the silica tube containing the sample side which can be measured (relative to the pressure in the empty silica tube) via the capacitance change occurring in a capacitor made up by the micro-membrane denoted above and a counter-electrode. The total change of pressure after a pressure jump has a linear relationship to the change in the deviation from stoichiometry. For more details see Ref. [7]. For the oxygen activity dependence of the deviation from stoichiometry in $Co_2SiO_{4+\delta}$ it was found that $\delta \propto a_{O_2}^{1/6}$ within the oxygen activity range covered by

the measurements. This result is consistent with doubly negatively charged cobalt vacancies and holes being the majority defects. Using the data provided in Ref. [7] one finds that δ in $Co_2SiO_{4+\delta}$ for an oxygen partial pressure of one atmosphere at 1145 °C is approximately $2.5 \cdot 10^{-4}$.

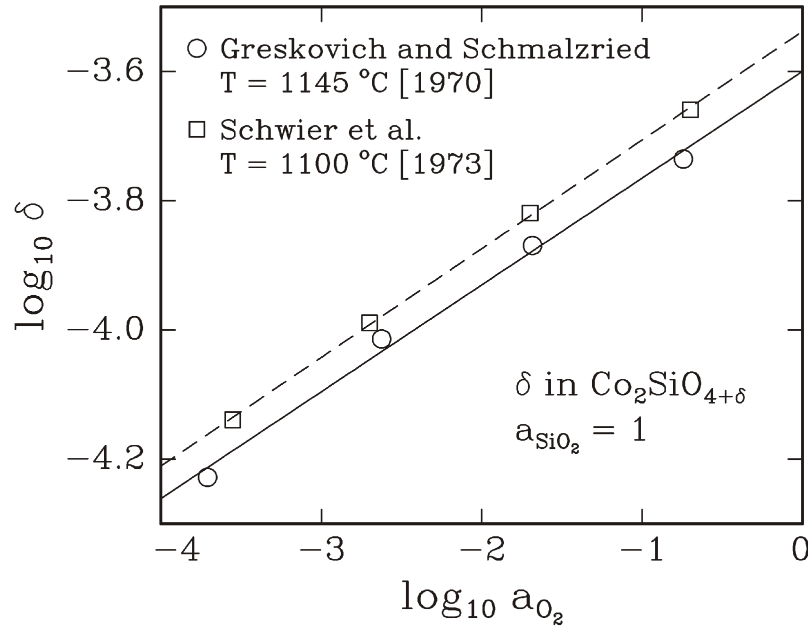

Figure 3.2: Data available from the literature [7,8] for the deviation from stoichiometry, δ, in $Co_2SiO_{4+\delta}$ at $a_{SiO_2} = 1$. The slopes of the lines shown are compatible with $\delta \propto a_{O_2}^{1/6}$, suggesting that vacancies on cobalt sites and holes are the majority defects at the conditions considered in this figure.

Schwier et al. [8] published several years later another set of data for the concentration of cation vacancies in $Co_2SiO_{4+\delta}$ at 1100 °C in the oxygen partial pressure range between $2 \cdot 10^{-1}$ and $2.8 \cdot 10^{-4}$ atm. These data were also obtained by tensi-volumetric measurements. These authors also found an oxygen activity

dependence $\delta \propto a_{O_2}^{1/6}$ within the oxygen activity range covered by their experiments. This result is consistent with doubly negatively charged vacancies on M-sites and holes (in this article assumed to be localized as Co^{3+} ions on Co^{2+} sites) being the majority defects in the range of the experiments. The non-stoichiometry data obtained by Schwier et al. [8] are shown in Figure 3.2 together with the data reported by Greskovich and Schmalzried [7] for comparison.

The electrical conductivity of Co_2SiO_4 was measured by Schwier and Schmalzried [9] at 1300 °C in air at atmospheric pressure. The samples used were polycrystalline Co_2SiO_4 with a 1 mol% excess of SiO_2. Hirsch [11] measured the electrical conductivity of Co_2SiO_4 as a function of oxygen activity and temperature. Systematic measurements of the oxygen activity dependence of the electrical conductivity were limited to oxygen activities between about $5 \cdot 10^{-7}$ to $2.5 \cdot 10^{-4}$ at 1267 °C at non-specified conditions with regard to the Co/Si-ratio or the thermodynamic activities of SiO_2, Co, CoO or Co_3O_4. A piece of a relatively impure single crystal of Co_2SiO_4 grown by the floating-zone method was used Hirsch's study. The concentrations of impurities being present and reported in Ref. [11], converted to mol ppm per mol of Co_2SiO_4, are 6910 for Mg, 6081 for Ni, 1555 for Al, 1503 for Fe, and up to 524 for Ca, up to 439 for Ti, and up 382 for Mn. Problematic are the relatively large concentrations of Al, Fe and Ti. Fe is expected to be present on M-sites; a fraction of it could be oxidized to Fe^{3+} ions, changing the charge neutrality balance. Al^{3+} ions, regardless whether accommodated on M- and/or on Si-sites, also change this balance. Ti^{4+} ions do the same if present on M-sites. During the measurements, samples were held between iridium foil

electrodes next to Pt-Pt/10%Rh thermocouples. The conductivity of the single crystal used was measured “at 45° to the [100] and [001] direction” (space group not specified, most likely Pbnm). The accuracy of the conductivity measurement results was reported to be within ± 2 %. Oxygen activities were established by using CO/CO_2 gas mixtures. Hirsch's electrical conductivity data for Co_2SiO_4 are shown in Figure 3.3 together with the result of a single conductivity measurement by Schwier and Schmalzried [9]. Hirsch [11] reported for the oxygen activity dependence of the electrical conductivity, σ, of Co_2SiO_4 that $\sigma \propto a_{O_2}^{1/7.7}$. This oxygen dependence is weaker than that observed at higher oxygen activities in the non-stoichiometry studies discussed above for the deviation from stoichiometry δ.

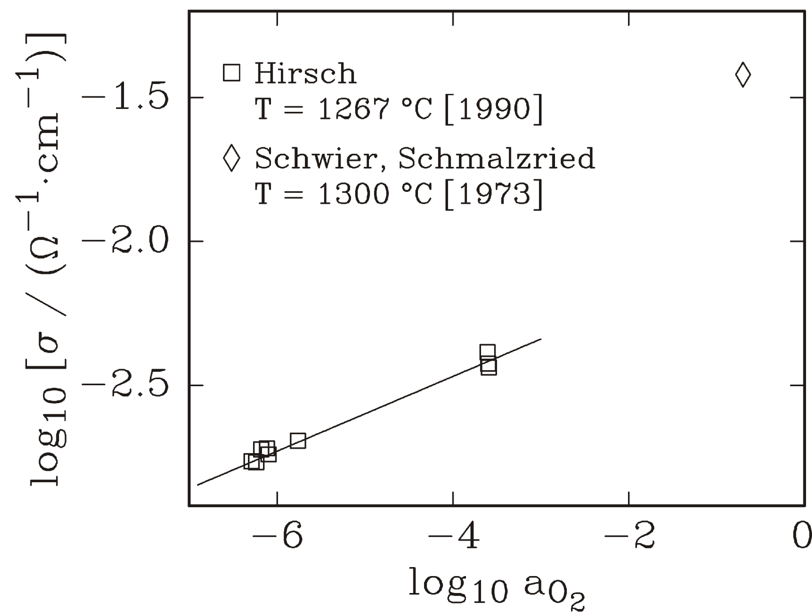

Figure 3.3: Data available from the literature [9,11] for the electrical conductivity of Co_2SiO_4. The line summarizing the data from Ref. [11] corresponds to $\sigma \propto a_{O_2}^{1/7.7}$.

Hirsch [11] suggested that this weaker oxygen activity dependence may be due to an oxygen partial pressure dependence of the mobility of holes or simply be the result of a limited ability to observe the oxygen activity dependence over a sufficiently large oxygen partial pressure range in order to obtain more reliable information. Other possibilities, which were not discussed by Hirsch, are that the impurities present in the sample used for the measurements and/or a significant thermal electronic disorder could be responsible for the observed oxygen activity power dependence at lower oxygen activities.

Windhager and Borchardt [5] performed tracer diffusion experiments in polycrystalline samples of Co_2SiO_4 with unknown impurity level using the stable isotope Si-30 and the radioactive isotope Co-60 in air at atmospheric pressure. The temperature range of the measurements was between about 1200 and 1300 °C. The tracer diffusion results from Windhager and Borchardt's study for Co_2SiO_4 with $a_{SiO_2} = 1$ are shown in Figure 3.4 in combination with two data points for the tracer diffusion of oxygen, one reported by Borchardt and Schmalzried [12] and the other one cited in Ref. [5]. As stated in Ref. [12], the latter data represent upper limits for the oxygen diffusivity. As one can see in Figure 3.4, the oxygen diffusion is slower than the diffusion of Co and Si at the conditions considered in the figure. This finding is in agreement with the result of studies of the solid state reaction between SiO_2 and CoO leading to the formation of Co_2SiO_4. In these studies Borchardt and Schmalzried [13] found that this reaction is governed by the diffusion of Co and Si cations, indicating that the diffusion of oxygen is slower than that of Si and Co.

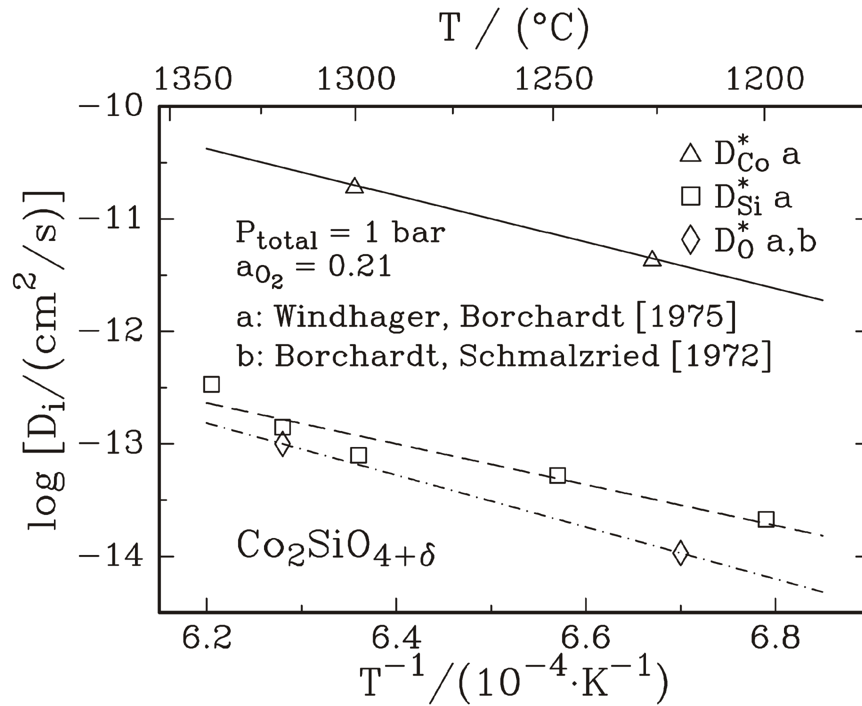

Figure 3.4: Temperature dependence of diffusion coefficients for Co, Si and O diffusing in Co_2SiO_4 in air at atmospheric pressure available from the literature. The values for D^*_{Co} are from Ref. [17] and for D^*_{Si} from Ref. [12]. One value for D^*_O at 1320 °C is from Ref. [12] and the second one for 1220 °C was found cited in Ref. [17].

Morioka [14] determined diffusion coefficients for the interdiffusion between cobalt and magnesium for olivines of the type $(Co_xMg_{1-x})_2SiO_4$ after annealing diffusion couples consisting of single crystals of cobalt and magnesium silicate and using the Boltzmann-Matano analysis for deriving values of interdiffusion coefficients. Single crystals of Co_2SiO_4 and Mg_2SiO_4 were cut into cubes and placed in contact along the same crystallographic axes in a quartz crucible while being held together with Pt wire. The diffusion anneal was performed in air at

atmospheric pressure in the temperature range between 1150 and 1400 °C. Information regarding Mg/Si- or Co/Si-ratios or activities of SiO_2, Co, Co-oxides or MgO is not available, except a statement that the samples where held in a crucible of silica. The determined interdiffusion coefficients were found to increase with temperature and with the concentration of Co_2SiO_4. Based on values of interdiffusion coefficients determined for a composition range between 0 and 90 mol% Co_2SiO_4, it was stated that the mobilities of Co and Mg are largest for diffusion along the c-axis (= [001] orientation) and lowest for that along the b-axis (= [010] orientation). Three cobalt concentration profiles reported by Morioka [14] have been used by the authors of this paper to estimate values for the component diffusion coefficient of Mg in pure Co_2SiO_4 at 1200 °C for diffusion along the three principle axes. This estimate leads to the conclusion that at very large concentrations of Co_2SiO_4 $D_{Mg[001]} > D_{Mg[010]} > D_{Mg[100]}$. The errors in this estimate are expected to be relatively large due to the lack of data points close to pure Co_2SiO_4. Therefore, the obtained ratio $D_{Mg[001]}:D_{Mg[010]}:D_{Mg[100]}$ = 4.3:1.4:1 should be considered more as a trend than its face value. For sure one can say that the diffusion of Mg in Co_2SiO_4 along the c-axis is by a factor of about 3 to 4 faster than that along the other two axes.

Using a SIMS technique, Andersson et al. [15] measured tracer diffusion coefficients for Si-30 diffusing in Co_2SiO_4 single crystals with a_{SiO_2} = 1 and a_{O_2} = 0.21 in the temperature range between 1050 and 1330 °C. For the temperature range between 1050 and 1150 °C, in Ref. [15] denoted as “extrinsic range”, a value of 119 kJ/mol was obtained for an activation enthalpy of motion

while for the temperature range from 1150 to 1330 °C, an activation enthalpy value of 361 kJ/mol was obtained which reportedly includes an enthalpy of motion and a defect formation enthalpy. The tracer diffusion coefficients of Si-30 measured in Co_2SiO_4 at 1350 °C had the largest value for diffusion along the [001] orientation and similar values for the diffusion along the [100] and [010] orientations, reportedly obeying the relation $D^*_{Si[001]}:D^*_{Si[010]}:D^*_{Si[100]} = 7.89:1.03:1$.

Ricoult and Kohlstedt [16] determined data for the creep behavior of Co_2SiO_4. Co_2SiO_4 single crystals grown by the floating-zone method and being internally buffered with SiO_2 and CoO, respectively, or not being buffered, were used during their measurements. Information on impurities in these crystals can be found in Ref. [16]. The direction of measurement was chosen to be the [110] orientation because, according to Ricoult and Kohlstedt [16], in this case only one slip system is activated, thus reducing the scattering of the data. For the oxygen activity dependence of the creep rate, $\dot{\varepsilon} = d\varepsilon / dt$, $\dot{\varepsilon} \propto a_{O_2}^{0.16 \pm 0.02}$ was reported for the temperature range between 1100 to 1300 °C. The activation enthalpy was summarized as 681 ± 146 kJ/mol. According to Ricoult and Kohlstedt [16] the observed oxygen activity dependence of the strain rate can be attributed to two different mechanisms. One possibility is that the rate-limiting step is the motion of negatively charged jogs along edge dislocations via the diffusion of silicon vacancies and a second one is that positively charged kinks are the creep-controlling defects and the creep is glide-controlled [16]. The first mechanism denoted above is unlikely to dominate because silicon vacancies are difficult to form for electrostatic interaction reasons, and, also, because, according to

Borchardt and Schmalzried [13] and Windhager and Borchardt [17], the diffusion of oxygen is slower than the diffusion of silicon.

From the preceding literature review it follows that the current understanding of point defects and defect-related transport properties of cobalt orthosilicate, Co_2SiO_4, is still rather limited. To improve this situation we have performed an experimental study of the orientation-dependent diffusion of cobalt in high purity, synthetic single crystals of Co_2SiO_4 as a function of crystallographic orientation, temperature and oxygen activity. The oxygen activity dependence of the diffusion of cobalt along the three principle orientations was studied at 1300 °C. In addition, the temperature dependence of the cobalt tracer diffusion along the orientations denoted above was investigated at $a_{O_2} = 1$ in the range between 1200 and 1300 °C. In this article, experimental results for cation tracer diffusion coefficients measured by using "home-grown" cobalt orthosilicate single crystals are reported and analyzed with regard to dependencies on oxygen activity, temperature and crystal orientation, including the types of point defects being involved.

3.3. Experimental

In this section a brief summary of growing single crystals of Co_2SiO_4 by using the floating zone method is given. Furthermore, details about the tracer diffusion work performed in this study are provided.

3.3.1. Crystal Growth

The Co_2SiO_4 single crystals used in this study were grown in air at atmospheric pressure by the floating zone method using a single ellipsoid image furnace. The details of crystal growth and characterization are described elsewhere [10]. The feed rods used for single crystal growth were prepared from powders derived via a sol-gel synthesis route. The grown crystals were typically 30-60 mm in length and 6-10 mm in diameter. The growth directions were the three principle orientations [100], [010] and [001]. The cobalt-to-silicon ratio in a grown single crystal was determined to be about 2:1.015. As expected for such a silica excess and intended for experimental studies of defect-related properties, a few silica precipitates were observed by TEM in grown crystals. The dislocation densities were found to be on the order of 10^5 to 10^6 /cm^2. As explained in Ref. [10], these densities were determined by polishing, subsequent chemical etching and counting of etch pits. Two types of impurities, Na and Al, were identified to be present in significant concentrations in grown crystals by using the ICP-AES technique; the concentrations of both of these impurities were at a level of about 100 mol ppm. The opposite relative charge states of Na^+ and of Al^{3+} ions, if, as assumed, being present on Co^{2+} sites, let the influences of these two impurities

cancel each other out to some extent. In view of the magnitude of the degree of the deviation from stoichiometry, δ, in cobalt silicate, $Co_2SiO_{4+\delta}$, it is expected that the presence of the impurities denoted above does not have a very significant effect on the experimental results obtained for this study for the cobalt tracer diffusion, at least not at higher oxygen activities.

3.3.2. Cobalt Tracer Diffusion Experiments

Using the single crystals grown as described above, cobalt tracer diffusion experiments were performed as a function of the crystallographic orientation, temperature and oxygen activity using the radioactive isotope Co-60. The temperature range of measurements was between 1200 and 1300 °C. Grown single crystals were oriented using the Laue back reflection technique with a precision of better than 0.5° and then sectioned perpendicular to the three principal axes into discs with 1.5 to 2 mm in thickness and 6 to 8 mm in diameter. Each disc was then pre-annealed for 3 to 4 days at the temperature and oxygen activity selected for the subsequent diffusion experiment to achieve equilibrium point defect concentrations. Oxygen activities were established by using pure oxygen, mixtures of nitrogen and air, and CO/CO_2 gas mixtures.

After pre-annealing, the samples were ground plane-parallel with a grinding wheel containing diamonds with a size of 64 µm. After that, the radioactive isotope Co-60 was applied in the form of an aqueous chloride solution onto one of the two large, ground surfaces of each sample. Diffusion anneals were performed at the same conditions as being present during pre-annealing. The length of the diffusion

anneals, t, varied between 5 and 30 days, depending on the crystal orientation, oxygen activity and temperature, to obtain penetration profiles of 40 to 200 µm in length.

After a diffusion anneal, the annealed sample was removed from the furnace and then mounted onto a plane-parallel stainless steel sample holder for the following residual radioactivity profile analysis. This analysis is based on the measurement of the radioactivity of a sample before the removal of material (= initial activity) and after the removal of material (= residual activity). The initial activities, A (x=0,t), were measured using either a high resolution Ge detector (Ortec) or a scintillation detector. Layers of the sample were subsequently removed with a diamond grinding wheel containing diamonds with a size of 46 µm. The roughnesses of the sample surfaces obtained after machining using the two diamond wheels denoted above were of the order of about ± 1 µm as determined by using an optical non-contact surface profiler (ADE Phase Shift MicroXAM). Residual radioactivities of a given sample, A(x,t), were measured after each material removal by counting pulses produced by the interaction between γ-rays emitted by the sample and the used detector. x is the overall thickness of removed sample layers, beginning at the side where the radioactive tracer was first applied. By removing numerous layers of material residual activity profiles, A(x,t)/A(x=0,t) vs. x, were obtained. Based on the values of the two γ-ray energies associated with the decay of Co-60 (1.17 and 1.33 MeV [18]) and on the lengths of the residual radioactivity profiles considered in this study, it was acceptable to ignore the absorption of γ-radiation within the olivine samples.

Under the boundary conditions described above, the thin-film solution of Fick's 2nd law applies; this solution is

$$c_{Co}(\xi,t) = \frac{Q_{Co}}{\sqrt{\pi \cdot D^*_{Co} \cdot t}} \cdot \exp\left(- \frac{\xi^2}{4\,D^*_{Co} \cdot t} \right) \tag{3.1}$$

where $c_{Co}(\xi,t)$ is the concentration of Co at the distance ξ from the surface for the diffusion-annealing time t and Q_{Co} is the initial concentration of the Co tracer per unit area.

Residual radioactivities were measured after the removal of layers of material of the thickness x and residual radioactivity profiles were obtained which can be described by using Equation (3.2).

$$\frac{A(x,t)}{A(x=0,t)} = \frac{\int_x^\infty c_{Co}(\xi,t) \cdot d\,\xi}{\int_0^\infty c_{Co}(\xi,t) \cdot d\,\xi} = 1 - \operatorname{erf}\left(\frac{x}{2\sqrt{D^*_{Co} \cdot t}} \right) \tag{3.2}$$

As indicated in the middle part of this equation, the last part of it can be derived by integration of Equation (3.1). For determining values of cobalt tracer diffusion coefficients Equation (3.3) was used which contains the inverse function of the error function, erfi.

$$\operatorname{erfi}\left(1 - \frac{A(x,t)}{A(x=0,t)} \right) = \frac{x}{2\sqrt{D^*_{Co} \cdot t}} \tag{3.3}$$

When a = erfi(b), then b = erf(a). For a given diffusion-annealing time, t, the value of the cobalt tracer diffusion coefficient can be obtained from a least squares fit of Equation (3.3) to experimental data. The use of Equation (3.3) for data analysis instead of Equation (3.2) has the advantage by being a little more sensitive to data points obtained for larger penetration depths.

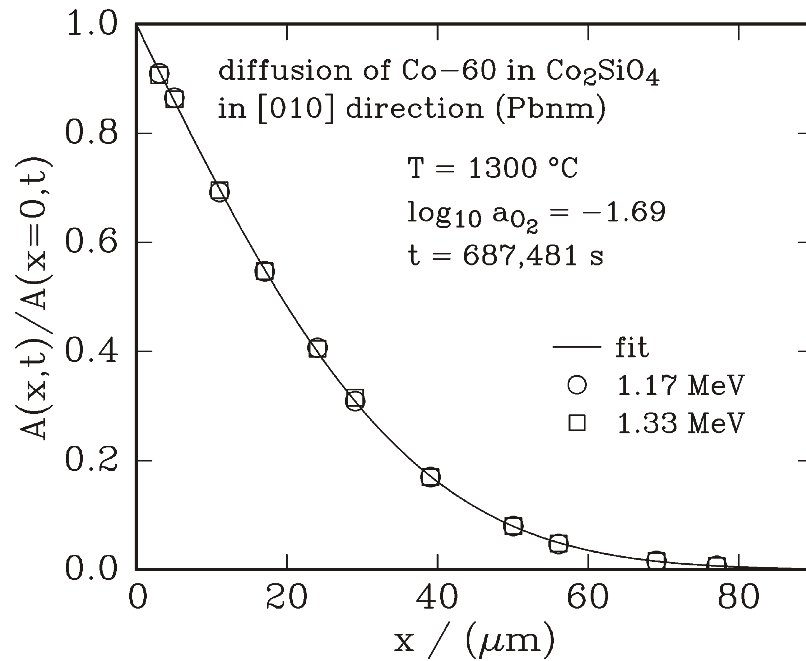

Figure 3.5: Normalized residual radioactivity profile, A(x,t)/A(x=0,t) vs. x. A(x,t) is the residual radioactivity measured when material of the thickness x has been removed from the sample and A(x=0,t) is the residual radioactivity before any material removal. t is diffusion-annealing time. The data shown are for a tracer diffusion experiment performed at 1300 °C at log $a_{O_2} = -1.69$ with a diffusion- annealing time t ≈ 687,500 s.

3.4. Results

An example for an experimentally determined residual radioactivity profile of the type A(x,t)/A(x=0,t) vs. x is shown in Figure 3.5. The line in the plot was obtained by fitting Equation (3.2) to the experimental data points. Figure 3.6 shows a plot of the type erfi(1 - A(x,t)/A(x=0,t)) vs. x. The line in this figure was obtained by fitting Equation (3.3) to the experimental data to determine values for D^*_{Co}. The differences between the values obtained for D^*_{Co} by fitting Equations (3.2) and (3.3)

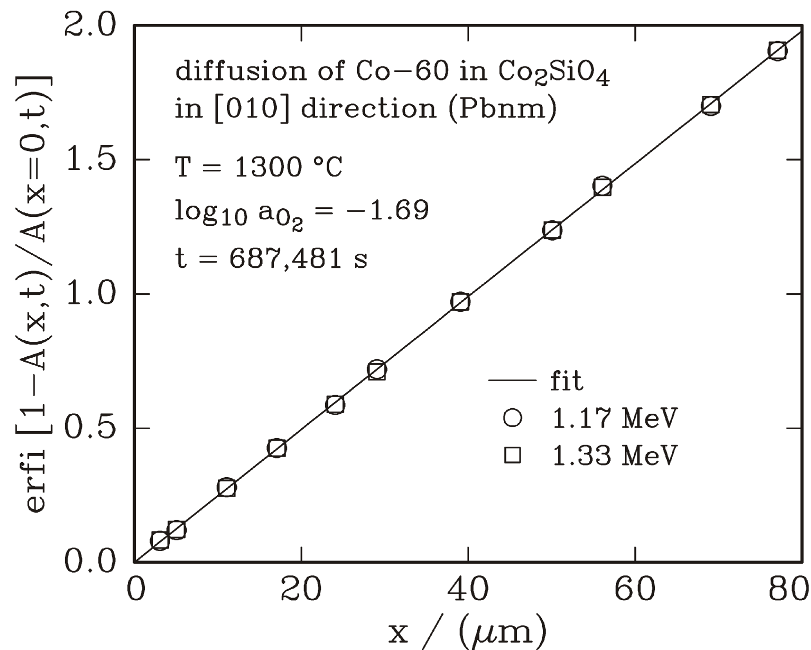

Figure 3.6: Plot of the inverse function of the error function of the argument [1 - A(x,t)/A(x=0,t)] vs. x for the same experiment as that considered in Figure 3.5. This type of plot was generated for all performed tracer diffusion experiments when determining values for cobalt tracer diffusion coefficients by fitting Equation (3.3) to the experimental data.

to the experimental data were only very small, at maximum of the order of 0.2 %. For the sake consistency, Equation (3.3) was used to determine the values of all cobalt tracer diffusion coefficients reported in this article.

The values of all experimentally determined tracer diffusion coefficients for Co-60 diffusing at 1200, 1250 and 1300 °C and at different oxygen activities in Co_2SiO_4 single crystals along the three principle orientations [100], [010] and [001] are listed in Table 3.1. The errors reported in this table are those obtained when fitting Equation (3.3) to the normalized residual radioactivities obtained from experiments. Additional errors are related to the measurement of diffusion-annealing temperatures and times, sample thicknesses and net counts, the latter two during the profile analyses. The real errors of the reported tracer diffusion coefficients are estimated to be about 5 % based on past experiences and the individual errors involved in determining the different parameters used to derive values for cobalt tracer diffusion coefficients.

As one can see from Table 3.1, data obtained for different crystals and referring to the same experimental conditions are in good agreement with each other. The data obtained for 1300 °C and different crystal orientations, plotted as a function of the oxygen activity, are shown in Figure 3.7 in comparison with a single data point for the diffusion of Co-60 in polycrystalline Co_2SiO_4 reported in Ref. [17]. Figure 3.7 shows cobalt tracer diffusion coefficients from the present work as a function of temperature for a_{O_2} = 1 in comparison with two data points

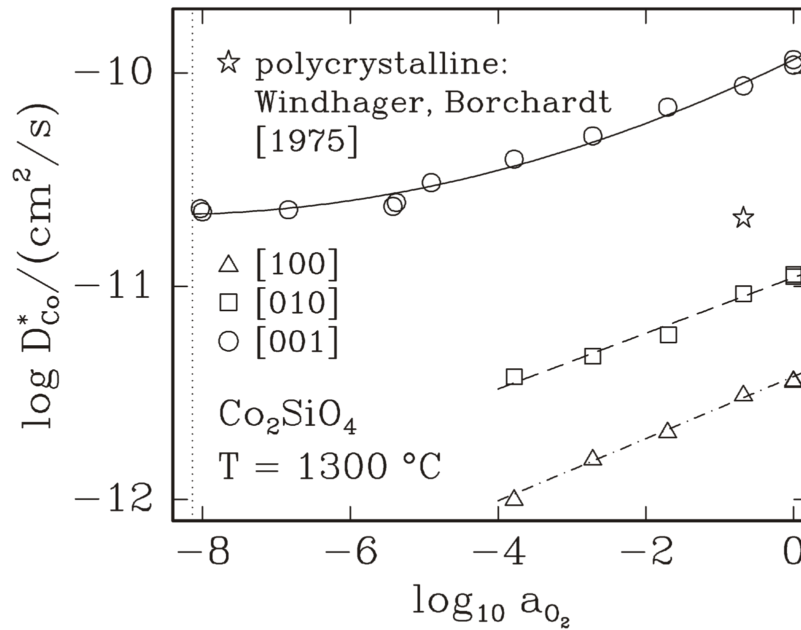

Figure 3.7: Tracer diffusion coefficients measured for the diffusion of cobalt in Co_2SiO_4 at 1300 ℃ and $a_{SiO_2} = 1$ along the principle orientations [100], [010] and [001] as a function of the oxygen activity. One data point from the literature [17] for the diffusion of Co in polycrystalline Co_2SiO_4 is also shown for comparison. The lines shown are guides to the eye only.

from Ref. [17] measured for the tracer diffusion of Co in polycrystalline Co_2SiO_4 in air at atmospheric pressure and extrapolated to $a_{O_2} = 1$ by assuming that $D^*_{Co} \propto a_{O_2}^{1/6}$.

Table 3.1: Cation tracer diffusion coefficients, D^*_{Co}, experimentally determined in this study for Co_2SiO_4 at $a_{SiO_2} = 1$ and different oxygen activities. $D° = 1\ cm^2/s$. The errors reported in this table are from least squares fits of Equation (3.3) to normalized residual radioactivity profiles. The overall errors are estimated to be of the order of 5 %, as discussed in Section 3.4.

a) T = 1300 °C, [100]

$\log_{10} a_{O_2}$	$\log_{10} (D^*_{Co}/D°)$	crystal #
0	−11.433 ± 0.024	100a
	−11.436 ± 0.021	100b
−0.678	−11.500 ± 0.044	100a
−1.704	−11.673 ± 0.019	100b
−2.718	−11.801 ± 0.016	100b
−3.782	−11.990 ± 0.014	100a

b) T = 1300 °C, [010]

$\log_{10} a_{O_2}$	$\log_{10} (D^*_{Co}/D°)$	crystal #
0	−10.954 ± 0.016	010a
	−10.944 ± 0.014	010b
−0.678	−11.035 ± 0.026	010a
−1.693	−11.227 ± 0.010	010b
−2.718	−11.328 ± 0.016	010a
−3.782	−11.424 ± 0.015	010b

c) T = 1300 °C, [001]

$\log_{10} a_{O_2}$	$\log_{10} (D^*_{Co}/D°)$	crystal #
0	−9.937 ± 0.026	001a
	−9.963 ± 0.014	001b
−0.678	−10.060 ± 0.031	001a
−1.704	−10.160 ± 0.010	001b
−2.718	−10.295 ± 0.019	001b
−3.782	−10.404 ± 0.018	001a
−4.904	−10.514 ± 0.016	001b
−5.376	−10.607 ± 0.022	001c
−5.422	−10.625 ± 0.025	001c
−6.838	−10.641 ± 0.017	001c
−8.001	−10.651 ± 0.019	001c
−8.030	−10.636 ± 0.018	001b

d) T = 1250 °C, $\log_{10} a_{O_2} = 0$

orientation	$\log_{10} (D^*_{Co}/D°)$	crystal #
[100]	−11.814 ± 0.018	100b
[010]	−11.337 ± 0.026	010b
[001]	−10.447 ± 0.016	001b
	−10.413 ± 0.014	001c

e) T = 1200 °C, $\log_{10} a_{O_2} = 0$

orientation	$\log_{10} (D^*_{Co}/D°)$	crystal #
[100]	−12.267 ± 0.045	100b
[010]	−11.733 ± 0.025	010b
[001]	−10.831 ± 0.020	001b

3.5. Discussion

First, it will be discussed which types of point defects need to be considered for modeling the point defect chemistry of Co_2SiO_4 based on previous and present observations. Then the cobalt tracer diffusion coefficients measured in this work will be compared with previous data and be analyzed with regard to their dependencies on crystal orientation, temperature and oxygen activity.

3.5.1. Point Defect Chemistry

In the following discussion, point defects are described by using the Kröger-Vink notation in its ionic version [19]. Results for point defect-related properties of cobalt orthosilicate reported in the literature [7,8,11] suggest that the majority defects present in $Co_2SiO_{4+\delta}$ at higher oxygen activities are vacancies on Co^{2+}-sites (= M-sites), $(V_{Co^{2+}})''$, and holes, the latter assumed to be present in the form of $(Co^{3+}_{Co^{2+}})^{\bullet}$. In the following text, no distinction is made between different M-sites, M1- and M2-sites, see the introduction. Based on the electrical conductivity data by Hirsch [11] discussed earlier it cannot be ruled out that electrons as minority defects influence the oxygen activity dependencies of point

defect concentrations at lower oxygen activities. The defect-related data currently available in the literature do not provide any hints on the possible presence of Co^{2+} ions on interstitial sites or of any cobalt ions on Si-sites as minority defects. However, tracer diffusion data from the present work suggest that Co^{2+} ions on interstitials sites, $(Co_I^{2+})^{\bullet\bullet}$, must also contribute to the cobalt tracer diffusion at lower oxygen activities. This suggests to consider $(V_{Co^{2+}})''$, $(Co_{Co^{2+}}^{3+})^{\bullet}$, e' and $(Co_I^{2+})^{\bullet\bullet}$ as important point defects for modeling the oxygen activity dependence of defect-related properties of $Co_2SiO_{4+\delta}$ at the conditions considered in this article in addition to impurities influencing point defect concentrations.

Since $Co_2SiO_{4+\delta}$ is a ternary compound, it follows from the Gibbs phase rule that one needs to define at given values of total pressure, P, and temperature, T, two other variables to unequivocally determine the thermodynamic state of this oxide. One variable of choice is usually the oxygen activity because it can be relatively easy controlled in experimental work. The second variable can be the activity of one component of $Co_2SiO_{4+\delta}$, e.g., of CoO, Co_3O_4, or SiO_2, or the Co/Si-ratio. As discussed in Ref. [6] the latter is experimentally very difficult and often impossible to achieve.

For the incorporation of oxygen into $Co_2SiO_{4+\delta}$ one can formulate different reactions, depending on which second variable discussed in the preceding paragraph is selected, If, for example, Co_2SiO_4 is present in equilibrium with CoO,

i.e., when the thermodynamic activity of CoO is one ($a_{CoO} = 1$), it is most useful to describe the oxygen incorporation by the reaction

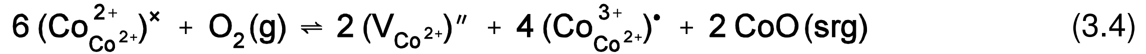

$$6\,(Co^{2+}_{Co^{2+}})^{x} + O_2(g) \rightleftharpoons 2\,(V_{Co^{2+}})'' + 4\,(Co^{3+}_{Co^{2+}})^{\bullet} + 2\,CoO\,(srg) \qquad (3.4)$$

The abbreviation *srg* stands for *sites of repeatable growth*. If a sample of Co_2SiO_4 has a fixed Co/Si-ratio, e.g., of exactly 2:1, it is most suitable to describe the incorporation of oxygen by the reaction

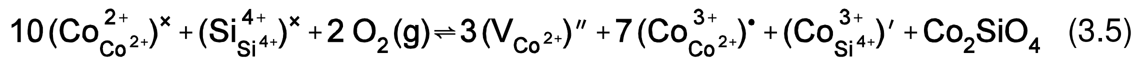

$$10\,(Co^{2+}_{Co^{2+}})^{x} + (Si^{4+}_{Si^{4+}})^{x} + 2\,O_2(g) \rightleftharpoons 3\,(V_{Co^{2+}})'' + 7\,(Co^{3+}_{Co^{2+}})^{\bullet} + (Co^{3+}_{Si^{4+}})' + Co_2SiO_4 \qquad (3.5)$$

If Co_2SiO_4 is present in equilibrium with SiO_2, i.e., $a_{SiO_2} = 1$, it is preferred to describe the incorporation of oxygen by the reaction

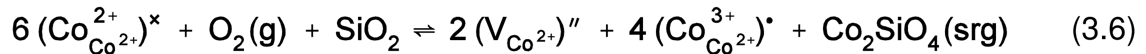

$$6\,(Co^{2+}_{Co^{2+}})^{x} + O_2(g) + SiO_2 \rightleftharpoons 2\,(V_{Co^{2+}})'' + 4\,(Co^{3+}_{Co^{2+}})^{\bullet} + Co_2SiO_4\,(srg) \qquad (3.6)$$

For taking into account electrons and Co^{2+} ions on interstitial sites as point defects in addition to vacancies and Co^{3+} ions on Co^{2+} sites (= holes) one needs to formulate two additional defect formation reactions. These are

$$0 \rightleftharpoons e' + h^{\bullet} \qquad (3.7)$$

and

$$(Co^{2+}_{Co^{2+}})^{x} + (V_I)^{x} \rightleftharpoons (V_{Co^{2+}})'' + (Co^{2+}_I)^{\bullet\bullet} \qquad (3.8)$$

The overall electroneutrality condition, taking in addition into account the presence of ions of the type Me^{+} and Mx^{3+} as impurities (assumed to be present on Co^{2+} sites) is

$$2\,[(V_{Co^{2+}})''] + [e'] + [(Me^{+}_{Co^{2+}})'] = 2\,[(Co^{2+}_{I})^{\bullet\bullet}] + [(Co^{3+}_{Co^{2+}})^{\bullet}] + [(Mx^{3+}_{Co^{2+}})^{\bullet}] \quad (3.9)$$

In Equation (3.9) the terms [i] denote concentrations of the defect species per unit of $Co_2SiO_{4+\delta}$. If cation vacancies and holes (holes = Co^{3+} ions on Co^{2+} sites) are the majority defects, one finds by making use of the reaction Equations (3.4) to (3.6) and of the electroneutrality condition that the concentrations of the majority defects and of the deviation from stoichiometry, δ, in $Co_2SiO_{4+\delta}$, are proportional to $a_{O_2}^{1/6}$ if $Co_2SiO_{4+\delta}$ is present in equilibrium with CoO or with SiO_2 and proportional to $a_{O_2}^{1/5.5}$ if the Co/Si-ratio is constant.

Since this article focuses on $Co_2SiO_{4+\delta}$ with an excess of SiO_2, the defect formation reactions (3.4) and (3.5) are ignored in the following. The equilibrium constant of the reaction described in Equation (3.6), when including all practically constant terms, i.e., the concentration of Co^{2+} ions on Co^{2+} sites and the thermodynamic activities of SiO_2 and of Co_2SiO_4, in this constant, can be formulated as

$$K_a = \frac{[(V_{Co^{2+}})'']^2 \cdot [(Co^{3+}_{Co^{2+}})^{\bullet}]^4}{a_{O_2}} \quad (3.10)$$

The equilibrium constant for the thermal electronic disorder reaction described in Equation (3.7), K_e, is

$$K_e = [e'] \cdot [h^{\bullet}] = [e'] \cdot [(Co^{3+}_{Co^{2+}})^{\bullet}] \tag{3.11}$$

and that of the Frenkel disorder reaction denoted in Equation (3.8), K_F, reads

$$K_F = [(V_{Co^{2+}})''] \cdot [(Co^{2+}_I)^{\bullet\bullet}] \tag{3.12}$$

The equation system defined by Eqs. (3.9) to (3.12) can be used for given values for the concentrations of impurities of the types Me^+ and Mx^{3+} and the equilibrium constants K_a, K_e and K_F to calculate concentrations of all point defects denoted in Equation (3.9) as a function of oxygen activity. This will be discussed later in this article when a Kröger-Vink diagram is introduced which is compatible with experimental observations made for defects and defect-related properties of Co_2SiO_4.

3.5.2. Comparison of Current Cobalt Tracer Diffusion Data with Earlier Diffusion Data

The cobalt tracer diffusion data obtained in this study for single-crystalline samples can be compared with two data points available for cobalt tracer diffusion coefficients, D^*_{Co}, from a study Windhager and Borchardt [17]. These data are shown in Figure 3.4 in comparison with data for the diffusion of Si and O from Ref. [17] and from Ref. [12], respectively. Windhager and Borchardt measured values for D^*_{Co} for Co_2SiO_4 in air at atmospheric pressure at about 1225 and

1300 °C using polycrystalline, melt-grown samples. One of these data points is shown in Figure 3.7 in comparison with data for single-crystalline samples from this study. Both data points, extrapolated to $a_{O_2} = 1$ by assuming that $D^*_{Co} \propto a^{1/6}_{O_2}$, are shown in Figure 3.8 in comparison with values for D^*_{Co} from this study as a function of temperature. The comparisons made lead to the not unexpected result that the values of the diffusion coefficients obtained for polycrystalline samples are found

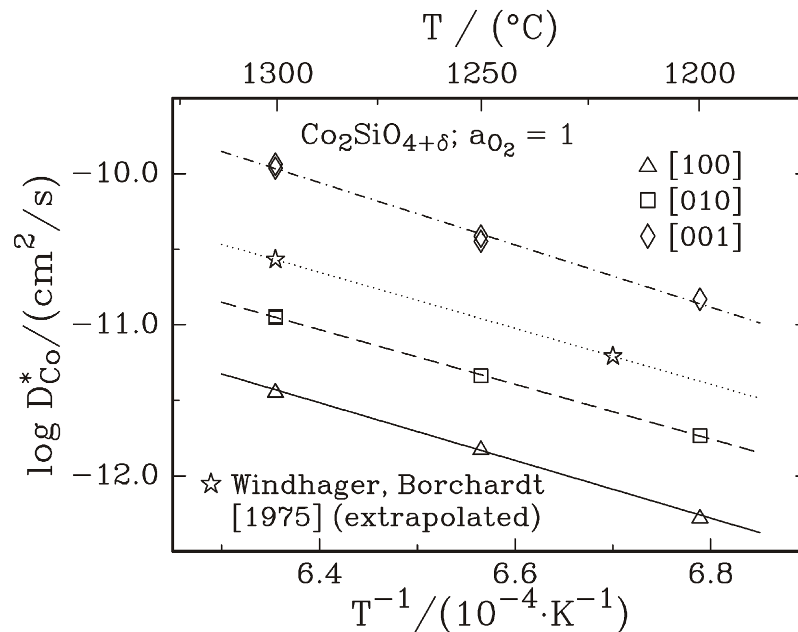

Figure 3.8: Temperature dependencies of cobalt tracer diffusion coefficients measured for Co_2SiO_4 at $a_{SiO_2} = 1$ between 1200 and 1300 °C along the principle orientations [100], [010] and [001] in pure oxygen at 1 atm total pressure. Two data points from the literature [17], extrapolated to $a_{O_2} = 1$, for the diffusion of Co in polycrystalline Co_2SiO_4 are also shown for comparison. The lines shown were generated by fitting Equation (3.13) to the experimental data shown in the plot.

somewhere between those obtained for the diffusion of Co in single crystals along the directions where this diffusion occurs fastest and slowest, respectively. Figure 3.8 suggests that the temperature dependencies of the diffusion of Co in single crystals and in polycrystalline samples are relatively similar.

Comparing the cobalt tracer diffusion data with those shown in Figure 3.4 for the diffusion of Si and O confirms earlier conclusions that the diffusion of Co along different orientations is at all temperatures considered in Figures 3.4 and 3.8 much faster than that of O and Si.

3.5.3. Orientation Dependence of Cobalt Tracer Diffusion

The results shown in Figure 3.7 indicate that the cobalt tracer diffusion coefficients measured along three principle orientations at 1300 °C follow the trend $D^{*}_{Co[001]} > D^{*}_{Co[010]} > D^{*}_{Co[100]}$ at all oxygen activities for which data for different crystal orientations are available. The same holds for the diffusion of Co at temperatures between 1200 and 1300 °C at $a_{O_2} = 1$, see Figure 3.8 For 1200 °C one finds for $a_{O_2} = 1$ for the ratio $D^{*}_{Co[001]}:D^{*}_{Co[010]}:D^{*}_{Co[100]}$ values of 27:3.4:1.0 and for 1300 °C values of 30:3.1:1.0. Since these ratios are very close to each other this suggests that the activation enthalpies for the motion of Co ions along different crystallographic orientations are relatively similar to each other. This is a relatively unexpected result in view of the anisotropy of the crystal structure of cobalt orthosilicate which should influence the activation barriers to be overcome by Co ions when diffusing along different crystal orientations and may be related to the fact that the temperature range covered is relatively small. In principle one would

expect a significant temperature dependence in diffusion coefficient ratios for different diffusion directions since the heights of the activation barriers to overcome should be different for different directions. This has been observed for the interdiffusion of Fe and Mg in $(Fe_xMg_{1-x})_2SiO_4$ [20,21] at constant values of the composition parameter x (= 0.07 in [21]) and of the oxygen activity. In this case, the degree of anisotropy in the interdiffusion increases with decreasing temperature.

However, one has also to consider that the diffusion of cobalt in Co_2SiO_4 along different crystal orientations can occur by elementary jumps in different directions and may involve a zigzag-type motion of ions. In the [001] direction, the diffusion occurs based on structural considerations most likely only by jumps in this direction between M1 sites while the motion in the direction [100] almost for sure involves sequences of individual jumps in different directions. Based on structural considerations one must expect for the diffusion along the [010] orientation jumps between neighboring M1 sites, jumps between neighboring M2 sites and also jumps between neighboring M1 and M2 sites. Zigzag-type diffusion may be the reason why the diffusivities vary only by a factor of about 3 between the [010] and the [100] direction while the diffusion along the [001] orientation occurs significantly faster.

Some data related to the anisotropy of the diffusion of cations in orthosilicates with the olivine structure which can be compared with the current data for the diffusion of Co in Co_2SiO_4 are summarized in Table 3.2. The observed trend

$D^*_{Co[001]} > D^*_{Co[010]} > D^*_{Co[100]}$ is in general agreement to that observed for the diffusion of iron ions in fayalite, Fe_2SiO_4. Tsai et al. [22,23] found for the iron tracer diffusion at 1130 °C that the ratio $D^*_{Fe[001]}:D^*_{Fe[010]}:D^*_{Fe[100]}$ varies a little with the oxygen activity; the mean value of this ratio is about 12:3:1. This trend was confirmed in optical point defect relaxation studies on Fe_2SiO_4 by Ullrich and Becker [24]. The trend in the orientation dependence denoted above is also in agreement with very recent observations made for the diffusion of Mn-54 in Mn_2SiO_4 [25]. For 1200 °C and $\log a_{O_2} = -1.7$ a ratio $D^*_{Mn[001]}:D^*_{Mn[010]}:D^*_{Mn[100]}$ of about 6:2.5:1 was found. Furthermore, the trend denoted above is also in agreement with the ratio of component diffusion coefficients estimated for the diffusion of Mg in Co_2SiO_4, see Section 3.2., of $D_{Mg[001]}:D_{Mg[010]}:D_{Mg[100]} = 4.3:1.4:1$. The agreement between the observed trends is no surprise since at all conditions, for which ratios were given above, diffusion via vacancies on M-sites is dominant. An interesting question that cannot be answered at this time is why the degree of anisotropy in the diffusion of cations varies for different transition metal orthosilicates and also for different ions being present on M-sites in a given compound. Detailed computational studies of this subject could possibly provide some insight.

Table 3.2: Data for selected olivine structure oxides: lattice parameters [1,27], ionic radii of divalent metal ions in six-fold coordination [28], diffusion coefficient sequences, and ratios characterizing the anisotropy of tracer diffusion coefficients. # The diffusion coefficient sequence refers for $(Fe_xMg_{1-x})_2SiO_4$ to interdiffusion coefficients for about 8 mol% Fe_2SiO_4; the given ratio is a mean value for T = 1000 - 1150 °C. * T = 1300 °C, ** T = 1130 °C, *** T = 1200 °C, **** T = 1100 °C. ¶ Mg_2SiO_4 containing varying levels of impurities. The letters a, b and c refer to diffusion along the principle directions [100], [010] and [001], respectively.

Me_2SiO_4	a / (Å)	b / (Å)	c / (Å)	r_{Me} / (Å)	D_{Me} sequence	$D_{Me[c]}:D_{Me[b]}:D_{Me[a]}$
Co_2SiO_4	4.781	10.299	6.000	0.79	c > b > a	29.7 : 3.1 : 1 * this work
Fe_2SiO_4	4.821	10.478	6.089	0.75	c > b > a	12 : 3 : 1 ** Ref. [22,23]
Mn_2SiO_4	4.871	10.636	6.232	0.81	c > b > a	6 : 2.5 : 1 *** $\log_{10} a_{O_2} = -1.7$ Ref. [25]
Mg_2SiO_4¶	4.758	10.214	5.984	0.86	c > a > b	6 : 1 : 1.5**** Ref. [26]
$(Fe_xMg_{1-x})_2SiO_4$	-	-	-	-	D_{int}: c > a > b#	4.9 : 1.3 : 1 Ref. [20]

Interesting is also, that the anisotropies observed for the tracer diffusion of Mg in Mg_2SiO_4 [26] and for the interdiffusion in $(Fe_xMg_{1-x})_2SiO_4$ on the M-sublattice [20,21] do not follow the sequence discussed in the preceding section. For the latter two cases, the diffusion is still fastest along the [001] orientation, but is slowest along the [010] orientation. The reasons behind this different behavior are currently unknown.

Finally, the finding by Andersson et al. [15] that $D^*_{Si[001]}:D^*_{Si[010]}:D^*_{Si[100]}$ = 7.89:1.03:1 in Co_2SiO_4 at 1350 °C and a_{O_2} = 0.21 is somewhat surprising. A diffusion coefficient sequence of the same type as that observed for the cobalt tracer diffusion in Co_2SiO_4 is not necessarily expected since the diffusion paths of Si ions must be very different from those of Co ions.

3.5.4. Temperature Dependence of the Cobalt Tracer Diffusion

To analyze the temperature dependence of the cobalt tracer diffusion in Co_2SiO_4 at a_{O_2} = 1 an Arrhenius-type equation, Equation (3.13), was fitted to the experimental data shown in Figure 3.8.

$$D^*_{Co} = D^o_{Co} \cdot \exp\left(-\frac{\Delta H}{R \cdot T} \right) \tag{3.13}$$

The values obtained for pre-exponential factors, D^o_{Co}, and for activation enthalpies, ΔH, and their errors are reported in Table 3.3 in comparison with analogous data obtained by fitting Equation (3.13) to two data points obtained for the diffusion of Co in polycrystalline Co_2SiO_4 from Ref. [17] by extrapolation to a_{O_2} = 1. The activation enthalpies, ΔH, contain two contributions, one from the formation of

defects, at $a_{O_2} = 1$ expected to be vacancies on M-sites and holes, ΔH_f, and one from the motion of Co via vacancies on M-sites, ΔH_m. Based on the defect modeling to be discussed in the following Section 4.5., a relatively speculative estimate for ΔH_f is about 38 kJ/mol. If this value should be true, one would have for the enthalpies of motion values of 328, 309 and 357 kJ/mol for diffusion along the orientations [100], [010] and [001], respectively. These are relatively large values, but are comparable to an activation enthalpy of motion reported for the tracer diffusion of Mg in extrinsic Mg_2SiO_4, in which the defect population is controlled by impurities, of 400 ± 60 kJ/mol [26]. To determine more reliable values for the enthalpy of motion for the diffusion of Co in Co_2SiO_4 it is desirable to establish a reliable data set for the deviation from stoichiometry, δ, in $Co_2SiO_{4+\delta}$ as a function of oxygen activity and temperature covering a large temperature range and to have Co tracer diffusion data available for a larger temperature range than that investigated in this study. The fact that the activation enthalpies found for the diffusion of Co in Co_2SiO_4 along the orientations [100] and [010] are very similar to each other may be related to a zigzag-type motion of cobalt ions as discussed in Section 3.5.3.

Table 3.3: Data derived from fitting Equation (3.13) to the cobalt tracer diffusion data for $a_{O_2} = 1$ shown in Figure 3.8. The data for single crystals with different orientation are from this work and those for polycrystalline samples from Ref. [17], extrapolated to $a_{O_2} = 1$.

sample	orientation	log $[D^{\circ}_{Co}/(cm^2/s)]$	$\Delta H/(kJ/mol)$
single crystal	[100]	0.71 ± 0.38	365.6 ± 11.3
single crystal	[010]	0.55 ± 0.38	346.5 ± 11.2
single crystal	[001]	3.14 ± 0.38	394.7 ± 11.2
polycrystalline		1.22	355

3.5.5. Oxygen Activity Dependence of Cobalt Tracer Diffusion

As discussed before, from non-stoichiometry and electrical conductivity data available in the literature and also from the cobalt tracer diffusion data obtained in this study it follows that vacancies and holes, the latter being formulated as Co^{3+} ions on Co^{2+} sites (= M-sites), are the majority defects at high oxygen activities. The cause for the oxygen activity dependence of the electrical conductivity data published by Hirsch [11], $\sigma \propto a_{O_2}^{1/7.7}$, could be the presence of electrons and/or impurities in significant concentrations in addition to holes and vacancies on M-sites. However, the presence of impurities in relatively large concentrations, see Section 3.2, compared to the point defect concentrations estimated later in this section based on the results of tensi-volumetric measurements [7,8] suggest that the defect population present in Hirsch's samples is to a large extent controlled extrinsically. The smaller oxygen activity dependence of the tracer diffusion

observed at lower oxygen activities could be the result of the presence of some Co-interstitials and/or of impurities. In the following a defect modeling is presented which makes use of the defect chemistry discussed in Section 3.5.1 and is compatible with experimental observations for defect-related properties of Co_2SiO_4.

The information currently available on such properties of Co_2SiO_4 is is far from being sufficient to reliably model the oxygen activity dependence of the diffusivity of cobalt in Co_2SiO_4. From the observed oxygen activity dependencies of the deviation from stoichiometry, δ, in $Co_2SiO_{4+\delta}$, $\delta \propto a_{O_2}^{1/6}$, one can conclude that cation vacancies and holes, the latter assumed to correspond to Co^{3+} ions on M-sites, are the majority defects at high oxygen activities. This conclusion is supported by the oxygen activity dependence observed for the cobalt tracer diffusion at high oxygen activities, which is close to $D^*_{Co} \propto a_{O_2}^{1/6}$. In order to possibly be also compatible with the oxygen activity dependencies observed for the electrical conductivity by Hirsch [11], despite the potential impurity problems associated with these data, and for the cobalt tracer diffusion at lower oxygen activities, one needs to consider together with the presence of impurities also electrons and cation interstitials contributing to the transport of charge and matter, respectively.

To perform a modeling of the oxygen activity dependence of the cation tracer diffusion one needs first to develop an appropriate Kröger-Vink diagram which involves the calculation or estimate of point defect concentrations as a function of the oxygen activity at given values for temperature and total pressure for the

thermodynamic condition the considered oxide is in, e.g., in equilibrium with SiO_2. The most extensive set of tracer diffusion coefficients is available for 1300 °C for the orientation [001] of Co_2SiO_4 in equilibrium with SiO_2. Therefore, it was attempted to derive a Kröger-Vink diagram which is compatible with these diffusion data and could also be used to model electrical conductivity data, if such would be available for the conditions denoted above. For this purpose estimates were needed for equilibrium constants, beginning with that for the reaction denoted in Equation (3.6). The data most directly linked to this reaction are those for δ in $Co_2SiO_{4+\delta}$ in equilibrium with SiO_2 shown in Figure 3.2 for temperatures of 1100 and 1145 °C. These data, if taken at face value, suggest that δ slightly increases with decreasing temperature at a given oxygen activity. This is somewhat unexpected and uncommon. If cation vacancies and holes are the majority defects in transition metal-containing oxides one usually observes an increase of the deviation from stoichiometry with increasing temperature. Since the two temperatures denoted above are relative close to each other and two data sets differ only by about 15 % it may very well be that the type of temperature dependence just discussed is not real and the result of systematic errors in one or both studies which produced these data. Therefore, data for the temperature dependence of the deviation from stoichiometry in other oxides of the type Me_2SiO_4 were looked at. For Fe_2SiO_4 such data were not found. However, some data were found for $(Fe_xMg_{1-x})SiO_4$ at 1130 and 1200 °C as a function of the composition parameter x [29] which allow, by extrapolating data for 1200 °C to x = 1, an estimate whether δ in $Fe_2SiO_{4+\delta}$ increases or decreases with temperature

at a given oxygen activity. Based on such an estimate the expectation that δ in $Fe_2SiO_{4+\delta}$ increases with temperature at a given oxygen activity was confirmed. Much stronger support for such a temperature dependence is available from data for δ in $Mn_2SiO_{4+\delta}$ in equilibrium with $MnSiO_3$ [6]. For this compound experimental data for δ are available for a larger temperature range, 1000 to 1200 ℃. These data can be used for making an estimate for the temperature dependence of the variation of δ in $Co_2SiO_{4+\delta}$ by assuming that the temperature dependencies of δ are similar for $Co_2SiO_{4+\delta}$ and $Mn_2SiO_{4+\delta}$. Using this assumption and further assuming that the value of log δ in $Co_2SiO_{4+\delta}$ at 1122.5 ℃ and at $a_{O_2} = 1$ is the mean of the two values resulting for log δ when extrapolating the data for the two data sets shown in Figure 3.2 to $\log a_{O_2} = 0$, one obtains for log δ at 1300 ℃ and $\log a_{O_2} = 0$ an estimated value of −3.41. The increase of δ at $\log a_{O_2} = 0$, when increasing the temperature from 1122.5 to 1300 ℃, is about 45 %. The estimated value of the logarithm of the cobalt vacancy concentration, log $[(V_{Co^{2+}})'']$, for 1300 ℃ and $\log a_{O_2} = 0$ is −3.71. To obtain this value, assuming that cobalt vacancies and holes are the majority defects, the value of the equilibrium constant K_a, see Equation (3.10), must be set to $10^{-21.06}$. For calculations, $K_a = 10^{-21}$ was used. Finding values for the equilibrium constants K_e, see Equation (3.11) and K_F, see Equation (3.12), is much more difficult and not possible in an unequivocal way with the currently existing data. Nevertheless, based on the observed oxygen activity dependencies of the cobalt tracer diffusion and also of the electrical conductivity (Hirsch [11]), the latter being used with some reservation due to the large impurity concentrations in Hirsch's samples, one can conclude that cation

interstitials must contribute to the cation tracer diffusion at lower oxygen activities and electrons possibly to the electrical conductivity. These conclusions remain valid when taking into account the impurities being present in the samples used in the present study.

Since no information is available on the relative mobilities of cations diffusing via vacancies and via interstitials and of electrons and holes, it is impossible to do any firm modeling for lower oxygen activities. One can only assume values for mobility ratios and then vary the values of K_e and of K_F until one finds a

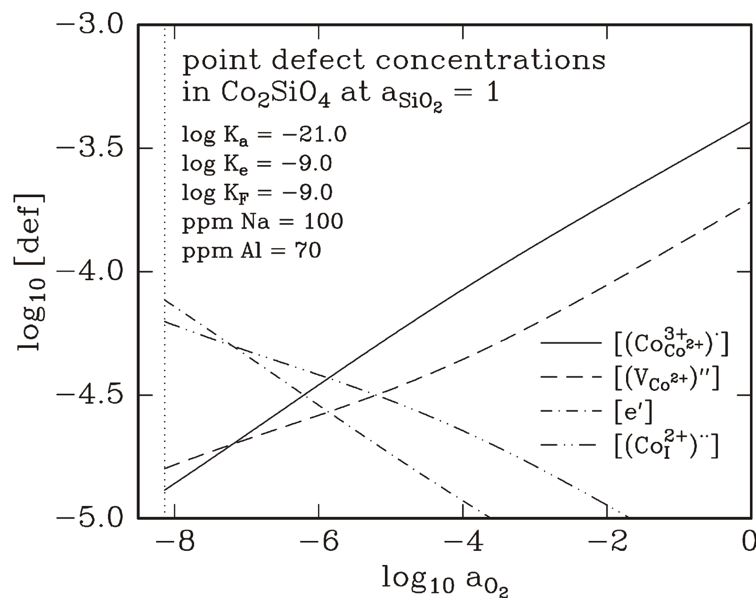

Figure 3.9: A partially estimated, somewhat speculative Kröger-Vink diagram for $Co_2SiO_{4+\delta}$ at 1300 °C and a_{SiO_2} = 1 which is compatible with all currently available information on oxygen activity dependencies of the deviation from stoichiometry, δ, the cobalt tracer diffusion and the electrical conductivity.

Kröger-Vink diagram which is compatible with all available experimental observations. This has been done and the result is the diagram shown in Figure 3.9. The impurity concentrations used for generating this figure, 100 mol ppm Na^+ and 70 mol ppm Al^{3+} are from Ref. [10] in which the growth of the single crystals used in this study is described in detail. The presence of these impurities is the reason that the oxygen activities at which $[e']$ = $[h^{\bullet}]$ and at which $[(V_{Co^{2+}})'']$ = $[(Co_I^{2+})^{\bullet\bullet}]$, respectively, are different from each other.

As indicated in Figure 3.9, the values used for K_e and K_F when generating the figure are identical. Since the enthalpies for the formation of electrons and holes, see the reaction described in Equation (3.7), and for the formation of Frenkel pairs, see the reaction denoted in Equation (3.8), are usually different, it can very well be that at some temperature K_e and K_F become identical. However, currently there is no proof that such a special situation occurs for Co_2SiO_4 at exactly 1300 °C. While the classic predominance of ionic disorder in compounds such as NaCl and AgCl is well known, there are not many examples for a predominant thermal electronic disorder in ionic materials. Two examples are CuO [30] and Fe_2O_3 [31]. The electrical conduction in these two non-stoichiometric compounds [32,31] is electronic and the electrical conductivity is independent of oxygen activity at high temperatures.

Further support that the defect modeling presented in Figure 3.9 is reasonable from a qualitative point of view are data available in the literature for the electrical conductivity of manganese silicate, Mn_2SiO_4, and very recent, unpublished data

for the manganese tracer diffusion in this orthosilicate. The electrical conductivity data reported for about 1200 °C in Ref. [33] show a minimum for the electrical conductivity as a function of oxygen activity while manganese tracer diffusion data for 1200 °C [25] also show a minimum at a similar oxygen activity. Such a combination of oxygen activity dependence minima can only occur when the equilibrium constants for the thermal electronic disorder and a thermal ionic disorder of Frenkel-type have very similar values.

Oxygen activity dependencies of the cobalt tracer diffusivity and of the electrical conductivity obtained by using the defect concentrations shown in Figure 3.9 and assuming a mobility ratio of 0.37 for the diffusion of cobalt via interstitials relative to that for diffusion via vacancies are shown in Figure 3.10a in comparison with experimental values for the Co tracer diffusion along the [001] orientation at 1300 °C. In Figure 3.10b three lines are shown which demonstrate what the oxygen activity dependence of the electrical conductivity would be if the mobility of electrons would be 0.5, 1 and 2 times that of holes. While the oxygen activity dependence at high oxygen activities is well described by $\sigma \propto a_{O_2}^{1/6}$, the Kröger-Vink diagram allows for the presence of a smaller oxygen activity dependence at lower oxygen activities and also for the occurrence of a minimum in the electrical conductivity, depending on the mobilities of electrons and holes relative to each other.

Due to its somewhat speculative nature the modeling just discussed should not be taken by its face value but instead be considered as a guideline to understand

the trends observed in oxygen activity dependencies of defect-related properties of cobalt silicate. Much more experimental work is needed to establish firm data for the variation of the oxygen content in $Co_2SiO_{4+\delta}$ and for the electrical conductivity, both as a function of oxygen activity and temperature.

3.6. Conclusions

The results obtained in this study for the oxygen activity dependence for the tracer diffusion of cobalt in cobalt silicate, $Co_2SiO_{4+\delta}$, at 1300 °C suggest that this diffusion is mainly governed by vacancies on cobalt sites (= M-sites) and at low oxygen activities also influenced by cobalt ions on interstitial sites. The diffusivity of cobalt ions varies significantly with the crystal orientation. It is fastest along the orientation [001] and slowest along the [100] orientation (space group used: Pbnm). At 1300 °C and $a_{O_2} = 1$, $D^*_{Co[001]}:D^*_{Co[010]}:D^*_{Co[100]} \approx 30:3:1$. The enthalpy of motion varies with the direction of diffusion between about 310 and 360 kJ/mol. It is largest for the orientation [001] and smallest for [010]. To further improve the reached limited level of understanding of point defects and defect-related properties, it is necessary to establish firm data for the variation of the oxygen content in $Co_2SiO_{4+\delta}$ and for the electrical conductivity, both as a function of oxygen activity and temperature. The currently available data for these quantities are insufficient. For a better understanding of anisotropy effects in the transport of matter and charge in Co_2SiO_4, computational work could be very beneficial to determine the energy barrier heights involved in different types of elementary transport processes.

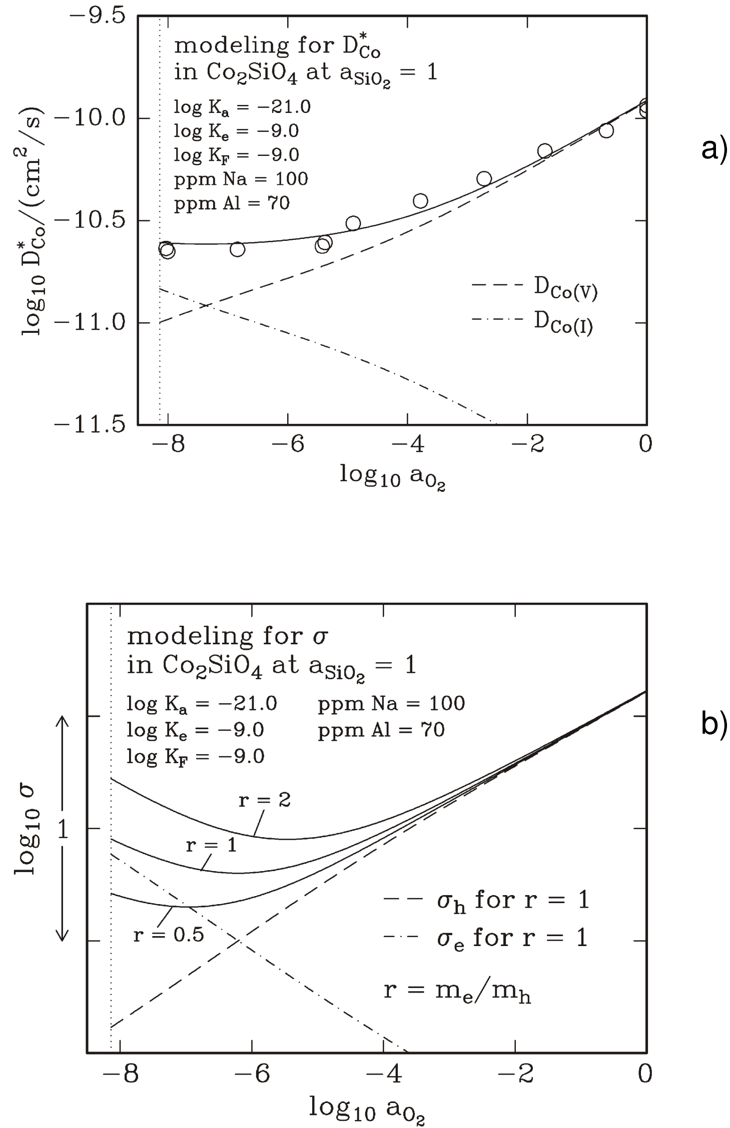

Figure 3.10: Comparison of oxygen activity dependencies obtained, departing from Figure 3.9, a) for the tracer diffusion coefficient of Co, D^*_{Co}, and b) for the electrical conductivity, σ, for Co_2SiO_4 at 1300 °C. To obtain values for D^*_{Co}, it was assumed that the diffusion via interstitials is 0.37 times as fast as that via vacancies. For the electrical conductivity three cases were considered; it was assumed that the mobility of electrons, m_e, is 0.5, 1 and 2 times, respectively, that of holes, m_h.

REFERENCES

[1] G.E. Brown, Jr., “Olivines and Silicate Spinels,” in 'Reviews in Mineralogy, Vol. 5: Orthosilicates, 2nd. Ed.,' P.H. Ribbe, Ed., Mineralogical Society of America, Washington, D.C., U.S.A., [1982] 275-381

[2] “International Tables for X-ray Crystallography,” Vol. 1: “Symmetry Groups,” N.F.M. Henry and K. Lonsdale, Eds., The Kynoch Press, Birmingham, U.K., [1965] Table 6.2.1, p. 548.

[3] B.J. Wanamaker and A.G. Duba, “Electrical Conductivity of San Carlos Olivines along [100] under Oxygen- and Pyroxene-Buffered Conditions and Implications for Defect Equilibria,” J. Geophys. Res., **98** (81) [1993] 489-500.

[4] R.N. Schock, A.G. Duba and T.J. Shankland, “Electrical Conduction in Olivines,” J. Geophys. Res., **94** (B5) [1989] 5829-5839.

[5] J.J. Roberts and J.A. Tyburczy, “Frequency Dependent Electrical Properties of Dunite as Functions of Temperature and Oxygen Fugacity,” Phys. Chem. Mineral, **19** (8) [1993] 545-561.

[6] J. Töpfer and R. Dieckmann, “Variation of the Oxygen Content and Point Defects in Tephroite, $Mn_2SiO_{4+\delta}$,” Solid State Ionics, **181** (11-12) [2010] 479-488.

[7] C. Greskovich and H. Schmalzried, “Nonstoichiometry and Electronic Defects in Co_2SiO_4 and in $CoAl_2O_4$-$MgAl_2O_4$ Crystalline Solutions,“ J. Phys. Chem. Solids, **31** (4) [1970] 639-646.

[8] G. Schwier, R. Dieckmann and H. Schmalzried, “Point Defects in Mixed Oxide Phases. I. Defect Thermodynamics of Cobalt Magnesium Oxide $[(Co_xFe_{1-x})O]$ and Cobalt Magnesium Silicate $[(Co_xMg_{1-x})_2SiO_4]$ Mixed Phases” (in German), Ber. Bunsenges. Phys. Chem., **77** (6) [1973] 402-408.

[9] G. Schwier and H. Schmalzried, “Point Defects in Oxide Mixed Phases. II. Mobility of the Electron Holes in Cobalt Magnesium Oxide and Cobalt Magnesium Silicate Solid Solutions” (in German), Ber. Bunsenges. Phys. Chem., **77** (9) [1973] 721-726.

[10] Q. Tang and R. Dieckmann, “Floating-Zone Growth and Characterization of Single Crystals of Cobalt Orthosilicate, Co_2SiO_4,” J. Cryst. Growth., **317** (1) [2011] 119–127.

[11] L.M. Hirsch, “Electrical Conduction of Co_2SiO_4,” Phys. Chem. Miner., **17** (2) [1990] 187-190.

[12] G. Borchardt and H. Schmalzried, ”Diffusion in Orthosilicates” (in German), Ber. Dtsch. Keram. Ges., **49** (1) [1972] 5-9.

[13] G. Borchardt and H. Schmalzried, ”Solid State Formation of Orthosilicates”, Ber. Dtsch. Keram. Ges., **49** (12) [1972] 395-400.

[14] M. Morioka, “Cation Diffusion in Olivine - I. Cobalt and Magnesium,” Geochim. Cosmochim. Acta, **44** (5) [1980] 759-762.

[15] K. Andersson, G. Borchardt, O. Müller and G. Róg, “A Point-Defect Approach to the Silicon Sublattice in Orthosilicates at High Temperatures”, in: ‘Nonstoichiometric Compounds,’ C.R.A. Catlow and W.C. Mackridt, Eds., Advances in Ceramics, **23** [1987] 399-407.

[16] D.L. Ricoult and D.L. Kohlstedt, "Creep of Fe_2SiO_4 and Co_2SiO_4 Single Crystals in Controlled Thermodynamic Environments," Philos. Mag. A., **51** (1) [1985] 79-93.

[17] H.J. Windhager and G. Borchardt, “Tracer Diffusion and Disorder in the Orthosilicate Co_2SiO_4” (in German), Ber. Bunsenges. Phys. Chem., **79** (11) [1975] 1115-1119.

[18] B.J. Wilson, “The Radiochemical Manual,” 2nd Ed., The Radiochemical Centre, Amersham, 1966.

[19] F.A. Kröger and H.J. Vink, “Relations Between the Concentrations of Imperfections in Crystalline Solids,” in: F. Seitz and D. Turnbull, Eds., Solid State Physics - Advances in Research and Applications, Vol. 3, Academic Press, New York, [1956] 307-435.

[20] D.K. Buening and P.R. Buseck, "Fe-Mg Lattice Diffusion in Olivine", J. Geophys. Res., **78** (29) [1973] 6852-6862.

[21] D.J. Misener, “Cationic Diffusion in Olivine to 1400 °C and 35 kbar,” in: A.W. Hofmann, B.J. Giletti, H.S. Yoder, Jr. and R.A. Yund, Eds., ‘Geochemical Transport and Kinetics,’ Carnegie Institution of Washington, Washington D.C., [1974] 117-129.

[22] T.L. Tsai and R. Dieckmann, "Point Defects and Transport of Matter and Charge in Olivines, $(Fe_x Mg_{1-x})SiO_4$", Materials Science Forum, **239-241** [1997] 399-402.

[23] T.-L. Tsai, K.-D. Becker and R. Dieckmann, "Point Defects and Orientation-dependent Transport of Matter and Charge in Iron-containing Olivines," Solid State Ionics, **194** (1) [2011] 17-32.

[24] K. Ullrich and K.D. Becker, "Kinetics and Diffusion of Defects in Fayalite, Fe_2SiO_4," Solid State Ionics, 1**41-142** (1) [2001] 307-312.

[25] Q. Tang and R. Dieckmann, “Orientation, Oxygen Activity and Temperature Dependencies of the Diffusion of Manganese in Manganese Orthosilicate, Mn_2SiO_4,” to be published (in preparation).

[26] S. Chakraborty, J.R. Farver, R.Y. Yund and D.C. Rubie, "Mg Tracer Diffusion in Synthetic Forsterite and San Carlos Olivine as a Function of P, T and f_{O_2}," Phys. Chem. Miner., **21** (8) [1994] 489-500.

[27] N. Morimoto, S. Akimoto, K. Goto and M. Tokonami, "Crystal Structures of High Pressure Modifications of Mn_2GeO_4 and Co_2SiO_4," Phys. Earth Planet. Inter., **3** [1970] 161-165.

[28] R.D. Shannon, "Revised Effective Ionic Radii and Systematic Study of Interatomic Distances in Halides and Chalcogenides," Acta Cryst., **A32** (5) [1976] 751-767.

[29] T.-L. Tsai and R. Dieckmann, “Variation of the Oxygen Content and Point Defects in Olivines, $(Fe_xMg_{1-x})_2SiO_4$, $0.2 \leq x \leq 1.0$,” Phys. Chem. Miner., **29** (10) [2002] 680-694.

[30] H.H. v. Baumbach, H. Dünwald and C. Wagner. “Conductivity Measurements on Cupric Oxide” (in German), Z. Physik. Chem., **B22** [1933] 226-230.

[31] R. Dieckmann, “Point Defects and Transport in Hematite ($Fe_2O_{3-\varepsilon}$),” Phil. Mag. A, **68** (4) [1993] 71-82.

[32] Y.D. Tretyakov, V.F. Komarov, N.A. Prosvirnina and I.B. Kutsenok, “Nonstoichiometry and Defect Structures in Copper Oxides and Ferrites,” J. Solid State Chem., **5** (2) [1972] 157-167.

[33] C. Stüber and W. Laqua, “Point Defects of Tephroite. I. The Electrical Conductivity of Mn_2SiO_4,” Z. Phys. Chem., **206** (1-2) [1998] 197-218.

CHAPTER 4

FLOATING-ZONE GROWTH AND CHARACTERIZATION OF SINGLE CRYSTALS OF MANGANESE ORTHOSILICATE, Mn_2SiO_4 *

4.1. Abstract

Using a floating zone technique and a passive afterheater, good quality single crystals of manganese orthosilicate, Mn_2SiO_4, were grown along the three principle orientations in a reducing gas atmosphere at atmospheric pressure. The grown crystals were typically 5 to 7 mm in diameter and 20 to 40 mm in length. Well developed facets were found on the periphery of some of the crystals grown along the [100] orientation (space group: Pbnm). Laue back reflection was used to determine orientations of grown crystals and of facets formed at the outer surface. Dislocation densities ranging between 10^5 and 10^6 per cm^2 were determined by optical microscopy after polishing and chemical etching. By using X-ray powder diffraction it was determined that a thermodynamically favored decomposition of grown single crystals of manganese silicate during cooling after crystal growth did not occur. Concentrations of impurities and the degree of a desired silica excess present in the grown crystals were determined by using the ICP-AES technique. The presence of intended silica-rich precipitates was confirmed by electron microprobe analysis.

* Reprinted from a manuscript by Qi Tang and Rüdiger Dieckmann. A shortened version of this manuscript was submitted to J. Cryst. Growth for publication.

4.2. Background

Manganese orthosilicate, Mn_2SiO_4, also known as tephroite, is a member of the olivine family minerals. Olivines are the major components of the Earth's upper mantle and have chemical compositions of the type Me_2SiO_4 where Me can refer to one or a combination of different chemical elements. Other common members of the olivine family minerals include Mg_2SiO_4 (forsterite), Fe_2SiO_4 (fayalite), $CaMgSiO_4$ (monticellite) and $CaMnSiO_4$ (glaucochroite). Olivine compounds have an orthorhombic crystal structure (space group: Pbnm). This crystal structure is based on a distorted hexagonal close packing of oxygen anions with Si cations occupying tetrahedral and Me cations occupying octahedral interstices of the oxygen sublattice. Two types of octahedra containing Me cations, M1 and M2, exist. M1 sites are located at centers of symmetry and M2 sites are present on mirror planes perpendicular to the c-axis when the space group Pbnm is used [1].

Due to the olivine-type compounds in the Earth's upper mantle, many geological processes are influenced by the types and concentrations of point defects being present in olivines at high temperatures. Therefore, defect-related properties of olivine-type compounds such as the electrical conductivity and diffusivities have been the subject of many studies, especially by Earth scientists. References related to the electrical conduction of olivine-structure minerals can be found in Ref. [2] and such related to diffusion in olivines in a recent review by Chakraborty [3]. Despite of all these efforts, point defects in and defect-related properties of olivine compounds are still far from being well understood. One

reason for this is that in most experimental studies of defect-related properties samples of natural minerals or of synthesized samples with relatively large impurity concentrations have been used. Depending on the types and concentrations of the impurities being present in olivine samples, their defect-related properties are often to a significant extent or even completely controlled by impurities.

To achieve a detailed understanding of point defects and defect-related properties of olivine-type compounds it is necessary to study sufficiently pure samples with known impurity concentrations. Due to the non-cubic, orthorhombic crystal structure of olivines, defect-related transport properties of these compounds are anisotropic, i.e., are tensors. To investigate experimentally the orientation dependence of defect-related transport properties of olivine-type compounds, e.g., electrical conductivity and tracer diffusivities, the use of single crystals of such compounds with high purity and well-known, low impurity concentrations is required. Another requirement is that the thermodynamic state of such samples must be carefully controlled. In the case of Mn_2SiO_4 this can in principle be achieved by exactly fixing the Mn/Si-ratio or by having traces of a second, either Si-rich or Mn-rich, phase being present. Since sufficiently exact fixing the Mn/Si-ratio is practically impossible, see Ref. [4], and different Mn-rich phases may coexist with Mn_2SiO_4, for the crystal growth work reported here it was decided to produce single crystals of Mn_2SiO_4 with traces of a Si-rich secondary phase. The goal of the single crystal growth work reported in this article was to provide suitable samples for experimental studies of the electrical conductivity and the tracer diffusion of Mn in Mn_2SiO_4 by growing well characterized, good quality

single crystals of manganese silicate, containing traces of a silica-rich secondary phase, along the three principle orientations.

4.2.1. Previous Single Crystal Growth of Mn_2SiO_4 and Similar Orthosilicates

In order to obtain suitable Mn_2SiO_4 single crystals for transport property studies, it is critical to choose a suitable method for growing the targeted single crystals. Various techniques used in the past for manganese silicate single crystal growth by different authors, as well as techniques used for growing other transition metal-containing orthosilicates single crystals, are reviewed and discussed below.

Finch et al. [5] used the Czochralski method to synthesize optically transparent single crystals of Mn_2SiO_4. The crystals were grown from manganese silicate melts contained in heavy-walled platinum crucibles held at temperatures between 1420 and 1460 °C under an atmosphere of moist argon containing 4 % H_2 and 2 to 4 % water. It was estimated that the oxygen activity, a_{O_2}, was about 10^{-10} ($a_{O_2} = P_{O_2}/P^{\circ}_{O_2}$ with $P^{\circ}_{O_2}$ = 1 atm; P_{O_2} = oxygen partial pressure). The melting temperature of Mn_2SiO_4 at this oxygen activity was 1315 ± 5 °C. One problem the authors faced was that, when melts containing MnO and SiO_2 are brought into contact with Pt at high temperatures and low oxygen activities, then some Mn dissolves into Pt, leading to an increase in the SiO_2-content of the melt. To reduce losses of MnO from the melt during crystal growth, platinum crucibles used as containers for the melt were pre-exposed to solid Mn_2SiO_4 at 1400 °C and log $a_{O_2} \approx -10$ for at least 24 hours. The dissolution of Mn into Pt reportedly can cause crucible failure and also leads to increasingly poorer crystal quality with growth time due to a gradual

increase of the SiO_2-content in the melt. As pointed out by Finch et al. [5], keeping the melt composition close to that corresponding to a Mn:Si-ratio of 2:1 was of crucial for achieving good quality crystal growth. Gradual losses of MnO from the melt caused by the dissolution of Mn into Pt lead to an increased tendency for the formation of defects, voids and secondary phase inclusions in the growing crystals. Periodic additions of MnO to the melt were made during crystal growth to compensate for losses of MnO from the melt. Finch et al. [5] state that good quality single crystals of Mn_2SiO_4 were grown along the three principle orientations, [100], [010] and [001], at growth rates as high as 1 cm/h and seed rotation speeds ranging from 10 to 20 rpm. Grown crystals were cooled to room temperature in less than one hour causing considerable strain but no visible signs of cracking. The grown crystals were of up to 1 cm in diameter and 3 cm in length. The color of the crystals was reported to be brownish black under reflected light and rose under transmitted light. The (010) plane was reported to be the predominant cleavage plane in the grown crystals. Lattice parameters of grown crystals were determined by X-ray diffraction and are listed in Table 4.1. In addition, edge-defined film-fed growth (EFG) experiments were used examine the effect of the melt composition on the sample perfection at similar growth conditions as present in the Czochralski crystal growth experiments. Optically transparent samples could only be produced by using the EFG technique from melts which had a Mn:Si ratio 2:1. As the composition of the melt became more SiO_2-rich, it became very difficult or impossible to growth rapidly good quality EFG films. A smaller influence of the

melt composition on the EFG growth was observed when an excess of MnO was present in the melt instead of an excess of SiO_2.

Czochralski growth of Mn_2SiO_4 has also been performed by Takei [6] under gas atmospheres of nitrogen of unspecified purity and of N_2/H_2-mixtures containing 0.2 vol% H_2. Ir crucibles with a wall thickness of 1.6 mm were used as containers for the melt. Seed crystals of Mn_2SiO_4 were prepared by using crystalline rods of Mg_2SiO_4 as initial seeds. The growth directions were along the [100] and [001] axes and the growth rates were 3 to 5 mm/h. Cooling after crystal growth occurred at a rate of 200 °C/h. The grown crystals were up to 20 mm in diameter and 100 mm in length. Lattice parameters of grown crystals were determined by using X-ray diffraction; the values obtained are listed in Table 4.1. As grown crystals were reported to be dark or almost opaque when observed under room light; cut and polished thin sections of the crystals, however, were transparent. No visible internal imperfections including cracks, gas bubbles and inclusions were observed in the crystals grown. Two tiny facets of (010) were found on the peripheral surface of crystals grown along the [100] orientation. The concentration of Mn^{3+} in grown crystals was reported to vary between 0 and about 1.6 wt%. Despite of the presence of Mn^{3+} and the use of starting material with a molar Mn:Si-ratio of 2:1 the molar Mn:Si-ratio in grown crystals was reportedly found to vary between 2 and 2.1. This finding is surprising. Based on the observations made by Finch at al. [5] of problems related to the dissolution of Mn onto the Pt containers used in their single crystal growth work and based on the fact that there exists a very large solubility of Mn in Ir according to Ref. [7], one should expect an enrichment of SiO_2

in the melt and with that in the growing crystal relative to the molar Mn:Si-ratio of two.

In a one page communication Takei and Hosoya [8] reported to have grown sizable single crystals of Mn_2SiO_4 using the floating-zone method. The atmosphere during the crystal growth was N_2 or Ar. The feed rods used during the crystal growth were prepared via a ceramic synthesis route using a starting materials corresponding to a molar Mn:Si-ratio of 2. The growth rate was 1 mm/h and the counter-rotational speeds were 30 rpm/h. Single crystal growth occurred along the [100] orientation. The typical dimensions of the grown crystals were 5 to 8 mm in diameter and 20 to 50 mm in length. Further characterization results for the grown crystals were not reported.

Various methods were used in the past to grow single crystals of other transition metal-containing orthosilicates. For the congruently melting cobalt orthosilicate, Co_2SiO_4, the crystal growth techniques used include chemical transport reactions, Schmid [9], a Bridgeman technique, Naka et al. [10], a flux method, Wanklyn [11], and floating zone methods, Hosoya and Takei [12] and the authors of this article [13]. For the also congruently melting iron orthosilicate, Fe_2SiO_4, the crystal growth methods employed before include a hydrothermal technique, Hirano et al. [14], a Czochralski method, Finch et al. [15], and floating zone methods, Takei [16] and Tsai et al. [17]. Single crystals of the incongruently melting nickel silicate, Ni_2SiO_4, were grown by Ozima [18] using a high temperature solution (flux) method, rather than the type of techniques used for

growing single crystals of the congruently melting transition metal-containing orthosilicates denoted above.

Based on the preceding literature review and the fact that manganese silicate is a congruently melting compound, single crystal growth from the melt is the preferable approach to obtain sizable, very pure single crystals for experimental studies of defect-related properties. Since the dissolution of manganese silicate components, especially of Mn, into noble metal container material is significant and has the potential to lead to compositional changes in a melt when held in a container, the use of a containerless growth method, i.e., of the floating zone method, was concluded to be most suitable for preparing very pure single crystals of Mn_2SiO_4 for defect-related studies. This approach avoids potential compositional changes in the melt due to interaction with container material and also the introduction of impurities into the melt from container material.

4.2.2. Thermodynamic Stability of Mn_2SiO_4

Before discussing experimental work performed related to the growth of manganese orthosilicate silicate single crystals, the conditions at which Mn_2SiO_4 is thermodynamically stable in the temperature range of interest for this study are reviewed. Since Mn_2SiO_4 is a ternary compound, at a given total pressure, the thermodynamic stability range of Mn_2SiO_4 corresponds to a three-dimensional (3-D) object in the temperature - oxygen activity - Mn/Si-composition space. Lines on the surface of the 3-D object denoted above represent changes from one phase being in equilibrium with manganese silicate to another phase being in

equilibrium with Mn_2SiO_4. Such lines representing different phase equilibria can be projected onto the oxygen activity vs. temperature plane to generate a 2-D diagram for the thermodynamic stability range of Mn_2SiO_4. A summary for the 2-D thermodynamic stability range of Mn_2SiO_4 can be found in Ref. [4]. Figure 4.1, which was generated by making use of data discussed in Ref. [4], shows the

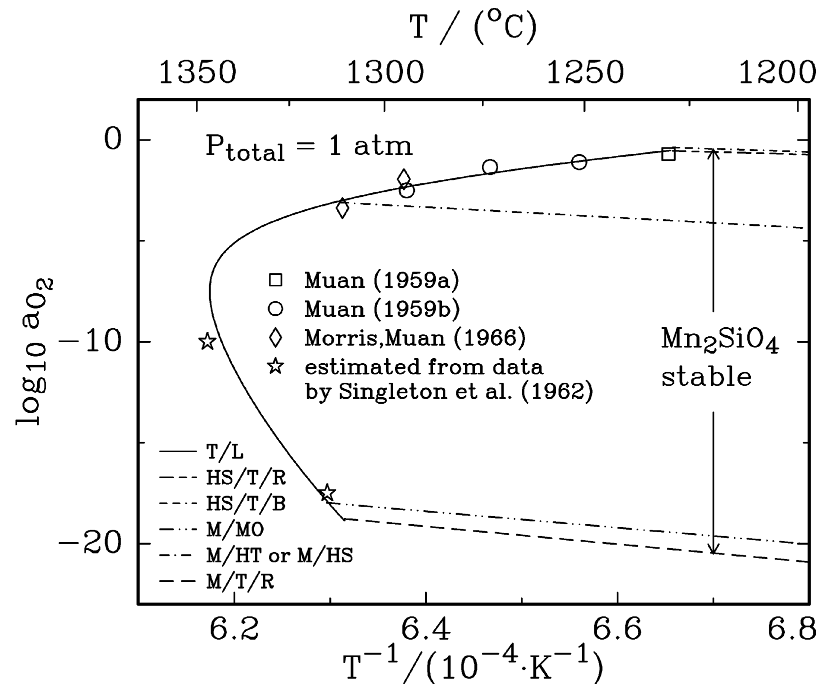

Figure 4.1: A diagram showing data related to the thermodynamic stability range of manganese orthosilicate at high temperatures close to the melting temperature of Mn_2SiO_4 at 1 atm total pressure. Information about the data used to derive this diagram can be found in Ref. [4]. The abbreviations used in this figure and their meanings are T = tephroite (Mn_2SiO_4), L = liquid silicate, HT = hausmannite (α-Mn_3O_4), HS = cubic Mn_3O_4 (β-Mn_3O_4), R = rhodonite ($MnSiO_3$), B = braunite (nominally Mn_7SiO_{12}), M = Mn and MO = MnO.

stability range of Mn_2SiO_4 at 1 atm total pressure as a function of oxygen activity and temperature at high temperatures near the melting temperature of Mn_2SiO_4. Suitable parameters for single crystal growth, i.e., for oxygen activity and temperature, were selected by making use of Figure 4.1. Atmospheres and temperatures for calcination and sintering during polycrystalline material preparation were chosen based on a plot published in Ref. [4] and covering a larger temperature range.

In addition, for understanding what may happen during cooling of a grown single crystal of Mn_2SiO_4 with silica excess it is also necessary to review the thermodynamic stabilities of the manganese silicates Mn_2SiO_4 and $MnSiO_3$. The latter phase is intended to be present in the form of a small amount of precipitates to fix the thermodynamic state of Mn_2SiO_4 in high temperature studies of defect-related properties of this oxide. Figure 4.2 is a temperature vs. composition phase diagram of the system Mn_3O_4-SiO_2 at 1 atm total pressure and at $\log a_{O_2} = -2.5$ generated based on data published by Muan [19]. From Figure 4.2 it follows that Mn_2SiO_4 may decompose upon cooling into Mn_3O_4 and braunite, the latter nominally having the composition Mn_7SiO_{12}. $MnSiO_3$ may decompose into Mn_7SiO_{12} and SiO_2 upon cooling. According to other phase diagrams of the same nature, but for different oxygen activities, also reported by Muan [19], the decomposition temperatures for both Mn_2SiO_4 and $MnSiO_3$ phases decrease with decreasing oxygen activity. If thermodynamic equilibrium cannot be established during cooling for kinetic reasons, decomposition may occur at temperatures lower than the equilibrium decomposition temperatures and metastable phases may be

present or decomposition may not occur at all. The dashed lines in Figure 4.2 are related to the presence of Mn_2SiO_4 and $MnSiO_3$ as metastable phases and can be ignored at this point; they will be discussed later.

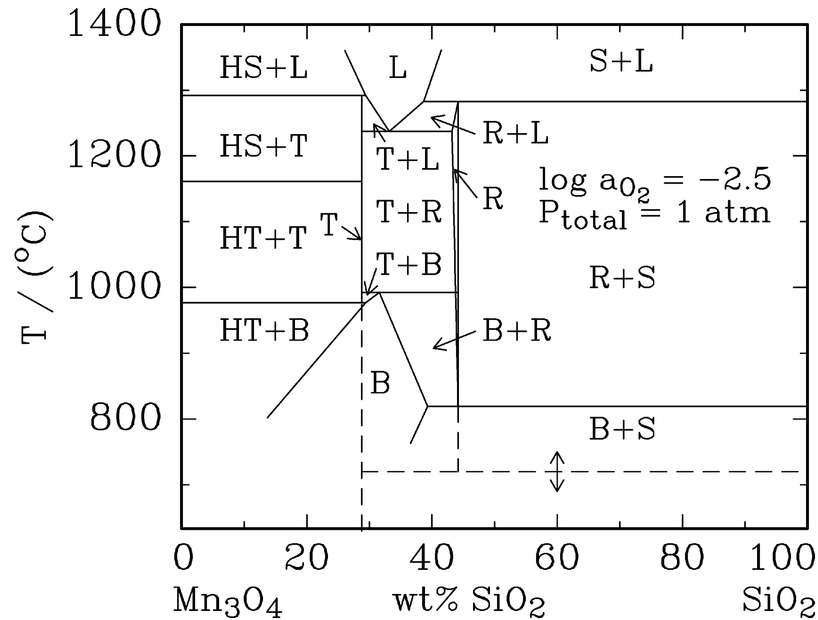

Figure 4.2: Phase diagram for the system Mn_3O_4-SiO_2 at $\log_{10} a_{O_2} = -2.5$ and 1 atm total pressure after Muan [19]. In addition to the abbreviations used in Figure 4.1, S is used as an abbreviation for tridymite (SiO_2). The dashed lines in the figure refer to the possibility that metastable phases could be formed upon cooling due to decomposition of Mn_2SiO_4 and $MnSiO_3$.

By using the data for the equilibria between Mn_2SiO_4, Mn_3O_4 and $MnSiO_3$ and between Mn_2SiO_4, Mn_3O_4 and Mn_7SiO_{12} shown in Figure 4.1, one can in principle calculate the temperatures at which a decomposition leading to the formation of

$MnSiO_3$ and Mn_7SiO_{12}, respectively, may occur. Prerequisite for doing this is to have knowledge on the local chemical composition of Mn_2SiO_4 which determines the local oxygen activity in Mn_2SiO_4 and which may very significantly differ from that being present in the gas atmosphere surrounding a cooling crystal of Mn_2SiO_4. Two limiting cases exist with regard to local oxygen activities in the non-stoichiometric compound $Mn_2SiO_{4+\delta}$ during cooling. Actual local oxygen activities in the interior of a grown crystal during cooling may be anywhere between those corresponding to the two limiting cases discussed below in more detail.

One of these limiting cases corresponds to no changes in the oxygen content during cooling at all. In this case the local composition in a cooling crystal determines the local oxygen activity and with that whether a crystal is locally thermodynamically stable or not. The second limiting case is present when the oxygen content in a cooling crystal corresponds always to that determined by the oxygen activity established in the gas atmosphere surrounding the crystal and the local temperature. For making stability predictions for the limiting cases denoted above one needs information on the oxygen content of the non-stoichiometric compound $Mn_2SiO_{4+\delta}$ as a function of temperature and oxygen activity at a given total pressure.

In the crystal growth experiments performed in this study CO/CO_2 gas mixtures with a fixed $CO:CO_2$ ratio were present in the surrounding of growing crystals, for details see the experimental section. The oxygen activity in the gas phase as a function of temperature can for this case be calculated based the equilibrium

between CO, CO_2 and O_2. Cooling paths in a log a_{O_2} vs. 1/T diagram corresponding to the two limiting cases for a CO/CO_2 gas atmosphere containing 20 vol% CO have been calculated and are illustrated in Figure 4.3. For calculating the line for the case of no composition changes, data for the variation of the oxygen content in the non-stoichiometric compound $Mn_2SiO_{4+\delta}$ from Ref. [4] and for calculating the line for equilibrium with a CO/CO_2 mixture with 20 vol% CO data for the equilibrium between CO_2, CO and O_2 from Ref. [20] were used. In the temperature range considered in Figure 4.3, when maintaining a constant oxygen content in $Mn_2SiO_{4+\delta}$ during cooling after solidification in a CO/CO_2 gas atmosphere with 20 vol% CO, the local oxygen activity in the solid phase increases as the temperature decreases while the oxygen activity continuously decreases when Mn_2SiO_4 is in equilibrium with the surrounding gas atmosphere during cooling. In the first case, Mn_2SiO_4 may decompose upon cooling while this is not possible in the second case at elevated temperatures. If decomposition is possible, it depends on the height of kinetic barriers and on rates of transport of matter whether any significant decomposition occurs or not, and, if it should occur, which degree of undercooling is required for decomposition to occur. If a large degree of undercooling is required, it may very well be that decomposition does not occur until reaching a location far outside of the thermodynamic stability range of Mn_2SiO_4.

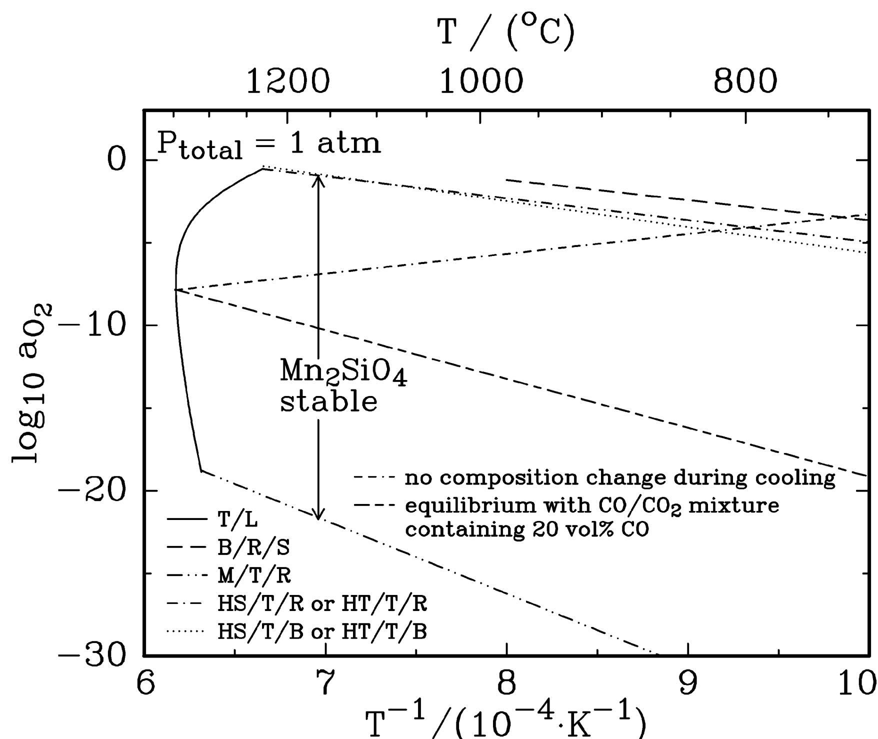

Figure 4.3: Oxygen activity vs. temperature diagram for Mn_2SiO_4 grown from the melt surrounded by a CO/CO_2 gas atmosphere containing 20 vol% CO. Lines representing data for the local oxygen activity in a grown single crystal versus temperature for limiting cases possible for compositional changes in Mn_2SiO_4 during cooling are shown in comparison with lines referring to different phase equilibria. The limiting cases considered with regard to compositional changes in Mn_2SiO_4 are i) that no compositional changes occur after solidification and ii) that compositional changes occur in such a way that the non-stoichiometric compound $Mn_2SiO_{4+\delta}$ has at every location at a given temperature the value of δ corresponding to that of $Mn_2SiO_{4+\delta}$ being in equilibrium with a CO/CO_2 mixture containing 20 vol% CO. The diagram suggests that in the case of no or limited local compositional changes in a grown Mn_2SiO_4 crystal during cooling some decomposition may occur.

In addition to Mn_2SiO_4 precipitates of the secondary phase intended to be present, $MnSiO_3$, may also decompose during cooling. $MnSiO_3$, may decompose into braunite nominally Mn_7SiO_{12}, and SiO_2, see Figure 4.2. The oxygen activity at which the decomposition of the $MnSiO_3$ secondary phase may occur at a given temperature can be determined based on the data used for generating the line representing the $MnSiO_3/Mn_7SiO_{12}/SiO_2$ equilibrium, see Figure 4.1. As it will be discussed later in more detail, indications for a decomposition of $MnSiO_3$ during cooling have been found for some of the crystals grown.

4.3. Experimental

The experiments performed for growing single crystals of Mn_2SiO_4 for defect-related studies include the synthesis of powders of Mn_2SiO_4 with an excess of silica via two different routes, a ceramic and a sol-gel route, the production of very dense polycrystalline rods of Mn_2SiO_4, suitable for being used as feed rods and for generating initial seed crystals, the production of a first set of small Mn_2SiO_4 single crystal seeds, and finally, involving the use of a passive afterheater, the growth of larger single crystals along the three principle orientations, as well as some characterization of the single crystals grown. The following sections provide details about the experimental work.

4.3.1. Powder Synthesis

For producing very pure single crystals of Mn_2SiO_4 being suitable for studying defect-related properties, it is critical to employ a powder synthesis method which

allows to keep the concentrations of contaminants introduced during powder synthesis at a minimum. Using a conventional ceramic route is most popular and convenient for synthesizing ceramic materials. However, when using this method, repeated grinding and long time high temperature treatments are usually necessary for a successful synthesis, often introducing significant concentrations of impurities into the synthesis product. A better approach, which allows the production of high purity powders of Mn_2SiO_4, is the use of a sol-gel powder synthesis route. However, this method has some disadvantages, including the high cost of very pure raw materials and long processing times.

In this study both a ceramic and a sol-gel route were employed for powder syntheses. First, a ceramic synthesis route was used to produce a sufficient amount of Mn_2SiO_4 powder for making polycrystalline feed rods for the generation of first single crystal seeds of Mn_2SiO_4. Later, a sol-gel synthesis route was used to synthesize very pure Mn_2SiO_4 powders for making polycrystalline feed rods for the growth of larger single crystals to be used for studying defect-related and orientation-dependent transport properties.

In the ceramic synthesis, the two starting materials, $MnCO_3$ (Sigma-Aldrich, 99.9 %) and SiO_2 (Strem, 98 %), were combined in a 2:1 molar ratio, mixed by ball milling using Teflon® balls in polyethylene bottles for 24 hours and then calcined at atmospheric pressure for 24 hours at 720 ℃ in CO/CO_2 gas mixtures with $\log a_{O_2} \approx -17$ and using quartz crucibles as containers. In order to avoid an explosion-like decomposition of $MnCO_3$ into MnO and CO_2, the heating rate of the

furnace used for calcining was kept at about 30 °C/h in the temperature range between 300 and 500 °C. After calcining for 24 hours and subsequent ball milling, a very careful manual grinding of the calcination product utilizing a porcelain mortar and a pestle was performed to decrease the particle size of the resulting powder. Obtaining sufficiently fine powder by grinding after calcination was necessary to allow for producing relatively dense rods by isostatic pressing and subsequent sintering for later use in single crystal growth experiments. As stated before, the type of atmosphere and the temperature used for calcination were selected based on existing knowledge on the thermodynamic stability range of Mn_2SiO_4. By using X-ray powder diffraction it was determined that two phases, MnO and SiO_2, were present in the powder obtained after calcination.

For the sol-gel synthesis, one starting material was manganese metal in the form of chips (Goodfellow, 99.98+ %). Nitric acid (Sigma-Aldrich, 99.999 %) was used to dissolve manganese chips in a glass flask emerged in a water bath over a period of 3 to 4 days. The manganese chips were first soaked in HPLC-grade water and slowly exposed to increasing concentrations of HNO_3 in order to avoid a fierce reaction at the beginning of the dissolution of the metal. The water bath containing the glass flask was then heated to 50 °C to increase the rate of the chemical reaction between the nitric acid and the manganese chips. After the manganese metal was fully dissolved, a suitable amount of tetraethyl orthosilicate (Sigma-Aldrich, 99.999 %), which allows for the formation of Mn_2SiO_4 with a 0.5 mol% excess of SiO_2, was added to the manganese nitrate solution. An appropriate amount of ethanol (Sigma-Aldrich, 99.5+ %) was added into the

solution together with the tetraethyl orthosilicate in order to avoid a too rapid gelation. The solution was initially stirred using a magnetic stirrer to completely mix the solvents. A slow hydrolysis leading to gelation occurred while the solution was kept thereafter without stirring at 50 °C for about 6 hours to evaporate water and alcohol. After that, an aqueous ammonium hydroxide solution containing 28 wt% NH_3 (Sigma-Aldrich, ≥ 99.99 %, i.e., containing less than 100 weight ppm metal impurities) was added before complete gelation to adjust the pH of the solution to about 7. The addition of ammonium hydroxide increased the viscosity of the solution. After the addition of ammonium hydroxide, liquid nitrogen was used to fully freeze the flask containing the sample before freeze-drying in order to prevent rapid foaming at the initial stage of freeze-drying. The frozen product was then freeze-dried under vacuum using a freeze-drier (Labconco Freeze-zone 7750020). During freeze-drying, the temperature of the frozen gel increased and the gel started to melt. The solvents in the sample including ethanol and water containing ammonium hydroxide were gradually removed from the sample. Generally, it took 4 to 5 days to complete the freeze-drying process. A quartz rod was used to lightly break down the crumbles obtained after freeze-drying. These dried powders were then heated to 500 °C at a rate of 10 °C/h to avoid any rapid, explosion-like decomposition in the temperature range between 100 and 200 °C and held at the latter temperature for 10 hours in air at atmospheric pressure to decompose organic and nitrate residues. No crystalline phases were identified by X-ray powder diffraction in all sol-gel route-derived powders. Since the calcination described before was not performed in an atmosphere within the thermodynamic stability

range of manganese orthosilicate, it was necessary to carry out a second calcination at higher temperature within the stability range of Mn_2SiO_4. This second calcination was done in CO/CO_2 mixtures with log $a_{O_2} = -17$ at atmospheric pressure at 720 °C for 24 hours using quartz crucibles as containers. The second calcination condition used for sol-gel route-derived powders was identical to that used for ceramic route-derived powders. The sol-gel route-derived powders obtained after the second calcination step were examined by X-ray powder diffraction. The phases being present were MnO and SiO_2, i.e., not yet the desired phase Mn_2SiO_4. The latter phase was obtained later during the feed rod preparation.

4.3.2. Feed Rod Preparation

Very carefully ground powders obtained from the ceramic synthesis and fine grained powers resulting from the sol-gel synthesis were used to produce dense, polycrystalline rods of Mn_2SiO_4 for single crystal growth. When preparing feed rods from sol-gel route-derived powders special efforts, including wearing gloves and using dedicated latex tubing, were made to avoid the introduction of impurities.

In both cases powders derived by using the syntheses routes described before were filled into latex tubes (North America Latex; tubes 12 cm in length and 12 mm in diameter with a wall thickness of 0.1 mm). A latex tube clamped at one end containing powder was isostatically pressed for one hour using glycerine as fluid medium at a pressure of approximately 1.8×10^8 Pa. After that the pressed green body having a cylindrical shape was carefully removed from the latex tube. Green

bodies were sintered in a quartz crucible in a vertical furnace at 1220 °C in a reducing atmosphere at atmospheric pressure with log a_{O_2} = −7 which was obtained by flowing a CO/CO_2 gas mixture through the furnace used for sintering. The sintering times were 4 days for rods made from powder prepared by the ceramic synthesis and 2 days for rods prepared from powder produced via the sol-gel route. After sintering, XRD powder diffraction was used to identify the phases being present. The only phase identified within the resolution limit of this technique (1 to 2 %) was Mn_2SiO_4. As expected, the silica-rich precipitates intended to be present within the polycrystalline rods derived from sol-gel route-derived powders could not be detected by XRD since the amount of traces of silica-rich precipitates was below the detection limit of this technique. The resulting sintered rods were typically 6 to 7 mm in diameter and 40 to 70 mm in length. The densities of the sintered rods varied between 80 and 90 % of the theoretical density of Mn_2SiO_4.

4.3.3. Seed Crystal Preparation

The dense polycrystalline manganese silicate rods prepared as described above were used as starting materials for producing single crystals of Mn_2SiO_4. A single ellipsoid image furnace (NEC model SC-N35HS/50XS) was used for the producing first Mn_2SiO_4 seed crystals and for the following single crystal growth by using the floating zone method. The infrared radiation generated by a 3.5 kW halogen lamp located at one focal point of a gold-coated ellipsoidal mirror was focused by this mirror at the second focal point of the mirror. A tube of fused silica surrounding the crystal growth assembly allowed the use of controlled

atmospheres and prevented the deposition of evaporated sample material on the mirror.

For the first seed crystal preparation polycrystalline rods made from ceramic route- derived powder were used both as feed rod and seed. During the floating zone crystal growth, a polycrystalline feed rod of Mn_2SiO_4 attached to the upper shaft of the instrument was slowly moved down towards the hot zone. The tip of the feed rod partially melted and formed a droplet at its bottom as it moved close to the hot zone. Meanwhile a second polycrystalline Mn_2SiO_4 rod used as an initial seed and being mounted on an alumina sample holder on the lower shaft of the instrument was slowly moved up towards the focal point where a floating zone was intended to be formed. The top tip of the seed melted and formed a liquid cap on the solid seed below. Both shafts were rotated in opposite directions with speeds around 20-30 rpm/h and then slowly moved versus each other until the liquid ends became connected, leading to the presence of a floating zone. The melt in the floating zone was held together by surface tension against gravity. After forming a floating zone up to an hour of time was allowed for the this zone to stabilize. During this time the power of the heat-producing halogen lamp was fine-tuned to improve the stability of the floating zone. Crystal growth of Mn_2SiO_4 was performed in a reducing atmosphere based the melting and thermodynamic stability range of Mn_2SiO_4 as shown in Figure 4.1. The growth was attempted at different oxygen activities ($-3.7 > \log a_{O_2} > -10$) at atmospheric pressure using nitrogen, argon or CO/CO_2 gas mixtures in different experiments to identify suitable growth condititons. Finally, most of the crystal growth was performed in a CO/CO_2 gas

atmosphere containing 20 vol% CO. When gas mixtures with large CO/CO_2 ratios (CO/CO_2 volume ratio $\geq$ 1/9) were used, the gas mixtures were diluted with N_2 at a CO/CO_2:N_2 ratio of 1:9 to prevent carbon deposition.

After a stable floating zone was obtained, both the upper shaft holding the feed rod and the lower shaft holding the seed were simultaneously moved downwards with a maximum speed of 1 mm/h. The melt at the melt/seed interface then started to solidify and the solid at the melt/feed rod began to melt. As a result, the floating zone was moved upwards relative to the initial positions of the colder ends of the feed rod and the seed until most of the feed rod was used up. The dimensions of the floating zone were controlled by adjusting the power applied to the halogen lamp as well as the relative vertical speeds with which the feed rod and the seed were moved. Initially the bottom rod was lowered faster then the top rod so that the diameter of newly grown was reduced from about 6 to about 3 mm. This necking process helped to reduce the number of grains being present in the newly generated solid. After a few hours of growth, the diameter of the newly grown Mn_2SiO_4 was increased back to about 6 mm and kept at 6 mm for a few hours of further growth. In order to end the crystal growth, the vertical movements of both the feed rod and the seed were stopped while the counter rotation of both rods continued. A gradual decrease in the lamp power reduced the size of the floating zone and eventually the feed and seed rods became disconnected from each other. The entire process described above was repeated in many individual subsequent growth experiments over a period of about one month until a first single crystal of Mn_2SiO_4 was obtained. Laue back reflection was used to confirm

that a single crystal had been obtained and to determine its orientation. The first single crystal obtained was oriented by using the Laue back reflection technique to the [100] crystallographic orientation and then sectioned by using a wire saw along the [100] orientation for seeds for subsequent single crystal growth along the same orientation.

When attempting to grow larger single crystals of Mn_2SiO_4 along the [100] orientation intended to be used for preparing seed crystals from them for crystal growth along other orientations, severe cracking problems were encountered. As it will be discussed later more in detail, these problems are believed to be related to an inefficient absorption of radiation coming from the halogen lamp used in the image furnace for heating by solid Mn_2SiO_4. Such an inefficient absorption of radiation may lead during crystal growth by the floating zone technique to the presence of very large vertical and radial temperature gradients in freshly solidified single crystal material and often causes extensive cracking within crystals during floating zone growth. In order to overcome the observed cracking, a passive afterheater was designed and built to decrease the existing temperature gradients. The use of such an afterheater has allowed in the past in some cases to solve cracking problems occurring during crystal growth. As pointed out by Kitamura et al. [21], the use of an afterheater is critical for enabling the growth of transparent oxides by the floating zone technique using infrared radiation as the heating source. When growing such oxides, the temperature at the center of a growing crystal is higher than at its surface if the solid is less efficient in absorbing the infrared radiation than the melt is. In this case the melt/solid interface where the

newly grown crystal first forms adopts a concave shape towards the melt. Such a concave interface towards the melt increases the concentrations of inclusions, dislocations and bubbles formed along the center core of the newly grown crystals. The presence of these defects, in combination with residual stresses present in a crystal subjected to temperature gradients during cooling, often leads to intense cracking within grown crystals. The use of a passive afterheater can prevent the presence of a concave sold/melt interface and allow to have a convex sold/melt interface towards the melt during crystal growth. In this case, dislocations and other defects are swept away from the center of the crystal and tend to get eliminated during crystal growth.

The single ellipsoid image furnace used in this study has a relatively short hot zone (about 1 cm vertically) and steep vertical temperature gradients (around 250 to 350 °C/cm [22]). Steep temperature gradients within a cooling crystal can lead to highly stressed or even cracked crystals, as initially observed in this study for the float-zone crystal growth of Mn_2SiO_4. The use of an afterheater can effectively reduce steep temperature gradients below the hot zone of the image furnace to reduce mechanical stresses in crystals during growth. Also for this reason the use of an afterheater allows sometimes to produce higher quality single crystals during floating zone crystal growth compared to crystals obtained by growing without using an afterheater.

A cross-section of the passive afterheater used in this work for the growth of crack-free Mn_2SiO_4 single crystals is shown in Figure 4.4. As it can be seen in this

figure, a thin PtRh30 foil, which has a high reflectivity, was placed inside of an alumina tube, which is the top part of the passive afterheater, to reflect most of the infrared radiation coming from the focal point of the ellipsoid image furnace where the floating zone is located towards the growing crystal. The inner diameter of the PtRh30 foil folded in the shape of a tube was designed to be only 3 to 4 mm wider than the diameter of the grown crystal so that the afterheater can effectively reduce the temperature gradients around the focal point of the image furnace.The

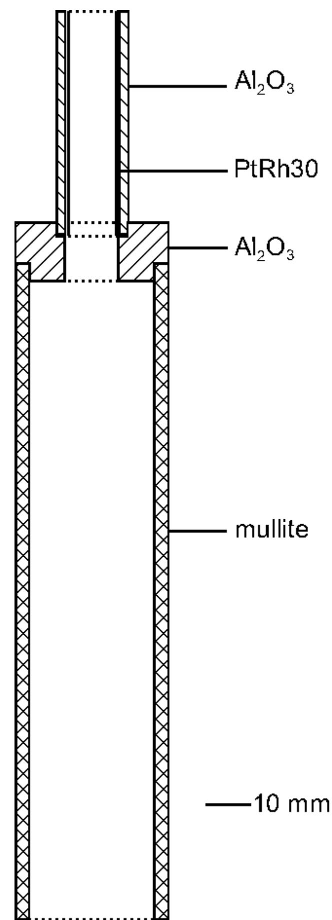

Figure 4.4: Schematic drawing of a newly designed and built passive afterheater to solve cracking problems which occurred during the growth of manganese orthosilicate single crystals.

middle part of the afterheater is an adapter made of alumina to connect the top alumina piece to the bottom piece made of mullite. The height of the afterheater was selected in such a way that its top surface is less than 1 mm below the lower solid/melt interface of the molten zone to control the interface shape. After also improving the geometry of the holders used for accommodating seed and feed materials used for single crystal growth in conjunction with the use of the afterheater described above, it became finally possible to grow large size crack-free single crystals of Mn_2SiO_4, see Figure 4.5a. An image of a severely cracked crystal grown without the use of an afterheater is shown in Figure 4.5b for comparison.

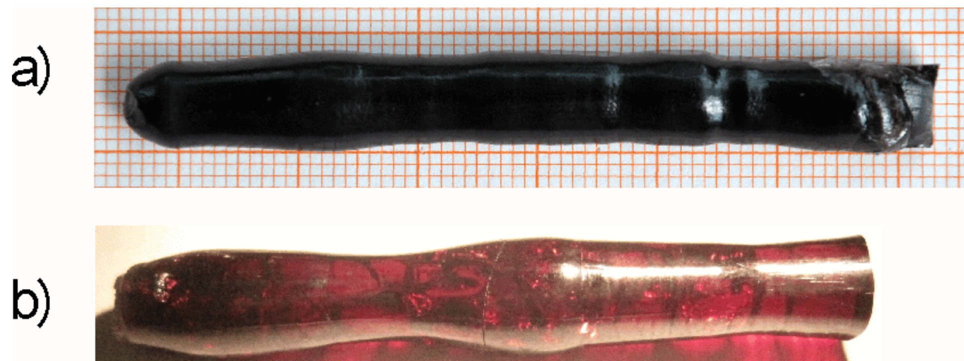

Figure 4.5: Photographs showing single crystals of Mn_2SiO_4 grown along the [100] orientation: a) image of a crack-free crystal grown using the passive afterheater described in Figure 4.4, and, for comparison, b) a photograph of a severely cracked single crystal of Mn_2SiO_4 grown without using an afterheater.

After solving the cracking problem by using a passive afterheater, one of the [100] seed crystals discussed before was used to grow a large single crystal along the [100] orientation with a diameter about 6 mm. Single crystals with a larger diameter proved to be are much more difficult to grow and usually contained cracks. The single crystal denoted above and grown along the [100] orientation was properly oriented by the Laue back reflection technique and cut into small seeds for growth along the [010] orientation. Additional seed crystals oriented along the [010] direction were grown using the first [010] seed crystal cut. A similar procedure was used to obtain a sufficient number of seed crystals for growth along the [001] orientation.

4.3.4. Crystal Growth

After producing a sufficient number of single crystal seeds suitable for crystal growth along the three principle orientations, large single crystals with very low impurity concentrations were grown using similar experimental procedures as employed for the production of the first seed crystals, except that now single crystal seeds and high purity feed rods were used. The growth conditions including the speeds for vertically moving the feed rod and the seed crystal, the counter-rotation speeds, the gas atmosphere and the passive after-heater employed when producing single crystal seeds were also used for growing large single crystals of Mn_2SiO_4. To obtain crystals with low concentration of impurities polycrystalline feed rods made from powders synthesized by a sol-gel route were used and all handling of seed crystals and feed rods was done very carefully to avoid

contamination, i.e., gloves were worn and carefully cleaned sample holders were used. In order to successfully grow larger Mn_2SiO_4 single crystals, it was essential to very carefully align the feed rod, the seed crystal and the passive afterheater relative to the shafts used to rotate them within the image furnace during crystal growth. This was especially important when a needle-like crystal was employed as the seed and the afterheater was present which could have interfered with the movement of the newly grown crystal if there any significant misalignments would have existed. Proper vertical alignment was also required when preparing for single crystal growth, i.e., before heating up the image furnace one needed to move the bottom of the feed rod and the top end of the seed crystal close to the focal point where the floating zone was later formed upon heating. This alignment helped to avoid large temperature gradients by fast vertical movements for joining the seed crystal and the feed rod when forming a floating zone. During the crystal growth, the rate for moving the seed crystal was about 1 mm/h. The rate of moving the feed rod was chosen so that the diameter of the grown crystal was kept roughly constant. Very careful control and fine adjustment of the halogen lamp power and a stable gas flow were necessary to avoid failure of crystal growth. As a final result, crack-free single crystals along the three principle orientations were successfully grown. The typical dimensions of the single crystals grown were 5 to 6 mm in diameter and 20 to 40 mm in length.

4.3.5. Characterization

The grown single crystals were oriented by using the Laue back reflection technique. The same technique was used to identify the orientation of facets that appeared on some of the crystals grown along the [100] orientation. A real-time back reflection Laue camera system (model MWL 110, Multiwire Laboratories, Ltd., Ithaca, NY, U.S.A.) was used to obtain Laue back reflection patterns. These patterns were analyzed by employing the software (NorthStar, Version 5.10) provided with the instrument to identify the direction along which a single crystal was grown.

A good measure for the single crystal quality is the dislocation density. To determine such densities, approximately 3 to 4 mm thick disks of single crystals of Mn_2SiO_4 grown along the three principle orientations were cut perpendicular to their growth directions. These disks were mounted in epoxy and carefully polished first using a series of SiC grinding papers and then fine-polished using alumina pastes. Optical microscopy was used to observe the surfaces of samples as the polishing progressed. It was observed that secondary precipitates started to become visible when the samples became sufficiently fine-polished. After the polished surfaces reached a mirror-like finish, chemical etching was performed at room temperature with aqueous solutions of HCl. A solution containing about 3 wt% ($\approx$ 5.25 mol%) HCl was used as the etchant for disks cut perpendicular to the [100] and [010] directions. For etching surfaces aligned perpendicular to the [001] orientation a solution containing 0.5 wt% ($\approx$ 0.875 mol%) HCl was used. For

the [100] orientation the etching time was 2.5 hours while it was 20 minutes for the [010] orientation and 12 minutes for the [001] orientation. Etch pits generated at dislocations intercepting the polished surface were observed by optical microscopy. Images of etch pit-containing areas were taken and values for the number of dislocations per unit area were determined by manually analyzing images, i.e., by counting the etch pits being present in a selected area.

Scanning electron microscopy was employed to confirm the presence of secondary phase precipitates of $MnSiO_3$ within the matrix of Mn_2SiO_4 single crystals grown from starting materials intentionally containing a small excess of silica. To prepare a cross-section of a sample for back-scattered electron imaging, a disk of a grown crystal was obtained by cutting and then polished by using a series of SiC grinding papers until a mirror-like surface was obtained. The instrument used for obtaining SEM images was a an electron microprobe with SEM imaging capabilities (JEOL 8900 microprobe, JEOL Ltd., Peabody, MA).

In order to determine lattice parameters for a grown single crystal of Mn_2SiO_4, the X-ray powder diffraction technique was used. The instrument employed was a theta-theta X-ray diffractometer (Scintag, model PAD-X) in conjunction with appropriate software (Jade, Version 7) from Materials Data, Inc., (MDI). To obtain powders appropriate for lattice parameter determination, a piece of a grown Mn_2SiO_4 single crystal was crushed by using a so-called diamond mortar with pestle (both made of hardened alloy tool steel) and subsequently ground to produce a fine powder using a porcelain mortar and pestle. Then, to provide a

standard for the lattice parameter determination, an appropriate amount of silicon powder was added and carefully mixed with the Mn_2SiO_4 powder. XRD-scans covered the range between 20° and 55° and were conducted at a rate of 0.1° per minute. The XRD spectrum obtained was calibrated relative to the silicon standard peak at 28.4422°. The software Jade (Version 7) was used for analyzing the diffraction pattern by performing a least squares fit of diffraction intensities related to the orthorhombic crystal structure of Mn_2SiO_4 to experimentally obtained spectra.

Inductively coupled plasma atomic emission spectroscopy (ICP-AES) was used to determine the manganese-to-silicon ratio and the concentrations of a variety of impurities being present. The instrument used for this analysis was an ICP-AES system Model ICAP61E (Thermo Electron, Waltham, MA). A step-by-step ICP analysis was performed to determine the impurity levels being present and also the manganese-to-silicon ratio after each important step involved in synthesizing single crystals of Mn_2SiO_4, starting with the sol-gel synthesis described before. The samples analyzed were manganese metal dissolved in aqueous HNO_3 (Sample A), the solution from the previous step with added TEOS and ethanol (Sample B), a sintered polycrystalline rod of Mn_2SiO_4 (Sample C) and a grown single crystal (Sample D).

As reported in Ref. [13], in ICP analyses of Co_2SiO_4, when an appreciable amount of HF was used to dissolve silicate samples, residual HF present in solutions to be analyzed for the concentration of silicon reacted with a glass

nebulizer used in the ICP analysis instrument. Due to this reaction between HF and the glass nebulizer, additional silicon was introduced into solutions to be analyzed by dissolving some glass material, causing huge errors in the concentrations to be determined. To prevent such errors, the amount of HF used to dissolve silicate crystals needs to be kept as small as possible. For Co_2SiO_4 it was verified that the use of only a few droplets for dissolving Co_2SiO_4 and employing diluted solutions for ICP analyses did allow to determine reliable values for concentrations of silicon. Therefore, this approach was adopted for preparing diluted solutions of Mn_2SiO_4 for ICP-AES analyses. In order to prepare such a solution, a concentrated aqueous solution of HCl was used to dissolve small, cube-like pieces obtained from a grown crystal of Mn_2SiO_4, each with a volume of about 1 mm^3, at room temperature in a Teflon® beaker. To accelerate the dissolution process the solution was heated about 3 times, each time for about 10 hours, to 50 °C. After about one week, about three times a small droplet of HF was added into the solution until the crystal pieces were fully dissolved after about another one to two weeks. Finally, the obtained solution was diluted to concentrations of Mn and Si of the order of 10 weight ppm. This allowed to perform reliable ICP analyses.

As mentioned in the background section, the high purity single crystals of Mn_2SiO_4 grown in this study were prepared for experimental measurements of defect-related transport properties of this material. Manganese tracer diffusion coefficients in Mn_2SiO_4 were measured by making use of the single crystals grown as described above. The radioactive isotope Mn-54 was used for these

measurements. Preliminary results have been obtained from measurements performed at 1200 °C and in the oxygen activity range between $\log_{10} a_{O_2} = -13.2$ and -0.8 by using single crystals of Mn_2SiO_4 grown along the three principle orientations. Oxygen activities were established by gas mixtures of air and N_2 or CO and CO_2 in proper ratios and pumping gas mixtures through the annealing furnace. Details of the experiments performed, their results and a discussion of the relations between point defects and the orientation dependence of transport properties of Mn_2SiO_4 will be reported elsewhere [23].

4.4. Results and Discussion

As stated earlier, the growth of larger high quality single crystals of Mn_2SiO_4 by using the floating zone method was not possible without using an afterheater, in contrast to earlier successful growth of Co_2SiO_4 [13] and of Fe_2SiO_4 [16,17] by the same method without using an afterheater. The reason for this is most likely the very different absorption of radiation by the different orthosilicates denoted above. Figure 4.6 shows values for absorption coefficients, α, reported in the literature for Co_2SiO_4 at 1000 °C [24], for Fe_2SiO_4 at 1130 °C [25] and such data for Mn_2SiO_4 at room temperature, the latter calculated from transmittances reported in Ref. [6], for wave lengths corresponding to those of the most significant radiation emitted by the type of tungsten halogen lamp used in this work.

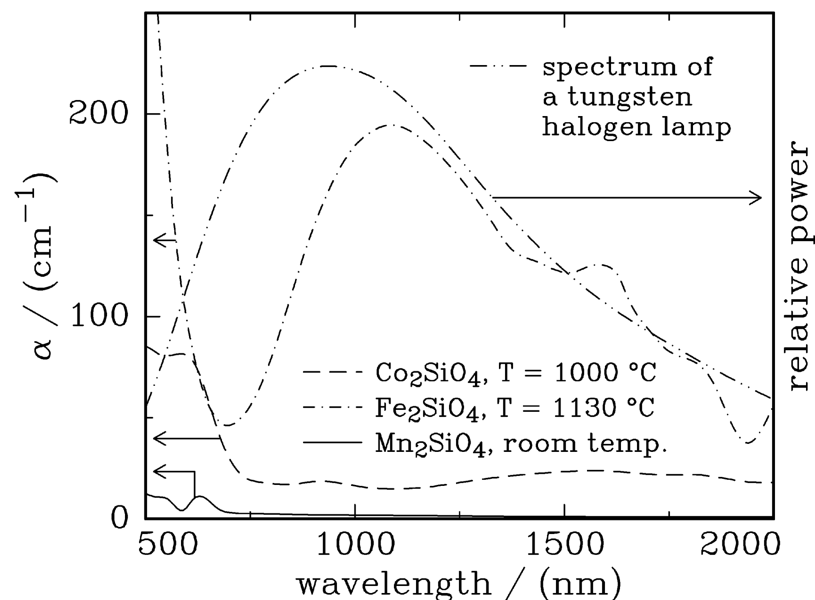

Figure 4.6: Absorption coefficients, α, for the transition metal-containing orthosilicates Co_2SiO_4, Fe_2SiO_4 and Mn_2SiO_4 as a function of the wavelength in comparison with a spectrum typical for the type of tungsten halogen lamp used in this study for heating during crystal growth. The data for Co_2SiO_4 are from Ref. [24] and those for Fe_2SiO_4 from Ref. [25]. The data for α for Mn_2SiO_4 have been derived from transmittance data reported in Ref. [6]. single crystal of Mn_2SiO_4 grown without using an afterheater.

The absorption coefficient, α, is related to the transmittance, Tr, given by the ratio between the intensities of the transmitted, I, and the incident radiation, I_0, as follows

$$\alpha = -\frac{1}{d} \cdot \log_{10} Tr = -\frac{1}{d} \cdot \log_{10} \frac{I}{I_0} \tag{4.1}$$

In Equation (4.1) d is the thickness of the sample for which α is determined by measuring Tr or I and I_0, respectively. Although absorbances increase somewhat,

but not dramatically, with increasing temperature, see, e.g., Ref. [24], the data shown in Figure 4.6 indicate that the absorption of radiation by solid Mn_2SiO_4 during growth must be much smaller than that by solid Co_2SiO_4 and Fe_2SiO_4, i.e., solid Mn_2SiO_4 is relatively transparent for the radiation emitted by the halogen lamp used. As pointed out by Kitamura et al. [21] such a transparency may cause that the temperature at the center of a growing crystal is higher than at its surface if the solid is less efficient in absorbing the infrared radiation than the melt is. This seems to be the case for Mn_2SiO_4. If this is true, then the melt/solid interface, where the newly grown crystal first forms, adopts a concave shape towards the melt, leading to an increase of the concentrations of inclusions, dislocations and bubbles formed along the center core of a newly grown crystal and often to intense cracking. As stated before, the use of a passive afterheater allowed to overcome the initially observed cracking problems and finally allowed the growth of larger, crack-free single crystals of Mn_2SiO_4.

High quality single crystals were successfully grown along the three principle orientations [100], [010] and [001] by using the floating-zone technique. Figure 4.5 shows images of two single crystals of Mn_2SiO_4 grown in this study. Figure 4.5a shows a crack-free crystal grown along the [100] orientation with the use of the afterheater described in Figure 4.4. Figure 4.5b shows for comparison a single crystal of Mn_2SiO_4 crystal grown without the use of an afterheater. As one can see from Figure 4.5b, the latter crystal is of low quality and contains many cracks. The crack-free crystals grown in this study were black in color under normal light and optically transparent under intense light. The grown crystals were 5 to 7 mm in

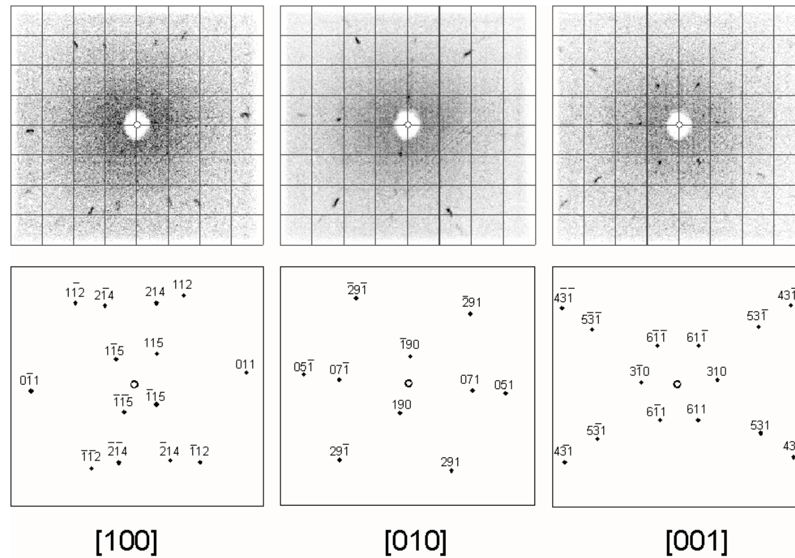

Figure 4.7: Laue back reflection patterns for single crystals of Mn_2SiO_4 grown along different principle orientations. The top row shows experimentally obtained patterns and the bottom row simulated ones.

diameter and 20 to 40 mm in length. The crystals obtained were fine-oriented using the Laue back reflection technique.

Figure 4.7 shows experimentally determined Laue diffraction patterns for Mn_2SiO_4 single crystals grown along the three different principle orientations in comparison with simulated patterns for these orientations. By comparing calculated and experimentally obtained patterns it was confirmed that single crystals of Mn_2SiO_4 were grown along the three principle orientations.

Electron microprobe analysis was used to determine the composition of the matrix and also of the secondary phase present in a grown crystal of Mn_2SiO_4. As discussed earlier in this article, Mn_2SiO_4 may under certain circumstances decompose upon cooling into hausmanite, Mn_3O_4, and braunite, nominally

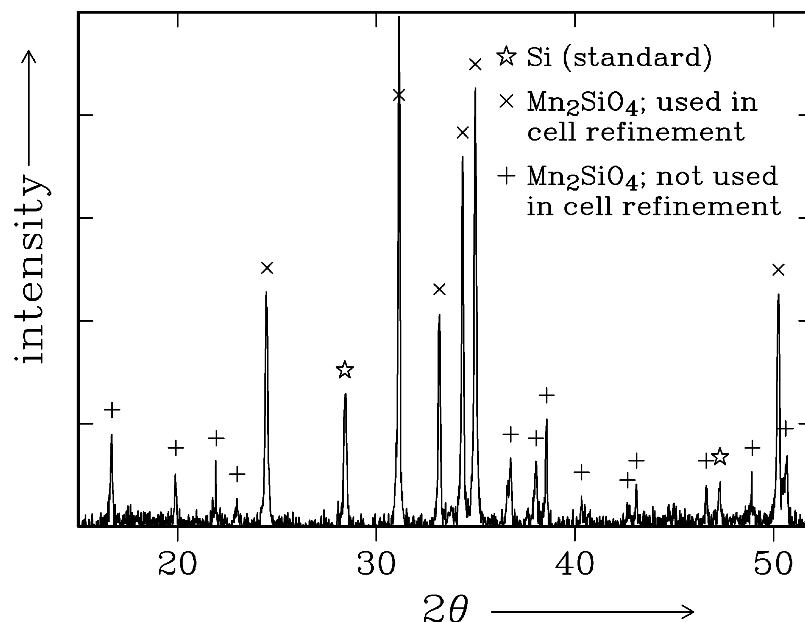

Figure 4.8: XRD spectrum of a powder obtained by crushing and grinding a grown Mn_2SiO_4 single crystal and mixing this powder with silicon powder to provide a standard for lattice parameter determination. This spectrum suggests also that there was no significant decomposition of Mn_2SiO_4 into braunite, nominally Mn_7SiO_{12}, upon cooling. The only phase identified was that of Mn_2SiO_4. The symbol ☆ denotes peaks related to the Si standard. The symbols × and + both refer to peaks related to Mn_2SiO_4 and indicate which peaks were used in the cell refinement for determining lattice parameters (×) and which ones not (+).

Mn_7SiO_{12}. X-ray powder diffraction patterns of powders obtained after crushing and grinding single crystals, e.g., that shown in Figure 4.8, did not show any hints for such a decomposition within the detection limit of XRD. In addition, an electron microprobe analysis confirmed that the composition of the matrix corresponds to the chemical formula Mn_2SiO_4. The secondary phase intended to be present in grown crystals was determined by electron microprobe analysis to be silica-rich as planned. Based on knowledge of the stability range of manganese orthosilicate, see, e.g., Figure 4.2, the silica-rich phase was identified to be rhodonite, $MnSiO_3$. As shown in Figure 4.9, in some cases, when the crystal growth was carried out for a very long period of time, a sufficient amount of time was available for an

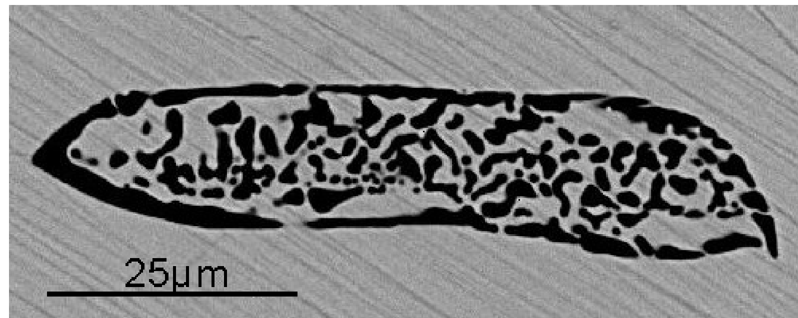

Figure 4.9: Back-scattered electron image of a part of a single crystal of Mn_2SiO_4 which shows a precipitate of $MnSiO_3$ that further decomposed upon cooling, most likely into Mn_2SiO_4 and silica (SiO_2).

inclusion consisting of the secondary phase $MnSiO_3$ to decompose at lower temperatures into two other, more stable phases. An electron microprobe analysis showed that the composition of material present in an area composed mostly of

dark colored regions inside of the inclusion visible in Figure 4.9 corresponds to a molar Mn:Si:O-ratio of about 1:2.5:6 while that for an area composed mostly of light colored regions inside of this inclusion is about 1.6:1:3.6. These results for composition ratios suggest that inclusions originally consisting of the secondary phase $MnSiO_3$ have decomposed during cooling into metastable Mn_2SiO_4 and stable SiO_2.

It remains unclear why braunite, nominally Mn_7SiO_{12}, was not observed in any of the crystals investigated for the type of phases being present. If cooling after solidification would have occurred following the path denoted in Figure 4.3 for cooling without any composition changes, one would expect based on thermodynamic grounds to find braunite being present in a cooled crystal. Not finding this phase at all could indicate that cooling followed a path similar to that one shown in Figure 4.3 for the case in which a crystal is during cooling always in thermodynamic equilibrium with the surrounding gas phase. Since completely or partially following such a path is very unlikely due to slow mass transport within a cooling crystal, which would be required for establishing thermodynamic equilibrium, it is most likely that the kinetic barriers to overcome for transforming Mn_2SiO_4 into braunite and hausmannite are too high to allow for any significant phase transformation during cooling.

The observation made for the transformation of precipitates of $MnSiO_3$ into Mn_2SiO_4 and SiO_2 is also unexpected from a solely thermodynamic point of view. Based on the phase diagram shown in Figure 4.2 and similar ones reported in

Ref. [19] one would expect that precipitates of $MnSiO_3$ decompose during cooling into braunite and SiO_2. Not observing any indications for the presence of braunite suggests that it is much easier to form metastable Mn_2SiO_4 and SiO_2 instead of the thermodynamically stable phases Mn_7SiO_{12} and SiO_2 due to kinetic reasons, i.e., the presence of high nucleation barriers and slow transport of matter, if the transformation involves nucleation and growth. It may be that the presence of the surrounding matrix of Mn_2SiO_4, which makes in unnecessary to form Mn_2SiO_4 nuclei for decomposing precipitates of $MnSiO_3$ into Mn_2SiO_4 and SiO_2 plays an important role for avoiding the formation of any braunite instead of Mn_2SiO_4 when inclusions of the secondary phase in$MnSiO_3$ decompose during cooling.

The cross-sections of single crystals of Mn_2SiO_4 grown along different orientations have different shapes. For crystals grown along the [100] direction, the cross-sections have an almost round shape. For crystals grown along the other two principle orientations, the cross-sections have oval shapes. Not all single crystals grown have well developed facets at the surface. One pair of small facets along the (010) plane was usually found for crystals grown along the [100] orientation. Similar observations for the shapes of cross-sections and the presence of facets have been reported earlier by Tsai et al. [17] and by Tang and Dieckmann [13] for single crystals of iron silicate, Fe_2SiO_4, and cobalt silicate, Co_2SiO_4, respectively, all grown along the orientation [100].

Table 4.1: Lattice parameters of Mn_2SiO_4 reported in the literature in comparison with values obtained in this study. Space group used: Pbnm. The standard deviations are given in parentheses in units of the last digit of the cited value.

a (Å)	b (Å)	c (Å)	Year	Reference
4.904(1)	10.601(3)	6.259(1)	1972	[26]
4.875(2)	10.521(3)	6.238(3)	1975	[5]
4.904	10.567	6.254	1976	[6]
4.9023(6)	10.5964(16)	6.2567(9)	1980	[1]
4.904(2)	10.603(3)	6.252(2)	2010	[4]
4.909(2)	10.609(2)	6.260(2)		this work

The values found by using X-ray powder diffraction for the lattice parameters of a single crystal of Mn_2SiO_4 grown in this study are a = 4.909(2) Å, b =10.609(2) Å and c = 6.260(2) Å. The standard deviations are given in parentheses in units of the last digit of the cited value. Figure 4.8 shows the XRD spectrum of a powder obtained by crushing and grinding a grown Mn_2SiO_4 single crystal and mixing it with Si powder used as a standard for a lattice parameter determination. The six main peaks for Mn_2SiO_4 denoted in Figure 4.8 by “x” were employed for determining the lattice parameter values denoted above. A summary of lattice parameter values reported in the literature [1,5,6,4,26] and the values denoted above is provided in Table 4.1. The lattice parameter values obtained in this study agree reasonablely well with the data from the literature listed in the table.

The dislocation densities found for single crystals grown along the three principle orientations were on the order of 10^5 to 10^6 per cm^2. As stated before, disks used for determining the dislocation densities were prepared by cutting perpendicular to the growth direction from single crystals grown along the three principle orientations. Before etching, the single crystal disks were first polished until scratch-free surfaces were obtained, the polished disks were then immersed in the HCl solution of appropriate concentrations at room temperature. For disks cut perpendicular to the [100] and [010] orientations, an aqueous solution containing about 3 wt% of HCl was appropriate to produce etch pits useful for determining dislocation density values, with etching times of 2.5 hours and 20 minutes, respectively. For crystals grown along the [001] orientation, using an aqueous solution containing about 0.5 wt% of HCl and an etching time of 12 minutes was successful. The need for significantly varying the conditions for successful etching surfaces with different surface orientations indicates that the chemical reactivity of Mn_2SiO_4 towards aqueous solutions of HCl significantly varies with the surface orientation. The etching occurs fastest on surfaces perpendicular to the orientation [001] and slowest on surfaces perpendicular to the orientation [100]. Figure 4.10 shows an image obtained by using an optical microscope of a sample obtained by cutting perpendicular to the [100] orientation, polishing and etching under appropriate conditions as described above to reveal the etch pits for dislocation density determination.

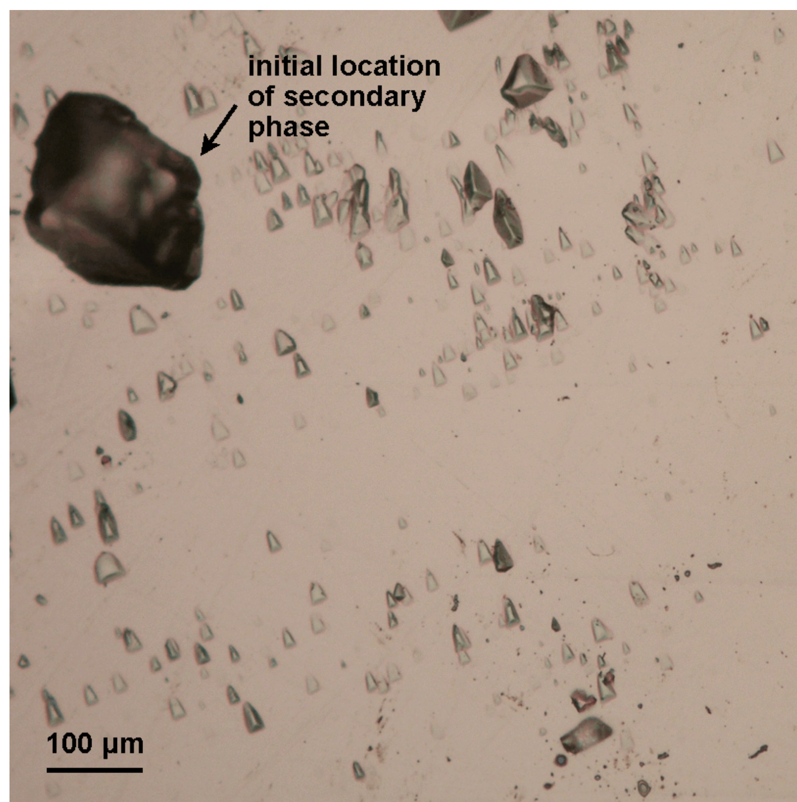

Figure 4.10 Image of the surface of a disk of Mn_2SiO_4 prepared by cutting perpendicular to the growth direction [100] after polishing and etching by using an aqueous solution of HCl. The image was obtained by using an optical microscope.

As stated in the experimental section of this article, solutions containing dissolved materials from different stages of the manganese silicate sample preparation, see above, were used for determining the concentrations of impurities being present. Table 4.2 contains a complete list of the impurities analyzed for. The types of the impurities analyzed for were selected either because they may lead to the presence of alio-valent ions in Mn_2SiO_4 which may influence the type and concentrations of the point defects present in a sample and/or due to having

a large potential to become incorporated during the synthesis. As indicated in Table 4.2, all metallic impurities analyzed for were present in concentrations below 10 mole ppm. These concentrations in comparison with the data for the point defect concentrations reported in Ref. [4] suggest that the impurity levels present in the samples cannot have a large influence on point defect-related properties of Mn_2SiO_4 studied separately. ICP-AES analyses were also used for determining values for the manganese-to-silicon ratio. The molar Mn:Si ratios determined for Samples B, C and D (denoted earlier) were 2:1.004, 2:1.007 and 2:1.008, i.e, all samples had small Si excesses, between 0.4 and 0.8 mol%, as intended.

Table 4.2: Impurities considered and concentrations determined for them by using the ICP-AES technique for analyzing reaction products at different stages of the sol-gel synthesis and of a grown single crystals of manganese silicate, Mn_2SiO_4. Here, ppm refers to the number of moles of an element analyzed for per mole of Mn_2SiO_4.

elements	concen-trations (ppm) in Sample A	concen-trations (ppm) in Sample B	concen-trations (ppm) in Sample C	concen-trations (ppm) in Sample D
Na	2	2	3	4
Al	4	5	7	7
Ca	1	2	2	2
Co	2	2	3	3
Mg	3	3	4	4
Ni	3	4	5	5
Zn	3	3	4	4
As, B, Ba, Cd, Cu, Fe, K, Mo, P, Pb, S, Se, Sr, Ti, V, Y	not detected	not detected	not detected	not detected

Preliminary results of manganese tracer diffusion experiments have been obtained for the diffusion of radioactive Mn-54 in Mn_2SiO_4 along the orientations [001], [010] and [100] at 1200 °C in the oxygen activity range between $\log_{10} a_{O_2}$ = −13.2 and −0.8 using the single crystals grown. These results indicate that the manganese diffusion occurs fastest in the [001] direction and slowest in the [100] direction. The diffusion in the [001] direction is about 6.5 times faster than that in the [100] direction and the diffusion in the [010] direction is by a factor of about 2.5 faster than that in the [100] direction. The manganese tracer diffusion coefficients have a minimum as a function of oxygen activity at 1200 °C. The observed oxygen activity dependence suggests that cation vacancies and interstitials both contribute to the manganese diffusion at 1200 °C. More details on the tracer diffusion measurements denoted above, the results obtained and a detailed discussion of them will be reported elsewhere [23].

4.5. Summary

Single crystals of manganese orthosilicate, Mn_2SiO_4, of good quality have been successfully grown along the three principle orientations, [100], [010] and [001], by using the floating zone method and a passive afterheater in a controlled, reducing atmosphere at atmospheric pressure. The typical dimensions of the grown crystals were 20 to 40 mm in length and 5 to 7 mm in diameter. Dislocation densities were found to be on the order of 10^5 to 10^6 cm^{-2}. Well developed facets were observed for some crystals grown along the [100] orientation. A small amount of intended inclusions of a secondary phase was observed by SEM and

the inclusions were confirmed to consist of silica-rich material as intended. The individual concentrations of all alio-valent impurities analyzed for were determined by using the ICP-AES technique and found to be smaller than 10 mole ppm. Single crystals grown in this study were used to perform some manganese tracer diffusion experiments at 1200 °C in the oxygen activity range between log a_{O_2} = −13.2 and −0.8. For the tracer diffusion coefficients, $D^*_{Mn[hkl]}$, for the diffusion of Mn-54 in Mn_2SiO_4 along different orientations the trend $D^*_{Mn[001]} > D^*_{Mn[010]} > D^*_{Mn[100]}$ was observed.

REFERENCES

[1] K. Fujino, S. Sasaki, Y. Takeuchi and R. Sadanaga, "X-ray Determination of Electron Distributions in Forsterite, Fayalite and Tephroite," Acta Cryst., **B37** (3) [1981] 531-518.

[2] G. Nover, "Electrical Properties of Crustal and Mantle Rocks - a Review of Laboratory Measurements and Their Explanation," Surv. Geophys., **26** (5) [2005] 593-651.

[3] S. Chakraborty, "Diffusion Coefficients in Olivine, Wadsleyite and Ringwoodite," in: "Diffusion in Minerals and Melts," Y. Zhang and D.J. Cherniak, Eds., Rev. Mineral. Geochem., **72** [2010] 603-639.

[4] J. Töpfer and R. Dieckmann, "Variation of the Oxygen Content and Point Defects in Tephroite, $Mn_2SiO_{4+\delta}$," Solid State Ionics, **181** (11-12) [2010] 479-488.

[5] C.B. Finch, G.W. Clark and O.C. Kopp, "Growth of Single-Crystal Mn_2SiO_4 (Tephroite) by Czochralski and Edge-Defined Film-FED (EFG) Techniques," J. Cryst. Growth, **29** (3) [1975] 269-272.

[6] H. Takei, "Czochralski Growth of Mn_2SiO_4 (Tephroite) Single Crystal and Its Properties," J. Cryst. Growth, **34** (1) [1976] 125-131.

[7] H. Okamoto, "The Ir-Mn (Iridium-Manganese) System," J. Phase Equilib., **17** (1) [1996] 60-62,

[8] H. Takei and S. Hosoya, “Growth and Properties of Olivine Single Crystals by the Floating-Zone Method,” in 'Advances in Earth and Planetary Sciences, Vol. 12: High-Pressure Research in Geophysics,' S. Akimoto and M.H. Manghnani, Eds., Center for Academic Publications, Tokyo, Japan, [1982] 537-547.

[9] H. Schmid, “Synthesis of Cobalt (II) Orthosilicate by Transport of SiO_2 via SiF_4 and Reaction of CoF_2 (Solid) with SiO_2 (Solid)” (in German), Z. Anorg. Allg. Chem., **327** (1-2) [1964] 110-112.

[10] S. Naka, H. Furuhashi and T. Noda, “Crystal Growth of Cobalt Olivine (Co_2SiO_4),” J. Ceram. Soc. Jpn., **76** (6) [1968] 179-183.

[11] B.M. Wanklyn, “Growth of Silicate and Germanate Crystals from PbO-SiO_2 (GeO_2) Fluxes,” J. Cryst. Growth, **37** (1) [1977] 51-56.

[12] S. Hosoya and H. Takei, “Growth of Co_2SiO_4 by the Floating-Zone Method,” J. Japan. Assoc. Cryst. Growth, **5** (3) [1978] 101.

[13] Q. Tang and R. Dieckmann, “Floating-Zone Growth and Characterization of Single Crystals of Cobalt Orthosilicate, Co_2SiO_4,” J. Cryst. Growth, **317** (1) [2011] 119-127.

[14] S. Hirano, Y. Iwai, S. Somiya and S. Saito, “Hydrothermal Growth of Fayalite Crystals,” in 'High-Pressure Science and Technology, Vol. I: Physical Properties and Material Synthesis,' K.D. Timmerhaus and M.S. Barber, Eds., Plenum, New York, NY, [1979] 970-976. (Proceedings 6th AIRAPT Conference, 1977, University of Colorado).

[15] C.B. Finch, G.W. Clark and O.C. Kopp, “Czochralski Growth of Single-Crystal Fayalite under Controlled Oxygen Fugacity Conditions,” Am. Mineral., **65** (3-4) [1980] 381-389.

[16] H. Takei, “Growth of Fayalite (Fe_2SiO_4) Single Crystal by the Floating-Zone Method,” J. Cryst. Growth, **43** (4) [1977] 463-468.

[17] T.L. Tsai, S.A. Markgraf and R. Dieckmann, “Floating-Zone Growth and Characterization of Fe_2SiO_4 Single Crystals,” J. Cryst. Growth, **169** (4) [1996] 759-763.

[18] M. Ozima, “Growth of Nickel Olivine Single Crystals by the Flux Method,” J. Cryst. Growth, **33** (1) [1976] 193-195.

[19] A. Muan, “Stability Relations among Some Manganese Minerals,” Am. Mineral., **44** (9-10) [1959] 946-960.

[20] H. Peters and H.H. Möbius, “Electrochemical Investigation of the Equilibria $CO + 1/2\ O_2 \rightleftarrows CO_2$ and $C + CO_2 \rightleftarrows 2\ CO$” (in German), Z. Physik. Chem., **209** (5/6) [1958] 298-309.

[21] K. Kitamura, S. Kimura and K. Watanabe, "Control of Interface Shape by Using Heat Reservoir in FZ Growth with Infared Radiation Convergence Type Heater," J. Cryst. Growth, **57** (3) [1982] 475-481.

[22] R. Subramanian, M. Higuchi and R. Dieckmann, "Growth of Nickel Aluminate Single Crystals by the Floating Zone Method," J. Cryst. Growth, **143** (3-4) [1994] 311-316.

[23] Q. Tang and R. Dieckmann, "Orientation and Oxygen Activity Dependence of the Diffusion of Manganese in Manganese Orthosilicate, Mn_2SiO_4," in preparation.

[24] J. Shi, S. Dlugocz , S. Ganschow, S.G. Ebbinghaus and K.D. Becker, "Optical In-situ Spectroscopy of High Temperature Properties," Z. Kristallogr., **226** (1) [2011] 89-92.

[25] K. Ullrich and K.D. Becker, "Kinetics and Diffusion of Defects in Fayalite, Fe_2SiO_4," Solid State Ionics, **141-142** [2001] 307-312.

[26] O. Nishizawa and Y. Matsui, "An Experimental Study on Partition of Magnesium and Manganese between Olivine and Orthopyroxene," Phys. Earth Planet. In., **6** (5) [1972] 377-384.

CHAPTER 5

ORIENTATION, OXYGEN ACTIVITY AND TEMPERATURE DEPENDENCIES OF THE DIFFUSION OF MANGANESE IN MANGANESE ORTHOSILICATE, Mn_2SiO_4 *

5.1. Abstract

The diffusion of manganese in manganese silicate, Mn_2SiO_4, in equilibrium with $MnSiO_3$ was experimentally studied as a function of crystallographic orientation, oxygen activity and temperature using high purity synthetic single crystals of manganese silicate. The oxygen activity dependence of the manganese cation diffusion in Mn_2SiO_4 along the three principle orientations at 1200 °C suggests that, at high oxygen activities, manganese cations move via different types of vacancies, most likely isolated manganese vacancies, $(V_{Mn^{2+}})''$, and possibly neutral associates, $\{2(Mn^{3+}_{Mn^{2+}})^{\bullet}\cdot(V_{Mn^{2+}})''\}^{\times}$, the latter being minority defects. At lower oxygen activities, the oxygen activity dependence of the manganese tracer diffusion becomes smaller than that at higher oxygen activities and eventually becomes negative at very low oxygen activities. The latter is attributed to an increased concentration of manganese interstitials at lower oxygen activities. The temperature dependence of the manganese tracer diffusion along the three principle orientations was experimentally investigated between 1150 and 1250 °C at $\log a_{O_2} = -2.7$ ($a_{O_2} = P_{O_2}/P^{\circ}_{O_2}$ with $P^{\circ}_{O_2} = 1$ atm) and between 1150 and 1300 °C

* Reprinted from a manuscript by Qi Tang and Rüdiger Dieckmann that was submitted to Solid State Ionics for publication.

at log a_{O_2} = −9.8. The results obtained suggest that the orientation dependence of the diffusion of manganese in Mn_2SiO_4 does not vary very significantly with temperature. When using the space group Pbnm to describe crystal orientations, the ratio found for the manganese tracer diffusion coefficients at log a_{O_2} = −2.7 is approximately $D^*_{Mn[001]} : D^*_{Mn[010]} : D^*_{Mn[100]} = 5.3 : 2.2 : 1$.

5.2. Background

Manganese orthosilicate, Mn_2SiO_4, also known by its mineral name Tephroite, is a ternary compound belonging to the olivine family. Most prominent oxide compounds with the olivine structure include silicates, germanates, and phosphates. The general chemical formula for orthosilicates with the olivine structure is Me_2SiO_4, where Me stands for one or a combination of several metallic components. The most commonly found metals of the type Me in olivine minerals are Mg and transition metals like Fe, Mn and Co. Due to the ability of transition metal ions to change their valence state, the oxygen content of transition metal-containing orthosilicates changes when the oxygen activity is varied. For denoting an excess or a lack of oxygen, one can use the parameter δ in the formula $Me_2SiO_{4+\delta}$. This article focuses on manganese orthosilicate, Mn_2SiO_4.

The crystal structure of olivines, including tephroite, is orthorhombic. The standard for denoting the crystal symmetry of olivines is using the space group Pnma [1]. However, most commonly, and also in this article, the space group Pbnm is employed for this purpose. The olivine structure is composed of an almost hexagonally close-packed array of oxygen ions, in which Me cations are located

in octahedral interstices of the oxygen sublattice, while Si cations are located in tetrahedral interstices of this sublattice. SiO_4^{4-} tetrahedra present in orthosilicates do not share any oxygen ions with each other. Two distinct octahedral sites exist for Me cations, M1 and M2 sites. All M1 sites are lined up in the [001] direction.

The non-cubic structure of compounds with the olivine structure causes an anisotropy of transport properties of olivines, e.g., of the diffusivity of Me-ions and of the electrical conductivity. Although transport of matter and charge in olivine-type orthosilicates has been the subject of numerous studies, most of them focusing on naturally occurring olivines, this subject is not yet well understood in detail. The types and concentrations of the point defects involved in transport of matter and/or charge are often only poorly or not at all known. The influence of the type of Me ions being present on the degree of the anisotropy of transport properties is not yet understood at all.

One major obstacle for reaching a more fundamental understanding of the point defect structure and defect-related properties of olivines is a lack of sufficiently large, high purity single crystals with unequivocally defined thermodynamic states. Many earlier investigations of defect-related properties, e.g., diffusion and electrical conductivity studies, were performed using either natural olivine samples or synthetic samples with relatively high concentrations of alio-valent impurities. The point defect structure in such olivines can be very significantly influenced or often completely controlled by the alio-valent impurities being present. Therefore, results obtained from studies of defect-related properties

using the type of samples discussed above can be very different from those which one would obtain when using impurity-free samples.

Only in sufficiently pure, large-grained or single crystalline transition metal-containing olivines is the transport of matter and charge at high temperatures governed by intrinsic point defects. Otherwise, extrinsic defects, e.g., impurities, and/or other structural defects like grain boundaries significantly influence or completely control transport of matter and charge. It is only possible to obtain insights into the anisotropy of defect-related transport properties when suitable single crystals are available. Systematic investigations of point defect-related properties like the variation of the oxygen content, the cation tracer diffusion and the electrical conduction in very pure, single crystalline samples are most suitable to improve the current limited understanding of point defects in transition metal-containing olivines and related properties.

Based on the Gibbs phase rule, two thermodynamic variables need to be fixed in order to unequivocally determine the thermodynamic state of ternary compounds at given values of the total pressure and the temperature. One of the thermodynamic variables usually chosen is the oxygen activity, a_{O_2} (= $P_{O_2}/P^{\circ}_{O_2}$ with $P^{\circ}_{O_2}$ = 1 atm), which is experimentally easy to control. Possible choices for the second thermodynamic variable to be fixed are, in the case of Mn_2SiO_4, the manganese-to-silicon ratio and the activity of a secondary phase (Mn-metal, Mn-oxides or $MnSiO_3$). As discussed in length in Ref. [2], sufficiently precise control of the Mn/Si-ratio cannot be achieved due to insufficient composition control during powder synthesis and single crystal growth. In experimental work, it is practically

impossible to reproducibly establish a sufficiently well-defined Mn/Si-ratio in any samples of Mn_2SiO_4. If, instead of fixing the Mn/Si-ratio, the equilibria between Mn_2SiO_4 and Mn-metal or Mn-oxides are selected to control the thermodynamic state of Mn_2SiO_4, complications arise due to the transformation of Mn to $Mn_{1-\Delta}O$ or $Mn_{3-\delta}O_4$ upon oxygen activity changes. In this study, a small amount of the silica-rich secondary phase $MnSiO_3$ was intentionally introduced into Mn_2SiO_4 single-crystalline samples to unequivocally define the thermodynamic state of Mn_2SiO_4 at given values of total pressure, temperature and oxygen activity.

In order to prepare samples fulfilling the needs for performing studies of point defect- related properties of Mn_2SiO_4, manganese silicate single crystals were grown in a controlled atmosphere at atmospheric pressure along the three principle orientations by using the floating-zone method [3]. A sol-gel synthesis route was used for preparing high purity feed rods for growing single crystals for manganese tracer diffusion studies. The grown single crystals were 20 - 40 mm in length and 5 - 7 mm in diameter. Impurity concentrations and the degree of a desired excess of silica were determined by using the ICP-AES technique. The presence of an intended silica-rich secondary phase was confirmed by electron microprobe analysis. For more details about the single crystal growth see Ref. [3].

Before discussing previous work on point defects and defect-related properties of manganese orthosilicate, the conditions at which Mn_2SiO_4 is thermodynamically stable in the temperature range of interest for this study, i.e., between 1150 and 1300 °C, are briefly reviewed. A more detailed summary on the thermodynamic stability range of Mn_2SiO_4 was published by Töpfer and Dieckmann [2]. The results

of this summary were used in Ref. [3] for determining suitable values of oxygen activity and temperature for sample synthesis and, in this study, for determining such parameters for tracer diffusion experiments. According to the thermodynamic stability range of Mn_2SiO_4 reviewed in Ref. [2], Mn_2SiO_4 in equilibrium with $MnSiO_3$, i.e., at an activity of $MnSiO_3$ equal to one, is stable at 1300, 1250, 1200 and 1150 ℃ in the oxygen activity ranges of $-19.0 \leq \log a_{O_2} \leq -2.6$, $-19.9 \leq \log a_{O_2} \leq -1.1$, $-20.7 \leq \log a_{O_2} \leq -0.7$, and $-21.9 \leq \log a_{O_2} \leq -1.0$, respectively.

The point defect structure and defect-related properties of olivine-type compounds, such as the electrical conductivity and tracer diffusion, have been the subject of many previous studies. Recent reviews on electrical conductivity and diffusion studies in olivine type orthosilicates, most of them being minerals, can be found in Refs. [4] and [5]. Only a few investigations on the point defect structure and defect-related properties of Mn_2SiO_4 have been reported in literature; these are briefly reviewed below. Throughout this paper the Kröger-Vink notation in its ionic version [6] is used for denoting point defects.

Bai et al. [7] have measured electrical conductivities, σ, for Mn_2SiO_4 in the temperature range of 850 to1200 ℃ and in an oxygen activity range of $-11 \leq \log a_{O_2} \leq -2$. The samples used were single crystals grown by the Czochralski method. Two different buffering conditions were considered, samples being present either in equilibrium with a manganese oxide or with rhodonite, $MnSiO_3$. Bai et al. [7] reported that the concentrations of alio-valent impurities in the manganese silicate single crystals used were 320 mole ppm for mono-valent impurities and 300 mole ppm for tri-valent impurities (mole ppm = 10^6 times the

number of moles of impurity ions per mole of Mn_2SiO_4). For high oxygen activities, Bai et al. [7] observed an oxygen activity dependence, d log σ / d log a_{O_2}, of about 1/6 while a slightly smaller dependence was found at lower oxygen activities. Based on the oxygen activity dependence of the electrical conductivity, they modeled the point defect structure of Mn_2SiO_4 by assuming that, at high oxygen activities, vacancies on manganese sites, $(V_{Mn^{2+}})''$, and Mn^{3+} ions on Mn sites, $(Mn^{3+}_{Mn^{2+}})^{\bullet}$, are majority defects and that, at low oxygen activities, Mn^{3+} ions on Mn sites, $(Mn^{3+}_{Mn^{2+}})^{\bullet}$, and electrons, e', both contribute to the electrical conduction. Values for electrical conductivities of Mn_2SiO_4 were measured along two crystallographic orientations, [100] and [010], and σ was reported to be 2.5 to 3.0 times larger for the electrical conduction along the [100] orientation than along the [010] orientation.

The electrical conductivity of Mn_2SiO_4 was also studied by Stüber and Laqua [8] by using impedance spectroscopy at several temperatures between 1101 and 1197 °C as a function of oxygen activity in the range of $-16 \leq \log a_{O_2} \leq -0.67$. The samples used for these studies were oligo-crystals grown from a melt and containing on average 5 to 7 smaller single crystals in a crystal volume of about 1 cm^3. Impurity concentrations were not reported. In Ref. [8] it is claimed that electrical conductivity data were obtained for three sample buffer situations, for Mn_2SiO_4 i) being in equilibrium with Mn-oxides, ii) being in equilibrium with $MnSiO_3$, and iii) for “stoichiometric” Mn_2SiO_4 with a Mn:Si-ratio equal to two. However, information given in Ref. [8] and, in more detail, in the doctoral thesis on which Ref. [8] is based [9], leads to doubts that the thermodynamic states of the

samples investigated were really those stated above. In Refs. [8] and [9] it is reported that cylindrical samples with a diameter of about 7 mm and lengths ranging between 4 and 7 mm were used in the conductivity measurements. During each of these measurements, a cylindrical sample was held between two platinum electrodes being pressed onto its flat ends. In all experiments, the formation of $MnSiO_3$ was observed near the electrodes, locally fixing the thermodynamic state to that of the Mn_2SiO_4/$MnSiO_3$ equilibrium at the temperature and oxygen activity established in the surrounding of the sample and not to that corresponding to a Mn:Si-ratio of 2 or to an equilibrium between Mn_2SiO_4 with a manganese oxide. For samples that had been used in electrical conductivity measurements and reportedly were in equilibrium with a manganese oxide, it was stated that traces of MnO were detected within the samples. This indicates that the thermodynamic state of such samples was not constant within the entire sample, i.e., that the samples were not homogeneous. Some of the information provided in Refs. [8] and [9] proves that the thermodynamic state of all samples reportedly having a Mn:Si-ratio of 2 or being in a buffered state corresponding to equilibria between Mn_2SiO_4 and Mn or a manganese oxide was non-uniform. Therefore, the conductivity data reported for such samples cannot be attributed to any well defined thermodynamic state of Mn_2SiO_4. Using these data for discussing the variation of defect-related properties as a function of thermodynamic variables at constant temperature and pressure is therefore questionable. The only set of samples for which a local variation of the thermodynamic state should not have existed are those reportedly being in equilibrium with $MnSiO_3$. However, as discussed further below, these data are also questionable. Nevertheless, based

on observed oxygen activity dependencies of the electrical conductivity Stüber and Laqua [8] proposed that at high oxygen activities, vacancies on manganese sites, $(V_{Mn^{2+}})''$, Mn^{3+} ions on Si sites, $(Mn^{3+}_{Si^{4+}})'$, and on Mn sites, $(Mn^{3+}_{Mn^{2+}})^{\bullet}$, are majority defects and that, at low oxygen activities, the influence of electrons is increased due to the transition from a component activity-dependent disorder to a thermal electronic disorder.

Results obtained from electrical conductivity measurements reportedly using $MnSiO_3$-buffered Mn_2SiO_4 at about 1200 °C performed by Bai et al. [7] and by Stüber and Laqua [8] are shown in Figure 5.1 for comparison. When comparing the latter data with those obtained for single crystals by Bai et al. [7] and

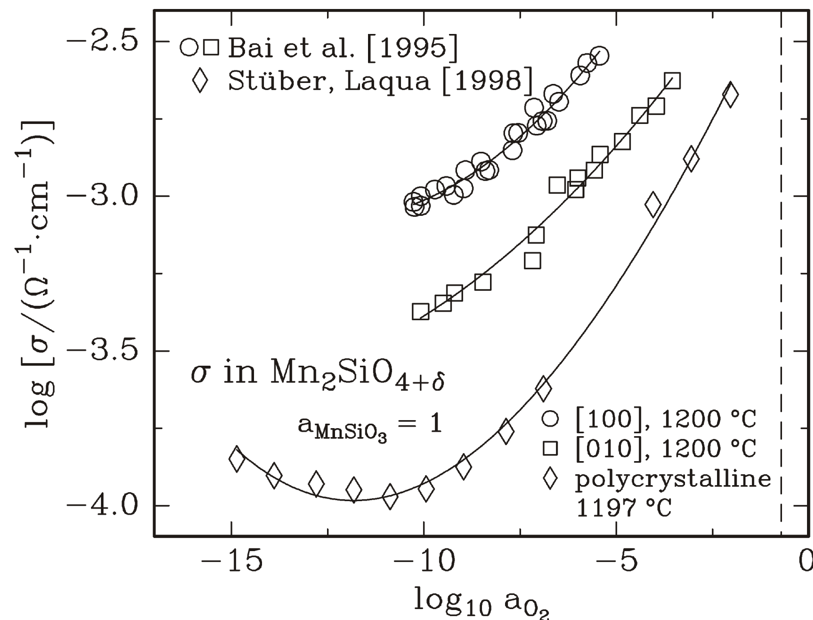

Figure 5.1: Data available from the literature [7,8] for the oxygen activity dependence of the electrical conductivity of Mn_2SiO_4 in equilibrium with $MnSiO_3$ at about 1200 °C.

additionally taking data for the anisotropy of the electrical conduction in Fe_2SiO4 [10], which has the same crystal structure as Mn_2SiO_4 has, into account, it seems that the values reported by Stüber and Laqua [8] for the electrical conductivity in polycrystalline Mn_2SiO_4 in equilibrium with $MnSiO_3$ are much too small, making them also questionable. This conclusion is based on the fact that the electrical conductivity in the iso-structural Fe_2SiO_4 is the highest for the [001] direction and the lowest for the [010] direction [10]. The same type of anisotropy has also been experimentally observed for the electrical conduction in natural San Carlos olivines, which are iron-magnesium silicates containing a significant amount of impurities, and also for nominally iron-free forsterite, Mg_2SiO_4 [11]. For the anisotropy of the electrical conductivity of Mn_2SiO_4, according to Bai et al. [7], $\sigma_{[100]} > \sigma_{[010]}$, i.e., the same trend is followed as observed for Fe_2SiO_4 and for San Carlos olivines. Most likely, the trend $\sigma_{[001]} > \sigma_{[100]} > \sigma_{[010]}$ holds also for Mn_2SiO_4. If this expectation is fulfilled, then one would expect the electrical conductivity of polycrystalline Mn_2SiO_4 to be some average of the electrical conductivities found for the different principle orientations, provided that the grain boundaries do not very significantly block the transport of electronic carriers. Since the electrical conductivity values reported by Stüber and Laqua [8] are much lower than expected, it is unclear what they really refer to or whether they are related to experimental errors. In view of this situation these data are not considered further in this article.

Tracer diffusion coefficients for the diffusion of Mn and of other divalent cations along the orientation [001] in Czochralski grown single crystals of Mn_2SiO_4 were

measured by Morioka [12] in the temperature range of 1000 to 1200 ℃ in flowing nitrogen gas with a non-specified oxygen activity. The single crystals used were reported to have a slight excess of manganese. An Arrhenius-type temperature dependence of the manganese tracer diffusion coefficient was observed for the temperature range of interest. Morioka [12] did not investigate how the cation tracer diffusion in Mn_2SiO_4 changes with oxygen activity.

The variation in the oxygen content in $Mn_2SiO_{4+\delta}$ in equilibrium with $MnSiO_3$ was thermogravimetrically measured by Töpfer and Dieckmann [2] between 1000 and 1200 ℃ at a total pressure of about 0.5 atm as a function of oxygen activity to obtain absolute values for δ. Results obtained from these measurements for the variation in the oxygen content of $Mn_2SiO_{4+\delta}$ at 1200℃ are plotted in Figure 5.2 as

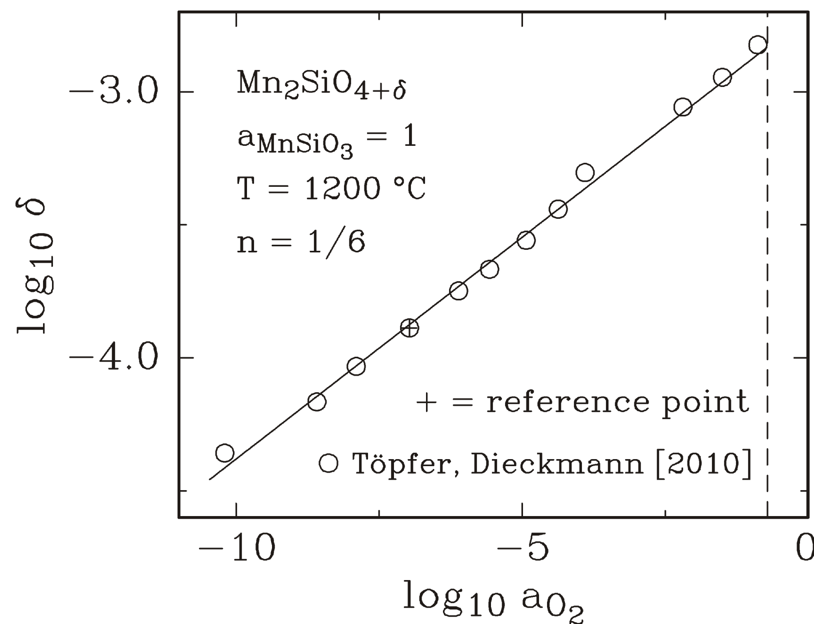

Figure 5.2: Data available from the literature [3] for the deviation from stoichiometry, δ, in $Mn_2SiO_{4+\delta}$ at $a_{MnSiO_3} = 1$ at 1200 ℃. The line summarizing the data from Ref. [3] corresponds to $\delta \propto a_{O_2}^{1/6}$.

a function of oxygen activity. As shown in Figure 5.2, at 1200 ℃ the value for δ varies from about 1.5×10^{-3} at $\log a_{O_2} = -0.88$ to below 10^{-4} at $\log a_{O_2} = -10$. The oxygen activity dependence of δ, $d \log \delta / d \log a_{O_2}$, was found to be close to 1/6 in the range of the measurements. Töpfer and Dieckmann [2] modeled the observed oxygen activity dependence of δ by assuming that vacancies on manganese sites, $(V_{Mn^{2+}})''$, Mn^{4+} ions on Si sites, $(Mn^{4+}_{Si^{4+}})^{\times}$, and Mn^{3+} on Mn sites, $(Mn^{3+}_{Mn^{2+}})^{\bullet}$ are majority defects. As reported in Ref. [2], the charge state +4 for Mn ions on Si-sites was selected based on results of density functional theory calculations performed by the Hennig-group at Cornell University.

Some results from earlier experiments attempting to determine variations of the oxygen content in manganese silicate are available from thesis work by Sandner [13,14]. A critical discussion of these data has been published in Ref. [2]. Inconsistencies between absolute values reported in Refs. [13] and [14] by a factor of two exist. In addition there are inconsistencies in the temperature dependencies of values reported in Ref. [14] for δ in Mn_2SiO_4 at different oxygen activites. It was pointed out in Ref. [2] that one possible source of errors in the data could be from the use of Pt-wire for holding samples during the measurements. Pt, when being in contact with Mn_2SiO_4 at high temperatures, dissolves Mn from this olivine, leading to a reduction of the content of Mn or even to the formation of some $MnSiO_3$. The degree of the dissolution of Mn into Pt increases with decreasing oxygen activity.

In this article, experimental data for the tracer diffusion of manganese in manganese orthosilicate as a function of oxygen activity, temperature and crystal orientations are reported. All data are for Mn_2SiO_4 being in equilibrium with $MnSiO_3$. Point defect models compatible with the experimental results are discussed.

5.3. Experimental

In this section, a brief summary of the floating zone growth of Mn_2SiO_4 single crystals as well as details related to the tracer diffusion work performed in this study are provided.

5.3.1. Single Crystal Growth

The Mn_2SiO_4 single crystals used in this study were grown in a reducing atmosphere at atmospheric pressure by the floating zone method utilizing a single ellipsoid image furnace. Details of the crystal growth and characterization of the single crystals grown are reported elsewhere [3]. A sol-gel synthesis route was employed to prepare Mn_2SiO_4 powder of high purity. This powder was used to produce dense, polycrystalline feed rods for single crystal growth. A passive afterheater was utilized during the crystal growth to increase the absorption of heat radiation by the growing crystal and, by doing this, avoid cracking of the single crystals. The grown crystals were typically 5 to 7 mm in diameter and 20 to 40 mm in length. The crystal growth directions were along the three principle orientations, [100], [010] and [001]. The Laue back reflection technique was used for determining the orientations of crystals and for orienting them. A grown

manganese silicate single crystal was determined to have 0.8 mol% silica excess. The expected presence of silica-rich precipitates was confirmed by electron microprobe analysis. Dislocation densities in grown manganese silicate single crystals were determined to be on the order of 10^5 to $10^6/cm^2$. As determined by the ICP-AES technique, all metallic impurities analyzed for were present at concentrations below 10 mole ppm. As reported in Ref. [3] for one of the Mn_2SiO_4 crystals grown, the following concentrations (in ppm, i.e., 10^{-6} moles per mole of Mn_2SiO_4) of the impurities analyzed for were determined: 4 for Na, 7 for Al, 2 for Ca, 3 for Co, 4 for Mg, 5 for Ni and 4 for Zn. As, B. Ma, Cd, Cu, Fe, K, Mo, Pb, S, Se, Sr, Ti, V and Y were not detected. In view of the magnitude of the degree of the deviation from stoichiometry, δ, in manganese silicate, $Mn_2SiO_{4+\delta}$, it is expected that the presence of the impurities denoted above does not have a large influence on the experimental results obtained in this study for the manganese tracer diffusion.

5.3.2. Manganese Tracer Diffusion Experiments

Using the single crystals grown as described above, manganese tracer diffusion experiments were conducted as a function of the crystallographic orientation, oxygen activity and temperature using the radioactive isotope Mn-54. The temperature range of the measurements was between 1150 and 1300 °C and the oxygen activity range was between $-13.3 \leq \log a_{O_2} \leq -0.86$. A similar approach as that used in a preceding investigation of the cobalt tracer diffusion in cobalt silicate [15] was adopted for this study. In this study, the radioactive tracer used was Mn-54. Mn-54 has a half life of 314 days and emits upon decay γ-rays with

an energy of 0.84 MeV [16]. The main procedures involved in the measurements of manganese tracer diffusion coefficients were sectioning of single crystals into disks, grinding single crystal disks plane-parallel, performing pre-annealing to establish equilibrium point defect concentrations, depositing of radioactive tracer, Mn-54, diffusion-annealing at the same temperature and oxygen activity used for pre-annealing, experimentally determining normalized residual radioactivity profiles, and finally analyzing them for determining values of manganese tracer diffusion coefficients. The pre-annealing time for samples with thicknesses between about 1 and 1.5 mm was approximately one day and the diffusion-annealing time, t, varied between 1 and 7 days, depending on the crystal orientation, oxygen activity and temperature. Residual radioactivities were determined by using a scintillation detector. For details about the performed residual radioactivity analysis, see Ref. [15].

For the diffusion of a tracer in a crystalline sample, the thin-film solution of Fick's second law denoted in Equation (5.1) applies.

$$c_{Mn}(\xi,t) = \frac{Q_{Mn}}{\sqrt{\pi \cdot D^*_{Mn} \cdot t}} \cdot \exp\left(- \frac{\xi^2}{4\, D^*_{Mn} \cdot t} \right) \tag{5.1}$$

In this equation, Q_{Mn} is the initial concentration of Mn-54 per unit area, D^*_{Mn} is the tracer diffusion coefficient of the diffusing species, Mn-54, and $c_{Mn}(\xi,t)$ is the concentration of Mn-54 at the distance ξ from the surface, where a thin film of Mn-54 was initially deposited, after diffusion-annealing for the time t.

In this study, the determination of values for tracer diffusion coefficients of manganese was based on experimentally measured residual radioactivity profiles. First, the initial radioactivity, A(x=0,t), was measured, and then layers of the sample were removed. Residual radioactivities of a given sample, A(x,t), were measured each time after removal of material with the thickness x, beginning at the side where the radioactive tracer was first applied. In addition, after each removal a value for the space coordinate was measured using a digital indicator. Based on the relatively high γ-energy involved in the decay of Mn-54 (0.84 MeV) and the lengths of the profiles considered in this study, the absorption of γ-rays within the manganese silicate samples investigated can be ignored when analyzing residual radioactivity profiles. If the absorption of γ-rays within a sample investigated can be ignored Equation (5.2) describes the normalized residual radioactivity, A(x,t)/A(x=0,t), as a function of diffusion annealing time, t, the manganese tracer diffusion coefficient, D^{*}_{Mn}, and the distance x from the original surface, where the tracer was originally applied. As indicated in the middle part of Equation (5.2), this equation can be obtained by integration departing from Equation (5.1).

$$\frac{A(x,t)}{A(x=0,t)} = \frac{\int_{x}^{\infty} c_{Mn}(\xi,t) \cdot d\xi}{\int_{0}^{\infty} c_{Mn}(\xi,t) \cdot d\xi} = 1 - \operatorname{erf}\left(\frac{x}{2\sqrt{D^{*}_{Mn} \cdot t}} \right) \tag{5.2}$$

For practically determining values of manganese tracer diffusion coefficients Equation (5.3) was used which contains the inverse function of the error function, erfi.

$$\mathrm{erfi}\left(1-\frac{A(x,t)}{A(x=0,t)}\right)=\frac{x}{2\sqrt{D^{*}_{Mn}\cdot t}} \tag{5.3}$$

When a = erfi(b), then b = erf(a). For given diffusion-annealing times, t, values of manganese tracer diffusion coefficients were obtained by least squares fits of Equation (5.3) to experimental data.

5.4. Results

Figure 5.3a shows an example for an experimentally obtained normalized residual radioactivity profile of A(x,t)/A(x=0,t) as a function of the penetration depth, x. To obtain the line shown Figure 5.3a, Equation (5.2) was fitted to the individual data points contained in the figure. Figure 5.3b shows a plot of the type erfi(1−A(x,t)/A(x=0,t)) vs. x for the same experimental data considered in Figure 5.3a. The line in this plot was obtained by fitting Equation (5.3) to the experimental data to determine values for D^{*}_{Mn}. As discussed in Ref. [15], the differences between the values obtained for D^{*}_{Mn} by fitting Equations (5.2) and (5.3) to the experimental data were negligible, at maximum of the order of 0.2 %. Since residual radioactivities measured at larger penetration depths have slightly more influence on the obtained values for tracer diffusion coefficients and making them a little more accurate when using Equation (5.3) for determining them.

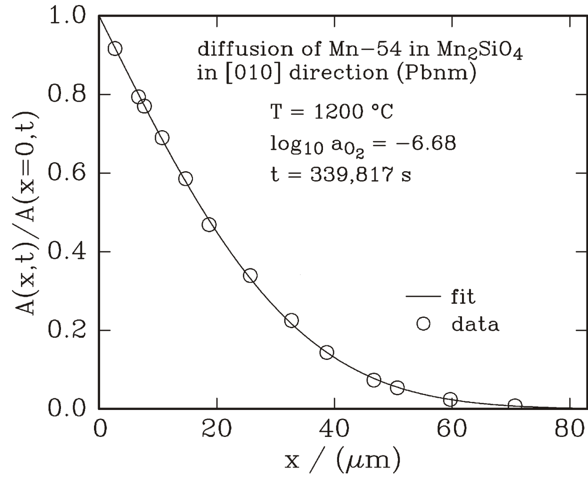

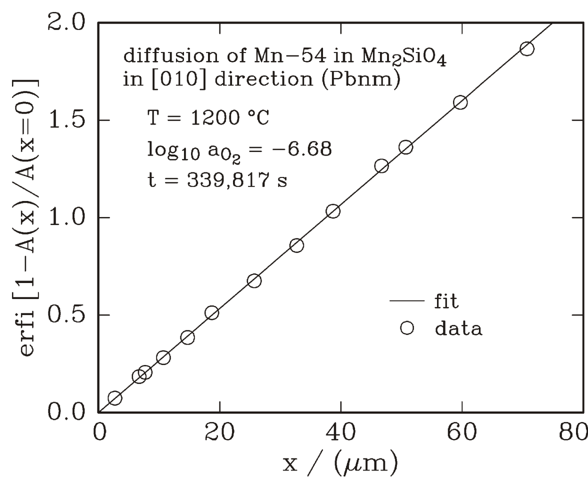

Figure 5.3: Example for experimental data: a) Normalized residual radioactivity profile, A(x,t)/A(x=0,t) vs. x. A(x,t) is the residual radioactivity measured after material of the thickness x has been removed from a sample and A(x=0,t) is the residual radioactivity before any material removal. t is diffusion-annealing time. The data shown are for a tracer diffusion experiment performed at 1200 °C at log a_{O_2} = −6.68 with a diffusion-annealing time t ≈ 340,000 s.

b) Plot of the inverse function of the error function of the argument [1−A(x,t)/A(x=0,t)] vs. x for the same experiment as that considered in Figure 5.3a. This type of plot was generated for all performed tracer diffusion experiments when determining values for manganese tracer diffusion coefficients by fitting Equation (5.3) to the experimental data.

This equation was used for determining all values of manganese tracer diffusion coefficients in manganese silicate reported in this article.

The measured manganese tracer diffusion coefficients for manganese silicate at 1150, 1200, 1250 and 1300 °C and at different oxygen activities for diffusion along the three principle orientations [100], [010] and [001] are reported in Table 5.1. The errors listed in this table are those obtained when fitting Equation (5.3) to the experimentally obtained normalized residual radioactivities. Further errors are introduced during the measurement of net counts, sample thicknesses determinations and the measurements of diffusion-annealing temperatures and times.

Based on past experiences and the individual errors involved when determining manganese tracer diffusion coefficients, the real errors of the reported manganese tracer diffusion coefficients are estimated to be about 5 %.

Table 5.1: Manganese tracer diffusion coefficients, D^{*}_{Mn}, experimentally determined in this study at $a_{MnSiO_3} = 1$ and different oxygen activities. $D° = 1$ cm^2/s. The errors reported in this table are from least squares fits of Equation (5.3) to normalized residual radioactivity profiles. The overall errors are estimated to be of the order of 5 %, as discussed in Section 5.4.

a) T = 1200 °C, [100]

$\log_{10} a_{O_2}$	$\log_{10} (D^{*}_{Mn}/D°)$	crystal #
−0.856	−9.797 ± 0.046	100b
−1.682	−10.029 ± 0.010	100a
−2.651	−10.408 ± 0.037	100b
−3.967	−10.888 ± 0.048	100a
−5.631	−11.323 ± 0.031	100b
−6.696	−11.414 ± 0.055	100a
−8.496	−11.497 ± 0.038	100c
−9.793	−11.546 ± 0.026	100a
−11.035	−11.548 ± 0.024	100b
−12.465	−11.501 ± 0.023	100c
−13.305	−11.453 ± 0.034	100b

b) T = 1200 °C, [010]

$\log_{10} a_{O_2}$	$\log_{10} (D^*_{Mn}/D^\circ)$	crystal #
−0.856	−9.402 ± 0.028	010b
−1.682	−9.646 ± 0.026	010a
−2.651	−10.060 ± 0.021	010b
−3.967	−10.420 ± 0.020	010a
−5.631	−10.864 ± 0.025	010c
−6.696	−10.986 ± 0.039	010a
−8.496	−11.081 ± 0.028	010c
−9.793	−11.131 ± 0.051	010a
−11.035	−11.123 ± 0.027	010c
−12.465	−11.093 ± 0.051	010a
−13.305	−11.046 ± 0.029	010b

c) T = 1200 °C, [001]

$\log_{10} a_{O_2}$	$\log_{10} (D^*_{Mn}/D°)$	crystal #
−0.856	−8.984 ± 0.006	001b
−1.682	−9.250 ± 0.018	001a
−2.651	−9.681 ± 0.032	001b
−3.967	−10.039 ± 0.031	001a
−5.631	−10.467 ± 0.024	001b
−6.696	−10.541 ± 0.040	001a
−8.496	−10.643 ± 0.025	001b
−9.793	−10.710 ± 0.044	001c
−11.035	−10.692 ± 0.025	001a
−12.465	−10.642 ± 0.029	001b
−13.305	−10.592 ± 0.030	001c

d) T = 1250 °C, $\log_{10} a_{O_2} = -2.666$

orientation	$\log_{10} (D^*_{Mn}/D°)$	crystal #
[100]	−10.016 ± 0.036	100c
[010]	−9.711 ± 0.017	010b
[001]	−9.349 ± 0.037	001b

e) T = 1150 °C, $\log_{10} a_{O_2} = -2.658$

orientation	$\log_{10} (D^*_{Mn}/D°)$	crystal #
[100]	−10.809 ± 0.031	100b
[010]	−10.440 ± 0.027	010c
[001]	−10.068 ± 0.025	001b

f) orientation = [001]

T (°C)	$\log_{10} a_{O_2}$	$\log_{10} (D^*_{Mn}/D°)$	crystal #
1300	−9.781	−10.080 ± 0.058	001b
1250	−9.792	−10.475 ± 0.030	001c
1150	−9.774	−11.047 ± 0.027	001b

The tracer diffusion coefficient data obtained for 1200 °C and different crystal orientations are plotted as a function of the oxygen activity in Figure 5.4 in comparison with a single data point for the diffusion of Mn-54 along [001] orientation in single crystalline Mn_2SiO_4 reported in Ref. [12]. Since the actual oxygen activity present during Morioka's measurements [12] was not reported, it was estimated based on use of nitrogen in the authors' laboratory that the oxygen activity established during Morioka's measurements by pumping nitrogen gas was probably about $10^{-3.7}$; this value was used in Figure 5.4 for presenting a diffusion coefficient value from Ref. [12]. Manganese tracer diffusion coefficients from the

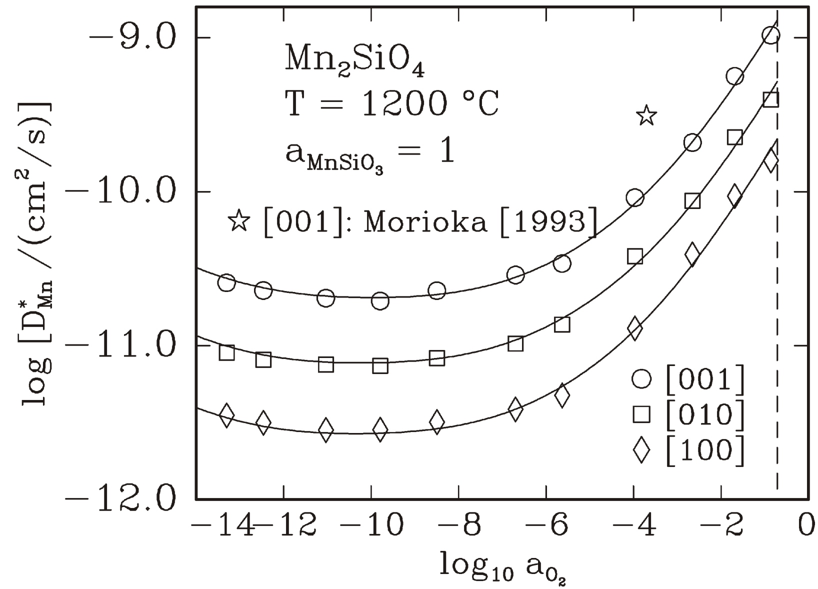

Figure 5.4: Tracer diffusion coefficients measured for the diffusion of manganese in Mn_2SiO_4 at 1200 ℃ and $a_{MnSiO_3} = 1$ along the principle orientations [100], [010] and [001] as a function of the oxygen activity. One data point from the literature [12] for the diffusion of Mn in a single crystal of Mn_2SiO_4 along the [001] orientation is also shown for comparison. The lines shown in the figure were obtained based on the defect modeling described in Section 4.1. The value of −3.7 used for $\log_{10} a_{O_2}$ for the data point reported by Morioka [12] is only an estimate by the authors of this article based on the statement in Ref. [12] that the diffusion occurred in a nitrogen atmosphere.

present work as a function of temperature are shown in Figure 5.5a for $\log a_{O_2}$ = −2.7 for all three principle orientations and in Figure 5.5b for $\log a_{O_2}$ = −9.8 for the [001] orientation.

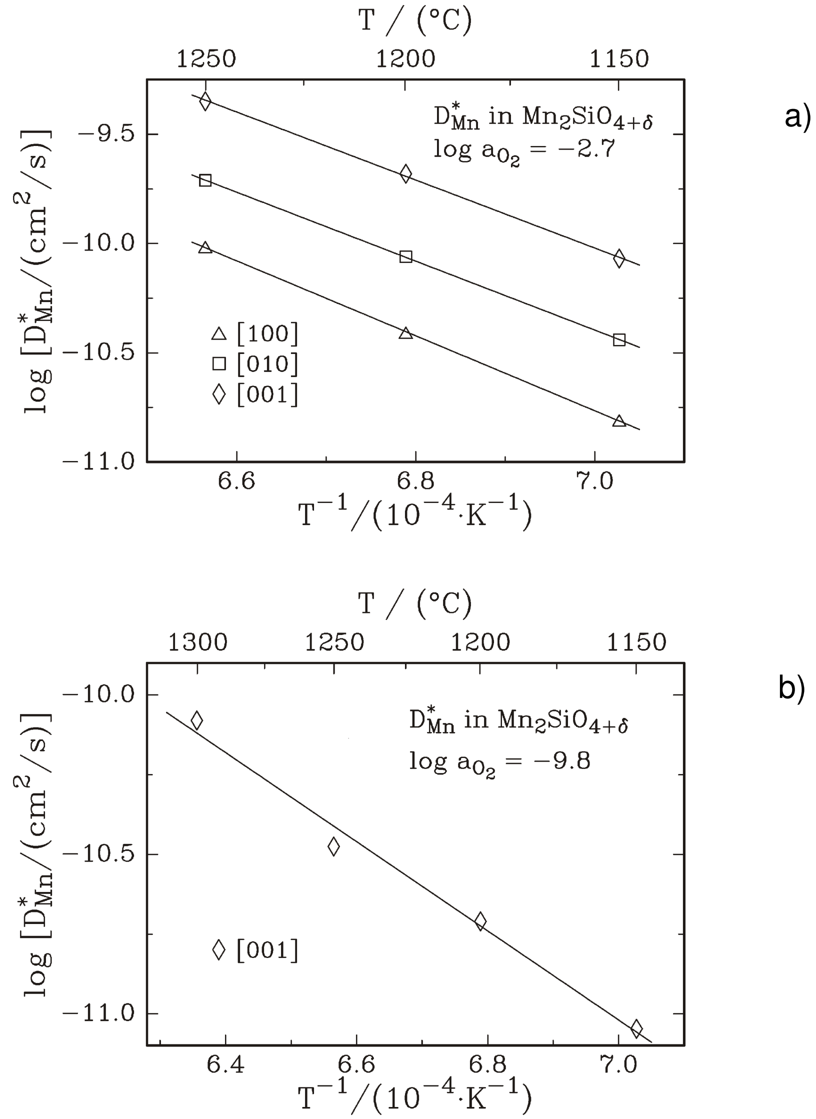

Figure 5.5: Temperature dependencies of manganese tracer diffusion coefficients measured for Mn_2SiO_4 at $a_{MnSiO_3} = 1$: a) for the diffusion of Mn-54 along the principle orientations, [100], [010] and [001], at $\log_{10} a_{O_2} \approx -2.7$ at 1 atm total pressure between 1150 and 1250 °C, and b) for the diffusion of Mn-54 along the [001] orientation at $\log_{10} a_{O_2} \approx -9.8$ at 1 atm total pressure between 1150 and 1300 °C. The lines shown were generated by fitting Equation (5.13) to the experimental data shown in the plot.

5.5. Discussion

5.5.1. Point Defect Chemistry

Previous results of point defect-related property measurements reported in literature [2,7,8] suggest that the majority point defects present in $Mn_2SiO_{4+\delta}$ at higher oxygen activities are vacancies on Mn^{2+}-sites, $(V_{Mn^{2+}})''$, holes, assumed to be present in the form of Mn^{3+} ions on Mn^{2+} sites, $(Mn^{3+}_{Mn^{2+}})^{\bullet}$, and manganese ions on silicon sites, $(Mn^{4+}_{Si^{4+}})^{\times}$. In the following discussion of the point defect chemistry of manganese silicate, there is no distinction being made between M1 and M2 sites because the experimental data considered do not allow any conclusions with regard to species being present on different M sites. At lower oxygen activities, the influence of electrons, e', as minority defects cannot be ignored based on results from electrical conductivity measurements [7,8]. Data from defect-related property measurements available in the literature do not show any indications of the presence of manganese ions on interstitial sites, $(Mn^{2+}_{I})^{\bullet\bullet}$, which could be of some importance at low oxygen activities. However, manganese tracer diffusion data reported in this article suggest that manganese ions on interstitial sites, $(Mn^{2+}_{I})^{\bullet\bullet}$, must contribute to the manganese tracer diffusion at low oxygen activities.

Since there are no hints from experimental data that Mn-ions on Si-sites are important, which, according to Ref. [2], would be expected to be Mn^{4+} ions, i.e., $(Mn^{4+}_{Si^{4+}})^{\times}$, such defects are ignored in the following discussion of the point defect chemistry of manganese silicate in equilibrium with $MnSiO_3$. In addition, the observed oxygen activity dependence of manganese tracer diffusion coefficients

at high oxygen activities cannot be explained in the basis of the diffusion of manganese via isolated manganese vacancies, $(V_{Mn^{2+}})''$, alone. One additional type of point defect, most likely a neutral associate, $\{2(Mn^{3+}_{Mn^{2+}})^{\bullet}\cdot(V_{Mn^{2+}})''\}^{\times}$, must also contribute to the diffusion of manganese in manganese silicate at high oxygen activities in order to account for the observed oxygen activity dependence at high oxygen activities.

Based on the preceding considerations, the important point defects to be considered for modeling the oxygen activity dependence of defect-related properties of $Mn_2SiO_{4+\delta}$ in this article are $(V_{Mn^{2+}})''$, $(Mn^{3+}_{Mn^{2+}})^{\bullet}$, e', $(Mn^{2+}_{I})^{\bullet\bullet}$ and $\{2(Mn^{3+}_{Mn^{2+}})^{\bullet}\cdot(V_{Mn^{2+}})''\}^{\times}$.

As discussed in the background section, an intended small amount of silica-rich secondary phase, $MnSiO_3$, was present in the manganese silicate samples used for the tracer diffusion studies to unequivocally determine the thermodynamic state of this ternary compound at given values of total pressure, temperature and oxygen activity. When $Mn_2SiO_{4+\delta}$ is in equilibrium with $MnSiO_3$, i.e., $a_{MnSiO_3} = 1$, a defect formation reaction describing the incorporation of oxygen into $Mn_2SiO_{4+\delta}$ can be formulated as

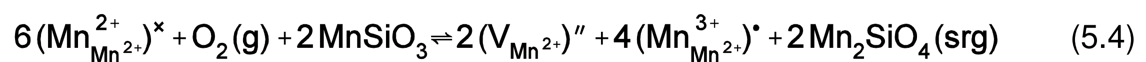

$$6(Mn^{2+}_{Mn^{2+}})^{\times} + O_2(g) + 2\,MnSiO_3 \rightleftharpoons 2(V_{Mn^{2+}})'' + 4(Mn^{3+}_{Mn^{2+}})^{\bullet} + 2\,Mn_2SiO_4(srg) \qquad (5.4)$$

The abbreviation srg stands for “site of repeatable growth”.

Two additional defect formation reactions need to be formulated to take into account the formation of electrons and of manganese ions on interstitial sites, e.g., the thermal electronic disorder reaction,

$$0 \rightleftarrows e' + h^{\bullet} \tag{5.5}$$

and the cation Frenkel disorder reaction,

$$(Mn_{Mn^{2+}}^{2+})^{x} + (V_I)^{x} \rightleftarrows (V_{Mn^{2+}})'' + (Mn_I^{2+})^{\bullet\bullet}. \tag{5.6}$$

The equilibrium constant for the reaction described in Equation (5.4), K_a, when incorporating all practically constant terms into K_a, can be formulated as

$$K_a = \frac{[(V_{Mn^{2+}})'']^2 \cdot [(Mn_{Mn^{2+}}^{3+})^{\bullet}]^4}{a_{O_2}} \tag{5.7}$$

In Equation (5.7) the terms [i] denote concentrations of the defect species i per formula unit of $Mn_2SiO_{4+\delta}$.

The equilibrium constant for the thermal electronic disorder reaction described in Equation (5.5), K_e, reads

$$K_e = [e'] \cdot [h^{\bullet}] = [e'] \cdot [(Mn_{Mn^{2+}}^{3+})^{\bullet}] \tag{5.8}$$

and that of the Frenkel disorder reaction denoted in Equation (5.6), K_F, is

$$K_F = [(V_{Mn^{2+}})''] \cdot [(Mn_I^{2+})^{\bullet\bullet}] \tag{5.9}$$

The overall electroneutrality condition, taking into account the presence of ions of the type Me^{+} and Mx^{3+} as impurities, assuming that these are present on Mn^{2+} sites, is

$$2[(V_{Mn^{2+}})''] + [e'] + [(Me^{+}_{Mn^{2+}})'] = 2[(Mn^{2+}_{I})^{\bullet\bullet}] + [(Mn^{3+}_{Mn^{2+}})^{\bullet}] + [(Mx^{3+}_{Mn^{2+}})^{\bullet}] \qquad (5.10)$$

For given values of the concentrations of impurities of the types Me^{+} and Mx^{3+} and of the equilibrium constants K_a, K_e and K_F, Eqs. (7) to (10) can be used to calculate the concentrations of all point defects contained in Equation (5.10) as a function of oxygen activity.

If neutral associates, $\{2(Mn^{3+}_{Mn^{2+}})^{\bullet} \cdot (V_{Mn^{2+}})''\}^{\times}$, are present as minority defects contributing significantly to the diffusion of manganese in Mn_2SiO_4, their formation can be described by the reaction

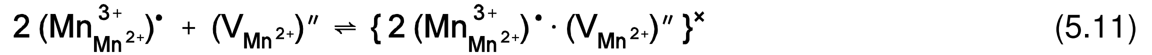

$$2\,(Mn^{3+}_{Mn^{2+}})^{\bullet} + (V_{Mn^{2+}})'' \rightleftharpoons \{2\,(Mn^{3+}_{Mn^{2+}})^{\bullet} \cdot (V_{Mn^{2+}})''\}^{\times} \qquad (5.11)$$

In principle, one could in addition also consider the formation of singly charged associates, $\{(Mn^{3+}_{Mn^{2+}})^{\bullet} \cdot (V_{Mn^{2+}})''\}'$, as additional minority defects. Doing this would introduce another unknown parameter into the defect modeling, but not provide any additional insights. Therefore, the possible presence of such associates was ignored in the performed defect modeling for the sake of simplicity.

Based on experimental data available for the variation of the oxygen content of $Mn_2SiO_{4+\delta}$ and for the transport of matter and charge in Mn_2SiO_4, it is not possible to calculate absolute values for the concentration of neutral associates

$\{2(Mn^{3+}_{Mn^{2+}})^{\bullet}\cdot(V_{Mn^{2+}})''\}^{\times}$ as minority defects without knowledge of the mobility of such a defect; this mobility is unknown. However it is possible to determine that the oxygen activity dependence of the concentration of these defects, $d\,[\{2(Mn^{3+}_{Mn^{2+}})^{\bullet}\cdot(V_{Mn^{2+}})''\}^{\times}]\,/\,d\log a_{O_2}$, is 0.5, provided that $(Mn^{3+}_{Mn^{2+}})^{\bullet}$ and $(V_{Mn^{2+}})''$ are the majority defects.

The discussion related to calculations of point defect concentrations as a function of the oxygen activity at given values of the equilibrium constants K_a, K_e and K_F will be continued in the following section in which a Kröger-Vink diagram is introduced which is compatible with experimental data obtained for the manganese tracer diffusion and available data in literature for other defect-related properties of manganese silicate.

5.5.2. Oxygen Activity Dependence of the Manganese Tracer Diffusion

As stated before, results of measurements of the variation of the oxygen content in $Mn_2SiO_{4+\delta}$ and of the electrical conductivity available in literature are compatible with isolated manganese vacancies and localized holes as majority defects at high oxygen activities. If isolated manganese vacancies and localized holes are majority defects, one can find by using the equation system defined in the previous section that the concentrations of majority defects and the deviation from stoichiometry, δ, in $Mn_2SiO_{4+\delta}$ are proportional to $a_{O_2}^{1/6}$. If the diffusion of manganese is only via isolated manganese vacancies and the electrical conduction in manganese silicate is only via hole conduction, the manganese cation diffusion coefficient and electrical conductivity are expected to be

proportional to $a_{O_2}^{1/6}$. However, results from measurements for the manganese tracer diffusion in manganese silicate communicated in this article show that at high oxygen activities the oxygen activity dependence of the manganese tracer coefficient, $d \log D^{*}_{Mn} / d \log a_{O_2}$, increases with increasing oxygen activity and approaches, but never exceeds, a value of one half.

A similar oxygen activity dependence of cation diffusion coefficients in a transition metal- containing orthosilicate was observed for the diffusion of Fe in Fe_2SiO_4 at high oxygen activities, see Ref. [10]. One likely explanation for the observed oxygen activity dependence of the manganese tracer diffusion at high oxygen activities is that the diffusion of manganese occurs at high oxygen activities, in addition to via isolated manganese vacancies, also via neutral associates formed between manganese vacancies and localized holes, $\{2(Mn^{3+}_{Mn^{2+}})^{\bullet}\cdot(V_{Mn^{2+}})''\}^{\times}$.

At lower oxygen activities, the oxygen activity dependence of the tracer diffusion becomes smaller and eventually the slope $d \log D^{*}_{Mn} / d \log a_{O_2}$ becomes negative. The observed change in the oxygen activity dependence of the manganese tracer diffusion can be attributed by an increased contribution of manganese interstitials to the manganese tracer diffusion. A similar observation of a smaller oxygen activity dependence of cation tracer diffusion coefficients at lower oxygen activities was made before in an experimental study of the diffusion of cobalt in cobalt orthosilicate, see Ref. [15].

For modeling the oxygen activity dependence of the manganese tracer diffusion, a Kröger-Vink diagram had to be generated which required calculations and/or estimates of point defect concentrations as a function of the oxygen activity at given total pressure and temperature for the condition that Mn_2SiO_4 is present in equilibrium with $MnSiO_3$, i.e., $a_{MnSiO_3} = 1$. The oxygen activity dependence of the manganese tracer diffusion in manganese silicate was measured in this study at 1200 °C in the oxygen activity range of $-13.3 \leq \log a_{O_2} \leq -0.86$. It was attempted to develop a Kröger-Vink diagram which is compatible with the cation tracer diffusion data from this study and that can also be used to model the electrical conductivity and the variation of the oxygen content in $Mn_2SiO_{4+\delta}$. Starting with an estimate for the equilibrium constant K_a, see Equation (5.7), for the defect formation reaction described in Equation (5.4), the most relevant data are those for δ in $Mn_2SiO_{4+\delta}$ in equilibrium with $MnSiO_3$ at 1200 °C which are shown in Figure 5.2. An extrapolation of the data for 1200 °C to $a_{O_2} = 1$ leads to an estimated value for $\log \delta = -2.72$. If it is assumed that manganese vacancies and holes are the majority defects this leads to $\log [(V_{Mn^{2+}})''] = -2.72$ for 1200 °C and $a_{O_2} = 1$. To obtain this value, the value of the equilibrium constant K_a needs to be set to be $10^{-15.12}$. For further calculations a rounded value of $K_a = 10^{-15}$ was used. Estimates for values of the equilibrium constants K_e and K_F are currently not possible due to a lack of sufficient knowledge of the mobilities of Mn-ions diffusing by an interstitial or interstitialcy diffusion mechanism and of holes and electrons. From the observed oxygen activity dependence of the manganese tracer diffusion in manganese silicate, it can be concluded that manganese interstitials must

contribute significantly to the manganese tracer diffusion at low oxygen activities. These conclusions remain valid when taking into account the impurity concentrations found for the type of samples used for the experiments reported in this study. The observations for the oxygen activity dependence of the electrical conductivity reported in the literature [7,8] suggest that there must be an increased concentration of electrons at lower oxygen activities. As stated above, due to a lack of information on the mobilities of electrons and holes and on relative mobilities of manganese cations diffusing via manganese vacancies and interstitials, it is impossible to unequivocally model point defect concentrations at lower oxygen activities. The approach adopted for this study was to assign values to relative mobilities and then to vary the values of K_e and K_F until a Kröger-Vink diagram was found which is compatible with all available (sufficiently reliable) experimental data. The oxygen activity dependence observed for the diffusion of manganese in manganese silicate at high oxygen activities is attributed to a very significant contribution of highly mobile minority defects, $\{2(Mn^{3+}_{Mn^{2+}})^{\bullet}\cdot(V_{Mn^{2+}})''\}^{\times}$, at high oxygen activities. However, based on the experimentally observed oxygen activity dependence of the variation of the oxygen content of $Mn_2SiO_{4+\delta}$, associates of the type $\{2(Mn^{3+}_{Mn^{2+}})^{\bullet}\cdot(V_{Mn^{2+}})''\}^{\times}$ can only be present as minority defects having a much higher mobility than isolated vacancies on M-sites. Such a behavior, also found for the diffusion of iron in Fe_2SiO_4 [10], is quite unusual and not yet understood. No conclusion can be drawn with regard to absolute values of the concentrations of $\{2(Mn^{3+}_{Mn^{2+}})^{\bullet}\cdot(V_{Mn^{2+}})''\}^{\times}$.

As indicated in Figure 5.6 by an arrow, the line shown for such concentrations in this figure is only tentative and can shift to somewhat larger or to smaller concentrations. If isolated manganese vacancies and localized holes are majority defects, as suggested by the observed oxygen activity dependencies of the variation of the oxygen content and the electrical conductivity, it follows that the concentration of $\{2(Mn^{3+}_{Mn^{2+}})^{\bullet}\cdot(V_{Mn^{2+}})''\}^{\times}$ is proportional to $a_{O_2}^{1/2}$. In order to allow for a modeling of point defects, a value of $10^{-4.2}$ was assumed for the concentration of the neutral associates $\{2(Mn^{3+}_{Mn^{2+}})^{\bullet}\cdot(V_{Mn^{2+}})''\}^{\times}$ at a_{O_2} = 1. Because

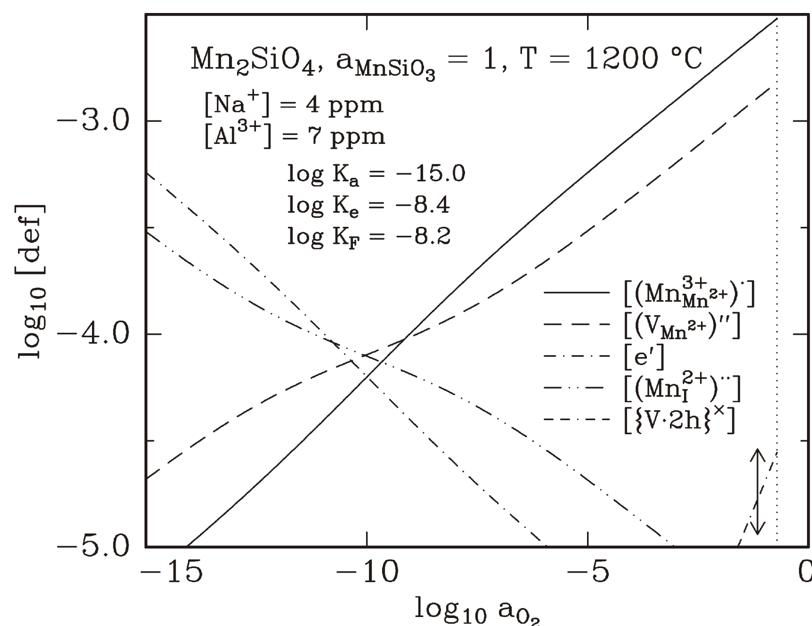

Figure 5.6: An estimated Kröger-Vink diagram for $Mn_2SiO_{4+\delta}$ at 1200 °C and a_{MnSiO_3} = 1 which is compatible with all currently available, reliable information on oxygen activity dependencies of the deviation from stoichiometry, δ, the cation tracer diffusion and the electrical conductivity.

$\{2(Mn^{3+}_{Mn^{2+}})^{\bullet}\cdot(V_{Mn^{2+}})''\}^{\times}$ is a neutral defect, the absolute value selected for the concentration of $[\{2(Mn^{3+}_{Mn^{2+}})^{\bullet}\cdot(V_{Mn^{2+}})''\}^{\times}]$ had no influence on the results of the calculation of the concentrations of the electrically charged point defects contained in the electroneutrality condition, Equation (5.10).

The impurity concentrations in the manganese silicate samples considered when establishing a Kröger-Vink diagram were 4 mol ppm Na^{+} and 7 mol ppm Al^{3+}, in agreement with the values reported in Ref. [3] for the concentrations of impurities in crystals grown for this study. As a final result of the efforts to establish a Kröger-Vink diagram, which is compatible with experimental observations considered as reliable, is shown in Figure 5.6. As discussed earlier in the background section of this article, the electrical conductivity data reported in Ref. [8] are believed to be non-reliable and were therefore not considered for deriving Figure 5.6.

As one can see in Figure 5.6, there exists a small difference between the oxygen activities where $[e'] = [h^{\bullet}]$ and where $[(V_{Mn^{2+}})''] = [(Mn^{2+}_{I})^{\bullet\bullet}]$. The reason for this difference is that the concentrations of the impurities considered, Na^{+} and Al^{3+}, do not cancel each other out in the electroneutrality condition, Equation (5.10). If these concentrations would be equal, there would be no difference between the two oxygen activities denoted above.

According to Figure 5.6 the thermal electronic disorder in Mn_2SiO_4 is concluded to be relatively large and not very different in magnitude from the Frenkel disorder on the M-sublattice. This is not a very common behavior. However, a similar

conclusion was already reached before for the iso-structural orthosilicate Co_2SiO_4 at 1300 °C [15]. As discussed in Ref. [15] a large thermal electronic disorder is not often observed in oxides, but it does occur. Oxides like CuO [18] and Fe_2O_3 [19] even have a predominant thermal electronic disorder leading to oxygen activity-independent electrical conductivities.

Plots showing log D^*_{Mn} vs. log a_{O_2} for the orientation [001], Figure 5.7a, and log σ vs. log a_{O_2}, Figure 5.7b, were derived by using the same set of values for equilibrium constants as utilized for generating Figure 5.6. Impurity concentrations corresponding to those of the Mn_2SiO_4 samples considered in the figures were taken into account. Values for the mobilities of ionic and electronic defects were adjusted so that experimental data closely matched calculated diffusivities and conductivities, respectively. The relatively good description of the experimentally observed oxygen activity dependencies of the manganese tracer diffusion and the electrical conduction supports the developed point defect model for Mn_2SiO_4. Further support is provided by the relatively good description of the oxygen activity dependence of the deviation from stoichiometry δ in $Mn_2SiO_{4+\delta}$ by the discussed point defect model and the parameters used for it. Calculated values for δ in comparison with data derived for δ from the results of thermogravimetric measurements reported in Ref. [2] are shown in Figure 5.7c.

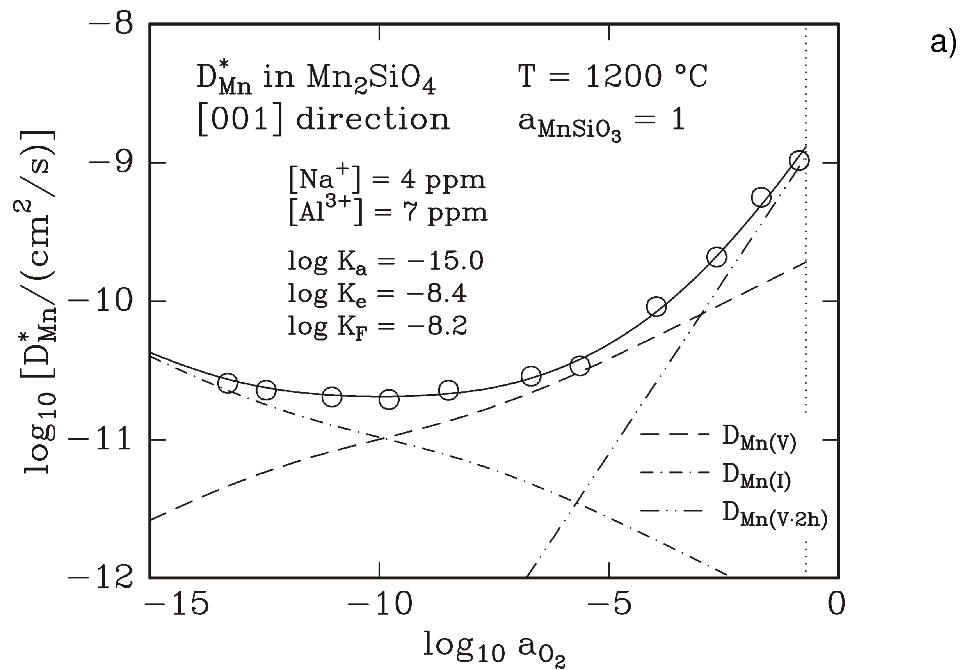

a)
D*Mn in Mn2SiO4
[001] direction
T = 1200 °C
aMnSiO3 = 1
[Na+] = 4 ppm
[Al3+] = 7 ppm
log Ka = −15.0
log Ke = −8.4
log KF = −8.2
DMn(V)
DMn(I)
DMn(V·2h)
log10 [D*Mn/(cm2/s)]
log10 aO2
−8
−9
−10
−11
−12
−15
−10
−5
0

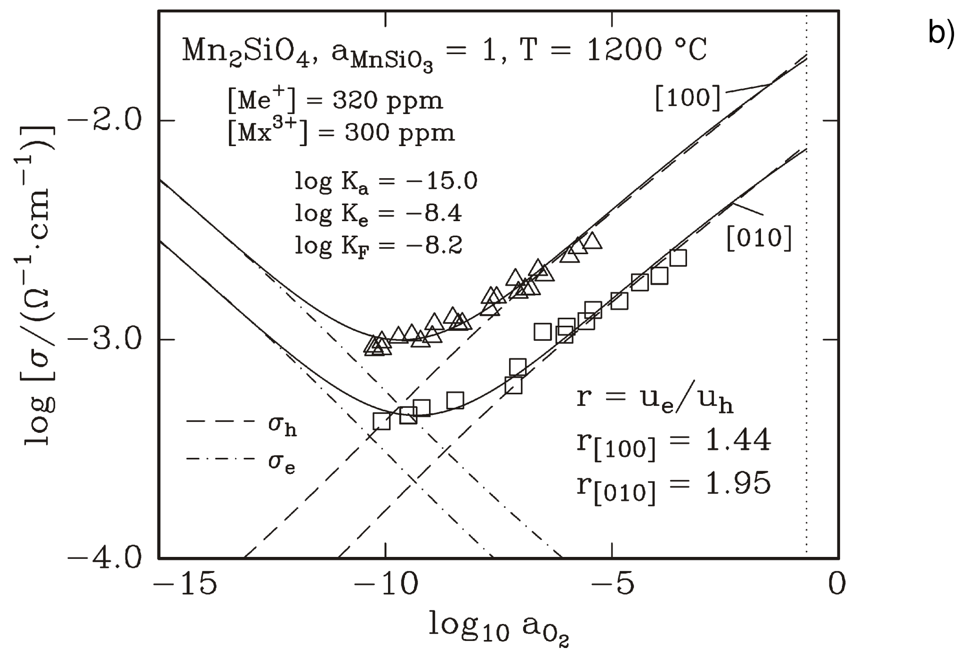

b)
Mn2SiO4, aMnSiO3 = 1, T = 1200 °C
[Me+] = 320 ppm
[Mx3+] = 300 ppm
log Ka = −15.0
log Ke = −8.4
log KF = −8.2
[100]
[010]
σh
σe
r = ue/uh
r[100] = 1.44
r[010] = 1.95
log [σ/(Ω−1·cm−1)]
log10 aO2
−2.0
−3.0
−4.0
−15
−10
−5
0

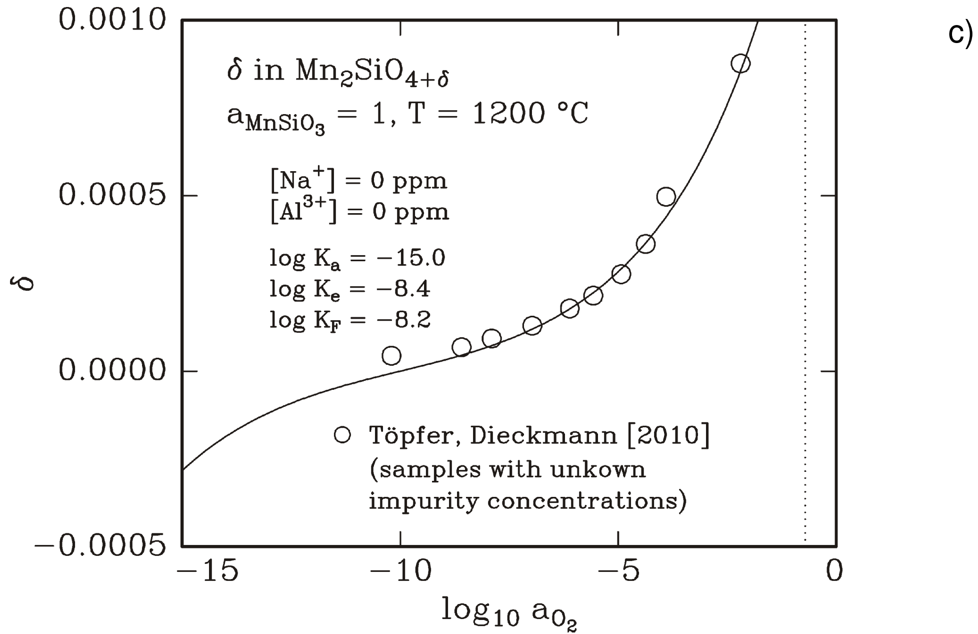

Figure 5.7: Comparison of oxygen activity dependencies obtained, departing from Figure 5.6, a) for the tracer diffusion coefficient of Mn-54 diffusing along the direction [001], D^*_{Mn}, b) for the electrical conductivity, σ, for the directions [100] and [010] (the data points shown are from Ref. [7]), and c) for the deviation from stoichiometry, δ, for $Mn_2SiO_{4+δ}$ in equilibrium with $MnSiO_3$ at 1200 °C.

For deriving Figure 5.7a, which contains data for the manganese tracer diffusion along the [001] orientation in Mn_2SiO_4 in equilibrium with $MnSiO_3$ at 1200 °C, it was assumed that the mobility of Mn ions diffusing via manganese interstitials is 1.05 as large as that of such ions diffusing via doubly charged manganese vacancies. Values for the tracer diffusion coefficient of manganese cations diffusing via neutral associates, assumed to be $\{2(Mn^{3+}_{Mn^{2+}})^{\bullet}\cdot(V_{Mn^{2+}})''\}^{\times}$ and being present as very mobile minority defects, were determined based on

observed oxygen activity dependencies of the manganese cation diffusivity, the oxygen activity dependence, d $[\{2(Mn^{3+}_{Mn^{2+}})^{\bullet}\cdot(V_{Mn^{2+}})''\}^{\times}]$ / d log a_{O_2}, of 0.5 expected based on the defect chemistry for these associates, and the absolute values of the manganese tracer diffusion coefficients found at high oxygen activities. If the concentration values shown in Figure 5.6 are assumed to be correct and the geometrical correlation involved in the manganese tracer diffusion is ignored, then the logarithms of the diffusion coefficients (in cm^2/s) of the different defect species considered are for isolated manganese vacancies −6.60, for manganese interstitials −6.58 and for the associates denoted above −4.10 for diffusion in the orientation [001]. In reality, the latter value can be very different because the concentrations of the associates can significantly differ from those denoted in Figure 5. 6.

The results obtained when modeling the oxygen activity dependence of the manganese tracer diffusion in Mn_2SiO_4 for the directions [010] and [100] are similar to those shown in Figure 5.7a for diffusion in the [001] direction, see the lines shown in Figure 5.4 which are based on the defect modeling performed in this article. However, the adjustable parameters referring to mobilities of Mn ions via cation vacancies, associates and interstitials are somewhat different. The mobility of manganese ions diffusing via manganese interstitials is for diffusion in the [010] direction 0.94 times as large as that of such ions diffusing via doubly charged manganese vacancies. For diffusion along the [100] direction, a value of 0.9 was found for the mobility ratio denoted before. Overall this mobility ratio seems not to change very significantly with the direction of the cation diffusion.

5.5.3. Oxygen Activity Dependence of the Electrical Conduction in Mn_2SiO_4

For discussing the oxygen activity dependency of the electrical conductivity, it is useful to first consider which fraction of charge is transported by the motion of ions. The Nernst-Einstein equation, see Equation (5.12), can be used to estimate this contribution.

$$\sigma_i = \frac{z_i^2 \cdot F^2 \cdot D_i \cdot c_i}{R \cdot T} \qquad (5.12)$$

In this equation, z_i is the ionic charge number of the diffusing species i, F is the Faraday constant, c_i is the concentration of the species i, R is the gas constant and T is the temperature in K. According to the Kröger-Vink diagram shown in Figure 5.6, $\log D^*_{Mn}/(cm^2/s)$ is -10.592 at the lowest and -8.984 at highest oxygen activity considered for the diffusion of Mn along the [001] orientation. Using the value of 0.745 from Ref. [17] as an estimate for the correlation factor involved in D^*_{Mn}, $z_{Mn} = 2$, $c_{Mn} = 0.04$ mol/cm^3 and $T = 1200$ °C, leads to the result that $\log \sigma^*_{Mn}/(\Omega^{-1} \cdot cm^{-1}) = -5.38$ at the lowest and -3.77 at the highest oxygen activity denoted above. These values in comparison with the electrical conductivity values communicated in Figure 5.1 indicate that the charge transport via ionic conduction is negligibly small compared to the experimentally obtained electrical conductivities.

Despite of the problem that the conductivity values reported by Stüber and Laqua [8] for Mn_2SiO_4 in equilibrium with $MnSiO_3$ are much too low, it was attempted to model the oxygen activity dependencies of these data shown in

Figure 5.2. Since the impurity concentrations of the samples studied by Stüber and Laqua are unknown, it was attempted to use the values of the equilibrium constants employed for deriving Figure 5.6 and varying impurity concentrations to model the data denoted above. It was found that it is not possible to describe the data reported by Stüber and Laqua [8] for the electrical conductivity of Mn_2SiO_4 in equilibrium with $MnSiO_3$ at lower oxygen activities at 1200 °C by assuming the presence of any dopants on Mn sites at relatively high concentrations and using the equilibrium constants denoted above. Because the reported conductivity values are much too low to possibly be attributed to bulk conductivities and grain boundaries may have played a significant role in the overall conduction behavior observed by Stüber and Laqua [8], no further modeling attempts were made using data reported by these authors.

However, the oxygen activity dependence of the electrical conductivity data reported by Bai et al. [7] can be described reasonably well based on the point defect model discussed before, see Figure 5.7b. To obtain the curves shown in this figure for the conduction along the [100] direction, departing from the concentrations of holes and electrons denoted in Figure 5.6, a value of 1.44 was used for the ratio, r, of the mobilities of electrons, $u_{e'}$, and holes, $u_{h^\bullet}$, and for the electrical conduction along the [010] orientation r = 1.95 was used. The individual values of the electrochemical mobilities of holes and electrons used for generating Figure 5.7b are for conduction in the [100] direction $u_{h^\bullet} = 3.35 \cdot 10^{-3}$ $cm^2/(V \cdot s)$ and $u_{e'} = 4.82 \cdot 10^{-3}$ $cm^2/(V \cdot s)$ and for conduction in the [010] direction $u_{h^\bullet} = 1.30 \cdot 10^{-3}$ $cm^2/(V \cdot s)$ and $u_{e'} = 2.53 \cdot 10^{-3}$ $cm^2/(V \cdot s)$.

5.5.4. Temperature Dependence of the Manganese Tracer Diffusion

An Arrhenius-type equation, Equation (5.13), was fitted to tracer diffusion data for diffusion of Mn in the [001] direction at two different oxygen activities, $a_{O_2} = 10^{-2.7}$ and $a_{O_2} = 10^{-9.8}$.

$$D^*_{Mn} = D^o_{Mn} \cdot \exp\left(-\frac{\Delta H}{R \cdot T}\right) \tag{5.13}$$

While, according to the defect and diffusion modeling discussed before, cation vacancies and neutral associates are expected to govern the manganese tracer diffusion at $a_{O_2} = 10^{-2.7}$, at $a_{O_2} = 10^{-9.8}$, cation vacancies and cation interstitials both should contribute to the manganese diffusion. The tracer diffusion data analyzed were the tracer diffusion coefficients listed in Table 5.1 for oxygen activities close to $\log a_{O_2} = -2.7$ and $\log a_{O_2} = -9.8$, respectively. Figures 5.5a and 5. 5b show the data used to determine temperature dependencies of the manganese tracer diffusion in Mn_2SiO_4 at the two oxygen activities denoted above.

Results obtained for pre-exponential factors, D^o_{Mn}, and for activation enthalpies, ΔH, and their errors are reported in Table 5.2 in comparison with analogous data obtained by fitting Equation (5.13) to three data points obtained for the diffusion of Mn in single crystalline Mn_2SiO_4 from Ref. [12]. Activation enthalpies, ΔH, contain contributions related to the formation of point defects and to the motion of ions via point defects.

Table 5.2: Values obtained for pre-exponential factors, D°_{Mn}, and for activation enthalpies, ΔH, by fitting Equation (5.13) to manganese tracer diffusion data for $\log_{10} a_{O_2} = -2.7$ and diffusion along the three principle orientations [100], [010] and [001], see Figure 5.5a, and data for $\log_{10} a_{O_2} = -9.8$ for diffusion along the [001] orientation, see Figure 5.5b. One data point available from Ref. [12], denoted by the symbol * in this table, is also listed. ** The value of −3.7 for $\log_{10} a_{O_2}$ is only an estimate which is based on the statement in Ref. [12] that the diffusion occurred in a nitrogen atmosphere and on an estimate by the authors of this article.

sample	$\log_{10} a_{O_2}$	temperature range (°C)	orientation	$\log_{10}$ $[D^{\circ}_{Mn}/(cm^2/s)]$	ΔH/(kJ/mol)
single crystal	−2.7	1150 - 1250	[100]	1.24 ± 0.44	328 ± 12.4
single crystal	−2.7	1150 - 1250	[010]	0.64 ± 0.44	301.9 ± 12.4
single crystal	−2.7	1150 - 1250	[001]	0.87 ± 0.44	297.8 ± 12.4
single crystal	−9.8	1150 - 1300	[001]	−1.23 ± 0.28	267.7 ± 8.0
single crystal *	−3.7**	1100 - 1200	[001]	−1.87	215

Since, based on the performed defect modeling and the modeling of the oxygen activity dependence of the diffusion of manganese, multiple defects are involved in the diffusion at $a_{O_2} = 10^{-2.7}$ (isolated cation vacancies and associates) and at $a_{O_2} = 10^{-9.8}$ (isolated cation vacancies and manganese interstitials) the data currently available do not allow the determination of values for individual activation enthalpy contributions. Nevertheless, the data listed in Table 5.2 for $\log a_{O_2} = -2.7$ suggest that ΔH is largest for the orientation in which the diffusion is slowest, i.e., for the [100] direction, and smallest for the orientation in which the diffusion is fastest, i.e., for the [001] direction. Since the relative contributions of the transport via associates and via isolated manganese vacancies may change with temperature, it is not possible to attribute this trend for ΔH in an unequivocal way to differences in enthalpies of motion for the diffusion of Mn in different orientations. It is unclear why the activation enthalpy determined using diffusion data from Ref. [12] is significantly smaller than those obtained in this study.

The activation enthalpy found for the manganese tracer diffusion along the [001] direction at $a_{O_2} = 10^{-9.8}$ is by about 30 kJ/mol smaller than that for the manganese tracer diffusion at $a_{O_2} = 10^{-2.7}$. The reasons for this behavior are unknown.

The pre-exponential factors derived from the diffusion data determined in the present work differ at $\log a_{O_2} = -2.7$ at maximum by a factor of about 4, i.e., they do not vary dramatically for the defect population being present which changes somewhat, but not severely, with temperature within the considered temperature

range. The errors in the logarithms given in Table 5.2 for the pre-exponential factors at this oxygen activity are ± 0.44, i.e., correspond to a factor of 2.75. At log a_{O_2} = −9.8, however, the defect population is fundamentally different from that at log a_{O_2} = −2.7. This is probably the reason why the value of the pre-exponential factor found for log a_{O_2} = −9.8 is quite different from the values observed for the diffusion of manganese in different directions at log a_{O_2} = −2.7.

5.5.5. Orientation Dependence of the Manganese Tracer Diffusion

The data shown in Figure 5.4 indicate that the manganese tracer diffusion coefficients measured along three principle orientations at 1200 °C follow the trend $D^*_{Mn[001]} > D^*_{Mn[010]} > D^*_{Mn[100]}$ at all oxygen activities for which data for different crystal orientations are available. The same trend was found for the diffusion of Mn at temperatures between 1150 and 1250 °C at log a_{O_2} = −2.7 and between 1150 and 1200 °C at log a_{O_2} = −9.8. At log a_{O_2} = −2.7, one finds at 1150 °C, 1200 and 1250 °C for the ratio $D^*_{Mn[001]} : D^*_{Mn[010]} : D^*_{Mn[100]}$ values of 5.5 : 2.3 : 1, 5.3 : 2.2 : 1 and 4.6 : 2.0 : 1. The similarity of these ratios suggests that the overall activation enthalpies for the diffusion of Mn ions along the different crystallographic orientations considered are similar to each other, in agreement with the activation enthalpy data listed in Table 5.2.

As stated before, the M1 sites in Mn_2SiO_4 are lined up in the [001] direction, allowing for direct jumps in this direction. Direct jumps in the [100] and [010] directions are not possible. Diffusion of manganese ions into these two directions must therefore involve a zig-zag-like motion involving different types of elementary

jumps. Since the anisotropy in the manganese diffusion is not very large and the overall activation energies found for the transport of Mn in the different orientations considered in this work are relatively similar this suggests that the individual barrier heights involved in the different elementary jumps contributing to diffusion must be relatively similar.

Some data related to orientation dependence of the diffusion of cations in transition metal-containing orthosilicates with the olivine structure were summarized earlier by the authors of this article in Ref. [15]. Though different values have been reported for the ratios of cation tracer diffusion coefficients of Me in transition metal-containing orthosilicates of the type Me_2SiO_4, the general trend for such ratios is that the diffusion in the [001] direction occurs fastest and that in the [100] direction slowest. The largest ratios were found for the diffusion of Co in Co_2SiO_4 at 1300 ℃ ($D^*_{Co[001]} : D^*_{Co[010]} : D^*_{Co[100]} = 30 : 3 : 1$). The corresponding ratio for the diffusion of Fe in Fe_2SiO_4 at 1130 ℃ was found to be 12 : 3 : 1 [10] while that found for the diffusion of Mn in Mn_2SiO_4 in this article is on the order of 5 : 2 : 1. While the general trend in the cation diffusion coefficients denoted above seems to be related to the olivine crystal structure, it is unclear what causes the differences in the ratios considered above for different transition metal ions. Computational work could provide some insight into this subject. Some more discussion related to the orientation dependence of transport properties of transition-metal containing orthosilicates can be found in Ref. [15].

5.6. Conclusions

Experimental data obtained in this study for the oxygen activity dependence for the manganese tracer diffusion in manganese silicate, $Mn_2SiO_{4+\delta}$, at 1200 °C suggest that the diffusion of manganese is, at high oxygen activities, via isolated manganese vacancies and also possibly neutral associates formed between manganese vacancies and localized holes, and, at lower oxygen activities, also influenced by manganese ions on interstitial sites. The trend found for the diffusivity along different crystallographic orientations showed that $D^*_{Mn[001]} > D^*_{Mn[010]} > D^*_{Mn[100]}$. At 1200 °C and $\log a_{O_2} = -2.7$, $D^*_{Mn[001]} : D^*_{Mn[010]} : D^*_{Mn[100]} = 5.3 : 2.2 : 1$. The activation enthalpy for the diffusion of manganese in Mn_2SiO_4 varies with diffusion direction; the values found vary between 260 and 290 kJ/mol.

REFERENCES

[1] "International Tables for X-ray Crystallography," Vol. 1: "Symmetry Groups," N.F.M. Henry and K. Lonsdale, Eds., The Kynoch Press, Birmingham, U.K., [1965] Table 6.2.1, p. 548.

[2] J. Töpfer and R. Dieckmann, "Variation of the Oxygen Content and Point Defects in Tephroite, $Mn_2SiO_{4+\delta}$," Solid State Ionics, **181** (11-12) [2010] 479-488.

[3] Q. Tang and R. Dieckmann, "Floating-Zone Growth and Characterization of Single Crystals of Manganese Orthosilicate, Mn_2SiO_4," J. Cryst. Growth, submitted.

[4] G. Nover, "Electrical Properties of Crustal and Mantle Rocks - a Review of Laboratory Measurements and Their Explanation," Surv. Geophys., **26** (5) [2005] 593-651.

[5] S. Chakraborty, "Diffusion Coefficients in Olivine, Wadsleyite and Ringwoodite," in: "Diffusion in Minerals and Melts," Y. Zhang and D.J. Cherniak, Eds., Rev. Mineral. Geochem., **72** (1) [2010] 603-639.

[6] F.A. Kröger and H.J. Vink, "Relations Between the Concentrations of Imperfections in Crystalline Solids," in: F. Seitz and D. Turnbull, Eds., Solid State Physics - Advances in Research and Applications, Vol. 3, Academic Press, New York, [1956] 307-435.

[7] Q. Bai, Z.C. Wang and D.L. Kohlstedt, “Manganese Olivine I: Electrical Conductivity,” Phys. Chem. Minerals, **22** (8) [1995] 489-503.

[8] C. Stüber and W. Laqua, “Point Defects of Tephroite. I. The Electrical Conductivity of Mn_2SiO_4,” Z. Phys. Chem., **206** (1-2) [1998] 197-218.

[9] C. Stüber, “Point defect disorder and electrical conductivity in Mn_2SiO_4 (tephroite),” (in German), Doctoral thesis, University of Giessen, Germany, [1993].

[10] T.-L. Tsai, K.-D. Becker and R. Dieckmann, "Point Defects and Orientation-dependent Transport of Matter and Charge in Iron-containing Olivines," Solid State Ionics, **194** (1) [2011] 17-32.

[11] R.N. Schock, A.G. Duba and T.J. Shankland, “Electrical Conduction in Olivine,” J. Geophys. Res., **94** (B5) [1989] 5829-5839.

[12] M. Morioka, “Cation Diffusion in Olivines - III. Mn_2SiO_4 System,” Geochim. Cosmochim. Acta, **47** (12) [1983] 2275-2279.

[13] R. Sandner, “On the Possibility to Use Chemical Analytical Methods (Here: the Bunsen Method) for Determining the Point Defect Disorder in Mn_2SiO_4 (Tephroite),” (in German), Diploma Thesis, University of Giessen, Germany, [1986].

[14] R. Sandner, “Non-Stoichiometry and Disorder in Mn_2SiO_4,” (in German), Doctoral Thesis, University of Giessen, Germany, [1993].

[15] Q. Tang and R. Dieckmann, "Orientation, Oxygen Activity and Temperature Dependencies of the Diffusion of Cobalt in Cobalt Orthosilicate, Co_2SiO_4," Solid State Ionics, **212** [2012] 66-76.

[16] B.J. Wilson, "The Radiochemical Manual," 2nd Ed., The Radiochemical Centre, Amersham, 1966.

[17] J. Hermeling and H. Schmalzried, "Tracerdiffusion of the Fe-cations in Olivine ($Fe_xMg_{1-x}SiO_4$) (III)," Phys. Chem. Miner., **11** (4) [1984] 161-166.

[18] H.H. v. Baumbach, H. Dünwald and C. Wagner. "Conductivity Measurements on Cupric Oxide" (in German), Z. Physik. Chem., **B22** [1933] 226-230.

[19] R. Dieckmann, "Point Defects and Transport in Hematite ($Fe_2O_{3-\varepsilon}$)," Phil. Mag. A, **68** (4) [1993] 71-82.

CHAPTER 6

SUMMARY AND CONCLUDING REMARKS

This study was devoted to improve the current understanding of the point defect structure and of defect-related transport properties of transition metal-containing orthosilicates of the type Me_2SiO_4 with Me = Co and Mn. The diffusion of cobalt in cobalt orthosilicate, Co_2SiO_4, in equilibrium with SiO_2 and the diffusion of manganese in manganese orthosilicate, Mn_2SiO_4, in equilibrium with $MnSiO_3$ were experimentally studied as a function of oxygen activity, crystallographic orientation and temperature. Modeling of the oxygen activity dependence of the cation tracer diffusion and of point defect concentrations in cobalt orthosilicate and manganese orthosilicate was performed based on experimental observations from this study and relevant literature data.

Although the transport of matter and charge in olivine-type orthosilicates has been the subject of many previous studies, especially by Earth Scientists, using naturally occurring or synthetic olivine samples, this subject is not yet well understood. One underlying problem related to many previous studies is the use of samples with variations of chemical compositions and, more importantly, with relatively large impurity concentrations. In addition, defect-related transport properties of orthosilicates with olivine structure are orientation dependent. Consequently it is necessary to have high quality single crystals of such materials available.

In order to prepare samples fulfilling the needs for performing more meaningful studies of point defect-defect related transport properties of Co_2SiO_4 and Mn_2SiO_4, sizable single crystals of cobalt and manganese orthosilicate with intended silica excess were grown along the three principle orientations [100], [010] and [001] by using the floating-zone method. A sol-gel synthesis route was adopted for preparing high purity feed rods for growing these single crystals. A variety of techniques, including Laue back reflection, X-ray powder diffraction, transmission electron microscopy, scanning electron microscopy, optical microscopy and the ICP-AES technique, were used for characterization of grown single crystals. Results from the characterization efforts showed that the single crystals grown were of high purity, high quality and thermodynamically well defined, i.e., had a sufficient excess of SiO_2. The effect of alio-valent impurities present in the grown single crystals on the point defect population of orthosilicates was only relatively small due to the high crystal purity. In addition, the thermodynamic stability ranges of cobalt and manganese orthosilicate were reviewed for selecting temperatures and atmospheres for feed rod preparation, single crystal growth and studies of defect-related properties.

The radioactive isotopes Co-60 and Mn-54 were used to investigate the diffusion of transition metal cations in the grown cobalt and manganese orthosilicate single crystals by analyzing residual radioactivity profiles. Experimental data were obtained for the oxygen activity, orientation and temperature dependencies of the cobalt tracer diffusion in cobalt orthosilicate and of the manganese tracer diffusion in manganese orthosilicate.

The oxygen activity dependence of the diffusion of cobalt in Co_2SiO_4 was established for diffusion along the three principle orientations at 1300 °C in the oxygen activity range of $-8 \leq \log a_{O_2} \leq 0$. A close to 1/6 power dependence was obtained for the oxygen activity dependence of the tracer diffusion coefficient of Co diffusing in cobalt orthosilicate along the three principle orientations at high oxygen activities. A smaller oxygen activity dependence of the diffusion of cobalt was found at low oxygen activities. The observed oxygen activity dependence of the cobalt tracer diffusion in cobalt orthosilicate at high oxygen activities is compatible with cobalt vacancies and holes as majority defects. The smaller oxygen activity dependence of the cobalt tracer diffusion coefficients at lower oxygen activities is most likely due to an increased concentration of cobalt interstitials.

The oxygen activity dependence of the diffusion of manganese in Mn_2SiO_4 along the three principle orientations at 1200 °C was investigated in the oxygen activity range between $\log a_{O_2} = -13.2$ and -0.8. The tracer diffusion coefficient of manganese diffusing in manganese orthosilicate at 1200 °C was found to be proportional to $a_{O_2}^{1/2}$ at high oxygen activities. A similar oxygen activity dependence of cation tracer diffusion coefficients for a transition metal-containing orthosilicate was reported already earlier also for the diffusion of iron in Fe_2SiO_4 [1]. At lower oxygen activities, the oxygen activity dependence of the manganese tracer diffusion coefficient becomes smaller than that at higher oxygen activities and eventually becomes negative at very low oxygen activities. A similar observation of a smaller oxygen activity dependence of cation tracer diffusion coefficients at

lower oxygen activities was made in this study for the tracer diffusion of cobalt in Co_2SiO_4. The observed oxygen activity dependence of the manganese tracer diffusion in manganese orthosilicate indicates that at high oxygen activities the majority defects in manganese orthosilicate are most likely manganese vacancies and holes while at lower oxygen activities there are increased concentrations of manganese interstitials and electrons. In addition, the observed oxygen activity dependence of the manganese tracer diffusion in manganese orthosilicate at high oxygen activities suggests that at high oxygen activities manganese cations move via different types of manganese vacancies, most likely isolated manganese vacancies, and very mobile minority defects, possibly neutral associates formed between isolated manganese vacancies and holes localized at manganese sites.

Arrhenius-type temperature dependencies were found for the cobalt tracer diffusion in cobalt orthosilicate and the manganese tracer diffusion in manganese orthosilicate in the temperature ranges considered in this study. The values calculated for overall activation enthalpies, ΔH, vary with the direction of diffusion between about 350 and 400 kJ/mol for the diffusion of cobalt in cobalt orthosilicate between 1200 and 1300 °C at $a_{O_2} = 1$, and between 300 and 330 kJ/mol for the diffusion of manganese in manganese silicate between 1150 and 1250 °C at $\log a_{O_2} = -2.7$. A reliable determination of values for the enthalpy of motion, ΔH_m, requires the establishment of a suitable data set for the deviation from stoichiometry in cobalt orthosilicate covering a large temperature range and cobalt tracer diffusion data measured for a larger temperature range than that considered in this work. The defect modeling performed for manganese orthosilicate and the

modeling of the oxygen activity dependence of the tracer diffusion of manganese suggest that multiple defects are involved in the diffusion of Mn in Mn_2SiO_4. The data currently available for the diffusion of Mn in Mn_2SiO_4 and for point defect concentrations do not allow the determination of meaningful values for enthalpies of motion, ΔH_m.

The trends observed for the anisotropy of the cation tracer diffusion in cobalt and manganese orthosilicates are similar. It was found that $D^*_{Me[001]} > D^*_{Me[010]} > D^*_{Me[100]}$ at all oxygen activities for which tracer diffusion data are available for different crystal orientations. This observed trend is in agreement with results of an earlier investigation of the tracer diffusion of iron in iron orthosilicate [1]. However the ratios found for the cation tracer diffusion coefficients for the diffusion along different principle orientations are different for cobalt orthosilicate, manganese orthosilicate and iron orthosilicate. The largest ratio was found for tracer diffusion coefficients for the diffusion of Co in cobalt orthosilicate at $a_{O_2} = 1$, which is approximately $D^*_{Co[001]}:D^*_{Co[010]}:D^*_{Co[100]} = 27:3.4:1$ at 1300 ℃ while the ratio found for tracer diffusion coefficients of Mn diffusing in manganese silicate at $\log a_{O_2} = -2.7$ is approximately $D^*_{Mn[001]}:D^*_{Mn[010]}:D^*_{Mn[100]} = 5.3:2.2:1$ at 1200 ℃. For the iron tracer diffusion in iron orthosilicate at 1130 ℃ it was reported [1] that the ratio $D^*_{Fe[001]}:D^*_{Fe[010]}:D^*_{Fe[100]}$ varies a little with the oxygen activity with a mean value of this ratio of about 12:3:1. The agreement between the observed trends of anisotropy is no surprise since at the oxygen activities and temperatures for which ratios were given above, diffusion of transition metal cations via vacancies on

M-sites is dominant. An interesting, but unanswered question is that why the degree of anisotropy in the tracer diffusion of cations is different for various transition metal orthosilicates. Detailed computational investigations of this subject could possibly provide some insight into this topic.

Estimates of point defect concentrations as a function of oxygen activity were performed for cobalt and manganese orthosilicate by developing appropriate Kröger-Vink diagrams for a given total pressure of 1 atm and selected temperatures. The performed modelings of point defect concentrations are compatible with experimental observations for the cation tracer diffusion in the transition metal-containing orthosilicates considered in this study and with relevant literature data for variations in the oxygen content and for the electrical conductivity of cobalt and manganese orthosilicate. However, based on the current knowledge of defect-related properties of cobalt and manganese orthosilicate it is impossible to unequivocally determine the point defect structure of these oxides. Due to this problem the performed modelings should be considered more as guidelines for understanding of the trends in oxygen activity dependencies of point defect concentrations and of defect-related properties, rather than being taken by their face values.

To allow for a better modeling of the oxygen activity dependencies of point defect concentrations in and of defect-related properties of transition metal-containing orthosilicates, future systematic investigations of defect-related properties, such as the cation tracer diffusivity, the variation in the oxygen content

and the electrical conductivity over larger ranges of oxygen activity and temperature using thermodynamically well defined transition metal-containing orthosilicates with low impurity concentrations are necessary.

Reference

[1] T.L. Tsai, K.D. Becker and R. Dieckmann, “Point Defects and Orientation-dependent Transport of Matter and Charge in Iron-containing Olivines,” Solid State Ionics, **194** (1) [2011] 17-32.